SISSA
Scuola
Internazionale
Superiore di
Studi Avanzati

Physics Area - PhD course in
Theory and Numerical Simulation of Condensed Matter

Entanglement and Quantum Complexity in Monitored Quantum Many-Body Systems

Candidate:
Alessio Paviglianiti

Advisor:
Prof. Alessandro Silva

Academic Year 2024-2025

Abstract

Out-of-equilibrium quantum many-body systems stand at the forefront of modern theoretical physics, addressing fundamental questions on thermalization, transport, and universal phenomena. These fields, already well established in condensed matter, statistical physics, quantum optics, and quantum information theory, are progressively gaining even greater relevance with the rapid development of quantum technologies and simulation, which inherently operate in dynamical regimes. In recent years, the traditional paradigm of unitary quantum evolution has been expanded to include measurements, opening new directions in out-of-equilibrium physics. At the core of these advances lie measurement-induced phase transitions (MIPTs), which have emerged as a new class of dynamical critical phenomena characterizing the general behavior of monitored quantum dynamics. When external monitoring intertwines with unitary evolution, many-body quantum correlations change their structure, giving rise to distinct entanglement phases of matter. This discovery has sparked enormous interest in MIPTs, leading to significant advances in open quantum systems, entanglement theory, and more broadly quantum complexity.

Despite much progress, a full understanding of monitored many-body dynamics is far from complete, leaving several open questions on the nature of MIPTs, their experimental observability, and the possibilities offered by measurements to enhance control over synthetic quantum matter. These issues persist due to the intrinsic complexity of the problem and the lack of efficient tools to study it, mainly caused by the stochastic character of monitored evolution. This thesis addresses these challenges by expanding the investigation of measurement-induced phenomena in new settings and introducing innovative probes of entanglement and many-body quantum complexity for MIPTs. A core question we investigate is the role of symmetries, non-ergodicity, and especially integrability in measurement-induced criticality, which dramatically affect the non-equilibrium phases. We further explore how these phenomena extend beyond bipartite quantum correlations to multipartite entanglement and quantum non-stabilizerness, highlighting the non-trivial interplay between measurements and complexity notions rooted in quantum information theory. Finally, we focus on the compelling problem of decoherence, modeling how noise spoils entanglement structures.

These findings, supported by advanced numerical simulations and theoretical analysis, deepen the current understanding of entanglement, complexity, and integrability in monitored quantum many-body systems, offering new perspectives on their rich behavior. In parallel, we address the experimental problem of dissipation in MIPTs, which is of key relevance for practical implementations. We anticipate the present investigation to foster future research on the nature of monitored dynamical critical phenomena and, more broadly, the applications of measurements in quantum state evolution.

List of publications

The topics presented in this thesis are based on the following publications.

[1] **A. Paviglianiti**, A. Silva,
Multipartite entanglement in the measurement-induced phase transition of the quantum Ising chain,
Physical Review B, **108**, 184302 (2023), selected as Editors' Suggestion.

Chapter 3

[2] **A. Paviglianiti**, X. Turkeshi, M. Schirò, A. Silva,
Enhanced Entanglement in the Measurement-Altered Quantum Ising Chain,
Quantum, **8**, 1576 (2024).

Chapter 5

[3] **A. Paviglianiti**, G. Lami, M. Collura, A. Silva,
Estimating Nonstabilizerness Dynamics Without Simulating It,
PRX Quantum, **6**, 030320 (2025).

Chapter 8

[4] **A. Paviglianiti**, G. Di Fresco, A. Silva, B. Spagnolo, D. Valenti, A. Carollo,
Breakdown of Measurement-Induced Phase Transitions Under Information Loss,
Quantum, **9**, 1781 (2025).

Chapter 4

[5] **A. Paviglianiti**, A. Silva,
Enhancing Revivals Via Projective Measurements in a Quantum Scarred System,
Physical Review Letters, **135**, 090402 (2025).

Chapter 9

[6] E. Tirrito, L. Lumia, **A. Paviglianiti**, G. Lami, A. Silva, X. Turkeshi, M. Collura,
Magic phase transitions in monitored gaussian fermions,
arXiv:2507.07179 (2025).

Chapter 6

[7] **A. Paviglianiti**, L. Lumia, E. Tirrito, A. Silva, M. Collura, X. Turkeshi, G. Lami,
Emergence of Generic Entanglement Structure in Doped Matchgate Circuits,
arXiv:2507.12526 (2025).

Chapter 7

Introduction

Since its inception around a century ago, quantum mechanics has revolutionized our understanding of the laws of Nature, shaping the development of modern science and technology. Quantum systems are governed by rules that are foreign to the classical world, introducing fundamental concepts such as state uncertainty and *entanglement* [8, 9]. In many-body systems, these principles enable the emergence of rich and complex *out-of-equilibrium* behavior. The broad problem of quantum dynamics has become one of the most fascinating and insightful frontiers of contemporary physics, encompassing key fields including thermalization [10–16], quantum thermodynamics [17–19], non-equilibrium universality [20, 21], and localization [22–26]. While many paradigms describing the evolution of quantum systems are now well established, exploring quantum dynamics poses an outstanding challenge due to the intrinsic complexity of quantum states, leaving several fundamental questions still unanswered despite decades of progress. Crucially, the interest in non-equilibrium quantum systems extends far beyond the realm of theoretical physics, finding major applications in experimental studies and, especially, technological implementations. In recent years, remarkable advances in quantum computing and simulation [27–30] have enabled unprecedented control over synthetic quantum matter. Noisy intermediate-scale quantum devices [31–33] now allow the direct exploration of paradigmatic models of quantum statistical physics, such as the Ising chain [34–38], with never-before-seen coherence times and fidelity. Quantum simulators operate in regimes that are intrinsically far from equilibrium, as quantum operations are implemented through sequences of gates that evolve the state. For these reasons, developing a deep understanding of many-body dynamics and its mechanisms is essential not just for science, but also for the development of next-generation quantum technologies.

The investigation of quantum dynamics is not restricted to isolated systems, but extends to the realm of *open quantum systems* [39–41]. The evolution of quantum particles can be significantly altered by coupling to an environment, inducing state mixing, decoherence, and relaxation toward a stationary regime. These phenomena can even be leveraged to engineer non-equilibrium phases of matter and dissipative phase transitions [42–44] with distinct properties from their unitary counterparts. The main theoretical framework to model open systems is provided by the Lindblad master equation [39, 45, 46], which forms the foundation for characterizing dissipation in quantum optics, condensed matter, and quantum computing platforms. While this approach fully describes the evolution of quantum observables, it is insufficient for capturing *non-linear* functionals of the state, including connected two-point correlations, entanglement, and signatures of non-equilibrium critical-

ity. However, such non-linear properties are essential, as their behavior determines *measurement-induced phase transitions* (MIPTs) [47–69], a recently discovered class of non-equilibrium critical phenomena that cannot be seen at the level of the Lindblad equation. These transitions arise in *monitored* quantum many-body systems, where unitary dynamics is perturbed by non-unitary, stochastic measurements, and exhibit critical behavior in the properties of typical random trajectories. In this context, the role of measurements extends beyond merely extracting information, making them active elements that evolve the state.

MIPTs have been under intense investigation since their discovery and remain an extremely active area in the study of non-equilibrium many-body systems. These transitions elude the conventional framework of statistical physics, which is based on order parameters, free energy landscapes, and spontaneous symmetry breaking. Instead, they have a fundamentally distinct identity rooted in the *quantum information* content of many-body wavefunctions, most notably given by the entanglement entropy [8, 9, 70–72]. In generic systems, measurements act as disentangling operations, typically inducing a transition from volume-law to area-law entangled phases, controlled by the monitoring rate. This paradigm, now relatively well understood, has since been extended to different probes of measurement-induced criticality, including state purity [51, 73–75], quantum fluctuations [76–80], and quantum non-stabilizerness [81–88]. Despite these advances, developing a complete description of MIPTs remains a formidable task, mainly owing to the stochastic and far-from-equilibrium nature of the dynamics. Crucial insights have been obtained through random quantum circuit [48, 50, 89, 90] and replica Keldysh field-theoretical approaches [91–96], yet the search for exactly-solvable models of measurement-induced phenomena is still ongoing. Monitored many-body systems also pose major challenges on the experimental side. The stochastic nature of the evolution demands a probabilistic sampling over an exponentially large number of quantum trajectories, an issue known as the *postselection problem*. Furthermore, extracting non-linear quantities such as entanglement adds a second layer of exponential complexity, often requiring state tomography techniques [97, 98]. As a result, cutting-edge experimental investigations struggle with scalability [99–101], and sometimes rely on hybrid approaches that combine hardware data with classical simulations to mitigate resource overhead [102, 103].

The work presented in this thesis focuses on expanding the understanding of monitored many-body systems by addressing key open questions on the nature and manifestations of MIPTs. A major driving point of this research is the exploration of the role of integrability [104–109] in entanglement transitions, particularly in relation to the Gaussian nature of non-interacting fermionic systems [110–119]. In fact, contrary to generic models, it is now understood that monitored free fermions do not exhibit any volume-law entangled phase at any finite measurement rate, and may instead give rise to a logarithmic phase depending on other symmetries [49, 55–57, 91, 92, 94]. In parallel, we investigate which probes of correlations and quantum complexity, beyond entanglement, exhibit signatures of measurement-induced critical behavior, as well as what kinds of novel non-equilibrium phenomena can emerge when a many-body system undergoes non-unitary dynamics. We further study how external monitoring affects the structure of quantum correlations, potentially giv-

ing rise to patterns and scalings that are atypical of standard quench dynamics or ground-state properties. Finally, we analyze the impact of decoherence on MIPTs, which is of fundamental importance for any experimental implementation.

To explore these directions, we combine analytical tools in exactly-solvable models and large-scale numerical simulations, employing techniques such as fermionic Gaussian states, stabilizer (Clifford) circuits [120–124], and tensor networks [125–129]. Beyond the conventional von Neumann entropy for bipartite entanglement, we focus on different quantum information-theoretic notions, most notably *multipartite entanglement* and the quantum Fisher information (QFI) [8, 130–135], which probe the long-range nature of quantum correlations, as well as non-stabilizerness or *magic*, quantifying the complexity of states relative to efficiently-simulable stabilizer codes. Through this approach, we aim to achieve a well-rounded characterization of monitored many-body systems. This not only lays the groundwork for future theoretical developments on dynamical phase transitions and quantum complexity, but also paves the way to potential practical implementations, as non-unitary evolution realized by measurements offers a promising path for enhancing control over quantum devices.

This thesis is organized as follows. The first two chapters provide the necessary background on the main topics addressed in the subsequent sections. In detail, Chapter 1 introduces key concepts of entanglement and complexity in *closed* many-body systems. The aim is to present the main notions, such as entanglement entropy, stabilizer Rényi entropies (SREs), and Gaussianity, that play a central role throughout the thesis. At the same time, we establish the behavior of these quantities under unitary dynamics, setting the stage for understanding how measurements affect their evolution. Chapter 2 then offers a general overview of open quantum systems. Starting from the Kraus operator formalism, we proceed through the Lindblad master equation and, eventually, address MIPTs. We review the key results on monitored dynamics currently established in the literature, thereby clarifying the context in which the present research develops.

As mentioned previously, one of the central questions of this thesis is understanding how the presence of symmetries due to integrability alters the physics of MIPTs. To this end, non-interacting fermionic systems provide a powerful framework to investigate monitored dynamics and benchmark it against generic random circuits. This allows for the use of analytical tools based on quasiparticle descriptions, and enables efficient large-scale numerical simulations that are essential to distinguish genuine entanglement scaling behavior from finite-size effects. In Chapter 3, we investigate MIPTs in the paradigmatic quantum Ising chain in a transverse field, implementing a continuous monitoring protocol that preserves the free-fermionic nature of the dynamics. Moving beyond the conventional study of the entanglement entropy, we focus on multipartite quantum correlations witnessed by the QFI. We demonstrate that the QFI not only exhibits a MIPT, but also reveals a richer non-equilibrium phase diagram compared to that of the entanglement entropy. In detail, measurements drive a transition between regimes where correlations are short-ranged and where entanglement extends to long distances.

The main experimental challenge in probing measurement-induced phenomena lies in the need to reproduce a given quantum trajectory multiple times to access its

non-linear features. These properties are obscured when observables are averaged over random measurement outcomes according to the Born rule. This suggests that decoherence, arising from the mixing of different quantum trajectories, can progressively mask MIPTs. Chapter 4 is dedicated to investigating this problem. Building on our previous results on the monitored Ising chain, we examine how partial information loss of measurement outcomes impacts the critical correlations of the state. The purpose of this study is twofold: on one hand, it models decoherence in monitored systems, which is essential for any realistic implementation; on the other, it addresses whether the postselection problem can be mitigated by relaxing the constraint of focusing solely on single realizations and allowing for a controlled degree of trajectory averaging. We find that any finite rate of information loss suppresses long-range correlations, gradually interpolating toward the Lindblad limit, where no signature of measurement-induced criticality remains.

In the following Chapter 5, we shift focus to a different setting where given quantum states, such as quantum Ising ground states, are perturbed by projective measurements without any form of unitary dynamics. This framework, known as that of projected ensembles, enables the investigation of how measurements alone reshape the structure of quantum correlations, possibly giving rise to novel patterns and effects. In particular, we show how this protocol can enhance entanglement by generating new quantum correlations in atypical random realizations, as well as by extending their spatial range.

While the most striking manifestation of MIPTs appears in entanglement, other probes can also exhibit a dynamical transition. One such probe is quantum magic, quantified by SREs, which measures the classical complexity of tracking a state using the stabilizer tableau formalism. In condensed matter systems governed by Hamiltonian evolution, the dynamics of magic is typically trivial, showing a rapid initial growth followed by volume-law saturation. In Chapter 6, focusing on various free-fermionic systems, we show that subtle signatures of measurement-induced criticality emerge in the *subleading* scaling behavior of magic. Specifically, while the SREs retain their linear scaling with system size for all measurement rates, we observe a logarithmic correction that vanishes beyond a critical monitoring strength. These results highlight that external monitoring influences quantum dynamics beyond entanglement, impacting broader notions of many-body complexity.

So far, we have focused on Gaussian dynamics generated by free-fermionic Hamiltonians, which cannot induce interactions. As mentioned, this constraint alters dramatically the phenomenology of MIPTs, notably by preventing the emergence of a volume-law phase for the entanglement entropy. In the next chapters, we move beyond this paradigm by considering circuit and Hamiltonian models that incorporate non-Gaussian resources.

To explore the gradual crossover from free- to interacting fermionic behavior, Chapter 7 investigates how the entanglement structure generated by random circuits composed of Gaussian two-qubit unitaries changes upon the insertion of non-Gaussian gates, both with and without measurements. To keep the problem analytically and numerically tractable, we restrict to the class of stabilizer circuits, focusing on Clifford-Gaussian circuits doped with Clifford but non-Gaussian resources. We find that several features unique to Gaussian dynamics, such as diffusive entangle-

ment growth and the presence of a measurement-induced logarithmic phase, evolve as non-Gaussianity increases, progressively giving way to generic many-body behavior. Our results, supported by large-scale numerics and analytical insights from a mapping to a classical model, highlight the crucial role of fermionic interactions in enabling complex entanglement patterns unattainable through Gaussian dynamics alone.

In Chapter 8, we address the broad problem of non-stabilizerness dynamics in random quantum circuits. This is a notoriously challenging task due to the lack of efficient numerical tools for studying circuits beyond the Clifford group. To address this, we propose a classical algorithm that significantly simplifies the framework by enabling the calculation of magic measures without explicitly simulating the time evolution of quantum states, which is often the main computational bottleneck. This is achieved by iteratively restructuring the circuit geometry and gradually mapping it to an equivalent Clifford representation, where the entire magic dynamics is captured by a renormalization flow of an effective initial state. As a result, we unlock the study of SREs across a broad class of unitary and monitored settings at unprecedented system sizes. Leveraging this formalism, we investigate how magic stored in an initial state decays under monitored Clifford dynamics, revealing a dynamical purification transition controlled by the measurement rate.

In monitored many-body systems, the randomness introduced by measurements typically erases memory of initial conditions, driving the dynamics toward stationary regimes that retain no dependence (apart from global symmetries) on the starting state. To some extent, this effect is also present in purely unitary dynamics, where quantum information scrambling [136–139] leads to local thermalization. A natural question is how measurements affect *non-ergodic* systems [140–144], which inherently preserve memory of their starting conditions and evade thermalization at late times. Chapter 9 is dedicated to addressing this problem in the paradigmatic PXP model [145–152], a minimal description of Rydberg atom arrays that hosts many-body quantum scars. For particular initial states, the PXP dynamics exhibits anomalously long-lived oscillations of observables and revivals in state fidelity. Remarkably, measurements give rise to a dual phenomenology: when applied randomly in time, they restore equilibration, signaling a loss of memory; in contrast, when measurements are synchronized with the periodicity of the unitary dynamics, they enhance non-ergodic behavior, reinforcing the athermal character of the evolution. This not only shows that quantum scars interact with measurements in a highly non-trivial way, but also demonstrates that a time-structured monitoring can actively support coherent many-body behavior.

The physics of monitored many-body systems is remarkably rich, yet remains challenging to fully characterize, leaving several open questions. To conclude, Chapter 10 outlines promising directions for future investigations building upon the present research.

Contents

Chapter 1

Entanglement and many-body complexity

This chapter introduces the foundational concepts of entanglement and quantum complexity that form the basis for the analysis of measurement-induced criticality throughout this thesis. The discussion serves two main purposes. First, we review the most commonly used measures of entanglement and their behavior in closed quantum systems, both in and out of equilibrium, establishing the standard scaling laws (such as area, logarithmic, and volume laws for the entanglement entropy) typically encountered in condensed matter settings. This provides a benchmark for comparison with monitored dynamics. Second, we present two key formalisms employed in this thesis: fermionic Gaussian states and Clifford circuits. These frameworks enable efficient numerical simulations of many-body systems, used extensively throughout this work. Moreover, these paradigms naturally define notions of quantum complexity based on their inability to represent generic quantum states, thereby distinguishing between "easy" and genuinely complex states.

1.1 Entanglement in many-body systems

Entanglement [8, 9] is a cornerstone of quantum physics, encapsulating the notion that particles can exist in quantum correlated states. At its core, it reflects the impossibility of fully describing each constituent of a system individually without accounting for the presence of the others, no matter the way (i.e., the basis) we look at it. This intrinsic feature gives rise to many uniquely quantum phenomena, from teleportation [28, 153] to superconductivity [154], that have no analogue in classical physics.

In recent years, significant emphasis has been placed on developing tools to quantify entanglement. These efforts, typically rooted in quantum resource theory [155, 156], have lead to the discovery of a variety of entanglement measures and witnesses. From the perspective of quantum information, entanglement is viewed as a fundamental property that can be harnessed to implement specific tasks, for instance in quantum computation. Beyond this, different entanglement measures, most notably the entropy, are now routinely used in condensed matter and statistical physics to detect phases of matter [26, 70], topological order [157–159], and dynamical behavior [23, 72, 160–162].

The existence of entanglement was first demonstrated decades ago in a groundbreaking experiment confirming the violation of the Bell inequalities [163]. Today, advances in quantum control allow for its direct experimental quantification using

techniques such as quantum state tomography [97], classical shadows [98], or replica interference methods [164, 165]. Entangled states can now be prepared reliably across a range of platforms, and they play a central role in quantum metrology [166, 167], where they enhance the precision of parameter estimation protocols.

This section introduces three central entanglement measures that will appear throughout the thesis: the entanglement entropy, the quantum Fisher information (QFI), and the entanglement negativity. We also summarize their characteristic behavior in various standard states, which are now well established in both equilibrium and dynamical settings.

1.1.1 Entanglement entropy

Entanglement can be characterized as the distribution of quantum information over many degrees of freedom, in the sense that certain nonlocal correlations are lost when a state is observed only locally. To illustrate this, consider a bipartite quantum system composed of two parties, A and B, with associated Hilbert spaces $\mathcal{H}_A$ and $\mathcal{H}_B$, respectively. Any pure state $|\psi_{A,B}\rangle$ of the composite Hilbert space $\mathcal{H}_{A,B} = \mathcal{H}_A \otimes \mathcal{H}_B$ can be expanded as

$$|\psi_{A,B}\rangle = \sum_{j=1}^{D} \lambda_j \left|\varphi_j^A\right\rangle \otimes \left|\varphi_j^B\right\rangle, \tag{1.1}$$

known as the *Schmidt decomposition*. Here, $\lambda_j \in (0, 1]$ are the Schmidt coefficients, whose number is bounded by $D \leq \min\{\dim(\mathcal{H}_A), \dim(\mathcal{H}_B)\}$, and they satisfy the normalization condition $\sum_j \lambda_j^2 = 1$. The sets $\{\left|\varphi_j^A\right\rangle\}$ and $\{\left|\varphi_j^B\right\rangle\}$ form orthonormal bases belonging to $\mathcal{H}_A$ and $\mathcal{H}_B$, respectively. The local properties of subsystem A are fully encoded in the reduced density matrix

$$\hat{\rho}_A = \mathrm{Tr}_B \left|\psi_{A,B}\right\rangle \left\langle\psi_{A,B}\right| = \sum_{j=1}^{D} \lambda_j^2 \left|\varphi_j^A\right\rangle \left\langle\varphi_j^A\right|, \tag{1.2}$$

obtained by tracing out the degrees of freedom of B. For any $D > 1$, this is a mixed state: subsystem A contains contributions form different pure states $\left|\varphi_j^A\right\rangle$, weighted by probabilities λ_j^2, and thus $\hat{\rho}_A$ does not correspond to any single state in $\mathcal{H}_A$. This degree of uncertainty reflects the presence of entanglement: tracing over subsystem B misses nonlocal correlations between A and B, preventing a complete deterministic description of A alone. In contrast, when $D = 1$ the state reduces to the separable form $|\psi_{A,B}\rangle = |\varphi_A\rangle \otimes |\varphi_B\rangle$, and no entanglement is shared between the parties.

Bipartite entanglement can thus be quantified based on how much information is lost when part of the system is traced out, or equivalently how mixed the resulting reduced density matrix becomes. This is captured by the Rényi entropies

$$S_A^{(n)} = -\frac{1}{1-n} \log\left(\mathrm{Tr}\, \hat{\rho}_A^n\right), \tag{1.3}$$

with $n > 1$. Taking the limit of $n \to 1$, this expression reduces to the well-known entanglement entropy [9]

$$S_A = -\,\mathrm{Tr}(\hat{\rho}_A \log \hat{\rho}_A), \tag{1.4}$$

defined as the von Neumann entropy of $\hat{\rho}_A$. It can be easily shown that the entanglement entropy is a property of the bipartition, and thus satisfies $S_A = S_B$. Moreover, for pure states S_A meets all the criteria to qualify as a proper measure of entanglement, as established by quantum resource theory [155, 156]. First, it vanishes if and only if the state is separable, and it is strictly positive otherwise. Second, it is monotonic under local operations and classical communication (LOCC), meaning that such transformations cannot increase entanglement. Beyond these essential features, it also possesses other desirable properties, including convexity, additivity, and continuity.

For a many-body system of L components, such as spins or lattice sites, the entanglement entropy can be used to measure the bipartite quantum correlations between a subsystem $A \subset \{1, \dots, L\}$ (usually corresponding to a compact region) and its complementary. As discussed later, analyzing the scaling behavior of S_A as a function of the subsystem size $|A|$ is a powerful tool to characterize distinct phases of matter, both in ground states and in monitored dynamics. The main limitation of the entanglement entropy is that it does not provide a reliable measure of quantum correlations for mixed states. Indeed, if the composite system is described by a mixed density matrix $\hat{\rho}_{A,B}$, the reduced density matrix $\hat{\rho}_A$ can be mixed even in the absence of entanglement, simply because the global state is not pure. As a consequence, S_A cannot be used to quantify bipartite correlations between two subsystems A and B that do not span the entire system. This problem can be addressed using alternative quantities, such as the mutual information [8, 168], whose definition is based on the entropy, or the entanglement negativity [8, 169–171] discussed in the following subsection.

Besides its operational use, entanglement can be regarded as a first notion of quantum complexity. While separable states are fully specified by $\mathcal{O}(L)$ parameters (e.g., the angles on the Bloch sphere for spin-1/2 qubits), highly-entangled states generally need storing the full wavefunction, which contains a number of amplitudes exponentially large in L. This concept is central to matrix product states (MPSs) [127–129], which represent entangled states using tensors whose sizes are controlled by the bond dimension χ. In general, higher entanglement implies a larger χ [1], and thus requires bigger tensors to store a state faithfully. This induces a natural distinction between "easy" states, which can be stored efficiently as MPSs, and genuinely complex ones, for which classical simulation becomes infeasible.

1.1.2 Entanglement negativity

Another important measure of entanglement is given by the negativity [8, 9, 169–171], which can be applied to mixed states as well. First, let us generalize the notion of separability to mixed state. Given a composite system of two parties A and B, a state is defined to be separable if its density matrix can be written as

$$\hat{\rho}_{A,B}^{\text{sep}} = \sum_j p_j \hat{\rho}_{A,j} \otimes \hat{\rho}_{B,j}, \tag{1.5}$$

[1] Specifically, χ is controlled by the number of non-zero (or non-negligible) Schmidt coefficients λ_j.

where $\hat{\rho}_{A,j}$ and $\hat{\rho}_{B,j}$ are proper density matrices (not necessarily pure) for the corresponding subsystems. Let us introduce two bases $\{\left|\varphi_j^A\right\rangle\}$ and $\{\left|\varphi_j^B\right\rangle\}$ of $\mathcal{H}_A$ and $\mathcal{H}_B$, respectively. Given a generic density matrix expanded as

$$\hat{\rho}_{A,B} = \sum_{i,j,m,n} \rho_{i,j;m,n} \left|\varphi_i^A\right\rangle \left\langle\varphi_j^A\right| \otimes \left|\varphi_m^B\right\rangle \left\langle\varphi_n^B\right|, \tag{1.6}$$

we define its partial transpose as

$$\hat{\rho}_{A,B}^{T_A} = \sum_{i,j,m,n} \rho_{i,j;m,n} \left|\varphi_i^A\right\rangle \left\langle\varphi_j^A\right| \otimes \left(\left|\varphi_m^B\right\rangle \left\langle\varphi_n^B\right|\right)^T = \sum_{i,j,m,n} \rho_{j,i;m,n} \left|\varphi_i^A\right\rangle \left\langle\varphi_j^A\right| \otimes \left|\varphi_m^B\right\rangle \left\langle\varphi_n^B\right|, \tag{1.7}$$

where the transposition is taken only with respect to basis elements of A. This notion can be used to define mixed-state entanglement based on the *Peres-Horodecki criterion* [172], stating that the partial transpose of any separable $\hat{\rho}_{A,B}^{\text{sep}}$ has non-negative spectrum. In other words, finding that $\hat{\rho}_{A,B}^{T_A}$ has one or more negative eigenvalue is a sufficient condition for the presence of bipartite entanglement.

This criterion enables the quantification of entanglement based on the extent to which the eigenvalues of the partial transpose become negative. We define the logarithmic entanglement negativity as

$$\mathcal{E}_A = \log ||\hat{\rho}_{A,B}^{T_A}|| = \log \left(\sum_j |\lambda_j| \right), \tag{1.8}$$

where $||\bullet||$ denotes the trace norm, and λ_j are the eigenvalues of $\hat{\rho}_{A,B}^{T_A}$. As for the entropy, $\mathcal{E}_A = \mathcal{E}_B$. For separable states, all λ_j are non-negative, and the logarithmic negativity vanishes due to the trace condition $\sum_j \lambda_j = 1$. In contrast, if one or more eigenvalue is negative the same constraint implies $\sum_j |\lambda_j| > 1$, resulting in non-zero entanglement. It is important to note that the Peres-Horodecki criterion provides only a sufficient condition for entanglement, not a necessary one. In general, there exist non-separable states whose partial transposes have non-negative spectra, leading to a vanishing logarithmic negativity. This is possible because $\mathcal{E}_A$ specifically captures *distillable* entanglement [9, 173], which refers to the possibility to extract maximally entangled states from multiple copies of the original one through LOCC. Despite this, the logarithmic negativity remains a valid entanglement measure within quantum resource theory, offering a complementary characterization to that of the entanglement entropy.

Physically, the Peres-Horodecki criterion can be interpreted by viewing transposition as the operation corresponding to time reversal. For separable states, applying time reversal to only part of the system still yields a valid state, and thus $\hat{\rho}_{A,B}^{T_A}$ must have a non-negative spectrum. In contrast, where the two subsystem are entangled the partial transpose may be unphysical, as signaled by negative eigenvalues. Following this interpretation, the definition of Eq. (1.8) applies to bosonic and spin systems, but it is inadequate for fermions due to their anticommutative nature. This lead to the introduction of the *twisted* partial transpose $\hat{\rho}_{A,B}^{\tilde{T}_A}$, based on the notion of fermionic time reversal, and of the fermionic logarithmic negativity [174–178] $\mathcal{N}_A = \log ||\hat{\rho}_{A,B}^{\tilde{T}_A}||$. We will discuss this quantity properly in Sec. 1.2.3 after introducing the framework of fermionic systems.

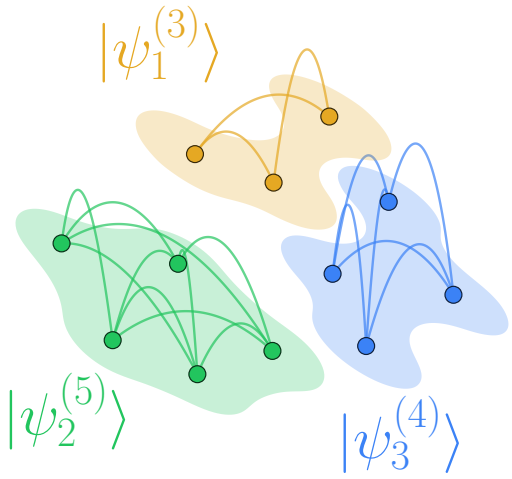

Figure 1.1: Cartoon illustrating the notion of k-producibility. Individual particles, denoted by spheres, are connected by arcs that represent quantum correlations. This is an example of a 5-producible state, as it can be factorized in clusters whose maximum size is 5.

1.1.3 Quantum Fisher information

So far we have addressed the problem of *how strong* bipartite entanglement is. A different way of characterizing quantum correlations poses instead the different question of *how many* constituents of a many-body system are entangled with each other. This point of view leads to the notion of multipartite entanglement[8, 9, 130–135]. Given a system of L elementary components, we define a k-producible state $|\psi\rangle \in \mathcal{H}$ if it can be written as $|\psi_{k\text{-prod}}\rangle = \otimes_{j=1}^{M} \left|\psi_j^{(n_j)}\right\rangle$, where $\left|\psi_j^{(n_j)}\right\rangle$ denotes a state of $n_j \leq k$ parties, and $\sum_{j=1}^{M} n_j = L$. Essentially, this state is separable in clusters of particles whose sizes n_j do not exceed k, as schematized in the cartoon of Fig. 1.1. From this definition, product states are 1-producible. Finally, a state is said to be k-partite entangled if it is k-producible but not $(k-1)$-producible, i.e., the size of the largest irreducible cluster is equal to k. The number k measures how widespread quantum correlations are, quantifying the minimum number of simultaneously entangled elements. The notion of multipartite entanglement is straightforwardly extended to mixed state, defining a k-producible density matrix as $\hat{\rho}_{k-\text{prod}} = \sum_j p_j \left|\psi_{k_j\text{-prod}}\right\rangle \left\langle\psi_{k_j\text{-prod}}\right|$ with $k_j \leq k$.

The previous definition of multipartite entanglement is impractical to calculate, as it requires to find the optimal basis representation of a state that highlights the true value of k. The QFI is a probe sensitive to multipartite quantum correlations that can also be evaluated explicitly in many-body settings. Given a density matrix, let $\hat{\rho} = \sum_j \lambda_j |\psi_j\rangle \langle\psi_j|$ be its diagonal representation in terms of its eigenvalues λ_j

and eigenstates $|\psi_j\rangle$. For any arbitrary Hermitian operator $\hat{O}$, we define the QFI of $\hat{\rho}$ as

$$F_Q[\hat{\rho}; \hat{O}] = 2 \sum_{i,j} \frac{(\lambda_i - \lambda_j)^2}{\lambda_i + \lambda_j} \left| \langle \psi_i | \hat{O} | \psi_j \rangle \right|^2, \tag{1.9}$$

where the sum runs only over indices such that $\lambda_i + \lambda_j > 0$. Remarkably, Eq. (1.9) simplifies drastically for pure states, in which case

$$F_Q[|\psi\rangle \langle\psi| ; \hat{O}] = 4 \mathrm{Var}[\hat{O}]_\psi = 4 \left(\langle \psi | \hat{O}^2 | \psi \rangle - \langle \psi | \hat{O} | \psi \rangle^2 \right). \tag{1.10}$$

The connection between the QFI and multipartite entanglement is established by the following criterion, proposed independently by Refs. [131, 132]. For spin 1/2 systems, consider the family of local operators

$$\hat{O}[\{\mathbf{n}_j\}] = \frac{1}{2} \sum_j \mathbf{n}_j \cdot \hat{\boldsymbol{\sigma}}_j, \tag{1.11}$$

where $\hat{\boldsymbol{\sigma}}_j = (\hat{\sigma}_j^x, \hat{\sigma}_j^y, \hat{\sigma}_j^z)$ is the array of Pauli operators, and $\mathbf{n}_j = (n^x, n^y, n^z)$ are unit vectors satisfying $||\mathbf{n}_j|| = 1$. When evaluated with respect to these operators, the QFI of a k-producible state is bounded by

$$F_Q \left[\hat{\rho}_{k-\mathrm{prod}}; \hat{O}[\{\mathbf{n}_j\}] \right] \leq sk^2 + r^2, \tag{1.12}$$

where $s = \lfloor L/k \rfloor$ is the integer part of L/k, and $r = L - sk$ is its remainder. This bound enables the estimation of multipartite entanglement: any violation of the inequality implies that the state is not k-producible, making it at least $(k+1)$-partite entangled. Equation (1.12) assumes a simplified form when k is a divider of L, in which case it reduces to

$$f_Q \left[\hat{\rho}_{k-\mathrm{prod}}; \hat{O}[\{\mathbf{n}_j\}] \right] = \frac{1}{L} F_Q \left[\hat{\rho}_{k-\mathrm{prod}}; \hat{O}[\{\mathbf{n}_j\}] \right] \leq k. \tag{1.13}$$

Hence, the QFI density f_Q serves as a probe of multipartite quantum correlations, as its value provides a direct estimate of how broadly quantum correlations extend across the system. Nevertheless, the QFI is only a *witness* of entanglement rather than a proper measure: the inequality only sets a lower bound on the degree multipartiteness, which could be higher than the value suggested by the previous criterion.

The inequality of Eq. (1.12) holds for any operator in the form of Eq. (1.11). As a consequence, different choices of $\hat{O}[\{\mathbf{n}_j\}]$ provide inequivalent estimates of multipartite entanglement. One can obtain the strictest possible bound by maximizing the QFI over the family of operators, i.e., over the unit vectors $\mathbf{n}_j$. In many practical situations, the state of interest may translational or even permutational invariance, which simplifies the task by assuming that the optimal $\hat{O}[\{\mathbf{n}_j\}]$ that maximizes the QFI mirrors the symmetry of the system. This possibly enables analytic estimates of multipartite entanglement. In general, disordered cases, however, the optimization must be carried out numerically. For pure states, the QFI density reduces to the simple form

$$f_Q \left[|\psi\rangle \langle\psi| ; \hat{O}[\{\mathbf{n}_j\}] \right] = \sum_{\alpha,\beta=x,y,z} \sum_{i,j} n_i^\alpha C_{i,j}^{\alpha,\beta} n_j^\beta, \tag{1.14}$$

where

$$C_{i,j}^{\alpha,\beta} = \langle\psi|\,\hat{\sigma}_i^\alpha \hat{\sigma}_j^\beta\,|\psi\rangle - \langle\psi|\,\hat{\sigma}_i^\alpha\,|\psi\rangle\,\langle\psi|\,\hat{\sigma}_j^\beta\,|\psi\rangle \tag{1.15}$$

are connected spin-spin correlators. Equation (1.14) is a quadratic functional of the vector variables $\mathbf{n}_j$, which can be maximized using heuristic algorithms such as simulated annealing [179, 180]. In many cases, f_Q exhibits multiple local maxima that lie close to the global one, complicating the optimization process. However, obtaining the true maximum is not strictly necessary, as near-optimal local maxima yield similar estimates of multipartite entanglement.

The QFI plays a central role in quantum metrology [166, 167], which addresses the problem of estimating a phase parameter θ from an evolved state of the form $\hat{\rho}_\theta = e^{-i\hat{H}\theta}\hat{\rho}_0 e^{i\hat{H}\theta}$. In this setting, the variance $(\Delta\theta)^2$ of any estimator is lower bounded by the quantum Cramér-Rao bound

$$(\Delta\theta)^2 \geq \frac{1}{MF_Q[\hat{\rho}_\theta;\hat{H}]}, \tag{1.16}$$

where M is the number of independent repetitions of the experiment. For operators $\hat{H}$ in the form of Eq. (1.11), it can be easily shown that separable states have $F_Q[\hat{\rho}^{\text{sep}};\hat{H}] \leq L$. In contrast, multipartite entangled states can show a different scaling, in general bounded by $F_Q[\hat{\rho};\hat{H}] \leq L^2$: this allows to push the quantum Cramér-Rao bound to much smaller values, thus indicating that multipartite entanglement enables greater precision in metrological applications.

In condensed matter settings, truly k-producible states as defined above are never encountered. In both equilibrium ground states and dynamical contexts, weak correlations are almost always present, making it unrealistic to expect the system to factorize exactly into independent clusters. This renders the formal notion of k-producibility impractical. In contrast, the QFI offers a physically meaningful characterization of multipartiteness, as it accounts not only for the mathematical structure of the state, but also for the strength of correlations. In practice, F_Q is rarely maximal, even when the true k is. In this sense, the QFI witnesses the *metrologically-useful* multipartite entanglement that can be harnessed in quantum phase estimation. As discussed later, this quantity successfully distinguishes short- and long-range correlations, thus proving its practical utility.

1.1.4 Entanglement in many-body eigenstates

The entanglement measures introduced so far exhibit particular scaling behaviors in eigenstates of typical many-body Hamiltonians. For example, the entanglement entropy features the well-known area-, logarithmic, and volume-law scaling forms, which can be used to distinguish different phases and regimes. Under the assumption that the Hamiltonian is ergodic and contains only local interactions, Table 1.1 summarizes the conventional entanglement scalings observed in 1D systems [26, 70, 71, 167, 171]. Here we consider a compact subsystem A of size $|A| \leq L/2$ for both S_A and $\mathcal{E}_A$ (for the negativity, the complementary subsystem is the rest of the system). These results follow from both numerical simulations and analytic results from exactly-solvable models. The entanglement entropy and the logarithmic negativity are usually similar and exhibit equal scaling behavior. In ground states,

they are always subextensive, but their specific behavior depends on the range of quantum correlations. For gapped (i.e., off-critical) Hamiltonians, correlation functions decay exponentially beyond a finite characteristic lengthscale, resulting in an area law [2] for bipartite entanglement. This fundamental result has been proved rigorously by Hastings in Ref. [126]. In this case, the QFI can only be extensive, resulting in an intensive multipartiteness of entanglement witnessed by f_Q. In contrast, critical states with algebraic correlations exhibit the anomalous logarithmic growth $S_A = c/3 \log |A|$ (assuming closed boundary conditions), where the prefactor c is the central charge of the associated conformal field theory. Such correlations can give rise to a superextensive scaling of F_Q with L, which signals long-range multipartiteness scaling as a power-law $f_Q \sim L^\alpha$.

State	S_A	$\mathcal{E}_A$	f_Q
Gapped ground state	const. (area law)	const.	const.
Critical ground state	$\log \lvert A \rvert$ (logarithmic law)	$\log \lvert A \rvert$	L^α
Bulk excited state	$\lvert A \rvert$ (volume law)	$\lvert A \rvert$	const.

Table 1.1: Typical entanglement behavior in many-body eigenstates of generic 1D Hamiltonians, under the assumptions of local interactions and ergodicity.

High-energy eigenstates lying in the bulk of the spectrum exhibit very different behavior. First, they manifest strong bipartite entanglement given by the volume law $S_A \sim |A|$. In quantum chaotic systems, it is now well-understood that the entanglement entropy of these states corresponds to a microcanonical thermodynamic entropy, as established by the Eigenstate Thermalization Hypothesis (ETH). Not only this explains the extensive scaling, but also establishes a direct connection between thermalization and scrambling of quantum information. Regarding multipartite entanglement, highly-excited states usually feature short-ranged correlation functions, resulting in an intensive QFI density. Having volume-law bipartite entanglement but low multipartiteness may seem paradoxical, but it is actually fully reasonable: in these states, quantum information is completely delocalized and accessible only through non-local, many-point correlation functions; in contrast, few-body correlations are typically weak.

In higher dimension, the previous paradigms of area and volume laws are still conjectured to hold quite generally, but both numerical tools and analytic methods are limited. In detail, assuming a subsystem A of size $|A| \sim L^d$ in d dimensions, the area-law behavior of gapped ground states corresponds to a scaling $S_A \sim |\partial A| \sim L^{d-1}$, where ∂A is the boundary of A. In contrast, the volume law becomes $S_A \sim L^d$. For critical states, one expects an area law with a logarithmic correction, i.e., $S_A \sim L^{d-1} \log L$.

There exist several examples of models that elude the previous paradigm. A first example is non-ergodic Hamiltonians [23–25, 140–144], which violate ETH through mechanisms such as localization or quantum scars. In disordered systems, localization prevents the scrambling of quantum information, resulting in excited eigenstates

[2] This nomenclature comes from the fact that the area enclosing A consists of isolated points, and thus it does not scale with the subsystem size.

with area-law entanglement entropy [26]. Quantum scars are instead special non-ergodic states found in models that are otherwise chaotic, and they exhibit either area-law or logarithmic scaling of S_A [145–152]. Another violation of Table 1.1 occurs in presence of long-range Hamiltonian interactions, such as in the Sachdev-Ye-Kitaev model [181, 182]. In these cases, strong bipartite correlations may be present even in the ground state, giving rise to a volume law [183].

1.1.5 Dynamics of entanglement

The unitary time evolution of quantum many-body systems typically induces a spatial spread of quantum correlations, resulting in entanglement growth [26, 72, 108, 160, 161]. A standard framework to investigate this phenomenon is the *quench dynamics* [104, 184–187] protocol, where the system is initially prepared in a separable state $|\psi_0\rangle$ and evolved in time under a Hamiltonian $\hat{H}$ to $|\psi_t\rangle = e^{-i\hat{H}t}|\psi_0\rangle$. In models with local interactions and ergodic dynamics, bipartite entanglement builds up linearly in time, showing a ballistic growth $S_A(t) \sim t$ until it saturates to a volume-law scaling $S_A \sim |A|$. This behavior reflects the delocalized nature of quantum information in time-evolved states: at large times, the unitary operator $e^{-i\hat{H}t}$ implements a highly non-local transformation that entangles locally-defined degrees of freedom across the entire system. The symmetries of $\hat{H}$ play a role in this process, typically affecting the prefactor of the saturation value.

In integrable systems, the linear growth of the entanglement entropy in time is understood analytically in terms of the celebrated *quasiparticle picture* [161]. Within this framework, the initial state $|\psi_0\rangle$ acts as a uniform source of entangled pairs of quasiparticle excitations, which spread ballistically through the system with opposite momenta. Each couple shared between regions A and B contributes $\mathcal{O}(1)$ to the total entanglement entropy, leading to the growth $S_A(t) \sim t$ and the eventual volume-law saturation. This formalism, now developed into the broader framework of generalized hydrodynamics [105, 107, 109], successfully captures several aspects of out-of-equilibrium dynamics in integrable systems, including transport and local equilibration to generalized Gibbs ensembles [11, 106, 186, 188].

In parallel to quantum quenches, analogous entanglement behavior is observed in random quantum circuits [50, 72, 189–191]. These provide a simplified description of generic many-body dynamics by digitizing the time evolution into sequences of local gates, as shown in Fig. 1.2. This approach offers the key advantage of enabling analytical calculations using random matrix theory (RMT) [192]. In the case of 2-qubit Haar-random gates, a first qualitative technique to estimate entanglement growth is given by the *minimal cut* method [50, 72], which does not even require RMT. Starting from the bipartition point between subsystems A and B at the final layer of the circuit, one considers all possible paths reaching the initial layer while avoiding the "blocks" corresponding to local unitaries. These paths are referred to as cuts, as they divide the circuit into two parts, and each of them intersects a number n_{cut} of gate legs. Defining $n_{\text{min}-\text{cut}}$ as the minimal n_{cut} over all cuts, one can show that the Rényi entropies satisfy the bound

$$S_n \leq n_{\text{min-cut}} \log q, \tag{1.17}$$

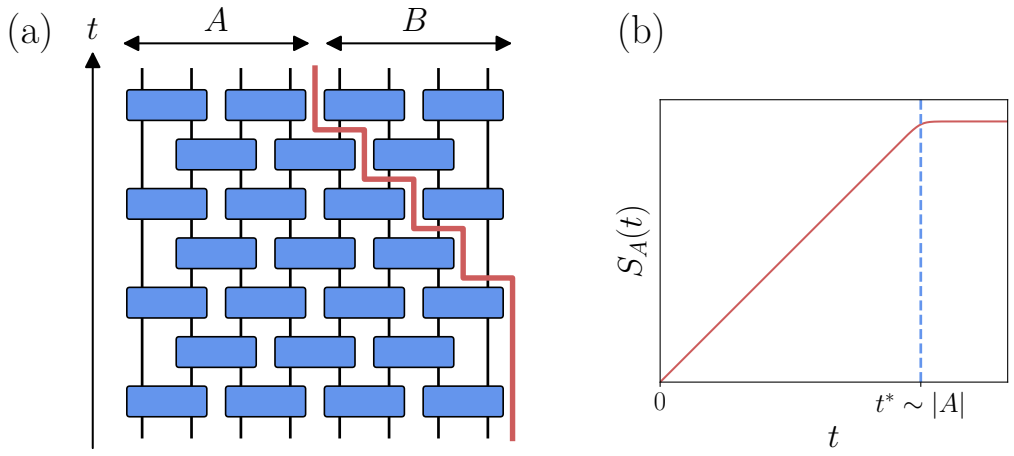

Figure 1.2: Illustration of the minimal cut method in random quantum circuits. (a) Given a circuit with brickwall structure, the minimal cut is given by the red path. (b) Sketch of the typical average entanglement entropy growth in random quantum circuits. After an initial ramp of extensive duration $t^* \sim |A|$, S_A saturates to a volume law.

where q is the local Hilbert space dimension. In brickwall circuits, the optimal path proceeds directly toward the boundary (see Fig. 1.2), leading to a linear growth $n_{\text{min-cut}} \sim t$ with the number of layers t. In finite-size systems, the cut eventually reaches the boundary is reached for sufficiently deep circuits, and can then continue to the start without crossing any other leg. This implies $n_{\text{min-cut}} = \min\{|A|, |B|\}$. While only upper bounds, these results reproduce the ballistic growth and volume-law saturation observed in random quantum circuits. Remarkably, this argument can be made rigorous using RMT, yielding the exact result

$$S_A^{(2)}(t) = n_{\text{min-cut}} \log\left(\frac{2q}{q^2+1}\right) \tag{1.18}$$

for the second Rényi entropy, valid in the regime $t \ll L$.

Regarding multipartite entanglement, the QFI density f_Q typically saturates to an intensive value after a quantum quench, indicating short-range correlations [193]. The explanation is similar to that for highly-excited Hamiltonian eigenstates: after a long time evolution, the system typically develops a finite correlation length, and multipartiteness thus remains low despite the presence of strong bipartite entanglement.

The standard picture of ballistic growth followed by volume-law saturation can break down in models featuring non-ergodicity, long-range interactions, or special symmetries. For instance, Anderson and many-body localized models typically exhibit much slower entanglement entropy growth after a quench [25, 26, 194], often logarithmic in time, and can thus take exponentially long to relax. On the other hand, long-range models can build up entanglement much more rapidly, potentially reaching the volume-law regime in an intensive time $t^* = \mathcal{O}(1)$. Finally, symmetries play key roles in entanglement dynamics and can sometimes slow down its growth. For example, in random circuits composed of fermionic Gaussian gates, also known

as *matchgates*, the entropy exhibits a peculiar diffusive growth $S_A(t) \sim \sqrt{t}$ [72, 195], and saturates to an extensive value after a time scaling as $t^* \sim |A|^2$.

1.2 Fermionic Gaussian states and non-Gaussian resources

Free-fermionic systems [110–115] are ubiquitous in quantum many-body physics. In condensed matter theory, they provide the simplest microscopic description of metals, and constitute one of the main pillars of standard perturbative approaches in the presence of weak interactions. Despite their relative simplicity, free fermions provide the foundational basis for understanding a wide range of many-body phenomena, including s-wave superconductivity [154], localization [22], topological effects [157], and quantum phase transitions [21, 117].

The defining feature of non-interacting fermions is the Gaussian structure of their quantum correlations. Specifically, free-fermionic states obey Wick's theorem, meaning that all higher-order correlators can be expressed in terms of two-point functions. As a result, Gaussian states are completely characterized by their correlation matrices [116, 117]. This property makes free systems efficiently simulable on classical computers and enables the analytic solvability of a broad class of models. These techniques are not only relevant to condensed matter theory but also to quantum statistical physics, as paradigmatic 1D spin models, such as the quantum Ising chain, can be mapped to non-interacting fermions. As a key application, this formalism enables the efficient computation of entanglement measures, and played a crucial role in establishing many of the typical entanglement features discussed in the previous section.

Importantly, efficiently simulable free-fermionic states can exhibit large entanglement entropy. This underscores that entanglement alone is not a sufficient measure of genuine quantum complexity, as its presence does not automatically imply classical intractability. A complementary notion of complexity is provided by non-Gaussianity [155, 196, 197], which quantifies how much the correlation structure of a state deviates from that of a non-interacting system satisfying Wick's theorem. Non-Gaussianity thus captures the difficulty of representing a generic state within the fermionic Gaussian formalism, and serves as a meaningful indicator of classical hardness.

In this section, we introduce the formalism of fermionic Gaussian states, which will be employed extensively in the thesis. We begin with the Jordan-Wigner mapping from spin chains to free-fermionic models, and then we review the standard techniques for studying ground-state and dynamical properties. Finally, we discuss non-Gaussianity as a measure of complexity and its key role in enabling universal quantum computation. A thorough discussion on the topics covered can be found, for instance, in Refs. [116, 117].

1.2.1 Jordan-Wigner transformation

A remarkable result in quantum many-body physics is the Jordan-Wigner transformation, which establishes a one-to-one correspondence between spin 1/2 degrees of freedom and fermionic operators. This mapping enables the exact solution of fundamental models of statistical physics, including the quantum Ising and XY chains. Below, we outline the main aspects of the Jordan-Wigner transformation and its applications.

Consider a system of L spin 1/2 variables and the associated Pauli operators $\hat{\sigma}_j^\alpha$, with $\alpha = x, y, z$. For each local Hilbert space, let us introduce the standard computational basis states $\{|\uparrow_j\rangle, |\downarrow_j\rangle\}$, defined as the eigenstates of $\hat{\sigma}_j^z$. We may interpret $|\uparrow_j\rangle \equiv |0_j\rangle$ as a local vacuum state, and $|\downarrow_j\rangle \equiv |1_j\rangle$ as a state hosting an excitation. Since each site is either empty or occupied, this perspective resembles the behavior of fermionic particles, as no more than one can occupy the same position at once due to the exclusion principle. To connect spin and fermionic degrees of freedom, consider the raising and lowering operators

$$\hat{\sigma}_j^\pm = \frac{\hat{\sigma}_j^x \pm i\hat{\sigma}_j^y}{2}, \tag{1.19}$$

that act as $\hat{\sigma}_j^+ |\downarrow_j\rangle = |\uparrow_j\rangle$, $\hat{\sigma}_j^- |\uparrow_j\rangle = |\downarrow_j\rangle$. These behave analogously to fermionic creation and annihilation operators $\hat{c}_j^\dagger, \hat{c}_j$. A proper relation is established by defining

$$\hat{\sigma}_j^+ = e^{i\pi \sum_{i<j} \hat{n}_i} \hat{c}_j, \tag{1.20a}$$

$$\hat{\sigma}_j^- = e^{i\pi \sum_{i<j} \hat{n}_i} \hat{c}_j^\dagger, \tag{1.20b}$$

where $\hat{n}_j = \hat{c}_j^\dagger \hat{c}_j$ are fermionic occupation number operators. The phase operators $e^{i\pi \sum_{i<j} \hat{n}_i}$ appearing in Eq. (1.20) are known as Jordan-Wigner strings, and they are fundamental to reproduce the correct fermionic algebra. Their necessity is due to the fact that spin operators on different site commute, whereas fermionic operators must anticommute, as

$$\left[\hat{\sigma}_i^+, \hat{\sigma}_j^-\right] = 0, \quad \left\{\hat{c}_i, \hat{c}_j^\dagger\right\} = 0 \quad \text{for } i \neq j. \tag{1.21}$$

The Jordan-Wigner string counts the number of sign flips required before raising or lowering the state, thereby enforcing the correct fermionic anticommutation relations at the cost of non-locality. Finally, Eq. (1.20) can be equivalently formulated in terms of Pauli operators, yielding

$$\hat{\sigma}_j^x = e^{i\pi \sum_{i<j} \hat{n}_i} (\hat{c}_j^\dagger + \hat{c}_j), \tag{1.22a}$$

$$\hat{\sigma}_j^y = i e^{i\pi \sum_{i<j} \hat{n}_i} (\hat{c}_j^\dagger - \hat{c}_j), \tag{1.22b}$$

$$\hat{\sigma}_j^z = 1 - 2\hat{n}_j. \tag{1.22c}$$

The Jordan-Wigner transformation can be used to map certain 1D spin models into quadratic fermionic Hamiltonians, which are thus non-interacting. Relevant examples that allow this take the form of XY chains of type

$$\hat{H} = -\sum_{j=1}^{L} \left(J_j^x \hat{\sigma}_j^x \hat{\sigma}_{j+1}^x + J_j^y \hat{\sigma}_j^y \hat{\sigma}_{j+1}^y + h_j \hat{\sigma}_j^z \right), \tag{1.23}$$

which play crucial roles in the theory of quantum phase transitions. Indeed, after applying Eq. (1.22) this Hamiltonian reduces to

$$\begin{aligned}\hat{H} = &-\sum_{j=1}^{L-1}\left[(J_j^x + J_j^y)\hat{c}_j^\dagger \hat{c}_{j+1} + (J_j^x - J_j^y)\hat{c}_j^\dagger \hat{c}_{j+1}^\dagger + \text{h.c.}\right] + \sum_{j=1}^{L} h_j(2\hat{n}_j - 1) \\ &+ e^{i\pi\hat{N}}\left[(J_L^x + J_L^y)\hat{c}_L^\dagger \hat{c}_{L+1} + (J_L^x - J_L^y)\hat{c}_L^\dagger \hat{c}_{L+1}^\dagger + \text{h.c.}\right],\end{aligned} \tag{1.24}$$

assuming periodic boundary conditions $\hat{\sigma}_{L+1}^\alpha \equiv \hat{\sigma}_1^\alpha$. The boundary term on the second line of Eq. (1.24) contains the Jordan-Wigner string $e^{i\pi\hat{N}}$, where $\hat{N} = \sum_{j=1}^{L} \hat{n}_j$ is the total number of fermions. In general, fermionic Hamiltonians always enjoy the $\mathbb{Z}_2$ parity symmetry $\left[\hat{H}, e^{i\pi\hat{N}}\right] = 0$. As a consequence, it is always possible to fix the parity sector to be even or odd by setting $e^{i\pi\hat{N}} = 1$ or $e^{i\pi\hat{N}} = -1$, respectively. In both cases Eq. (1.24) is bilinear in the fermionic operators, and can thus be solved analytically through explicit diagonalization (see the next subsection).

As a key example, for $J_j^x = 1$, $J_j^y = 0$, and $h_j = h$ Eq. (1.23) reduces to the paradigmatic quantum Ising chain in transverse field

$$\hat{H}_{\text{Ising}} = -\sum_j (\hat{\sigma}_j^x \hat{\sigma}_{j+1}^x) + h\sum_j \hat{\sigma}_j^z, \tag{1.25}$$

whose behavior under external monitoring will be discussed in detail in future chapters. Its fermionic counterpart obtained through the Jordan-Wigner transformation is the Kitaev chain

$$\hat{H}_{\text{Kitaev}} = -\sum_j (\hat{c}_j^\dagger \hat{c}_{j+1} + \hat{c}_j^\dagger \hat{c}_{j+1}^\dagger + \text{h.c.}) + h\sum_j (2\hat{n}_j - 1), \tag{1.26}$$

with periodic or antiperiodic boundary conditions for the odd and even parity sectors, respectively. This model is of central interest in condensed matter theory and quantum information, as it provides a minimal description of topological edge modes.

A crucial aspect of the Jordan-Wigner transformation is that $\hat{\sigma}_j^z$ corresponds to a quadratic number operator $\hat{n}_j$, as seen from Eq. (1.22c). As a consequence, terms like $\hat{\sigma}_j^z \hat{\sigma}_{j+1}^z$ map to quartic fermionic forms. These couplings break the Gaussian structure of the theory, making the model no longer solvable exactly.

Another limitation of this technique is its restriction to 1D systems. The mapping relies on a linear ordering of sites to define the Jordan-Wigner strings in Eq. (1.20). In 1D, this sorting is natural, as it follows the indexing of lattice sites. When taking the product of two operators like $\hat{\sigma}_j^x$ and $\hat{\sigma}_{j+1}^x$, their Jordan-Wigner strings cancel out because they are contiguous on the chain. In $d > 1$ dimensions, however, this simplification can be applied to only 1 of the d lattice directions: as a result, some interactions inevitably retain non-trivial Jordan-Wigner strings, thus preventing a general mapping to a quadratic fermionic Hamiltonian.

1.2.2 Formalism of Gaussian states

Free-fermionic states form a special subset of the Hilbert space characterized by having correlation functions with a factorizable structure according to Wick's theorem.

Mathematically, they are represented by density matrices that have a Gaussian form of type

$$\hat{\rho} = \frac{1}{Z} e^{-\sum_{\mu,\nu=1}^{2L} \hat{\psi}_\mu^\dagger K_{\mu,\nu} \hat{\psi}_\nu}, \tag{1.27}$$

where $\hat{\psi} = \left(\hat{c}_1, \ldots, \hat{c}_L, \hat{c}_1^\dagger, \ldots, \hat{c}_L^\dagger\right)$ and Z is a normalization coefficient. As discussed below, the eigenstates of any quadratic Hamiltonian $\hat{H}$ are in the form of Eq. (1.27), and the time-evolution operator $e^{-i\hat{H}t}$ preserves Gaussianity throughout the dynamics.

The matrix appearing in the exponential can always be parameterized as

$$K = \begin{pmatrix} A & B \\ -B^T & -A^T \end{pmatrix}, \tag{1.28}$$

where $A = A^\dagger$ and $B = -B^\dagger$ are $L \times L$ matrices. Assuming this particular structure, it is possible to express K in terms of the covariance matrix

$$G_{\mu.\nu} = \mathrm{Tr}\left(\hat{\rho}\hat{\psi}_\mu^\dagger \hat{\psi}_\nu\right), \tag{1.29}$$

which encodes all properties of the state. Specifically, it can be shown that

$$G = \frac{1}{1 + e^{2K}}. \tag{1.30}$$

Diagonalization of quadratic Hamiltonians – The main advantage of quadratic models is the possibility of diagonalizing them explicitly, providing access to their spectrum and many-body eigenstates. Consider the Hamiltonian

$$\hat{H} = \sum_{\mu,\nu} \hat{\psi}_\mu^\dagger \mathbb{H}_{\mu,\nu} \hat{\psi}_\nu, \tag{1.31}$$

and let us diagonalize $\mathbb{H} = \mathbb{H}^\dagger$ as

$$\mathbb{H} = \mathbb{U}^\dagger \Lambda \mathbb{U}, \tag{1.32}$$

where $\mathbb{U} = \mathbb{U}^\dagger$ is a unitary rotation, and Λ is a diagonal matrix storing the eigenvalues. Without any loss of generality, we may assume that $\mathbb{H}$ is in the form of Eq. (1.28): this can always be achieved by adding a constant that simply shifts the zero of energy, and thus does not affect physical properties. Following this choice, it can be shown that both $\mathbb{U}$ and Λ assume the particular structures

$$\mathbb{U} = \begin{pmatrix} U & V^* \\ V & U^* \end{pmatrix}, \tag{1.33}$$

where U and V are $L \times L$ matrices, and

$$\Lambda = \mathrm{diag}\left(\epsilon_1, \ldots, \epsilon_L, -\epsilon_1, \ldots, -\epsilon_L\right). \tag{1.34}$$

After defining the new fermionic operators

$$\hat{d}_j = \sum_{i=1}^{L} U_{j,i} \hat{c}_i + \sum_{i=1}^{L} V_{j,i}^* \hat{c}_i^\dagger, \tag{1.35}$$

which satisfy the canonical anticommutation relations $\left\{\hat{d}_i, \hat{d}_j^\dagger\right\} = \delta_{i,j}$, the Hamiltonian can finally be rewritten as

$$\hat{H} = \sum_{j=1}^{L} \epsilon_j (\hat{d}_j^\dagger \hat{d}_j - \hat{d}_j \hat{d}_j^\dagger) = \sum_{j=1}^{L} \epsilon_j (2\hat{d}_j^\dagger \hat{d}_j - 1). \tag{1.36}$$

The new fermionic representation is often referred to as the quasiparticle basis. Indeed, the Hamiltonian of Eq. (1.36) is written in a trivial form, containing a sum of L commuting number operators $\hat{d}_j^\dagger \hat{d}_j$ that count elementary excitations carrying energies ϵ_j. As a consequence, the many-body eigenstates of $\hat{H}$ coincide with the Fock states in this basis, and are identified by a set of L quasiparticle occupations $\{n_1, \ldots, n_L\}$. Assuming $\epsilon_n \geq 0$ [3], the ground state is the quasiparticle vacuum characterized by $\hat{d}_j^\dagger \hat{d}_j \left|\mathrm{GS}\right\rangle = 0$. Let us introduce $\hat{\phi} = (\hat{d}_1, \ldots, \hat{d}_L, \hat{d}_1^\dagger, \ldots, \hat{d}_L^\dagger)$, in analogy to $\hat{\psi}$. In general, any eigenstate specified by $|n_1, \ldots, n_L\rangle$ has a diagonal covariance matrix in this basis, specified by

$$D_{\mu.\nu} = \mathrm{Tr}\left(\hat{\rho}\hat{\phi}_\mu^\dagger \hat{\phi}_\nu\right) = \begin{cases} n_\mu \delta_{\mu,\nu} & \text{if } \mu \leq L, \\ (1 - n_\mu)\delta_{\mu,\nu} & \text{if } \mu > L. \end{cases} \tag{1.37}$$

The full covariance matrix G in the original fermionic representation is given by

$$G = \mathbb{U}^T D \mathbb{U}^*. \tag{1.38}$$

At last, it is straightforward to observe that the eigenstates of $\hat{H}$ have Gaussian structure. The density matrices of eigenstates can be formally written as

$$|n_1, \ldots, n_L\rangle \langle n_1, \ldots, n_L| = \lim_{\beta \to \infty} e^{-\beta \sum_{j=1}^{L} (-1)^{n_j} \hat{d}_j^\dagger \hat{d}_j}, \tag{1.39}$$

which is the exponential of a quadratic fermionic form.

Dynamics of Gaussian states – Another great advantage of working with free-fermionic states is that unitary evolution generated by quadratic Hamiltonians preserves Gaussianity, thus allowing to simulate the dynamics efficiently. A generic Gaussian unitary transformation takes the form

$$\hat{U} = e^{-i \sum_{\mu,\nu} \hat{\psi}_\mu^\dagger \mathbb{H}_{\mu,\nu} \hat{\psi}_\nu}, \tag{1.40}$$

where $\mathbb{H} = \mathbb{H}^\dagger$. These operations form the group $\mathcal{G}_N$ that the set of Gaussian states into itself. Gaussian operators, both unitary and not, always multiply into other Gaussian operators according to the product rule

$$e^{-\sum_{\mu,\nu} \hat{\psi}_\mu^\dagger A_{\mu,\nu} \hat{\psi}_\nu} e^{-\sum_{\mu,\nu} \hat{\psi}_\mu^\dagger B_{\mu,\nu} \hat{\psi}_\nu} = \lambda e^{-\sum_{\mu,\nu} \hat{\psi}_\mu^\dagger C_{\mu,\nu} \hat{\psi}_\nu}, \tag{1.41}$$

where $A = -A^T$ and $B = -B^T$, λ is a scalar factor, and C is determined by

$$e^C = e^A e^B. \tag{1.42}$$

[3] If a negative ϵ_n is present, it is sufficient to switch the roles of particles and holes by changing $\hat{d}_j \leftrightarrow \hat{d}_j^\dagger$ to redefine it to $-\epsilon_j$.

As an immediate application, for any Gaussian initial state $\hat{\rho}_0$ and quadratic Hamiltonian $\hat{H}$, the time evolved state $\hat{\rho}_t = e^{-i\hat{H}t}\hat{\rho}_0 e^{i\hat{H}t}$ is always Gaussian, thus proving the previously mentioned statement.

While in principle Eq. (1.41) can be used to compute the time evolution of a state, it is often more practical to work with correlation matrices directly. When the Hamiltonian $\hat{H}$ is fixed, it is optimal to work in the quasiparticle basis. From Eq. (1.37), we have

$$\begin{aligned} D_{\mu,\nu}(t) &= \mathrm{Tr}\Big(\hat{\rho}_t \hat{\phi}_\mu^\dagger \hat{\phi}_\nu\Big) = \mathrm{Tr}\Big(\hat{\rho}_0 e^{i\hat{H}t}\hat{\phi}_\mu^\dagger e^{-i\hat{H}t} e^{i\hat{H}t}\hat{\phi}_\mu e^{-i\hat{H}t}\Big) \\ &= M^*_{\mu,\mu}(t)\,\mathrm{Tr}\Big(\hat{\rho}_0\hat{\phi}_\mu^\dagger\hat{\phi}_\nu\Big)M_{\nu,\nu}(t) = M^*_{\mu,\mu}(t)D_{\mu,\nu}(0)M_{\nu,\nu}(t), \end{aligned} \tag{1.43}$$

where $M(t) = \mathrm{diag}(e^{-i\epsilon_1 t},\dots,e^{-i\epsilon_L t},e^{i\epsilon_1 t},\dots,e^{i\epsilon_L t})$. Using Eq. (1.38), the time-dependent covariance matrix reads

$$G(t) = \mathbb{U}^T M^*(t) U^* G(0) U^T M(t) U^*. \tag{1.44}$$

In some cases, for instance in circuits of Gaussian gates or in presence of measurements disrupting the unitary evolution, it may be convenient to evolve the covariance matrix by integrating its equation of motion. Let us define the $L\times L$ matrices

$$C_{i,j}(t) = \mathrm{Tr}\Big(\hat{\rho}_t \hat{c}_i \hat{c}_j^\dagger\Big), \tag{1.45a}$$

$$F_{i,j}(t) = \mathrm{Tr}(\hat{\rho}_t \hat{c}_i \hat{c}_j), \tag{1.45b}$$

which fully parameterize $G(t)$ as

$$G(t) = \begin{pmatrix} \mathbb{1} - C^T & F^\dagger \\ F & C \end{pmatrix}. \tag{1.46}$$

Consider a quadratic Hamiltonian as in Eq. (1.31), with the matrix $\mathbb{H}$ in the form

$$\mathbb{H} = \begin{pmatrix} \mathbb{H}_1 & \mathbb{H}_2 \\ -\mathbb{H}_2 & -\mathbb{H}_1 \end{pmatrix}, \tag{1.47}$$

which can always be assumed up to an overall constant energy shift of $\hat{H}$. Starting from the Schrödinger equation and applying Wick's theorem, we obtain

$$\begin{aligned} \partial_t C_{m,n}(t) &= i\,\mathrm{Tr}\left(\hat{\rho}_t\left(\hat{H}^\dagger \hat{c}_m \hat{c}_n^\dagger - \hat{c}_m \hat{c}_n^\dagger \hat{H}\right)\right) \\ &= -2i\left([\mathbb{H}_1, C(t)] + \mathbb{H}_2 F^\dagger(t) + F(t)\mathbb{H}_2\right), \end{aligned} \tag{1.48a}$$

$$\begin{aligned} \partial_t F_{m,n}(t) &= i\,\mathrm{Tr}\left(\hat{\rho}_t\left(\hat{H}^\dagger \hat{c}_m \hat{c}_n - \hat{c}_m \hat{c}_n \hat{H}\right)\right) \\ &= -2i\left[\{\mathbb{H}_1, F(t)\} + \mathbb{H}_2(\mathbb{1} - C^T(t)) - C(t)\mathbb{H}_2\right]. \end{aligned} \tag{1.48b}$$

1.2.3 Calculation of entanglement

Gaussian states enable the efficient computation of the entanglement probes introduced in Sec. 1.1. Before explaining how the calculations are made, it is convenient to introduce the Majorana fermionic operators

$$\hat{\gamma}_{2j-1} = \hat{c}_j^\dagger + \hat{c}_j, \tag{1.49a}$$

$$\hat{\gamma}_{2j} = i(\hat{c}_j^\dagger - \hat{c}_j), \tag{1.49b}$$

which satisfy the anticommutation relation $\{\hat{\gamma}_\mu, \hat{\gamma}_\nu\} = 2\delta_{\mu,\nu}$. In the following calculations, it is more convenient to express Gaussian operators in this basis, rather than using creation and annihilation ones. To this purpose, we introduce the Majorana covariance matrix

$$\Gamma_{\mu,\nu} = \frac{1}{2} \operatorname{Tr}\left(\hat{\rho}[\hat{\gamma}_\mu, \hat{\gamma}_\nu]\right), \tag{1.50}$$

which is purely imaginary and anti-symmetric.

Entanglement entropy – In order to compute the entanglement entropy S_A, we need access to the reduced density matrix $\hat{\rho}_A$. Let us assume that A contains $|A| = \ell$ sites. If the full system is described by a free-fermionic state, $\hat{\rho}_A$ will also be a Gaussian operator. In particular, the covariance matrix that specifies it is obtained by taking the submatrix of G with rows and columns corresponding to sites contained in subsystem A. Let

$$\hat{\rho}_A = \frac{1}{Z_A} e^{-\hat{H}_A} = \frac{1}{Z_A} e^{\frac{1}{4}\sum_{\mu,\nu=1}^{2\ell} \hat{\gamma}_\mu W_{\mu,\nu} \hat{\gamma}_\nu}, \tag{1.51}$$

where the operator $\hat{H}_A$ is known as *entanglement Hamiltonian*, as it fully encodes the entanglement entropy. Analogously to Eq. (1.30), one can show that the correlation matrix relative to subsystem A is given by

$$\Gamma_A = \tanh\left(\frac{W}{2}\right). \tag{1.52}$$

This matrix contains all information required to evaluate the entanglement entropy of subsystem A with the remainder. Here we report the main result, while a detailed derivation can be found in Refs. [116, 117]. The spectrum of Γ_A features eigenvalues appearing in opposite pairs $\pm\nu_j \in [-1, 1]$. The entanglement entropy is then given by

$$S_A = -\sum_{j=1}^{\ell} \left[\frac{1+\nu_j}{2} \log\left(\frac{1+\nu_j}{2}\right) + \frac{1-\nu_j}{2} \log\left(\frac{1-\nu_j}{2}\right)\right]. \tag{1.53}$$

Fermionic logarithmic negativity – As mentioned in Sec. 1.1.2, the definition of the entanglement negativity for fermionic system requires particular care. We now summarize the generalization of the partial transpose operation and the procedure to compute the fermionic logarithmic negativity. A complete discussion on the topic can be found in Refs.[174–178]. The idea to generalize the Peres-Horodecki criterion to fermionic systems relies on extending the partial transpose to a partial time reversal operation. Consider a density matrix

$$\hat{\rho} = \sum_{\mathbf{x}} w_{\mathbf{x}} \hat{\gamma}_1^{x_1} \dots \hat{\gamma}_{2L}^{x_{2L}} \tag{1.54}$$

expanded in the basis of Majorana operators, where $\mathbf{x} = (x_1, \dots, x_{2L})$ is a binary strings of 0's and 1's, and $w_{\mathbf{x}}$ are amplitudes (notice that these must vanish for odd values of $|\mathbf{x}|$). Let x_A be the substring obtained by considering only indices relative to subsystem A. The partial transpose for fermions is defined as

$$\hat{\rho}^{T_A} = \sum_{\mathbf{x}} w_{\mathbf{x}} i^{|\mathrm{x}_A|} \hat{\gamma}_1^{x_1} \dots \hat{\gamma}_{2L}^{x_{2L}}. \tag{1.55}$$

In contrast to the bosonic version, this definition ensures that for any Gaussian $\hat{\rho}$ its partial transpose is also Gaussian. A closely related object is the twisted partial transpose

$$\hat{\rho}^{\tilde{T}_A} = \hat{\rho}^{T_A}(-1)^{\hat{N}_A}, \tag{1.56}$$

which has a real spectrum and defines the fermionic logarithmic negativity

$$\mathcal{N}_A = \log ||\hat{\rho}^{\tilde{T}_A}||. \tag{1.57}$$

Let $\hat{\rho}$ be the Gaussian density matrix of the full system, divided in two complementary subsystems A and B. Let $|A| = \ell$ be the size of the first subsystem. We may represent the Majorana covariance matrix in block form as

$$\Gamma = \begin{pmatrix} \Gamma_A & \Gamma_{A,B} \\ \Gamma_{B,A} & \Gamma_B \end{pmatrix}, \tag{1.58}$$

where Γ_A and Γ_B are the covariance matrices of the two subsystems, whereas $\Gamma_{A,B}$ and $\Gamma_{B,A}$ are cross-correlation matrices between A and B. It can be shown that the covariance matrix of $\hat{\rho}^{T_A}$ is given by

$$\Gamma_+ = \begin{pmatrix} -\Gamma_A & i\Gamma_{A,B} \\ i\Gamma_{B,A} & \Gamma_B \end{pmatrix}, \tag{1.59}$$

and it is connected to the covariance matrix $\tilde{\Gamma}$ of $\hat{\rho}^{\tilde{T}_A}$ by the relation

$$\frac{\mathbb{1} + \tilde{\Gamma}}{\mathbb{1} - \tilde{\Gamma}} = \frac{\mathbb{1} + \Gamma_+}{\mathbb{1} - \Gamma_+} \begin{pmatrix} -\mathbb{1}_{2\ell\times 2\ell} & 0_{2\ell\times 2(L-\ell)} \\ 0_{2(L-\ell)\times 2\ell} & \mathbb{1}_{2(L-\ell)\times 2(L-\ell)} \end{pmatrix}. \tag{1.60}$$

Analogously to the entanglement entropy, the logarithmic negativity can be computed from the eigenvalues of $\tilde{\Gamma}$, which appear in pairs $\pm\tilde{\nu}_j$. The final formula is

$$\mathcal{N}_A = \sum_{j=1}^{L} \log\left(\left|\frac{1-\tilde{\nu}_j}{2}\right| + \left|\frac{1+\tilde{\nu}_j}{2}\right|\right) + \sqrt{\det \Gamma_A} \tag{1.61}$$

Quantum Fisher information and correlation functions – Given the explicit form of Eq. (1.14), calculating the QFI requires the knowledge of all connected spin-spin correlation functions. In spin systems, it is possible to evaluate them by mapping the Pauli expectation values into multi-point fermionic correlators using the Jordan-Wigner transformation, and breaking them down through Wick's theorem. Here we list the final results of these calculations [198, 199]. First, instead of working with the full covariance matrix Γ, let us introduce

$$(M_{\mathrm{o,o}})_{i,j} = \mathrm{Tr}(\hat{\rho}\hat{\gamma}_{2i-1}\hat{\gamma}_{2j-1}), \tag{1.62a}$$

$$(M_{\mathrm{e,e}})_{i,j} = \mathrm{Tr}(\hat{\rho}\hat{\gamma}_{2i}\hat{\gamma}_{2j}), \tag{1.62b}$$

$$(M_{\mathrm{o,e}})_{i,j} = \mathrm{Tr}(\hat{\rho}\hat{\gamma}_{2i-1}\hat{\gamma}_{2j}) = -(M_{\mathrm{e,o}})_{j,i}, \tag{1.62c}$$

where the indices "o" and "e" refer to odd and even Majorana operators, respectively. The correlation functions defined in Eq. (1.15) are given by

$$C^{z,z}_{m,n} = (M_{o,o})_{m,n}(M_{e,e})_{m,n} - (M_{o,e})_{m,n}(M_{e,o})_{m,n}. \tag{1.63a}$$

$$C^{x,x}_{m,n} = (-1)^{\frac{(n-m-1)(n-m)}{2}} \mathrm{Pf} \begin{pmatrix} (\mathbb{1} - M_{\mathrm{e,e}})^{[(m,n-1),(m,n-1)]} & -iM_{\mathrm{e,o}}^{[(m,n-1),(m+1,n)]} \\ -iM_{\mathrm{o,e}}^{[(m+1,n),(m,n-1)]} & -(\mathbb{1} - M_{\mathrm{o,o}})^{[(m+1,n),(m+1,n)]} \end{pmatrix}, \tag{1.63b}$$

$$C^{y,y}_{m,n} = (-1)^{\frac{(n-m+1)(n-m)}{2}} \mathrm{Pf} \begin{pmatrix} -(\mathbb{1} - M_{\mathrm{o,o}})^{[(m,n-1),(m,n-1)]} & -iM_{\mathrm{e,o}}^{[(m,n-1),(m+1,n)]} \\ -iM_{\mathrm{e,o}}^{[(m+1,n),(m,n-1)]} & (\mathbb{1} - M_{\mathrm{e,e}})^{[(m+1,n),(m+1,n)]} \end{pmatrix}, \tag{1.63c}$$

$$C^{x,y}_{m,n} = i(-1)^{\frac{(n-m+1)(n-m)}{2}} \mathrm{Pf} \begin{pmatrix} (\mathbb{1} - M_{\mathrm{e,e}})^{[(m,n),(m,n)]} & -iM_{\mathrm{e,o}}^{[(m,n),(m+1,n-1)]} \\ -iM_{\mathrm{o,e}}^{[(m+1,n-1),(m,n)]} & -(\mathbb{1} - M_{\mathrm{o,o}})^{[(m+1,n-1),(m+1,n-1)]} \end{pmatrix}, \tag{1.63d}$$

where $M^{[(r_1,r_2),(c_1,c_2)]}$ indicates the submatrix of M with rows from r_1 to r_2 and columns from c_1 to c_2. The other spin-spin correlators vanish: since they are given by expectation values of strings of an odd number of fermionic operators, they must be zero due to the $\mathbb{Z}_2$ parity symmetry.

1.2.4 Non-Gaussianity as a form of complexity

Fermionic Gaussian states provide a powerful framework for investigating many-body phenomena with efficient numerical simulations and analytic approaches. This possibility already indicates that the free-fermionic class cannot be considered genuinely "hard", as it does not harness the full exponential complexity of generic many-body states. Indeed, Gaussianity constrains correlations to obey Wick's theorem, thus preventing more complicated structures. For this reason, free-fermionic states supplemented with Gaussian unitaries are unable to achieve universal quantum computation, which requires the addition of non-Gaussian resources [155, 196, 197].

Once the Gaussian structure of a state is spoiled, it is no longer possible to represent it fully in terms of a covariance matrix. This makes it immediately harder to keep track of, requiring more computational time and resources. If the amount of injected non-Gaussian elements (e.g., gates) is low enough, it might still be possible to write the density matrix as a sum of Gaussian operators, enabling a generalization of the covariance matrix formalism to address this problem. However, the resource cost of this approach grows exponentially with non-Gaussianity, and this method quickly becomes unsustainable.

For these reasons, non-Gaussianity can be interpreted as a genuine notion of quantum complexity on par with entanglement. Given a density matrix $\hat{\rho}$, a way of characterizing its non-Gaussianity quantitatively is through the *relative entropy* [196]

$$\delta_{\mathrm{NG}} = \min_{\text{Gaussian } \hat{\rho}_G} \left[\mathrm{Tr}(\hat{\rho}\log\hat{\rho}) - \mathrm{Tr}(\hat{\rho}\log\hat{\rho}_G)\right]. \tag{1.64}$$

This expression is a quantum Kullback-Leibler divergence comparing $\hat{\rho}$ to the closest Gaussian density matrix $\hat{\rho}_G$, and it is non-negative. It can be shown that the minimum of Eq. (1.64) is achieved by the state $\hat{\rho}_G = \hat{\rho}_G[\Gamma]$ defined by the fermionic covariance matrix Γ of $\hat{\rho}$ [196]. Moreover, the relative entropy of non-Gaussianity simplifies to

$$\delta_{\mathrm{NG}} = \mathrm{Tr}(\hat{\rho}\log\hat{\rho}) - \mathrm{Tr}(\hat{\rho}_G[\Gamma]\log\hat{\rho}_G[\Gamma]). \tag{1.65}$$

For pure states, the von Neumann entropy of $\hat{\rho}$ vanishes, and δ_{NG} reduces to the entropy of $\hat{\rho}_G[\Gamma]$.

1.3 Clifford circuits and magic

Clifford operations are a special class of unitary gates spanned by the elementary set $\{\hat{H}, \hat{S}, C\hat{N}OT\}$, and they play a central role in quantum computation[120–124]. A key feature is that stabilizer states produced by Clifford circuits can be efficiently simulated by classical computers, as established by the Gottesman-Knill theorem. As a consequence, Clifford evolution provides a natural framework for exploring digitized quantum many-body dynamics, addressing fundamental questions such as entanglement growth and quantum information scrambling. For this reason, as discussed in the next chapter, stabilizer states have proven essential in the study of monitored systems, where many foundational results on measurement-induced phase transitions have been obtained using these models.

A second fundamental application of Clifford transformations is in quantum error correction[120, 200–203]. Stabilizer codes lie at the core of most modern strategies to protect quantum algorithms against noise and decoherence. Within this framework, quantum information is encoded in logical states that are preserved by Clifford operations, enabling the possibility of measuring Pauli strings to detect and correct errors. This is essential for building fault-tolerant quantum devices that can be used to perform reliable quantum computations.

The theoretical formalism of Clifford operations is completely different from that of fermionic Gaussian states. Stabilizer states are fully characterized by a set of Pauli operators of which they are eigenstates. Thus, while both Clifford and Gaussian states are classically simulable, their simplicity stems from fundamentally different properties. The absence of Clifford structure, known as non-stabilizerness or quantum magic [81–88], defines yet another notion of quantum complexity, independent of non-Gaussianity. Magic quantifies the deviation from the stabilizer class, and serves as an essential resource for quantum universality.

We start this section by introducing the stabilizer formalism that enables the efficient simulation of Clifford evolution, and explain how to compute correlation functions and the entanglement entropy. We then introduce the stabilizer Rényi entropies (SREs), which are among the most widely used measures of quantum magic.

1.3.1 Stabilizer formalism

Given a system of L qubits, define the set of Pauli strings $\mathcal{P}_L = \{\hat{\mathbb{1}}, \hat{\sigma}^x, \hat{\sigma}^y, \hat{\sigma}^z\}^{\otimes L}$. A state $|\psi\rangle$ is a stabilizer if there exist L independent, commuting Pauli strings $\hat{g}_j \in \{\pm 1\}\mathcal{P}_L$, $[\hat{g}_i, \hat{g}_j] = 0$, that stabilize $|\psi\rangle$, i.e., $\hat{g}_i |\psi\rangle = |\psi\rangle$. In this context, independence of Pauli strings refers to the property that each $\hat{g}_j$ is not spanned by the set of all others. The operators $\hat{g}_j$ generate the stabilizer group $\mathcal{S} = \langle \hat{g}_1, \dots, \hat{g}_L \rangle = \{\prod_{j=1}^{L} \hat{g}_j^{x_j} | x_j = 0, 1\}$ of Pauli strings that stabilize $|\psi\rangle$. The knowledge of the L generators fully determines the state. Indeed, the density matrix $\hat{\rho} = |\psi\rangle \langle\psi|$ can be expressed as the product of projectors onto positive eigenstates of $\hat{g}_j$, i.e.,

$$\hat{\rho} = \prod_{j=1}^{L} \frac{1 + \hat{g}_j}{2} = \frac{1}{2^L} \sum_{\hat{P} \in \mathcal{S}} \hat{P}. \tag{1.66}$$

Crucially, the generators can be stored efficiently in an $L \times (2L+1)$ binary *stabilizer tableau* T in numerical simulations. Each row i describes a $\hat{g}_i$, specifying which local Pauli operator among $\{\hat{\mathbb{1}}, \hat{\sigma}^x, \hat{\sigma}^y, \hat{\sigma}^z\}$ appears on each site. This requires 2 bits per site, plus an additional bit to indicate the overall sign $\hat{g}_i$. A common way to encode this information in the tableau is given by

$$T_{i,2j} = \begin{cases} 0 & \text{if } \hat{g}_i \text{ has } \hat{\mathbb{1}} \text{ or } \hat{\sigma}^x \text{ on site } j, \\ 1 & \text{if } \hat{g}_i \text{ has } \hat{\sigma}^z \text{ or } \hat{\sigma}^y \text{ on site } j, \end{cases} \tag{1.67a}$$

$$T_{i,2j+1} = \begin{cases} 0 & \text{if } \hat{g}_i \text{ has } \hat{\mathbb{1}} \text{ or } \hat{\sigma}^z \text{ on site } j, \\ 1 & \text{if } \hat{g}_i \text{ has } \hat{\sigma}^x \text{ or } \hat{\sigma}^y \text{ on site } j. \end{cases} \tag{1.67b}$$

Each pair $(T_{i,2j}, T_{i,2j+1})$ indicates the presence or absence of $\hat{\sigma}^z_j$ and $\hat{\sigma}^x_j$, respectively. In this representation, $\hat{\sigma}^y_j$ corresponds to both bits being 1, since $\hat{\sigma}^y_j \propto \hat{\sigma}^z_j \hat{\sigma}^x_j$. The signs $s_i = \pm 1$ of the strings $\hat{g}_i$ can be stored in the first column $T_{i,1} = (1 - s_i)/2$. As an example, the state $(|00\rangle + i\,|11\rangle)/\sqrt{2}$ is stabilized by $\hat{g}_1 = \hat{\sigma}^z_1 \hat{\sigma}^z_2$ and $\hat{g}_2 = -\hat{\sigma}^x_1 \hat{\sigma}^y_2$, and its tableau is

$$T = \begin{pmatrix} 0 & 1 & 0 & 1 & 0 \\ 1 & 0 & 1 & 1 & 1 \end{pmatrix}. \tag{1.68}$$

Stabilizer states can be generated by Clifford operators starting from computational basis states. This class of operations is realized by the combination of three elementary gates, namely, the Hadamard gate

$$\hat{H} = \frac{1}{\sqrt{2}} \begin{pmatrix} 1 & 1 \\ 1 & -1 \end{pmatrix}, \tag{1.69}$$

the phase gate

$$\hat{S} = \begin{pmatrix} 1 & 0 \\ 0 & i \end{pmatrix}, \tag{1.70}$$

and the two-qubit CNOT gate

$$\hat{CNOT} = \begin{pmatrix} 1 & 0 & 0 & 0 \\ 0 & 1 & 0 & 0 \\ 0 & 0 & 0 & 1 \\ 0 & 0 & 1 & 0 \end{pmatrix}. \tag{1.71}$$

These basic constituents produce the Clifford group, which contains all unitary operators that map Pauli strings into other Pauli string. In detail, for any $\hat{U} \in \mathcal{C}_L$ and $\hat{P} \in \{\pm 1\}\mathcal{P}_L$, we have $\hat{U}\hat{P}\hat{U}^\dagger = \hat{P}' \in \{\pm 1\}\mathcal{P}_L$. Like stabilizer states, Clifford unitaries can also be represented efficiently using suitable tableaus. Any $\hat{U} \in \mathcal{C}_L$ is fully specified by its action on Pauli strings, which can be determined by tracking the conjugations $\hat{\sigma}^z_j \to \hat{U}\hat{\sigma}^z_j\hat{U}^\dagger$ and $\hat{\sigma}^x_j \to \hat{U}\hat{\sigma}^x_j\hat{U}^\dagger$ for every site j. As a result, the unitary tableau has size $2L \times (2L+1)$, where each row encodes a Pauli string with sign obtained by evolving $\hat{\sigma}^{z,x}_j$.

The dynamics generated by Clifford circuits can be tracked efficiently, as it preserves the stabilizer character of quantum states. This is established by the Gottesman-Knill theorem [122], ensuring that many-body systems prepared in $|\psi_0\rangle =$

$|0\rangle^{\otimes L}$ and evolved only with Clifford unitaries and projective measurements in the computational basis can be simulated efficiently on classical computers. The first part of the theorem is a direct consequence of how a Clifford $\hat{U} \in \mathcal{C}_L$ acts on Pauli matrices. In fact, if $|\psi_0\rangle$ is stabilized by $\hat{g}_j$ (which are $\hat{g}_j = \hat{\sigma}_j^z$ for the computational basis state considered above), the evolved $\hat{U}|\psi_0\rangle$ is stabilized by $\hat{g}' = \hat{U}\hat{g}_j\hat{U}^\dagger$. This follows from

$$\hat{g}_j'\hat{U}|\psi_0\rangle = \hat{U}\hat{g}_j|\psi_0\rangle = \hat{U}|\psi_0\rangle\,. \tag{1.72}$$

Hence, Clifford dynamics can be implemented by simply updating the stabilizer generators $\hat{g}_j \to \hat{g}_j'$, which will then describe the evolved state.

Measurements in the computational basis are implemented by the projector $(1 \pm \hat{\sigma}_n^z)/2$, where the sign corresponds to the measurement outcome picked randomly by sampling the Born rule probabilities (see Sec. 2.1 for a detailed review of quantum measurements). The state is updated to

$$|\psi\rangle = \frac{1}{\mathcal{N}}\frac{1 \pm \hat{\sigma}_n^z}{2}|\psi_0\rangle\,, \tag{1.73}$$

where $\mathcal{N} = \sqrt{(1 \pm \langle\psi_0|\,\hat{\sigma}_n^z\,|\psi_0\rangle)/2}$ guarantees the correct normalization. The new stabilizer generators $\hat{g}_j'$ are determined as follows, depending on which of two cases applies.

1. If the measured operator $\hat{\sigma}_n^z$ commutes with all generators $\hat{g}_j$, these operators will continue to stabilize the state even after the measurement. This is seen from

$$\hat{g}_j|\psi\rangle = \frac{1}{\mathcal{N}}\frac{1 \pm \hat{\sigma}_n^z}{2}\hat{g}_j|\psi_0\rangle = |\psi\rangle\,. \tag{1.74}$$

   Since $|\psi\rangle$ and $|\psi_0\rangle$ are stabilized by the same generators, they must coincide. This means that $|\psi_0\rangle$ is an eigenstate of the measured operator, and thus the projection has no effect.

2. If $\hat{\sigma}_n^z$ does not commute with one or more $\hat{g}_j$, then it must anticommute with them. Without any loss of generality, suppose $\{\hat{\sigma}_n^z, \hat{g}_1\} = 0$. We proceed by defining $\hat{g}_1' = \pm\hat{\sigma}_n^z$ (where the sign is the same as the measurement outcome), and

$$\hat{g}_j' = \begin{cases} \hat{g}_j & \text{if } [\hat{\sigma}_n^z, \hat{g}_j] = 0, \\ \hat{g}_1\hat{g}_j & \text{otherwise.} \end{cases} \tag{1.75}$$

   for $j > 1$. We can immediately check that the new set $\{\hat{g}_j'\}$ stabilizes the projected state of Eq. (1.73), as all $\hat{g}_j'$ commute with $\hat{\sigma}_n^z$.

Hence, computational basis measurements keep the state a stabilizer, and the update rule of its generators can be applied efficiently. This proves the second part of the Gottesman-Knill theorem.

1.3.2 Measuring Pauli correlators and entanglement

Stabilizer states $|\psi\rangle$ exhibit a particular correlation structure. First, all expectation values of Pauli strings is either zero or equal to ± 1. In addition, for any bipartition of

the system, the entanglement entropy assumes only values that ar integer multiples of $\log 2$. Below, we explain how to evaluate these quantities from the stabilizer tableau of a state.

Pauli expectation values – Given a Pauli string $\hat{P} \in \mathcal{P}_L$, consider the expectation value $\langle\psi|\,\hat{P}\,|\psi\rangle$. Suppose $\pm\hat{P} \notin \mathcal{S}$, which occurs if $\hat{P}$ anticommutes with at least one generator $\hat{g}_j$. In this case, using Eq. (1.66) we have

$$\mathrm{Tr}\big(\hat{\rho}\hat{P}\big) = \frac{1}{2^L}\sum_{\hat{P}'\in\mathcal{S}} \mathrm{Tr}\big(\hat{P}'\hat{P}\big) = 0, \tag{1.76}$$

because $\mathrm{Tr}\big(\hat{P}'\hat{P}\big)$ is non-zero only if $\hat{P} = \pm\hat{P}'$ (Pauli strings different from the identity are traceless), and this never occurs by assumption.

The expectation value of $\hat{P}$ is non-zero only when either $\hat{P}$ or $-\hat{P}$ is a stabilizer, in which case $\langle\psi|\,\hat{P}\,|\psi\rangle = +1$ or -1, respectively. This occurs when $\hat{P}$ commutes with all generators. In this case, there exists a bitstring $\mathbf{x} = (x_1, \dots x_L)$ such that $\hat{P} = \pm\prod_{j=1}^{L}\hat{g}_j^{x_j}$. To determine $\mathbf{x}$, let us introduce a binary representation $\mathbf{b} = (b_1, \dots b_{2L})$ of the string $\hat{P}$ using the convention from Eq. (1.67). Let us also define $\tilde{T}$ as the submatrix obtained by discarding the first column of the state tableau T. The bitstring $\mathbf{x}$ is found by solving the linear system

$$\tilde{T}^T\mathbf{x} = \mathbf{b} \tag{1.77}$$

over the Galois field GF(2) (i.e., modulo 2 arithmetic). Once $\mathbf{x}$ is known the operator $\prod_{j=1}^{L}\hat{g}_j^{x_j}$ is constructed efficiently, and comparing it to $\hat{P}$ determines the sign of the expectation value.

Entanglement entropy – The entanglement entropy of a stabilizer state can be evaluated efficiently from the tableau as well [72]. Given the expansion of Eq. (1.66), the reduced density matrix of any subsystem A is given by $\hat{\rho}_A = \frac{1}{2^L}\sum_{\hat{P}\in\mathcal{S}}\mathrm{Tr}_B\,\hat{P}$. The partial trace $\mathrm{Tr}_B\,\hat{P}$ is non-zero only if $\hat{P}$ is fully contained in subsystem A, i.e., its portion defined on the sites of B is the identity; in this case, $\mathrm{Tr}_B\,\hat{P} = 2^{L-|A|}\hat{P}_A$. Let $\mathcal{S}_A$ be the set of substrings $\hat{P}_A$ obtained from non-vanishing partial traces. It is trivially observed that $\mathcal{S}_A$ is a group itself. This implies that

$$\hat{\rho}_A^2 = \frac{1}{2^{2|A|}}\sum_{\hat{P}_A,\hat{P}'_A\in\mathcal{S}_A}\hat{P}_A\hat{P}'_A = \frac{\dim\mathcal{S}_A}{2^{2|A|}}\sum_{\hat{P}_A\in\mathcal{S}_A}\hat{P}_A = \frac{\dim\mathcal{S}_A}{2^{|A|}}\hat{\rho}_A, \tag{1.78}$$

and thus $\hat{\rho}_A$ is proportional to a projector. As a consequence, the reduced density matrix has a flat spectrum, i.e., all its non-zero eigenvalues λ_n are equal. The previous equation then yields

$$\lambda_n = \frac{\dim\mathcal{S}_A}{2^{|A|}}. \tag{1.79}$$

Lastly, the entanglement entropy is given by

$$\frac{S_A}{\log 2} = -\frac{1}{\log 2}\sum_{n=1}^{2^{|A|}/\dim\mathcal{S}_A}\lambda_n\log\lambda_n = |A| - \log_2(\dim\mathcal{S}_A), \tag{1.80}$$

where the number of non-zero eigenvalues is obtained by the normalization condition $\mathrm{Tr}\,\hat{\rho}_A = 1$.

The integer $\log_2(\dim \mathcal{S}_A)$ is equal to the number of independent generators of $\mathcal{S}_A$. Let $\tilde{T}_B$ be the submatrix of the tableau T obtained by dropping all columns $2j, 2j+1$ with $j \in A$, as well as the first column storing signs. This $L \times 2(L - |A|)$ matrix stores the generators of all partial strings $\hat{P}_B$. By definition, the dimension of $\mathcal{S}_A$ is equal to the number of $\hat{P}_B$ equal to the identity. If we compute the upper triangular representation of $\tilde{T}_B$ through Gaussian elimination over GF(2), the dimension of $\mathcal{S}_A$ will be given by 2 to the power of the number of rows of zeros, as they correspond to the identity $\hat{\mathbb{1}}_B$. Hence, we have $\log_2(\dim \mathcal{S}_A) = L - \mathrm{rank}(\tilde{T}_B)$. Finally recalling that $S_A = S_B$, it is possible to swap the roles of A and B in Eq. (1.80) to obtain

$$\frac{S_A}{\log 2} = |B| - \log_2(\dim \mathcal{S}_B) = L - |A| - [L - \mathrm{rank}(\tilde{T}_A)] = \mathrm{rank}(\tilde{T}_A) - |A|, \quad (1.81)$$

where $\tilde{T}_A$ is the tableau submatrix of subsystem A defined analogously to $\tilde{T}_B$.

1.3.3 Magic and stabilizer Rényi entropies

Stabilizer states are a viable tool for quantum error correction and for investigating many-body Clifford circuit dynamics. Still, they constitute a very special and discrete subset of the full Hilbert space, and they deviate from the complex behavior of generic quantum states in several aspects. Analogously to free-fermionic systems, universal quantum computation can be achieved by supplementing Clifford operations with a resource that breaks the stabilizer character of states, known as non-stabilizerness or quantum magic. The most common way to inject magic is through the non-Clifford T gate

$$\hat{T} = \begin{pmatrix} 1 & 0 \\ 0 & e^{i\pi/4} \end{pmatrix}, \quad (1.82)$$

which is sufficient to break the stabilizer representation despite its simplicity. Hence, the gradual inclusion of non-stabilizer resources drives the state away from the efficiently simulable class of stabilizers.

Magic [81–88] constitutes another way of characterizing quantum complexity alternative to entanglement and non-Gaussianity. While these different notions are not fully independent, in general they are inequivalent, and provide different perspectives on what it means for a state to be complicated. For instance, stabilizer states can have volume-law entanglement, and in contrast there exist product states with high non-stabilizerness. Understanding the connections between different ways of characterizing complexity and how their presence impacts many-body behavior is currently subject of intense investigation [204–237].

There exist several quantitative probes of non-stabilizerness. In this thesis, we focus on the SREs [83, 84] and the stabilizer nullity, which will be used in the following chapters. Other well-known measures, such as mana [82] and robustness of magic [86, 238], are not considered here. The n-SRE of a pure state is defined as

$$M_n = \frac{1}{1-n} \log_2 \left(\sum_{\hat{P} \in \mathcal{P}_L} \frac{1}{2^L} \langle \psi | \hat{P} | \psi \rangle^{2n} \right). \quad (1.83)$$

This quantity essentially measures the delocalization of the density matrix over the basis of Pauli string. For stabilizer states, there are 2^L Pauli operators for which $\langle\psi|\hat{P}|\psi\rangle^{2n} = 1$ (see Eq. (1.66)), whereas the expectation value vanishes for all others, thus yielding $M_n = 0$. Generic states can instead have a larger number of strings for which $0 < \langle\psi|\hat{P}|\psi\rangle^{2n} \leq 1$, resulting in a finite $M_n > 0$ for any non-stabilizer state. The SREs fulfill additivity and for $n \geq 2$ also monotonicity [84]. Despite the apparently complicated form of Eq. (1.83), which involves a sum over the exponentially many elements of the Pauli group, this quantity can be evaluated explicitly in fermionic Gaussian and matrix-product state through a stochastic sampling algorithm, making it a valuable probe of magic in many-body systems. For free-fermionic states, a description of the algorithm can be found in App. A.

A second useful measure is the stabilizer nullity ν, defined as the L minus the number of generators of a stabilizer group $\mathcal{S}$ of a state $|\psi\rangle$. In fact, general states may still have a partial stabilizer nature, in the sense that there exist $k < L$ generators $\hat{g}_j \in \{\pm 1\}\mathcal{P}_L$ that are however insufficient to fully represent the state through the stabilizer formalism. Formally, we define the stabilizer dimension r of $|\psi\rangle$ as the maximum integer R for which it is possible to write

$$|\psi\rangle = \hat{U}_{\text{Cliff}} \left(|0\rangle^{\otimes R} \left|\varphi^{(L-R)}\right\rangle \right), \tag{1.84}$$

where $\hat{U}_{\text{Cliff}}$ is a suitable Clifford operator, and $\left|\varphi^{(N-R)}\right\rangle$ is a state of $L - R$ qubits. The dimension r coincides with the number of generators $\hat{g}_j$, and it quantifies how many single-qubit stabilizer states can be distilled out of $|\psi\rangle$ using only Clifford operations. Thus, the stabilizer nullity is defined as $\nu = L - r$. Formally, it is also given by $\nu = \lim_{n\to\infty}(n-1)M_n$, and it can be shown to upper bound all SREs. Notice that the nullity is a discrete notion of magic, and as such it is rarely useful in condensed matter settings.

Similarly to the entanglement entropy, the previous measures of magic can exhibit volume-law scaling, and are bounded from above by the system size L. In generic quantum dynamics, either generated by a Hamiltonian or by a quantum circuit with non-stabilizer gates, the SREs grow rapidly and saturate to extensive values in a finite time. Ground states of typical many-body systems usually exhibit a volume law as well. Qualitatively, the SREs (and even more the nullity) can be intuitively thought as measures of how many elementary magic resources, like T gates, are needed to realize a state having Clifford operations available.

Mixed-state stabilizers and magic – The notion of stabilizerness can be generalized to mixed states. In analogy to Eq. (1.66), we define mixed stabilizer states [51, 123, 239] as the set of density matrices $\hat{\rho}$ in the form

$$\hat{\rho} = \prod_{j=1}^{k} \frac{1 + \hat{g}_j}{2}, \tag{1.85}$$

where $\hat{g}_1, \ldots, \hat{g}_k$ are $k \leq L$ independent Pauli generators that stabilize $\hat{\rho}$. For $k = L$, the set is complete and we recover pure stabilizer states. The SREs introduced above are no longer good measures of non-stabilizerness, as, for instance, they can be larger than zero for states in the form of Eq. (1.85). Still, as proposed in Ref. [83], this problem can be overcome for the second SRE by generalizing it to

$$\tilde{M}_2 = M_2 - S^{(2)}, \tag{1.86}$$

where $S^{(2)}$ is the second Rényi entropy (see Eq. (1.3)). This quantity is zero for mixed stabilizer states, non-negative, and it can be intuitively interpreted analogously to the original SRE for pure states.

It is worth pointing out that other notions of stabilizerness for mixed states have been considered in the literature. For example, Ref. [83] actually defines a larger class of mixed states as stabilizers, comprised by all density matrices in the form $\hat{\rho} = \left(\hat{\mathbb{1}} + \sum_{\hat{P}\in G} \hat{P}\right)/2^L$, where G is an arbitrary subset of $\{\pm 1\}(\mathcal{P}_L \backslash \{\hat{\mathbb{1}}\})$. $\tilde{M}_2$ vanishes for all these states. Instead, a completely different definition is often adopted when quantifying the robustness of magic [86, 238], where any convex combination of pure stabilizer states is regarded as a mixed stabilizer density matrix. This characterization is analogous to the notion of mixed-state separability. Based on this alternative definition, Eq. (1.86) is not a proper magic measure.

Chapter 2

Dynamics of open quantum systems

In quantum mechanics, measurements play a fundamentally different role compared to classical physics, as they can actively alter the state of the system through projective evolution. The addition of external monitoring to unitary quantum dynamics leads to the framework of open quantum systems, giving rise to a broad class of phenomena that depart from closed-system behavior [39–41]. This chapter reviews the main theoretical concepts describing quantum measurements, beginning with the formalism of *positive operator-valued measures* (POVMs) and expanding to quantum trajectories and the Lindblad master equation [45, 46]. These tools form the necessary background for understanding monitored quantum dynamics, which is the central focus of the thesis.

In the second part, we summarize the key results on measurement-induced phase transitions (MIPTs), establishing the general phenomenology of typical models studied in the literature. In particular, we discuss the standard MIPTs in random quantum circuits and free-fermionic systems, highlighting their main differences, and provide a perspective on recent experimental progress.

2.1 Quantum measurements and trajectories

Measurements arguably represent the central distinguishing feature between quantum and classical physics, owing to their intrinsically stochastic nature. In the early years of quantum theory, this challenged the classical notion of determinism, revealing that Nature is fundamentally probabilistic. When a quantum system is observed, not only is the outcome of the process inherently random, but the action also perturbs the state by collapsing it. As a result, measurements provide a second mechanism for altering quantum states, complementing unitary dynamics with non-unitary and stochastic evolution.

When unitary dynamics is interspersed with measurements, the evolution of the system branches into multiple possible paths in the Hilbert space, known as quantum trajectories [240–244]. This often complicates the theoretical analysis of open quantum systems due to the lack of tools to investigate disordered quantum dynamics. In practical implementations, each separate run of a monitoring protocol generates a different trajectory, making it possible to measure efficiently only ensemble-averaged observables in experiments. These are fully captured by the evolution of the average density matrix, which is governed by the celebrated Lindblad master equation under Markovian assumptions. This equation is also central to the theory of deco-

herence and dissipation due to environmental coupling, and has been instrumental in understanding steady-state relaxation and the effects of noise in open quantum systems.

This section introduces the standard formalism of POVMs and Kraus operators [39, 40, 240, 245], which are essential to describe generalized quantum measurements. We then present the concept of quantum trajectories and the stochastic Schrödinger equation, providing examples of commonly studied monitoring protocols. Finally, we derive and discuss the Lindblad master equation and its key properties.

2.1.1 Kraus operators

The theory of POVMs provides the framework to describe the most general type of quantum measurement. A measurement with $M > 1$ outcome is a stochastic process that maps a (not necessarily pure) initial state $\hat{\rho}$ into one of M possible final states $\hat{\rho}^{(m)}$, selected with probabilities determined by the Born rule. Within the formalism of POVMs, a measurement is specified by the assignment of M Kraus operators $\hat{A}_m$, satisfying the completeness relation

$$\sum_{m=1}^{M} \hat{A}_m^\dagger \hat{A}_m = \hat{\mathbb{1}}. \tag{2.1}$$

These determine the possible post-measurement states, which are defined as

$$\hat{\rho}^{(m)} = \frac{1}{p_m} \hat{A}_m \hat{\rho} \hat{A}_m^\dagger, \tag{2.2}$$

where $p_m = \mathrm{Tr}\left(\hat{\rho}\hat{A}_m^\dagger \hat{A}_m\right)$ is the Born rule probability corresponding to the m-th outcome. Equation (2.1) ensures that $\sum_{m=1}^{M} p_m = 1$ for any possible initial state, thus guaranteeing conservation of probability.

The simplest application of this formalism is that of a projective measurement of an observable $\hat{O}$, in which case the each Kraus operator coincides with a projector onto an eigenstate of $\hat{O}$; in this case, we have $\hat{A}_m = \hat{A}_m^\dagger = \hat{A}_m^\dagger \hat{A}_m$ [1]. For instance, a computational basis measurement of $\hat{\sigma}^z$ is represented by the Kraus operators $\hat{A}_0 = |0\rangle\langle 0|$ and $\hat{A}_1 = |1\rangle\langle 1|$ (we start counting from $m = 0$ for convenience of notation). For projective measurements, different Kraus operators project the state into mutually orthogonal subspaces of the Hilbert space. As a consequence, subsequent measurements of the same operator $\hat{O}$ yield the same outcome.

Beyond this case, the POVM formalism also allows the Kraus operators to not be projectors. This leads to generalized measurements, where the different $\hat{A}_m$ do not act on orthogonal eigenspaces. Such measurements can be practically implemented by coupling ancilla qubits to the physical ones and measuring them afterwards, which results in an indirect observation of the main system. To illustrate the general setup, let $\hat{\rho}$ be the state of the system, $|\varphi_A\rangle$ be that of an ancilla qubit, and $\hat{U}_{S,A}$ be a unitary operator coupling the two. We define the measurement protocol as the action of $\hat{U}_{S,A}$

[1] The Kraus operators are always defined modulo a global phase. Indeed, any redefinition $\hat{A}_m \to e^{i\varphi_m}\hat{A}_m$ is completely inconsequential in Eq. (2.2).

followed by a projective measurement of the ancilla in the computational basis. The two possible post-measurement states are given by

$$\hat{\rho}^{(m)} \otimes |m_A\rangle \langle m_A| = \frac{\langle m_A| \hat{U}_{S,A} |\varphi_A\rangle \hat{\rho} \langle \varphi_A| \hat{U}_{S,A}^\dagger |m_A\rangle}{p_m} \otimes |m_A\rangle \langle m_A| \tag{2.3a}$$

where $p_m = \mathrm{Tr}_S \left(\langle m_A| \hat{U}_{S,A} |\varphi_A\rangle \hat{\rho} \langle \varphi_A| \hat{U}_{S,A}^\dagger |m_A\rangle \right)$, and $m = 0, 1$. From this result, we can describe the measurement on the system alone by introducing the Kraus operators

$$\hat{A}_m = \langle m_A| \hat{U}_{S,A} |\varphi_A\rangle , \tag{2.4}$$

which only act on S and are not projectors in general. It is immediate to check that Eq. (2.1) is satisfied. Notice that the Kraus operators strictly depend on the details of how the coupling $\hat{U}_{S,A}$ is implemented, as well as the state $|\varphi_A\rangle$ the ancilla is prepared in.

A particular case of this is given by *weak measurements* [56, 240], obtained when the coupling is a short evolution $\hat{U}_{S,A} = e^{-i\epsilon \hat{H}_{S,A}}$, where $\epsilon \to 0$ is ideally infinitesimal. Since the interaction between system and ancilla is infinitesimal, the measurement performed on the latter will typically affect the former very weakly. An example of this is given by the single-qubit Kraus operators

$$\hat{A}_0 = \frac{1}{\sqrt{2}} \Big[|0\rangle \langle 0| + (1-\epsilon) |1\rangle \langle 1| \Big] + \mathcal{O}(\epsilon^2), \tag{2.5a}$$

$$\hat{A}_1 = \frac{1}{\sqrt{2}} \Big[|0\rangle \langle 0| + (1+\epsilon) |1\rangle \langle 1| \Big] + \mathcal{O}(\epsilon^2), \tag{2.5b}$$

which both slightly perturb the original state to $\hat{\rho}^{(m)} = \hat{\rho} + \mathcal{O}(\epsilon)$ and have $p_m \approx 1/2$. An alternative example of weak measurement is given by the Kraus operators

$$\hat{A}_0 = |0\rangle \langle 0| + \cos\epsilon \, |1\rangle \langle 1| , \tag{2.6a}$$

$$\hat{A}_1 = \sin\epsilon \, |1\rangle \langle 1| . \tag{2.6b}$$

In this case, the first Kraus operator $\hat{A}_0$ impacts infinitesimally the state, and it happens with probability $p_0 \approx 1$, whereas $\hat{A}_1$ implements a drastic projection to $|1\rangle$ but occurs only with a small probability $p_1 = \mathcal{O}(\epsilon^2)$. In the limit $\epsilon \to 0$, weak measurements are meaningful only in a suitable continuous time limit, where they are performed subsequently at each infinitesimal timestep dt of the dynamics. In this case, the appropriate scaling behavior for ϵ is $\epsilon \propto \sqrt{dt}$, and Eqs. (2.5) and (2.6) define the so-called quantum state diffusion and quantum jump protocols, respectively.

2.1.2 Quantum trajectories

Quantum measurements can be combined with unitary evolution, either continuous or generated by a circuit, to generate interesting non-equilibrium phenomena, such as MIPTs [47–52]. In this hybrid dynamics, the randomness of the monitoring induces multiple possible paths the system can take, giving rise to a number of quantum trajectories that is exponentially large in the number of measurements.

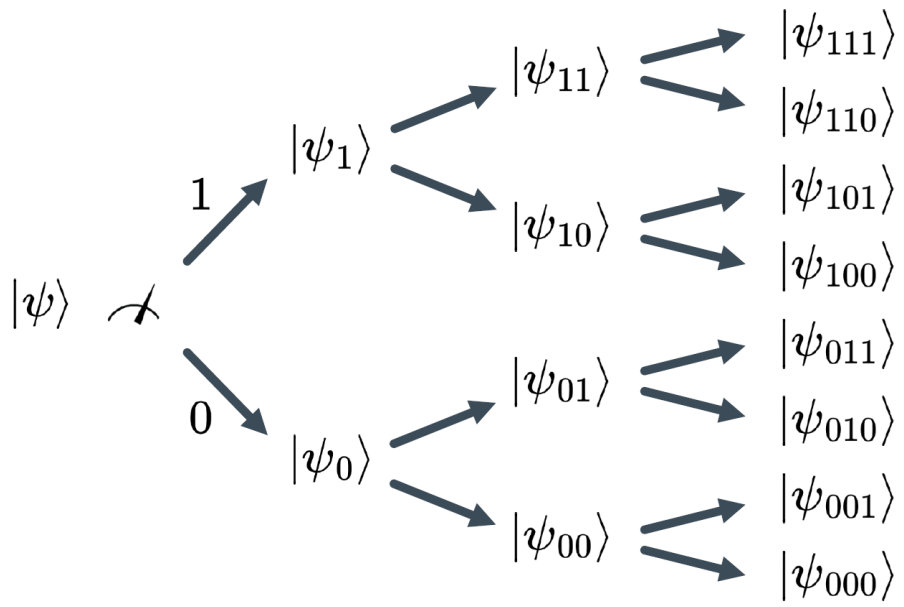

Figure 2.1: Schematic illustration of the branching of quantum trajectories induced by monitoring. Here we assume that each measurement has $M = 2$ possible outcomes, and it thus bifurcates each path.

This is pictorially illustrated in Fig. 2.1, showing the branching induced by binary measurements. Fixing the times at which all measurements are performed and their Kraus operators, a trajectory can be labelled by its record of measurement outcomes $(m_1, m_2, \dots)$.

Let us now consider a many-body system of L qubits evolving under the Hamiltonian $\hat{H}$. A commonly used monitoring protocol consists of performing projective measurements of single-site Hermitian operators $\hat{O}_j$ at random times, assuming a constant rate of measurement γ_j per qubit, typically taken to be uniform, $\gamma_j = \gamma$. When a measurement needs to be performed, the unitary evolution is momentarily stopped and resumed afterwards. In this setup the dynamics exhibits two sources of randomness, i.e., on the measurement outcomes as well as on their times and positions. When carrying out the hybrid evolution for a total time T, the average number of measurements performed on the full system will be γLT, which implies an exponentially large number $\sim e^{\gamma LT}$ of quantum trajectories. As an alternative to the projective measurement protocol, continuous monitoring is also typically considered, where each qubit of the system is uninterruptedly coupled to a detecting apparatus (i.e., a set of ancillae) implementing weak measurements at each instant of time [240].

In quantum circuits, the standard way of adding a monitoring is to alternate between a layer of unitary gates and a layer of (usually projective) measurements. This is illustrated in Fig. 2.2. In a measurement layer, each site is measured with a probability $p \in [0, 1]$, which is analogous to the rate γ in continuous implementations.

Stochastic Schrödinger equation – The evolution of a monitored system can be described theoretically through a stochastic Schrödinger equation, a formalism

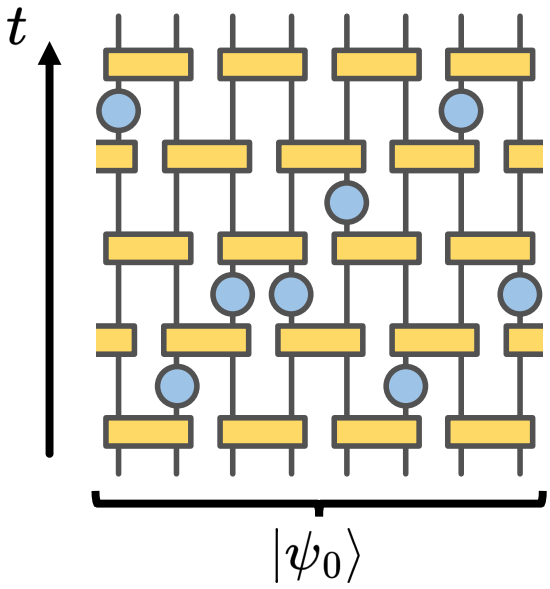

Figure 2.2: Typical structure of a monitored quantum circuit, alternating unitary layers to measurement ones.

particularly useful for continuous monitoring protocols [49, 55, 56, 246–250]. To illustrate it, consider the quantum jump protocol introduced in Eq. (2.6), which will also be used in the upcoming chapters. For convenience, we define the projector $\hat{L}_j = |0_j\rangle\langle 0_j|$ acting on the lattice site j. We set $\epsilon = \gamma dt$, in such a way that the Kraus operators acting on each qubit are given by $\hat{A}_{0,j} = \hat{\mathbb{1}}_j - \frac{\gamma dt}{4}\hat{L}_j$ and $\hat{A}_{1,j} = \sqrt{\gamma dt}\hat{L}_j$ to first order in dt. Here γ controls the frequency of quantum jump events, corresponding to the sudden projections implemented by $\hat{A}_1$. Starting from a pure state $|\psi_0\rangle$, let $|\psi_t\rangle$ be the state at time t. $|\psi_t\rangle$ is the result of a non-deterministic evolution, as quantum jumps occur probabilistically. Let us define the stochastic process

$$d\xi_{j,t} = \begin{cases} 1 & \text{with probability } p_{j,t} = \langle\psi_t|\hat{A}_{1,j}^\dagger\hat{A}_{1,j}|\psi_t\rangle = \gamma dt\,\langle\psi_t|\hat{L}_j|\psi_t\rangle\,, \\ 0 & \text{otherwise,} \end{cases} \tag{2.7}$$

which captures the statistics of quantum jumps: if $d\xi_{j,t} = 1$ we apply the Kraus operator $\hat{A}_{1,j}$, otherwise we use $\hat{A}_{0,j}$. We can write this compactly in the form of the evolution equation

$$|\psi_{t+dt}\rangle = \prod_{j=1}^{L}\left[(1-d\xi_{j,t})\frac{\hat{A}_{0,j}}{\sqrt{1-p_{j,t}}} + d\xi_{j,t}\frac{\hat{A}_{1,j}}{\sqrt{p_{j,t}}}\right]\Big(|\psi_t\rangle - i\hat{H}dt\,|\psi_t\rangle\Big) + \mathcal{O}(dt^2), \tag{2.8}$$

where $\hat{H}$ is the Hamiltonian of the system. The product of operators applied to the state generates all possible combinations of jump events occurring at time t. Since the probability of each jump scales with dt, we may neglect all terms of type $d\xi_{i,t}d\xi_{j,t}$ as well as $dtd\xi_{j,t}$, as they contribute only at order $\mathcal{O}(dt^2)$. After a straightforward calculation keeping only terms up to $\mathcal{O}(dt)$, we obtain the stochastic Schrödinger

equation

$$|\psi_{t+dt}\rangle = |\psi_t\rangle - idt\left[\hat{H} - i\frac{\gamma}{4}\sum_{j=1}^{L}\left(\hat{L}_j - \langle\psi_t|\,\hat{L}_j\,|\psi_t\rangle\right)\right]|\psi_t\rangle \\ + \sum_{j=1}^{L} d\xi_{j,t}\left(\frac{\hat{L}_j}{\sqrt{\langle\psi_t|\,\hat{L}_j\,|\psi_t\rangle}} - 1\right)|\psi_t\rangle\,. \tag{2.9}$$

The previous equation can be split into two contributions. First, we have a deterministic evolution governed by the effective Hamiltonian

$$\hat{H}_{\text{eff}} = \hat{H} - i\frac{\gamma}{4}\sum_{j=1}^{L}\left(\hat{L}_j - \langle\psi_t|\,\hat{L}_j\,|\psi_t\rangle\right), \tag{2.10}$$

which is not Hermitian. In particular, the measurement backaction corresponding to the outcome of not observing any jump generates an imaginary contribution that sums up to the original Hamiltonian. Notice that the constant terms $\langle\psi_t|\,\hat{L}_j\,|\psi_t\rangle$ ensure that normalization is preserved, as one can immediately check explicitly. Equation (2.10) alone generates the so-called *no-click limit* in which no quantum jump is recorded by the detectors. This is very different from not measuring the system at all: the qubits are still affected by the monitoring, which causes a non-unitary evolution. As we will see later, this limit provides a simple framework to understand basic features of MIPTs.

The other part of Eq. (2.9) (second line) encodes the quantum jumps, and it is entirely stochastic. These operators implement the projections $\hat{L}_j$ whenever $d\xi_{j,t} = 1$. Numerically, one can simulate the dynamics of the stochastic Schrödinger equation by implementing the no-click evolution and sampling $d\xi_{j,t}$ at each timestep [2]. When a jump occurs, the corresponding projection is applied.

2.1.3 Lindblad master equation

The evolution of observable expectation values averaged over the set of all quantum trajectories is captured by the ensemble-averaged state $\hat{\rho}_t$. For Hamiltonian models with monitoring protocols of the kinds mentioned above, the dynamics of the mean density matrix is governed by the well-known Lindblad master equation [39–41, 44]

$$\partial_t\hat{\rho}_t = \mathcal{L}\hat{\rho}_t \tag{2.11a}$$

$$\mathcal{L}\bullet = -i\big[\hat{H},\bullet\big] + \sum_k\left(\hat{L}_k\bullet\hat{L}_k^\dagger - \frac{1}{2}\big\{\hat{L}_k^\dagger\hat{L}_k,\bullet\big\}\right), \tag{2.11b}$$

where $\mathcal{L}$ is the Lindblad superoperator acting on the space of density matrices. Here, $\hat{H}$ is the Hamiltonian, and $\hat{L}_k$ are the Lindblad jump operators describing the interaction of the system with the external world, either representing the effect of measurements or the coupling with an environment; the corresponding part of

[2] In practical implementations, it is often more convenient to check whether or not a jump happens on each site independently, as in the original Eq. (2.8). This is usually simpler and mitigates errors due to using finite values of dt.

the Lindbladian is referred to as a dissipator, and it encodes non-unitary effects. This equation constitutes a foundational tool for studying open quantum systems in quantum optics, condensed matter theory, and quantum information. Its impact extends far beyond monitored systems, as it finds common applications in noise modeling, decoherence, and dissipation induced by coupling to a bath.

Equation (2.11b) provides the most general Lindbladian generating Markovian completely-positive and trace-preserving (CPTP) dynamics. This is also known as a *quantum channel*, meaning that it maps any valid density matrix $\hat{\rho}$ into a new one that is still physical, preserving trace and positive definiteness.

We can immediately derive the Lindblad equation for some of the monitoring protocols discussed previously. For example, consider a Hamiltonian evolution interspersed with local projective measurements on each site j, described by the Kraus operators $\hat{A}_{m,j}$ and occurring with a rate γ. At each timestep, there are two possibilities:

1. No measurement is performed. This happens with a probability $(1-\gamma dt)^N = 1-\gamma L dt + \mathcal{O}(dt^2)$.

2. Only one site, which we label j, is measured. This happens with a probability γdt. In this case, a Kraus operator $\hat{A}_{m,j}$ is picked using the Born rule probabilities $p_{m,j}$.

Processes involving two or more measurements at the same time contribute to order $\mathcal{O}(dt^2)$ and are thus neglected. The updated average density matrix is given by the sum over all possible final states weighted by their probabilities [3], yielding

$$\hat{\rho}_{t+dt} = \hat{\rho}_t - i\big[\hat{H}, \hat{\rho}_t\big] - \gamma dt \sum_j \Big(\hat{A}_{m,j}\hat{\rho}_t\hat{A}^\dagger_{m,j} - \hat{\rho}_t\Big) + \mathcal{O}(dt^2), \tag{2.12}$$

where we also introduced the Hamiltonian contribution. After using the completeness relation of Eq. (2.1) to rewrite $1 = \sum_m \hat{A}^\dagger_{m,j}\hat{A}_{m,j}$ and defining $\partial_t\hat{\rho}_t = \lim_{dt\to 0}(\hat{\rho}_{t+dt} - \hat{\rho}_t)/dt$, Eq. (2.12) assumes the Lindblad form of Eq. (2.11) with $\hat{L}_{m,j} = \sqrt{\gamma}\hat{A}_{m,j}$. An analogous derivation can be performed for the case of continuous measurements.

While a monitoring protocol is described by a unique master equation, the opposite is not true: each Lindblad equation can describe multiple possible stochastic Schrödinger equations, known as *unravelings*. These are useful for simulating ensembles of trajectories that average to the Lindblad result, which is almost always more convenient than working directly with the mixed average density matrix. Still, individual trajectories may exhibit very different properties in different unravelings.

Steady state – The Lindblad master equation is guaranteed to always have at least one steady state, corresponding to a fixed point of the dynamics [44]. This can be seen from the eigendecomposition of the Liouvillian. Let λ_n and $\hat{\eta}_n$ be the eigenvalues and eigenoperators of $\mathcal{L}$, respectively, satisfying $\mathcal{L}\hat{\eta}_n = \lambda_n\hat{\eta}_n$. The set $\{\hat{\eta}_n\}$ forms a basis for the space of operators, allowing any initial state $\hat{\rho}_0$ to be

[3] Note that the Born rule probabilities $p_{m,j}$ cancel out in Eq. (2.12) due to the denominator appearing in Eq. (2.2).

expanded as $\hat{\rho}_0 = \sum_n a_n \hat{\eta}_n$. From Eq. (2.11), the time-evolved density matrix is given by

$$\hat{\rho}_t = e^{\mathcal{L}t}\hat{\rho}_0 = \sum_n a_n e^{\lambda_n t}\hat{\eta}_n. \tag{2.13}$$

It can be shown that at least one eigenvalue, which we pick to be λ_0, vanishes, and all others satisfy $\mathrm{Re}(\lambda_n) \leq 0$. This implies that the term proportional to $\hat{\eta}_0$ in Eq. (2.13) stays constant in time, whereas all others decay over a timescale $\sim 1/\mathrm{Re}(-\lambda_n)$. Hence, $\hat{\eta}_0$ corresponds to a steady state of the open system evolution. In many situations it is unique, but particular models may exhibit additional infinite-lifetime modes with $\mathrm{Re}(\lambda_n) = 0$. In these cases, the steady state reached at long times may depend on the initial conditions, or the system might exhibit perpetual oscillations between modes that never decay. Assuming that $\hat{\eta}_0$ is the only steady state, the timescale needed to relax to it is controlled by the inverse of the Liouvillian gap $\Delta = \min_{n\neq 0} \mathrm{Re}(-\lambda_n)$.

Suppose that the Kraus operators used in the monitoring satisfy the property

$$\sum_{m=1}^{M} \hat{A}_m \hat{A}_m^\dagger = \hat{\mathbb{1}}, \tag{2.14}$$

which resembles the completeness relation of Eq. (2.1) but imposes a distinct condition. In this case the quantum channel is called *unital*, and it guarantees that the infinite-temperature (maximally mixed) state $\hat{\rho}_\infty = \hat{\mathbb{1}}/2^L$ is a steady state of the corresponding Lindblad equation. In fact, recalling that the jump operators $\hat{L}_m$ are proportional to $\hat{A}_m$ as derived earlier, it can be checked by explicit substitution in Eq. (2.11b) that unitality ensures $\mathcal{L}\hat{\rho}_\infty = 0$. This condition is always met for projective measurements, and often applies to generalized ones as well. An example of non-unital channel is the following. Given a set of Kraus operators $\hat{A}_m$ satisfying Eq. (2.14), introduce a set of outcome-dependent unitaries $\hat{U}_m$ and define $\hat{A}'_m = \hat{U}_m \hat{A}_m$. The new operators still describe a legitimate quantum measurement, as they fulfill Eq. (2.1), but they no longer obey Eq. (2.14). Physically, this corresponds to applying unitary gates conditional to the observed measurement outcome. This introduces biases in the dynamics, preventing the ensemble of trajectories from averaging to the infinite-temperature state.

2.2 Measurement-induced phase transitions

In many-body systems, monitored time evolution can give rise to dynamical phase transitions in the structure of quantum correlations. The basic mechanism is simple: unitary dynamics spreads quantum correlations and builds up entanglement, whereas local measurements disentangle degrees of freedom. The competition between these two effects, controlled by the monitoring rate, naturally suggests the existence of a critical transition. Since the pioneering works of Refs. [47–49], the literature on MIPTs has expanded rapidly [51–69, 247–265], investigating a variety of models and exploring the roles of symmetries, measurement protocols, and quantum complexity.

The main difficulty in studying MIPTs is that they are invisible to conventional ensemble-averaged observables. Entanglement transitions are properties of individual trajectories of the ensemble, and they typically show no signatures in the average density matrix generated by the Lindbladian [266, 267]. As mentioned before, in many cases the mean density matrix relaxes to the featureless infinite-temperature state at long times, *regardless of the measurement rate*, thus erasing any trace of the transition. As a consequence, probing MIPTs requires access to non-linear functionals of each trajectory, such as the entanglement entropy, which do not commute with ensemble averaging.

This theoretical issue extends to experiments. In practical implementations, trajectories are sampled from their ensemble. Measuring the non-linear properties of each path requires to reproduce it several times to collect statistics. However, the probability of each realization is exponentially suppressed in the total number of measurements, and thus recreating quantum trajectories randomly demands a prohibitive number of independent experimental runs. The problem of efficiently postselecting quantum trajectories, i.e., generating them with specific measurement outcomes on demand, remains arguably the main challenge of MIPTs. Some proposals to address this have been put forward [102, 268–272], either valid for special models or leveraging classical simulation, but no general solution is known. Finally, the difficulty is aggravated by the fact that measuring entanglement itself typically requires a large sample of copies of the same state, as in quantum state tomography.

In the following, we review the key properties of measurement-induced entanglement transitions, focusing on hybrid random circuits and monitored free fermions. For these models, we present the main results understood from numerical simulations and analytic insights. We then discuss alternative probes of MIPTs beyond the entanglement entropy, and finally summarize the key experimental realizations.

2.2.1 Entanglement transitions in hybrid random circuits

The standard setup of MIPTs in quantum circuits is shown in Fig. 2.2. The state, usually prepared in $|\psi_0\rangle = |0\rangle^{\otimes L}$, is evolved under alternating unitary and measurement layers of a 1D circuit, for an overall depth t of each of them. The probability of measurement per site at each layer is fixed to be p, and the monitoring is typically projective in the computational basis. The gates are usually sampled randomly from a given set, a common choice being the 2-qubit Clifford group $\mathcal{C}_2$ [47, 51, 53, 59–61], as it enables efficient simulation of the problem.

The key quantity we are interested in tracking is the entanglement entropy $S_A(t) \equiv S_\ell(t)$ for a compact subsystem of size $|A| = \ell \leq L/2$, averaged over the ensemble of random realizations of the circuit. At long times, the entropy relaxes to a steady-state value $\overline{S_A(\infty)}$ that exhibits three regimes depending on p:

1. Volume-law phase $\overline{S_\ell(\infty)} \sim \ell$ for $p < p_c$.
2. Logarithmic scaling $\overline{S_\ell(\infty)} \sim \log \ell$ at the critical point $p = p_c$.
3. Area-law phase $\overline{S_\ell(\infty)} \sim$ const. for $p > p_c$.

This is the standard behavior of measurement-induced entanglement transitions, holding for the majority of circuit models. Below the critical point, the system retains the strong volume-law correlations typical of the unitary case, whereas for $p > p_c$ the disentangling due to monitoring is too frequent to enable the build-up of entanglement. At $p = p_c$, the system becomes scale-invariant, featuring a logarithmic entanglement entropy characteristic of standard quantum critical points. Simulations suggest that the critical point may be described by a conformal field theory, though no rigorous microscopic connection is currently available.

The main numerical evidence for MIPTs is obtained by studying Clifford circuits, which enable the investigation of system sizes of hundreds of qubits. Haar-random circuits have also been studied [48, 52, 54, 58] for smaller values of L, and are consistent with the same behavior. In higher dimensions, the scaling behaviors of the different phases generalize to the corresponding volume and area laws, with a logarithmically-corrected area law at the critical point.

The critical point p_c is a non-universal property determined by the gate and measurement choices. Some universal features, such as critical exponents, emerge at criticality [48, 58–63, 273]. These indicate the existence of different universality classes for MIPTs, controlled by dimensionality, symmetries, and the unitary ensemble considered. For instance, Clifford and Haar-random circuits exhibit distinct correlation length critical exponents. It is worth noting that special symmetries may dramatically change the nature of the volume-to-area transition. For instance, if the circuit is composed of matchgates (corresponding to fermionic Gaussian unitaries), a logarithmic phase appears instead of a volume one for $p < p_c$ [274, 275]. In this case, the phenomenology is more similar to that of monitored free-fermionic Hamiltonians, discussed in the upcoming subsection.

Heuristic percolation mapping – The minimal cut approach introduced in Sec. 1.1.5 can be generalized to hybrid quantum circuits, and provides a qualitative understanding of the volume and area scalings of entanglement in the two phases. Here we briefly present the main idea, while a more detailed discussion can be found in Refs. [48, 50].

To complement the minimal cut method described earlier, we consider what happens when a path crosses a leg hosting a measurement in Fig. 2.2. Single-qubit projective measurements reset the system locally into a well-defined state, decoupled from the rest. This enables the cut to pass "for free" across a measurement, without increasing n_{cut}, as no entanglement to be erased is present. Hence, each measurement opens a wall, as represented schematically in Fig. 2.3a. The Rényi entropies still satisfy Eq. (1.17), and thus the tightest bound is obtained by finding the path that minimizes n_{cut} by passing through multiple broken legs.

This description enables an exact mapping to a classical bond percolation problem in 2D, as illustrated in Fig. 2.3b. The legs now define a square lattice where each side is open with probability p and closed with $1-p$. This statistical model can be solved exactly, and features a phase transition at $p_c = 1/2$ between a percolating phase for $p > p_c$, where the open bonds realize a cluster of infinite length, and a non-percolating one for $p < p_c$, where all clusters have finite size. In this context, $n_{\text{min-cut}}$ corresponds to the minimal number of walls crossed by the optimal path on the graph, and exhibits an analogous phase diagram. Assuming $1 \ll L \ll t$, one

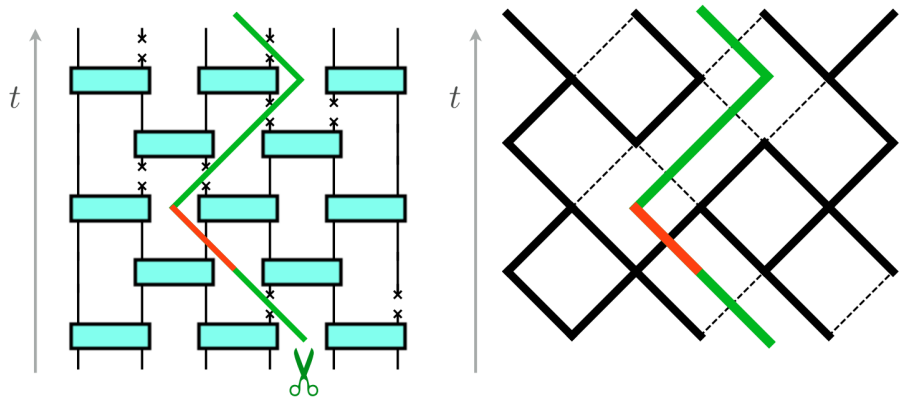

Figure 2.3: Illustration of the minimal cut mapping to a classical percolation model, taken from Ref. [48]. Left: in the hybrid circuit, local measurements break gate legs, allowing cuts to cross them without incrementing n_{cut}. Right: equivalent description in terms of a 2D percolating square lattice.

finds $n_{\text{min-cut}} \sim \ell$ for $p < p_c$, $n_{\text{min-cut}} \sim \log \ell$ at $p = p_c$, and $n_{\text{min-cut}} \sim$ const. for $p > p_c$.

While only qualitative, this simple description captures key features of entanglement transitions. The scaling behaviors shown by $n_{\text{min-cut}}$ capture the standard ones of MIPTs through the upper bound set by Eq. (1.17). However, the value $p_c = 1/2$ predicted by this mapping does not coincide with the true critical point found in explicit simulations of the hybrid circuit, and the associated critical exponents can differ from those of classical percolation.

2.2.2 Entanglement transitions in free-fermionic systems

We now shift to a Hamiltonian setting, considering free-fermionic systems subject to external monitoring that preserves Gaussianity, corresponding to Gaussian Kraus operators. Given their efficient classical simulability, these models provide a natural platform for investigating measurement-induced effects. In the standard protocol, the system is initially prepared in a product state, and undergoes unitary dynamics with either projective or continuous local monitoring using a rate γ per site.

The most striking feature of monitored free fermions is the instability of the volume-law entanglement scaling of the unitary evolution: any finite $\gamma > 0$ collapses it to a subextensive behavior [49, 55–57, 246–249]. The scaling properties of the entropy in weakly monitored free fermions in 1D have been the subject of intense debate over the last few years. Some studies reported the presence of a stable logarithmic phase below a critical γ_c, while others claimed that only an area law is present. Although no rigorous proof is available, it is now understood that the symmetry of the Hamiltonian plays a decisive role in the structure of the phase diagram. Models with $U(1)$ particle-number conservation do not exhibit any MIPT, and entanglement saturates to an area law $\overline{S_\ell(\infty)}$ for any finite value of γ. In contrast, BCS-like Hamiltonians with only $\mathbb{Z}_2$ symmetry possess an entangling phase exhibiting logarithmic scaling below a critical point γ_c.

This controversy was resolved also thanks to the development of field-theoretical

descriptions of monitored free fermions, given by non-linear sigma models (NLSMs) [91–95]. These are Keldysh field theories supplemented by a replica approach, enabling the calculation of non-linear properties. In particular, Ref. [92] considered a chain of hopping fermions with local density measurement, and found that at low γ the system develops a finite, though possibly very large, correlation length ξ. As a consequence, the entanglement entropy appears to scale logarithmically for $L \lesssim \xi$, but eventually saturates to an area law at larger system sizes. This result has been confirmed analytically by an independent study presented in Ref. [93], as well as numerically in Ref. [276] implementing large-scale simulations reaching up to $L \sim 16000$ in the 1D case. In contrast, Ref. [91] studied a Majorana model without $U(1)$ symmetry and obtained a scaling $\overline{S_\ell(\infty)} \sim \log^2 \ell$ at low γ from the NLSM. This suggests that, in the absence of particle-number conservation, monitored free fermions exhibit a stable entangling phase characterized by

$$\overline{S_\ell(\infty)} = a \log^2 \ell + b \log \ell + \mathcal{O}(1) \tag{2.15}$$

for $\gamma < \gamma_c$. The factor a is typically quite small, making the leading order behavior visible only at very large values of L. This explains why previous numerical simulations only detected a standard logarithmic growth.

Hybrid Gaussian fermionic circuits feature analogous phenomenology to the Hamiltonian case, exhibiting a logarithmic region at low measurement rates [89, 274, 275]. This will be explored in more detail in Chapter 7, where we analyze unitary gates that are simultaneously Gaussian and Clifford. In this setting, the dynamics of entanglement can be mapped to a Majorana loop model [253, 277], which is a classical statistical model proposed in the context of measurement-only quantum circuits. This enables an analytical approach to understand the phase transition.

Finally, generic monitored many-body Hamiltonians beyond free fermions typically exhibit a volume-to-area entanglement phase transition, as in Clifford and Haar-random circuits. The same holds for quadratic Hamiltonians with non-Gaussian measurement operators [258]. The fragility of the volume-law phase appears to be a direct consequence of Gaussianity, making it a defining characteristic of free fermions.

2.2.3 Signatures of measurement-induced criticality beyond entanglement

While the entanglement entropy is the standard probe for MIPTs, other non-linear quantities can reveal signatures of these critical phenomena as well. A notable example is found in Ref. [51], which considers an alternative point of view on monitored evolution. This work studies hybrid Clifford circuits initialized in the maximally-mixed density matrix $\hat{\rho}_\infty = \hat{\mathbb{1}}/2^L$. Throughout the dynamics, projective measurements gradually restore purity, eventually driving the system to a pure state. The purification time T of this process exhibits a phase transition controlled by the measurement rate. For $p > p_c$, measurements purify the density matrix rapidly in an intensive time $T \sim$ const. independent of L, whereas for $p < p_c$ the purification time grows exponentially as $T \sim e^{\lambda L}$. The critical point $p_c \approx 0.16$ coincides with that of

the entanglement phase transition in the same model, suggesting that the dynamical purification transition is a complementary manifestation of the same MIPT.

Quantum magic can also show qualitative changes in its scaling behavior induced by monitoring. When measuring a generic site j in the computational basis, the resulting state is stabilized by $\pm\hat{\sigma}^z_j$, partially restoring the stabilizer structure and thus erasing some magic. Therefore, as for entanglement, measurements act as a destruction mechanism for non-stabilizerness that competes with unitary evolution, potentially generating critical behavior. This problem has been addressed in Refs. [278, 279], which study measurement-induced magic transitions in T-doped hybrid Clifford circuits. When the number of T gates per layer is tuned to be $\mathcal{O}(1)$, non-stabilizerness measures display a rich phase diagram, featuring area-, subvolume-, and volume-law scaling of the stabilizer Rényi entropies (SREs). This phenomenon is not necessarily directly related to the entanglement transition, and thus it can present distinct phase boundaries. In Chapter 6 we report another type of magic MIPT in a Hamiltonian setting, where a phase transition is observed in the *subleading* behavior of SREs.

Quantum fluctuations of observables, quantified by variances of kind $(\Delta O)^2 = \langle \hat{O} \rangle^2 - \langle \hat{O} \rangle^2$, may also probe measurement-induced criticality. Note that this is a quadratic functional of the state, due to the presence of the squared expectation value of $\hat{O}$. An interesting example is given by *sharpening transitions* [76–79]. Consider a model with a conserved charge $\hat{Q}$ that commutes with the measurement protocol. For instance, one may consider local density measurements and take $\hat{Q}$ to be the total particle number. We prepare the system in a state $|\psi_0\rangle$ that spreads over multiple charge sectors (i.e., it is not an eigenstate of $\hat{Q}$). Throughout the dynamics, measurements will "sharpen" the charge, in the sense that they progressively collapse the state onto a unique eigensector. As a result, at long times $(\Delta Q)^2 = 0$. The measurement rate can tune a phase transition in the dynamical timescale for this sharpening, distinguishing fast and slow regimes. Unlike the mixed-state purification transition, the sharpening critical point can differ from that of the entanglement transition, highlighting a fundamental difference between these phenomena.

As a last example, multipartite entanglement provides another probe of many-body entanglement transitions that is inequivalent to the bipartite entropy. Its first application to the study of MIPTs is presented in Chapter 6. This and subsequent investigations [280] demonstrate that the phase diagram of quantum multipartiteness reproduces that of the entanglement entropy and highlights new phase boundaries, establishing its value as a complementary probe of MIPTs.

2.2.4 Experimental results

Due to the aforementioned problems of postselecting quantum trajectories and measuring entanglement, MIPTs have remained inaccessible to experiments for a long time. Despite these severe challenges, some outstanding experimental investigations have been recently carried out on different platforms. While standard implementations of the entanglement phase transition are limited to small system sizes that cannot be scaled up, they still manage to capture signatures of distinct measurement-induced phases. In addition, strategies that combine experimental data with clas-

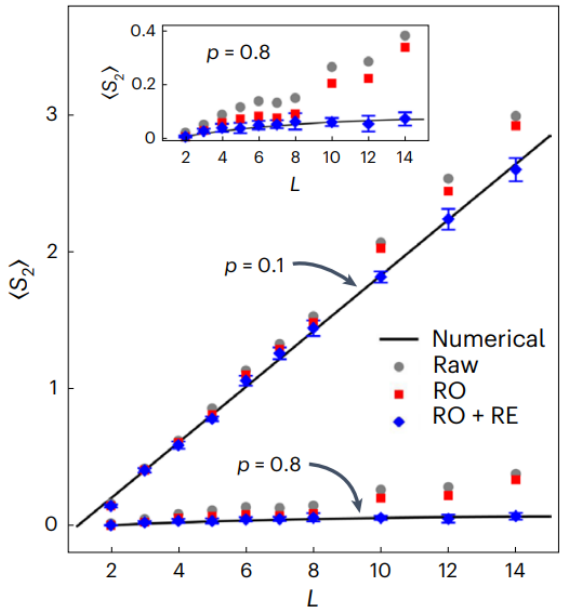

Figure 2.4: Experimental observation of a MIPT in Ref. [99]. The second Rényi entropy is measured as a function of the system size for two measurement rates $p = 0.1, 0.8$, setting a subsystem length $|A| = L/4$ (when $L/4$ is not integer, an interpolation between the closest ones is made). The labels "RO" and "RE" denote data points obtained implementing error-mitigation techniques.

sical simulations have been introduced to mitigate the exponential complexity of the problem, enabling the observation of MIPTs through hybrid quantum-classical probes.

Purely experimental approaches – A direct observation of a volume-to-area entanglement transition has been made by Ref. [99], implementing a hybrid quantum circuit on a superconducting processor. Here, the exponential overheads of postselection and quantum state tomography (needed to access the second Rényi entropy) are addressed by brute-force sampling an extremely large number of quantum trajectories. This allows the collection of sufficient statistics, but this approach is not scalable and is limited to $L = 14$. Figure 2.4 shows a strikingly clear signature of two scaling phases, visible even at the current system size. Analogous methods and results are reported by Ref. [102], which performs the experiment on superconducting qubits as well.

The complexity of the problem can be partially mitigated by abandoning the measurement of the entanglement of an extended subsystem, and focusing on the correlation of a single probe qubit instead [281]. This approach is followed by Ref. [100], which implements a monitored Clifford circuit evolution on a trapped-ion platform of up to $L = 14$ qubits. A single reference qubit R is initially entangled with the system, and the latter is then evolved with unitaries and measurements for a depth T. For $p < p_c$, measurements performed on the system are unable to disentangle the reference because its quantum correlations are scrambled, and thus the final reduced density matrix $\hat{\rho}_R$ remains mixed. In contrast, measurements successfully decouple the reference in the disentangling phase $p > p_c$, yielding a pure final state.

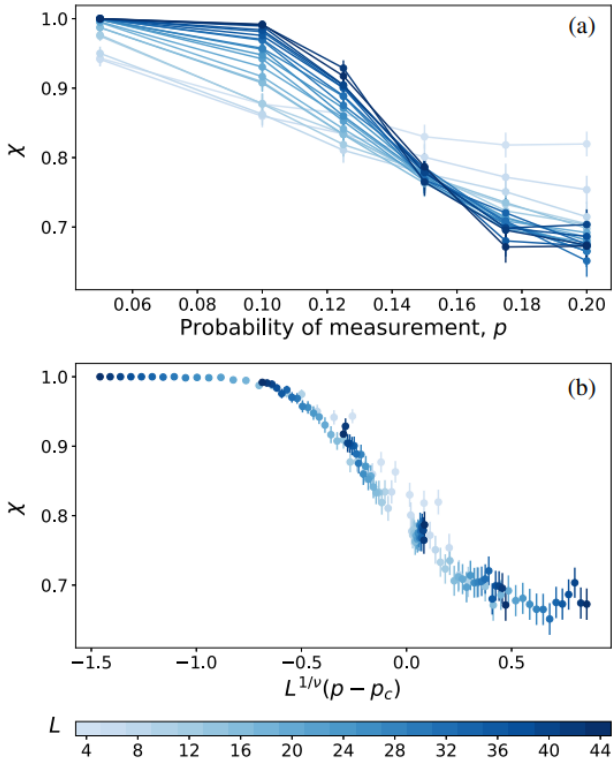

Figure 2.5: Signatures of criticality in the quantum-classical linear cross entropy presented in Ref. [103]. The number of physical qubits is $L/2$. Data from different system sizes exhibits a crossing, and collapses to a universal scaling function upon suitable rescaling.

Hybrid quantum-classical techniques – Given the scalability barriers set by postselection and quantum state tomography, hybrid quantum-classical order parameters have emerged as promising strategies to overcome these limitations. In Ref. [102], they experimentally demonstrate this idea on a system of up to $L = 70$ superconducting qubits. Similar to Ref. [100], the transition is witnessed by a reference qubit initially coupled to the monitored system. In this case, for each trajectory, the single-shot outcome of the final state of the reference qubit is cross-correlated with a classical prediction evaluated through numerical simulations. This enables the estimation of the von Neumann entropy of the probe qubit without the need to repeat quantum trajectories, which exhibits signatures of a dynamical phase transition.

A related proposal of a quantum-classical order parameter is the linear cross entropy. Given an initial state $\hat{\rho}$, let $\mathbf{m} = (m_1, m_2, \dots)$ be the collection of measurement outcomes of the monitored dynamics. We denote by $p^{\rho}_{\mathbf{m}}$ the probability of each quantum trajectory labeled by $\mathbf{m}$. The linear cross entropy for two initial states $\hat{\rho}_{1,2}$ is given by

$$\chi = \frac{\sum_{\mathbf{m}} p^{\rho_1}_{\mathbf{m}} p^{\rho_2}_{\mathbf{m}}}{\sum_{\mathbf{m}} (p^{\rho_2}_{\mathbf{m}})^2}, \tag{2.16}$$

and measures how distinguishable the two states are based on their measurement records. Eq. (2.16) can be interpreted as a statistical average of $p^{\rho_2}_{\mathbf{m}} / \sum_{\mathbf{m}} (p^{\rho_2}_{\mathbf{m}})^2$ over

the distribution $p^{\rho_1}_{\mathbf{m}}$. In an experiment, one explicitly implements the dynamics of $\hat{\rho}_1$, whereas the probabilities $p^{\rho_2}_{\mathbf{m}}$ are obtained through classical simulation of the evolution of $\hat{\rho}_2$. This is demonstrated in Ref. [103] with a superconducting device, considering hybrid Clifford circuits to perform this task efficiently. Figure 2.5 shows signatures of a MIPT in the linear cross entropy. Within this approach, the purpose of the experiment is to generate the outcomes $\mathbf{m}$ according to the correct statistics, while the averaged quantity is computed classically.

Chapter 3

Multipartite entanglement in the monitored quantum Ising chain

As discussed in the previous chapter, the most common way of characterizing measurement-induced phase transitions (MIPTs) is based on their bipartite entanglement, measured by the entanglement entropy. This approach is based on the interpretation that measurements compete with unitary dynamics in a clash between the erasure and the creation of quantum correlations. Investigations of the entanglement entropy have proved fundamental in distinguishing the behavior of generic interacting systems, exhibiting a volume-law phase [52, 257, 264, 282–284], from free-fermionic ones, which instead feature a logarithmic region at most [55, 56, 248, 285, 286]. Nevertheless, MIPTs also manifest in other properties [51, 73–77, 278, 279] of quantum trajectories, suggesting that the entanglement entropy alone might be insufficient to gain a complete picture of monitored quantum criticality.

Driven by this intuition, we now explore entanglement in a monitored many-body system beyond the bipartite level. The structure of multipartite correlations is potentially richer [130, 274, 287] and could give new insights for the characterization of the different phases. Specifically, in this chapter we investigate multipartite entanglement in a continuously monitored quantum Ising chain by means of the quantum Fisher information (QFI) [131, 132, 134, 135]. The goal is to understand if and to what extent multipartite correlations are sensitive to measurement-induced criticality. As our main result, we show that not only is the QFI a valid probe of MIPTs, but it also provides more information than the entanglement entropy, enabling a more in-depth analysis of the structure of quantum correlations.

The dynamics of the system we consider is described by a stochastic Schrödinger equation in the form of Eq. (2.9). Given its random nature, no analytical treatment of the full dynamics is available. For this reason, in order to develop a theoretical understanding of the properties of this system, we begin our analysis by investigating the no-click limit [56, 250, 264] generated by the effective non-Hermitian Hamiltonian. While not completely faithful to the full physics of the ensemble of quantum trajectories, this approach proves useful in establishing the scaling behaviors shown by the QFI density, which features a power-law regime $f_Q \sim L^p$ with $p > 0$ and a bounded phase with $f_Q \sim$ const.. Interestingly, multipartite entanglement exhibits the same phase boundaries as the entanglement entropy in the no-click limit, thus providing an equivalent characterization of measurement-induced criticality.

After this preliminary study, we move to the full dynamics generated by the stochastic Schrödinger equation, now relying on numerical results obtained from efficient Gaussian-state simulations. Here, the behavior of the QFI appears more

complex. While we still observe a transition between intensive and scaling entanglement, both bipartite and multipartite, qualitatively analogous to the no-click limit, we also find a third region with bounded QFI density yet logarithmic entanglement entropy. This highlights the presence of a third phase with strong yet finite-ranged correlations that is invisible from the calculation of bipartite entanglement alone.

The rest of the chapter is organized as follows. In Sec. 3.1, we introduce the quantum Ising chain and the quantum jump monitoring protocol we consider. Then, Sec. 3.2 presents the exact solution of the no-click limit and our results for the QFI, whereas Sec. 3.3 covers the case of the full dynamics involving quantum jumps. Last, we summarize our findings in Sec. 3.4.

3.1 Setup

Below, we consider MIPTs in a quantum Ising chain in transverse field

$$\hat{H}_0 = -\sum_j \hat{\sigma}_j^x \hat{\sigma}_{j+1}^x - h \sum_j \hat{\sigma}_j^z, \tag{3.1}$$

with L lattice sites and periodic boundary conditions. Within the formalism of positive operator-valued measures [240, 243, 244, 288, 289] presented in Sec. 2.1.1, we characterize entirely the measurement protocol by assigning suitable Kraus operators $\hat{A}_m$, $m = 1, \dots, M$, satisfying $\sum_m \hat{A}_m^\dagger \hat{A}_m = \hat{\mathbb{1}}$. In detail, given a state $|\psi_t\rangle$, the evolved state $|\psi_{t+dt}\rangle$ is obtained by applying a projector $\hat{A}_m$ to $|\psi_t\rangle$ and restoring the norm to 1. The choice of the Kraus operator is performed randomly with probabilities set by $p_m = \langle \hat{A}_m^\dagger \hat{A}_m \rangle_t$ (where $\langle \hat{O} \rangle_t = \langle \psi_t | \hat{O} | \psi_t \rangle$). In our case, we assume to measure the z-component of each spin randomly and independently of all others with a fixed rate γ. Since the full protocol can be broken down into single-site measurements, we use the local Kraus operators

$$\hat{A}_{0,j} = (\hat{\mathbb{1}} - \hat{L}_j) + \sqrt{1 - \gamma dt}\, \hat{L}_j, \tag{3.2a}$$

$$\hat{A}_{1,j} = \sqrt{\gamma dt}\, \hat{L}_j, \tag{3.2b}$$

where $\hat{L}_j = \frac{1}{2}(\hat{\mathbb{1}} + \hat{\sigma}_j^z)$, corresponding to a quantum jump protocol (see Eq. (2.6)). $\hat{A}_{0,j}$ has a probability $p_{0,j} = \mathcal{O}(1)$, and implements an infinitesimal drift towards a local spin state with down z-component. In contrast, $\hat{A}_{1,j}$ represents a rare but sudden jump to the state with up z-component, occurring with $p_{1,j} = \mathcal{O}(\gamma dt)$. The interplay of these Kraus operators can induce non-trivial magnetization dynamics [259, 290].

Using this generalized measurement protocol, the dynamics of the system is ruled by the stochastic Schrödinger equation [40, 291]

$$d|\psi_t\rangle = -i\hat{H} dt\, |\psi_t\rangle + \sum_j d\xi_{j,t} \left(\frac{\hat{L}_j}{\sqrt{\langle \hat{L}_j \rangle_t}} - 1 \right) |\psi_t\rangle\,, \tag{3.3}$$

where

$$\hat{H} = \hat{H}_0 - i\frac{\gamma}{4} \sum_j \left(\hat{\sigma}_j^z - \langle \hat{\sigma}_j^z \rangle_t \right) \tag{3.4}$$

is a non-Hermitian Hamiltonian [292] describing an effective non-unitary evolution in absence of jumps. The functions $d\xi_{j,t} = 0, 1$ are increments of independent Poisson processes satisfying $\overline{d\xi_{j,t}} = \gamma dt \langle \hat{L}_j \rangle_t$. The derivation of Eq. (3.3) follows the same discussion presented for Eq. (2.9).

The quantum Ising chain undergoing this monitoring protocol has been investigated in previous studies [56, 247, 248, 250], which highlighted a MIPT for the entanglement entropy. The scope of our study is to investigate the QFI in the stationary state of the dynamics generated by Eq. (3.3) and compare its behavior to S_A. Our goal is to understand whether multipartite entanglement exhibits any form of out-of-equilibrium critical behavior induced by measurements. As discussed in Sec. 1.1.3, the QFI of a state pure $|\psi\rangle$ is given by $F_Q[|\psi\rangle\langle\psi|, \hat{O}]$, and it is sensitive to the number of entangled degrees of freedom when evaluated with respect to operators of kind $\hat{O}[\{\mathbf{n}_j\}] = \frac{1}{2}\sum_j \mathbf{n}_j \cdot \hat{\boldsymbol{\sigma}}_j$. In this case, it reduces to $F_Q = \sum_{\alpha,\beta=x,y,z} \sum_{i,j} n_i^\alpha C_{i,j}^{\alpha,\beta} n_j^\beta$ (omitting the dependence on the state and the unit vectors for brevity), where $C_{i,j}^{\alpha,\beta} = \langle \hat{\sigma}_i^\alpha \hat{\sigma}_j^\beta \rangle - \langle \hat{\sigma}_i^\alpha \rangle \langle \hat{\sigma}_j^\beta \rangle$ are connected spin-spin correlators.

3.2 No-click limit

We start our analysis from the no-click limit, namely, the specific quantum trajectory generated by Eq. (3.3) in which all $d\xi_{j,t}$ are zero at all times, and no quantum jump occurs. Due to the non-Hermitianity of the effective Hamiltonian $\hat{H}$, at long times the dynamics converges to a pure stationary state, which can be determined analytically by diagonalizing the quadratic model. Even though this trajectory is exponentially unlikely, it can provide information on what can be expected in generic realizations of the full dynamics. In this section, we start by solving the model exactly and then present our results for the QFI, highlighting a MIPT.

3.2.1 Diagonalization of the non-Hermitian Hamiltonian

The effective Hamiltonian $\hat{H}$ remains integrable even if non-Hermitian, and can be diagonalized by using the Jordan-Wigner transformation 1.2.1 and proceeding in the same way as done for regular Hermitian quadratic models. The following derivation is similar to the one presented in Ref. [260].

The Hamiltonian of Eq. (3.4) can be mapped to a quadratic fermionic model by means of Eq. (1.22), which yields

$$\hat{H} = -\sum_{j=1}^{L-1} \left(\hat{c}_j^\dagger \hat{c}_{j+1} + \hat{c}_j^\dagger \hat{c}_{j+1}^\dagger + \text{h.c.}\right) + (-1)^{\hat{N}} \left(\hat{c}_L^\dagger \hat{c}_1 + \hat{c}_L^\dagger \hat{c}_1^\dagger + \text{h.c.}\right) + 2\left(h + i\frac{\gamma}{4}\right) \sum_{j=1}^{L} \hat{n}_j, \tag{3.5}$$

where $\hat{N} = \sum_j \hat{n}_j$ is the total number of fermions. Here and in all following instances, any additive constant to the Hamiltonian is disregarded. For simplicity, we also assume that L is even. While $\hat{N}$ itself is not conserved, its parity is a good quantum number. In our study, we work only with states in the even parity sector, and thus $\hat{H}$ is a BCS Hamiltonian with anti-periodic boundary conditions.

We shift to momentum space by introducing the momenta k satisfying $e^{ikL} = -1$, yielding $k = \pm\frac{2m-1}{L}\pi$, $m = 1, \dots, L/2$. We define the Fourier-space fermionic operators

$$\hat{d}_k = \frac{e^{-i\pi/4}}{\sqrt{L}} \sum_j e^{-ikj} \hat{c}_j, \tag{3.6}$$

which allow us to rewrite the Hamiltonian as $\hat{H} = \sum_{k>0} \hat{H}_k$, where

$$\begin{aligned} \hat{H}_k &= \begin{pmatrix} \hat{d}_{-k} & \hat{d}_k^\dagger \end{pmatrix} \begin{pmatrix} 2\cos k - 2h - i\frac{\gamma}{2} & -2\sin k \\ -2\sin k & -2\cos k + 2h + i\frac{\gamma}{2} \end{pmatrix} \begin{pmatrix} \hat{d}_{-k}^\dagger \\ \hat{d}_k \end{pmatrix} \\ &= \begin{pmatrix} \hat{d}_{-k} & \hat{d}_k^\dagger \end{pmatrix} \begin{pmatrix} \epsilon_k & \Delta_k \\ \Delta_k & -\epsilon_k \end{pmatrix} \begin{pmatrix} \hat{d}_{-k}^\dagger \\ \hat{d}_k \end{pmatrix}. \end{aligned} \tag{3.7}$$

The two-particle Hamiltonian $\hat{H}_k$ acts on the manifold of states $|0_k\rangle$, $|k\rangle = \hat{d}_k^\dagger |0_k\rangle$, $|-k\rangle = \hat{d}_{-k}^\dagger |0_k\rangle$, and $|k,-k\rangle = \hat{d}_k^\dagger \hat{d}_{-k}^\dagger |0_k\rangle$, where $|0_k\rangle$ is the vacuum of fermions with momenta $\pm k$. It is immediately checked that $\hat{H}_k$ acts trivially on states with a single fermion, namely, $\hat{H}_k |k\rangle = \hat{H}_k |-k\rangle = 0$. As a consequence, these states have no dynamics, and thus we focus on states with even occupation of $\pm k$ fermionic modes.

The eigenvalues of the Hamiltonian $\hat{H}_k$ are found in opposite pairs $\pm\Lambda_k$, where

$$\Lambda_k = 2\sqrt{1 - 2h\cos k + h^2 - \frac{\gamma^2}{16} + i\frac{\gamma}{2}(h - \cos k)}. \tag{3.8}$$

The complex square root requires the choice of a branch. For each k, we are free to define it in such a way that $\Lambda_k = E_k + i\Gamma_k$ (with $E_k, \Gamma_k \in \mathbb{R}$) has non-positive imaginary part $\Gamma_k \leq 0$. This choice is always possible, as eigenvalues come in pairs of opposite sign [1]. The Hamiltonian takes the diagonal form

$$\hat{H}_k = \Lambda_k \left(\hat{\tilde{\gamma}}_{-k} \hat{\gamma}_{-k} + \hat{\tilde{\gamma}}_k \hat{\gamma}_k \right) \tag{3.9}$$

in terms of new fermionic operators

$$\hat{\tilde{\gamma}}_k = \frac{-(\Lambda_k - \epsilon_k)\hat{d}_{-k}^\dagger + \Delta_k \hat{d}_k}{\sqrt{2\Lambda_k(\Lambda_k - \epsilon_k)}}, \tag{3.10a}$$

$$\hat{\gamma}_k = \frac{-(\Lambda_k - \epsilon_k)\hat{d}_{-k} + \Delta_k \hat{d}_k^\dagger}{\sqrt{2\Lambda_k(\Lambda_k - \epsilon_k)}}. \tag{3.10b}$$

The diagonal fermions satisfy the canonical anticommutation relations $\left\{\hat{\tilde{\gamma}}_k, \hat{\gamma}_{k'}\right\} = \delta_{k,k'}$, $\left\{\hat{\tilde{\gamma}}_k, \hat{\tilde{\gamma}}_{k'}\right\} = \{\hat{\gamma}_k, \hat{\gamma}_{k'}\} = 0$, but, differently from the Hermitian case, we have $\hat{\tilde{\gamma}}_k \neq \hat{\gamma}_k^\dagger$. Nevertheless, these can still be interpreted as creation and annihilation operators for non-Hermitian quasiparticles carrying complex energies Λ_k, and the operators $\hat{\tilde{\gamma}}_k \hat{\gamma}_k$ and $\hat{\tilde{\gamma}}_{-k} \hat{\gamma}_{-k}$ have the meaning of (non-conserved) number operators.

[1] The specific choice of the branch of the square roots is irrelevant, as long as a unique convention is adopted consistently.

3.2.2 Vacuum state and no-click dynamics

We now introduce the vacuum state of non-Hermitian quasiparticles. For each k, we define $|vac_k\rangle$ as the state that is annihilated by $\hat{\gamma}_{\pm k}$, obtaining

$$|vac_k\rangle = \frac{(\Lambda_k - \epsilon_k)\,|0_k\rangle - \Delta_k\,|k,-k\rangle}{\sqrt{|\Lambda_k - \epsilon_k|^2 + \Delta_k^2}}. \tag{3.11}$$

When acting on this state, the operators $\hat{\tilde{\gamma}}_{\pm k}$ add quasiparticles with complex energy Λ_k. In particular, within the same parity sector, we may define the state with two non-Hermitian quasiparticles $\hat{\tilde{\gamma}}_k\hat{\tilde{\gamma}}_{-k}\,|vac_k\rangle$, which, together with $|vac_k\rangle$, spans the same space as $|0_k\rangle$ and $|k,-k\rangle$. Any initial state within this space can then be represented as

$$|\psi_k(0)\rangle = \alpha\,|vac_k\rangle + \beta\,\hat{\tilde{\gamma}}_k\hat{\tilde{\gamma}}_{-k}\,|vac_k\rangle\,, \tag{3.12}$$

where $|\alpha|^2 + |\beta|^2 = 1$. Since we defined $\mathrm{Im}\,\Lambda_k$ to be negative, it follows from

$$|\psi_k(t)\rangle = \frac{e^{-i\hat{H}_k t}\,|\psi_k(0)\rangle}{\sqrt{\langle\psi_k(0)|\,e^{i\hat{H}_k^\dagger t}e^{-i\hat{H}_k t}\,|\psi_k(0)\rangle}} \tag{3.13}$$

that $|vac_k\rangle$ is the steady state of the dynamics reached for $t\to\infty$, as the exponential factor $e^{2\Gamma_k t}$ suppresses the relative weight of the state with quasiparticles. Considering all modes k, the overall vacuum state of the system is simply $|vac\rangle = \otimes_{k>0}\,|vac_k\rangle$.

The fermionic correlation matrix of the vacuum state can be computed analytically from Eq. (3.11). After a straightforward calculation (see Supplemental Material of Ref. [56] for the details), we obtain

$$(M_{\mathrm{o,o}})_{m,n} = \langle vac|\,\hat{\gamma}_{2m-1}\hat{\gamma}_{2n-1}\,|vac\rangle = \delta_{m,n} - \frac{4i}{L}\sum_{k>0}\sin(k(n-m))\frac{\Delta_k\mathrm{Im}(\Lambda_k-\epsilon_k)}{|\Lambda_k-\epsilon_k|^2+\Delta_k^2}, \tag{3.14a}$$

$$(M_{\mathrm{e,e}})_{m,n} = \langle vac|\,\hat{\gamma}_{2m}\hat{\gamma}_{2n}\,|vac\rangle = \delta_{m,n} + \frac{4i}{L}\sum_{k>0}\sin(k(n-m))\frac{\Delta_k\mathrm{Im}(\Lambda_k-\epsilon_k)}{|\Lambda_k-\epsilon_k|^2+\Delta_k^2}, \tag{3.14b}$$

$$\begin{aligned}(M_{\mathrm{o,e}})_{m,n} = \langle vac|\,\hat{\gamma}_{2m-1}\hat{\gamma}_{2n}\,|vac\rangle = &-\frac{2i}{L}\sum_{k>0}\cos(k(n-m))\frac{|\Lambda_k-\epsilon_k|^2-\Delta_k^2}{|\Lambda_k-\epsilon_k|^2+\Delta_k^2}\\ &-\frac{4i}{L}\sum_{k>0}\sin(k(n-m))\frac{\Delta_k\mathrm{Re}(\Lambda_k-\epsilon_k)}{|\Lambda_k-\epsilon_k|^2+\Delta_k^2},\end{aligned} \tag{3.14c}$$

already in the form defined in Eq. (1.62). These matrices then enable the calculation of spin-spin correlators through Eq. (1.63).

As reported by previous studies [247, 250], the no-click steady-state manifests a MIPT in the entanglement entropy $S_\ell = -\,\mathrm{Tr}\,(\hat{\rho}_\ell \ln\hat{\rho}_\ell)$ (where $\hat{\rho}_\ell$ is the reduced density matrix associated to a compact subsystem of ℓ spins) from an area law $S_\ell \sim$ const. to a logarithmic $S_\ell \sim \log\ell$. The development of scaling behavior in the stationary state can be directly linked to the closure of a gap in the decay rate of elementary excitations. For $|h|<1$ and $\gamma<\gamma_c(h) = 4\sqrt{1-h^2}$, the imaginary part Γ_k of the quasiparticle spectrum is gapless, and the entanglement entropy follows a logarithmic law. In contrast, outside this region it is gapped, and the entropy

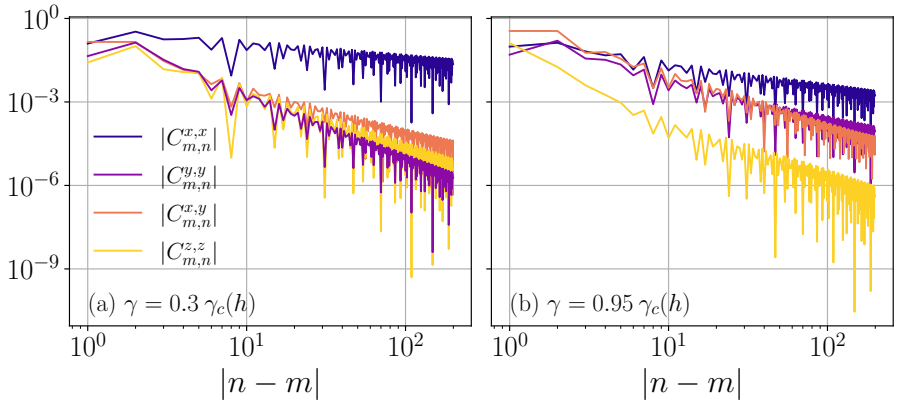

Figure 3.1: Spin-spin correlation functions of the no-click stationary state in the logarithmic phase, for a chain of $L = 8192$ spins, using $h = 0.2$ and (a) $\gamma/\gamma_c(h) = 0.3$, (b) $\gamma/\gamma_c(h) = 0.95$. The correlator with the slowest decay is $C^{x,x}_{m,n}$ in both cases, but near the boundary of the phase it decreases faster than in the bulk.

obeys an area law. This establishes a net phase separation obtained analytically. The momentum at which the gap of Γ_k closes below the critical line $\gamma_c(h)$ is $k^* = \arccos h$ [2]. Physically, this means that the system exhibits quasiparticle excitations with momentum $\pm k^*$ that do not decay in time.

3.2.3 Quantum Fisher information in the no-click limit

Beyond the entanglement entropy, signatures of the no-click MIPT can also be observed in the shape of correlation functions, which are crucial to the QFI (see Eq. (1.14)). In the gapped phase, the correlators $C^{\alpha,\beta}_{i,j}$ relax exponentially to zero with the distance $|j-i|$, whereas in the gapless phase they exhibit power-law decay modulated by sine-like oscillations, as shown in Fig. 3.1.

This difference impacts the QFI in the two phases. The maximization of the QFI can be equivalently seen as the search for the ground state energy of the classical energy functional $H_{\rm cl} = -F_Q[\{\mathbf{n}_j\}]$, in which the correlation functions set the interaction strengths. Hence, a shift of $C^{\alpha,\beta}_{i,j}$ from exponential to power-law implies a change from short- to long-range couplings in $H_{\rm cl}$. In particular, in the gapped phase $H_{\rm cl}$ is a short-range Hamiltonian, and thus it must have an extensive ground state energy $E_{\rm GS} \sim L$; as a consequence, the QFI density $f_Q = -E_{\rm GS}/L$ can only be intensive. Instead, in the gapless phase, the power-law decay of correlations opens up the possibility that $E_{\rm GS}$ scales super-extensively as $E_{\rm GS} \sim L^{1+p}$ with $p > 0$, which would give rise to $f_Q \sim L^p$. This is not automatically guaranteed by the algebraic shape of correlations, as it also depends on the exponent of the decay. Recalling the connection between the QFI density and multipartite entanglement, a scaling $f_Q \sim L^p$ would imply that the degree of multipartiteness of entanglement diverges as $\sim L^p$ only in the logarithmic phase.

[2] This specific value depends on the convention adopted for the Jordan-Wigner transformation of Eq. (1.22). In fact, swapping the definitions $\hat\sigma^+_j \leftrightarrow \hat\sigma^-_j$ results in the change $h \to -h$, and thus $k^* \to \pi - k^*$

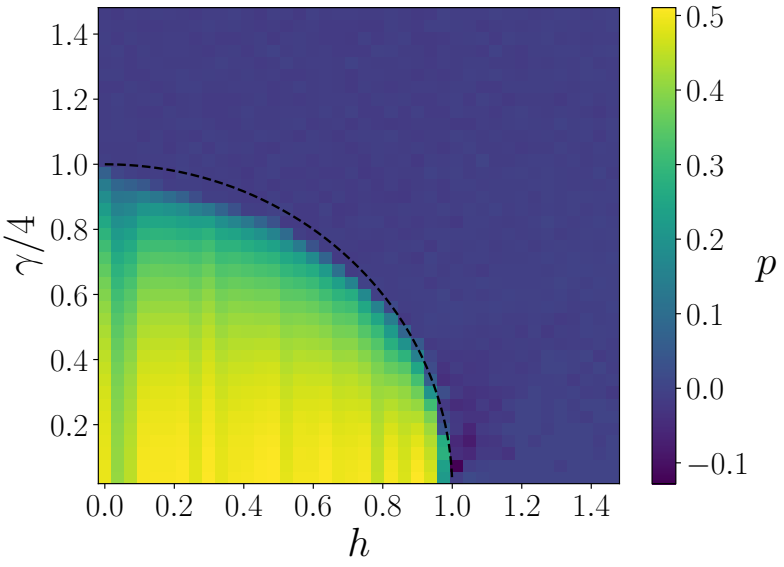

Figure 3.2: Exponent p of $f_Q \sim L^p$ as a function of h and γ in the no-click limit. The dashed curve corresponds to the critical line $\gamma_c(h)$ that separates the gapped and gapless phases. The exponent is extrapolated by fitting data for $L = 40 \div 170$.

We now test numerically this hypothesis. Numerically, the maximization of the QFI is performed with a classical simulated annealing algorithm [179, 180]. For each choice of the parameters h and γ, we evaluate the maximal QFI at different system sizes, and we fit the scaling of $f_Q^{\max}$ to extrapolate the exponent p. Figure 3.2 shows p in the parameter space. Based on whether $p = 0$ or $p > 0$, we distinguish two phases, which overlap very well with the area-law and logarithmic phases for the entanglement entropy delimited by the critical curve $\gamma_c(h)$. This indicates that the entanglement transition in the no-click limit is witnessed by multipartite entanglement as well.

Our numerical results suggest that p might be a universal function of the ratio $\gamma/\gamma_c(h)$ for all values of h. This is shown in Fig. 3.3, demonstrating a good collapse of data upon rescaling of the measurement rate. We point out that the effective central charge of the entanglement entropy behaves similarly, being a function of $\gamma/\gamma_c(h)$ only [260].

Optimal unit vectors – Surprisingly, despite the translational symmetry of the system, the operator $\hat{O}[\{\mathbf{n}_j\}]$ maximizing the QFI is not translationally invariant. In the gapless phase the optimal $\{\mathbf{n}_j\}_{\text{opt}}$ are approximately aligned along the longitudinal direction, and alternate between $+\mathbf{x}$ and $-\mathbf{x}$ with a wavevector $k = \pi - k^*$, where k^* is the momentum at which the gap of the quasiparticle decay rate closes. This is understood in terms of correlation functions. As seen in Fig. 3.1, $C^{x,x}_{i,j}$ is the slowest-decaying spin-spin correlator, ant thus the one that contributes the most to the QFI. This explains why the QFI is maximized by a configuration of unit vectors $\mathbf{n}_j$ along the x direction. Moreover, $C^{x,x}_{i,j}$ oscillates with a periodicity set precisely by $\pi - k^*$: while we could not prove it analytically, the ansatz

$$C^{x,x}_{m,n} \sim \frac{\cos((\pi - k^*)|n-m|)}{|n-m|^\lambda}, \tag{3.15}$$

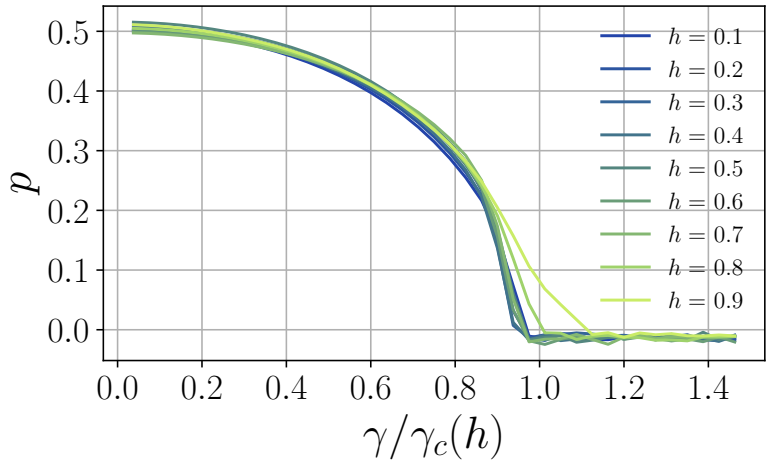

Figure 3.3: Exponent p of $f_Q^{\max} \sim L^p$ as a function of $\gamma/\gamma_c(h)$ for multiple values of h. The exponent decreases from $p \approx 0.5$ at $\gamma = 0$ to zero at $\gamma \approx \gamma_c(h)$, and it appears to depend on h only through $\gamma/\gamma_c(h)$.

fits very well the asymptotic behavior. This correlation function rules the leading order behavior of $f_Q^{\max}$ with L, and thus the optimal configuration $\{\mathbf{n}_j\}_{\text{opt}}$ must maximize its contribution in Eq. (1.14). Assuming Eq. (3.15) with $\lambda < 1$, and considering for simplicity a configuration $n_j^x = \cos((\pi - k^*)|i-j|)$, we obtain a contribution to the QFI that scales as $\sim L^{2-\lambda}$. Hence, the scaling exponent p of the QFI density may be estimated as $p = 1 - \lambda > 0$.

The operator $\hat{O}[\{\mathbf{n}_j\}_{\text{opt}}]$ that maximizes the QFI can be interpreted as a local order parameter due to its fluctuations, which are super-extensive exclusively in the critical gapless phase. This identification holds, for instance, for the quantum Ising chain $\hat{H}_0$, where the order parameter $\sum_j \hat{\sigma}_j^x$ maximizes the QFI providing $f_Q^{\max} \sim L^{3/4}$ at the critical point [133]. In the absence of any conventional order parameter $\hat{O}$ that changes from $\langle \hat{O} \rangle = 0$ to $\langle \hat{O} \rangle \neq 0$ when crossing the phase boundary, we believe this characterization is the most reasonable.

3.3 Dynamics with quantum jumps

The results on the QFI found in the no-click limit extend only partially to the full dynamics produced by Eq. (3.3). As we show in this section, bipartite and multipartite entanglement do not manifest equivalent behavior, and thus provide distinct information and phase boundaries. In particular, we observe a region featuring logarithmic entanglement entropy but intensive f_Q.

3.3.1 Entanglement dynamics and scalings

In our numerics, we start from a product state $|\psi_0\rangle$ with all spins along the positive z direction, and evolve it according to the stochastic Schrödinger equation. The quantum jump operators $\hat{L}_j$ are Gaussian, and thus preserve the free-fermionic character of the state throughout the time dynamics. As a consequence, the dynamics

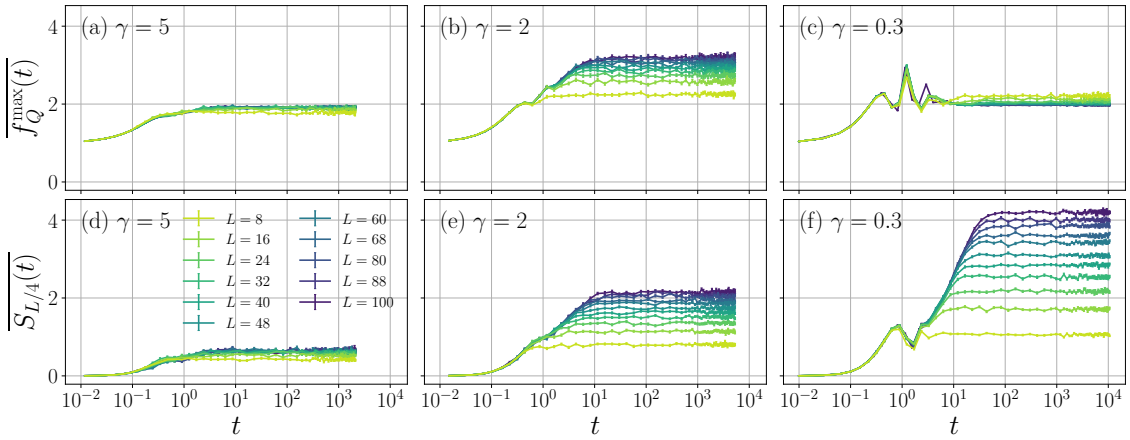

Figure 3.4: Dynamics of the disorder-averaged QFI density (top panels) and entanglement entropy (bottom panels) for $h = 0.2$ and (a), (d) $\gamma = 5$, (b), (e) $\gamma = 2$, and (c), (f) $\gamma = 0.3$.

can be fully characterized by the covariance matrix in the fermionic representation, enabling the efficient simulation of the problem. In detail, the evolution can be realized by generalizing Eq. (1.48) to the case of a non-Hermitian Hamiltonian, and implementing appropriate update rules to account for the effect of jumps. The details on the implementation are presented in App. B.

For each trajectory generated, we compute the maximal QFI using simulated annealing, as in the no-click limit. We then repeat the procedure multiple times independently, and take a statistical average. Performing the maximization *before* averaging over the state is crucial: this makes the optimal observable $\hat{O}[\{\mathbf{n}_j\}]$ trajectory-dependent, and makes the average maximal QFI density a proper nonlinear functional of the state. To make a comparison, we also evaluate the average entanglement entropy for a subsystem of length $\ell = L/4$.

The dynamics of these two quantities is shown in Fig. 3.4 for three choices of the measurement rate and a fixed h, though similar results are obtained qualitatively for other choices of the transverse field. After an initial growth, both the QFI density and the entanglement entropy saturate to steady-state values that exhibit different scaling properties. The entropy shows a shift from an area law at large γ to a scaling behavior at lower measurement rates. In contrast, the average maximal QFI density appears to saturate to an intensive value both at large and small γ, manifesting indefinite growth with the system size L only at intermediate measurement frequencies.

This behavior is better highlighted in Fig. 3.5, which presents directly the steady-state saturation values as functions of the system size. When γ is reduced below $\gamma_c(h)$ ($\gamma_c \approx 4$ for $h = 0.2$) $\overline{f_Q^{\max}(\infty)}$ appears to grow indefinitely with the system size L, as seen from the left panels. Our numerics suggest that the crossover of f_Q from an intensive to a size-dependent value occurs at the same γ_c at which S_ℓ transitions from area to logarithmic law, even though determining the critical measurement rate precisely is challenging. The growth of the QFI density below γ_c is consistent with a power-law $\sim L^p$, as in the no-click limit.

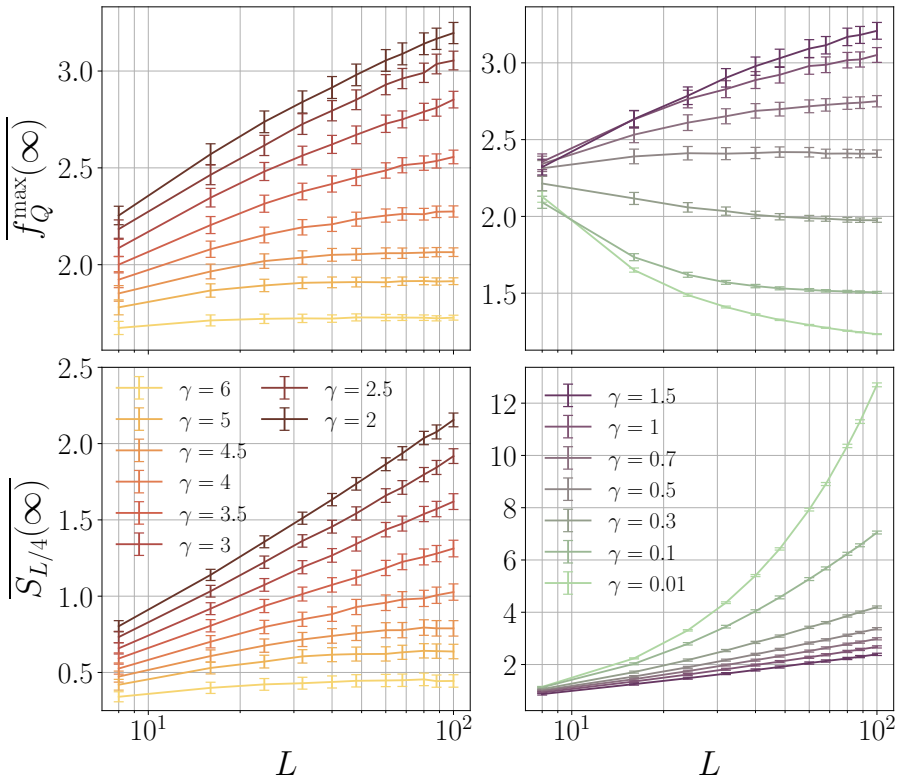

Figure 3.5: Disorder-averaged stationary QFI density and entanglement entropy, as functions of L, for $h = 0.2$ and multiple values of γ. Large (left panels) and small (right panels) values of γ are presented separately to help visualization. The stationary values are evaluated as long-time averages.

When γ is reduced further, we observe a new effect completely at odds with the no-click limit. The steady-state QFI density transitions back to an intensive value, as illustrated in the right panels of Fig. 3.5, in contrast to the entanglement entropy that instead grows further. Eventually, $S_{L/4}$ develops a volume law at very small measurement rates, which is a known finite-size effect occurring at $\gamma \sim 1/L$ [55], where the dynamics is approximately unitary and jumps are rare. These observations support the existence of a third measurement-induced phase, characterized by an intensive f_Q but a logarithmic entanglement entropy.

Given the finite-size effects shown by the entanglement entropy, one may suspect that the intensive behavior of the QFI density at low γ might be also due to the limited values of L considered. Indeed, volume-law entangled states often exhibit a bounded f_Q, especially in the long-time unitary dynamics following a quantum quench [193]: as such, when $S_{L/4}$ approaches an extensive scaling it is natural to expect the Fisher density to also converges to an intensive value. While the available numerics cannot rule out this possibility completely, there are two key observations that go against it. First, our results suggest that the entropy crossover takes place at around $\gamma \approx 0.1$, whereas the QFI density shows clear intensive behavior already at $\gamma \approx 0.5$. Second, in the upper right panel of Fig. 3.5 we observe that, at low γ, f_Q is monotonically decreasing with L. If the true behavior was $f_Q \sim L^p$, one would expect the opposite trend, as finite-size effect are weaker at larger system

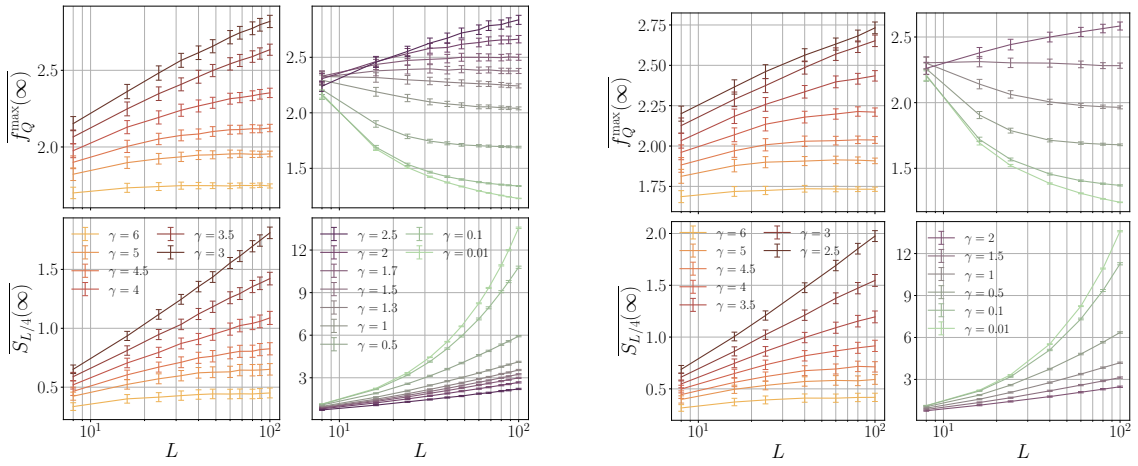

(a) $h = 0.7$ (b) $h = 1.2$

Figure 3.6: Disorder-averaged stationary QFI density and entanglement entropy, as in Fig. 3.5, for (a) $h = 0.7$ and (b) $h = 1.2$.

sizes. These observations support the conclusion that multipartite entanglement is intensive below a second critical point $\gamma_c'(h)$, and the third phase is stable.

In Fig. 3.6, we present analogous numerical results to Fig. 3.5 for other choices of h. We observe the same behavior qualitatively, and the boundaries of the three regions likely depend on h. Notice that a transition from area-law to logarithmic scaling in the entanglement entropy can be observed also for $h > 1$, in sharp contrast to the no-click limit. Hence, we conclude that while the analysis of Sec. 3.2 provides important analytic insights on the MIPT, its phase diagram is not inherited in presence of quantum jumps [247].

3.3.2 Shape of correlation functions

As in the no-click limit, the behavior of the QFI can be related to the shape of spin-spin correlation functions. Focusing on single quantum trajectories in the long-time regime, where $\overline{f_Q^{\max}(t)}$ has already reached saturation, we define the new distance-dependent correlators

$$\tilde{C}_\ell^{\alpha,\beta} = \frac{1}{L}\sum_j \left| C_{j,j+\ell}^{\alpha,\beta} \right| . \tag{3.16}$$

Numerically, we observe that all $\tilde{C}_\ell^{\alpha,\beta}$ are exponential at large $\gamma > \gamma_c$, whereas they decay as power laws at smaller γ, see Fig. 3.7. This crossover already indicates a qualitative difference between the two regimes. The power-law correlators suggest that the entangling phase is an extended critical region, compatible with the observation of a logarithmic entanglement entropy.

Given the analogy with the no-click limit, we expect that scaling behavior $f_Q \sim L^p$ with $p > 0$ is associated with a slow decay of correlations, namely, $\tilde{C}_\ell^{\alpha,\beta} \sim |\ell|^{-\lambda_{\alpha,\beta}}$ with $\lambda_{\alpha,\beta} < 1$. To test this, we simulate multiple trajectories and estimate $\lambda_{\alpha,\beta}$ at long times through numerical fits. Figure 3.8 presents the different exponents of a sample of $M = 50$ trajectories as functions of time. For $\gamma = 2$, at any time there is a

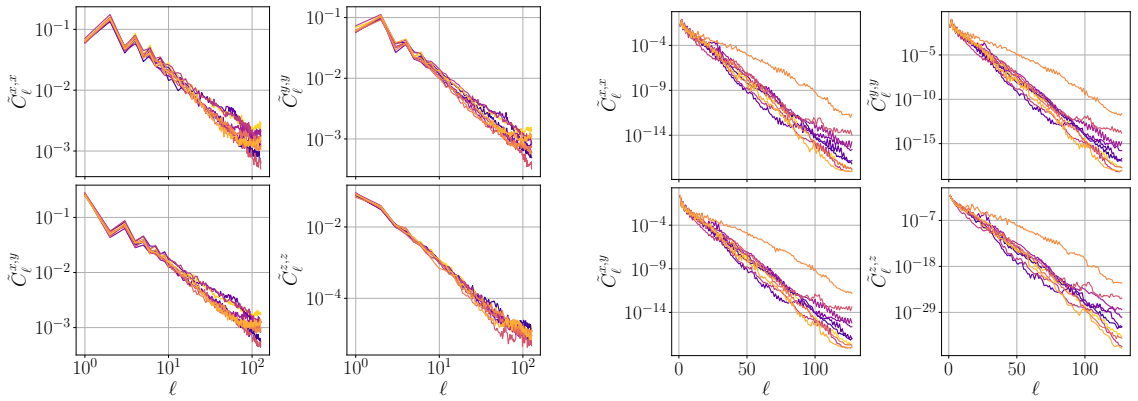

(a) $\gamma = 2$ (log-log scale) (b) $\gamma = 6$ (log-linear scale)

Figure 3.7: Correlators $\tilde{C}_\ell^{\alpha,\beta}$ at long time $t = 200$, for (a) $\gamma = 2$ and (b) $\gamma = 6$, using $L = 256$ and $h = 0.2$. The plots show 10 different random realizations. The overall trend is algebraic for $\gamma = 2$ and exponential for $\gamma = 6$.

finite number of trajectories with $\lambda_{\alpha,\beta} < 1$, indicating that this behavior is typical. In contrast, we never observe $\lambda_{\alpha,\beta} < 1$ for $\gamma = 0.3$, at least for the sample size considered.

Our results thus indicate that trajectories with $\lambda_{\alpha,\beta} < 1$ become atypical at low enough γ, and thus are no longer able to support a scaling behavior for multipartite entanglement. To better visualize this, we simulate $M = 100$ independent realizations and, for some fixed times t, we count the number $M_<$ of them with at least one $\lambda_{\alpha,\beta} < 1$. The ratio $M_</M$ thus estimates the probability of finding a trajectory able to support a scaling multipartite entanglement. As shown in Fig. 3.9, we estimate that a finite fraction of the ensemble of all trajectories yields slow-decaying correlators in the region $\gamma \lesssim 4$, which indicates an unbounded growth of f_Q with L in the thermodynamic limit. In contrast, $M_</M$ vanishes in a finite region at low γ, meaning that no random realization can support extended multipartiteness. This explains why f_Q returns intensive at low measurement rates. Still, our limited sample of $M = 100$ trajectories is not sufficient to establish whether or not a sharp transition takes place from this analysis.

3.4 Conclusions

In this chapter we presented the investigation of a continuously monitored quantum Ising chain from the novel point of view of multipartite entanglement, witnessed by the QFI. In the post-selected trajectory without quantum jumps, the multipartiteness of quantum correlations changes from limited to extended, reproducing the same phase diagram obtained from the entanglement entropy. When quantum jumps are introduced, the entanglement entropy and the QFI manifest distinct behaviors, and we observe a new region with bounded QFI density yet logarithmic entanglement entropy emerging at low γ. Our findings suggest that this is a third stable phase, visible only when combining the phase boundaries of bipartite and multipartite correlations. This is supported by the related investigation of Ref. [280] in

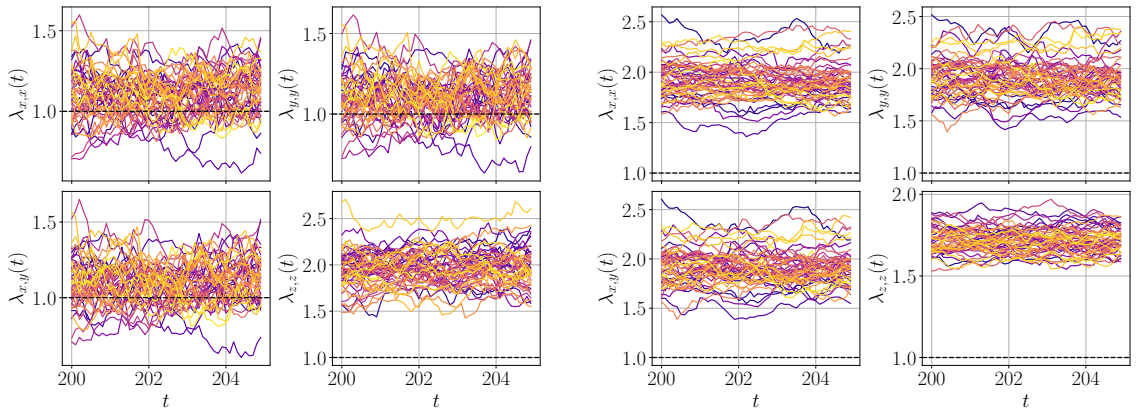

(a) $\gamma = 2$ (b) $\gamma = 0.4$

Figure 3.8: Exponents $\lambda_{\alpha,\beta}$ of $M = 50$ different quantum trajectories at long times $t \geq 200$, using $L = 256$, $h = 0.2$, (a) $\gamma = 2$ and (b) $\gamma = 0.4$. The exponents are extrapolated by fitting the power laws for $L = 10 \div 100$. Multiple typical trajectories have exponents below 1 when γ is large enough, whereas no one is found at low measurement rates.

random quantum circuits, where they also observe that the QFI and the entanglement entropy provide distinct critical lines. We stress that, in general, the bipartite and multipartite entanglement should not be expected to necessarily behave in the same way, as they probe very different aspects of quantum correlations.

In the no-click limit, we argue that the optimal operator $\hat{O}[\{\mathbf{n}_j\}_{\text{opt}}]$ maximizing the Fisher information shows properties resembling a conventional notion of order parameter. This interpretation is no longer straightforward in presence of jumps. For each random realization and at each time, the QFI is maximized by a different operator, making it impossible to design a unique, trajectory-independent order parameter. However, $\hat{O}[\{\mathbf{n}_j\}_{\text{opt}}]$ may still characterize criticality for each individual trajectory.

Some previous works in the literature [76–78, 80] characterize MIPTs using the fluctuations of observables, rather than entanglement. Since our investigation revolves around quantum fluctuations too, we now compare our manuscript with these studies, clarifying that our results are fundamentally different. First, Refs. [78, 80] demonstrate that the fluctuations of the total charge of a subsystem (e.g., half of the chain) manifest a phase transition, shifting from intensive to extensive when tuning the measurement rate. Unfortunately, no information on multipartite entanglement can be gained from this result, as the observable under investigation is not in the required form of Eq. (1.11). One may also be interested in the multipartite entanglement content of a subsystem alone, but in this case the QFI takes the more complicated form presented in Eq. (1.9), and is no longer directly related to quantum fluctuations. In contrast, Refs. [76, 77] do consider fluctuations of globally defined operators. Nevertheless, the models treated in these works are not spin systems as considered in the original Refs. [131, 132] that connect the QFI to multipartite entanglement. Still, even leaving aside this technicality, these papers observe a transition from zero to intensive fluctuations, and both cases correspond

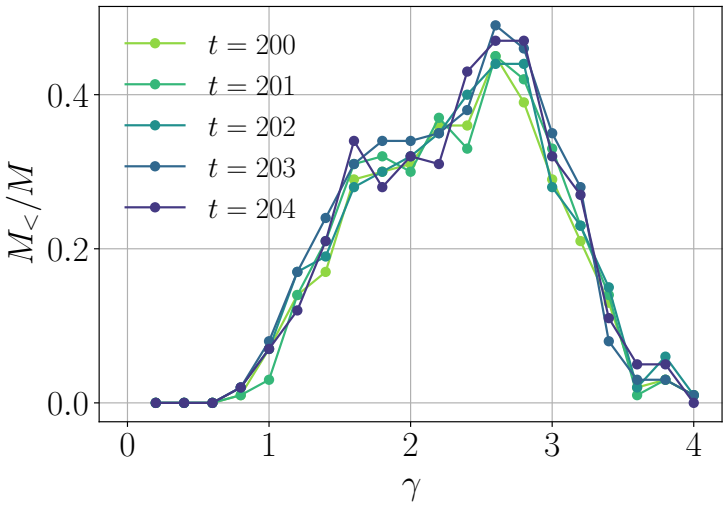

Figure 3.9: Fraction $M_</M$ of trajectories with exponents $\lambda_{\alpha,\beta} < 1$, for $M = 100$, $h = 0.2$, and multiple values of γ. Different curves correspond to different times $t = 200, 201, 202, 203, 204$ (light to dark colors) at which the exponents are measured. Data for $L = 256$, the power laws are fitted for $L = 10 \div 100$.

to a vanishing QFI density. In contrast, our analysis features a shift from extensive to super-extensive variance, explicitly demonstrating extended multipartiteness of quantum correlations.

We believe this study establishes the QFI as a valid probe of MIPTs, clarifying that multipartite entanglement can exhibit critical behavior under monitoring as well. Hence, this analysis paves the way to future investigations of multipartite correlations in monitored quantum dynamics [269, 280, 293]. Another compelling open problem is the development of a theoretical understanding of the whole phase diagram beyond the simplistic no-click description. Finally, our study does not attempt to determine the values of the critical points accurately due to the limited numerical results. In particular, performing the maximization of the QFI is the main computational bottleneck, allowing us to explore only up to $L = 100$. A precise characterization of the critical lines, and thus the shape of the phase diagram, is left for future work.

Chapter 4

Information loss in measurement-induced transitions

One of the main obstacles to the experimental observation of measurement-induced phase transitions (MIPTs) is the postselection problem. As discussed previously, the average state, often described by a Lindbladian evolution, typically does not preserve signatures of the phase transition, which are instead encoded in the properties of each trajectory. This introduces the necessity to postselect random realizations in order to resolve their individual properties, like we did in our analysis of correlation functions in the previous chapter. In realistic implementations, this issue is further complicated by imperfect detector efficiencies. For instance, when a quantum jump occurs, a faulty measurement apparatus might fail to capture it correctly, thereby reporting an incorrect outcome. The unreliability of measurement records inevitably introduces uncertainty in the trajectory followed by the system, and makes perfect postselection of a specific quantum trajectory impossible.

To address these challenges, in this chapter we investigate whether signatures of MIPTs persist under *partial* postselection [294–299], i.e., averaging over a restricted class of trajectories as opposed to the full ensemble. In other words, we ask if some features of the transition can still be observed when some measurement outcomes are not recorded, resulting in partial loss of information specifying a given trajectory. First, this approach allows us to examine how imperfect detection impacts the properties of the system. Second, it investigates whether the stringent requirement to focus on a unique trajectory can be relaxed, or if a perfect, resource-expensive postselection is inevitable. A positive answer would potentially offer an experimental advantage in accessing the elusive MIPTs.

Concretely, we consider a continuously monitored fermionic Kitaev chain whose evolution is governed by an effective non-Hermitian Hamiltonian with local fermionic losses. The protocol we use is very similar to the dynamics of the Ising chain discussed in the previous chapter, and in particular it exhibits the exact same no-click limit already presented in Sec. 3.2. We introduce a Liouvillian model that interpolates between the no-click trajectory, corresponding to a fully postselected evolution, and the Lindbladian limit [294], where no postselection occurs and all measurement outcomes are averaged over.

Our goal is to investigate the robustness of the no-click phase diagram under information loss. By computing exact fermionic correlators, the entanglement negativity, and the Liouvillian gap, we demonstrate that any degree of trajectory averaging destroys the no-click critical phase, thus eliminating the phase transition. This implies that the postselection problem cannot be mitigated, at least for the

model we consider. We show that imperfect postselection introduces an effective lengthscale that suppresses long-range correlations. Our findings clarify the mechanism by which trajectory averaging obscures MIPTs, and establish a framework for investigating partially postselected monitored dynamics.

The chapter is organized as follows. In Sec. 4.1 we introduce our Liouvillian model of partially postselected monitored dynamics. Section 4.2 details the derivation of the equation characterizing the steady state and its solution. Then, Sec. 4.3 presents the main result of our investigation: we compute the correlation length and demonstrate that only the fully postselected no-click limit can be critical. We substantiate this by evaluating the entanglement negativity of the steady state and the Liouvillian gap. Finally, we summarize and discuss our findings in Sec. 4.4.

4.1 Liouvillian Model

In this section we introduce the protocol we consider and derive the Liouvillian model that describes it. The open system description interpolates between two limit, the Lindbladian one where all trajectories are considered and the case of full postselection to a unique pure state. This approach enables a continuous crossover between these extremes, corresponding to partial postselection.

4.1.1 Protocol

We consider a Kitaev chain

$$\hat{H} = -\sum_{j=1}^{L} \left(\hat{c}_j^\dagger \hat{c}_{j+1} + \hat{c}_j^\dagger \hat{c}_{j+1}^\dagger + \text{h.c.} \right) + 2\mu \sum_{j=1}^{L} \hat{c}_j^\dagger \hat{c}_j \tag{4.1}$$

with periodic boundary conditions subject to a weak measurement protocol [240, 243, 289] defined by the Kraus operators

$$\hat{A}_{0,j} = e^{-\frac{dt}{2} \hat{L}_j^\dagger \hat{L}_j}, \tag{4.2a}$$

$$\hat{A}_{1,j} = \sqrt{dt} \hat{L}_j, \tag{4.2b}$$

where $\hat{L}_j = \sqrt{\gamma} \hat{c}_j$. This model is very similar to the one studied in the previous chapter. The Kitaev Hamiltonian is the fermionic version of the quantum Ising chain of Eq. (3.4) with $\mu = h$, but this time with periodic boundary conditions; moreover, $\hat{A}_{0,j}$ is the same as in Eq. (3.2a) at order $\mathcal{O}(dt)$. The Kraus operator $\hat{A}_{1,j}$ can induce the sudden emission of a fermion from the chain, which is spotted by a detector and will be referred to as a click. Since the losses occur randomly, different realizations of the protocol will give rise to distinct stochastic quantum trajectories, each labeled by the times and positions of its clicks.

We aim to investigate how the properties of the system are affected when the information identifying a specific trajectory is partially lost. To this end, we choose the no-click trajectory, identifying it with the limit of perfect postselection. We then assume that the monitoring instruments have a limited efficiency, so that they can miss clicks. Specifically, we assume that whenever a click occurs it is recorded only

with a certain probability $0 \leq q \leq 1$, whereas with probability $1-q$ the event goes unnoticed by the observer (false negative). As a consequence, when detectors report zero clicks, there is a finite probability that the state is not truly the no-click one. This implies that the no-click measurement record does not correspond to a pure state, but is instead described by an ensemble of trajectories affected by undetected events.

The paradigm of partial postselection has already been considered by Refs. [295, 296]. These works focus on quantities that are non-linear in the density matrix, and compute their averages over a restricted ensemble of trajectories. In our case, we are instead interested in linear observables and in the properties of the mixed steady state.

4.1.2 Liouvillian model

Let $\hat{\rho}_t$ be the density matrix of the system averaged over the ensemble of trajectories generated by the partially postselected dynamics. We will now derive a compact equation of motion in the form of a Liouville equation. The derivation is similar to that of Sec. 2.1.3, but accounting for the possibility that a measurement outcome is postselected to 0 (i.e., no click) with a probability q. For simplicity, consider the a single weak measurement on site j [1]. At each timestep, there are two possibilities:

1. The outcome is postselected to the no-click realization, and the state is updated by $\hat{A}_{0,j}$. This happens with probability q.

2. No postselection is performed, and there is uncertainty on the measurement outcome. This happens with probability $1-q$. In this case, the choice of the Kraus operator to apply is performed randomly by sampling the Born rule probabilities $p_{m,j} = \mathrm{Tr}\big(\hat{\rho}_t \hat{A}^\dagger_{m,j} \hat{A}_{m,j}\big)$.

Overall, the average density matrix at time $t+dt$ is a mixture of all possible final states, each weighted with the corresponding probability, thus yielding

$$\hat{\rho}_{t+dt} = q\frac{\hat{A}_{0,j}\hat{\rho}_t\hat{A}^\dagger_{0,j}}{p_0} + (1-q)\left[p_{0,j}\frac{\hat{A}_{0,j}\hat{\rho}_t\hat{A}^\dagger_{0,j}}{p_{0,j}} + p_{1,j}\frac{\hat{A}_{1,j}\hat{\rho}_t\hat{A}^\dagger_{1,j}}{p_{1,j}}\right]. \tag{4.3}$$

By expanding $\hat{A}_{0,j} \approx \hat{\mathbb{1}} - \frac{dt}{2}\hat{L}^\dagger_j\hat{L}_j$ in Eq. (4.3) and keeping only the leading order in dt, we finally get

$$\hat{\rho}_{t+dt} = \hat{\rho}_t - \frac{dt}{2}\Big\{\hat{L}^\dagger_j\hat{L}_j, \hat{\rho}_t\Big\} + qdt\langle\hat{L}^\dagger_j\hat{L}_j\rangle_t\hat{\rho}_t + (1-q)dt\hat{L}_j\hat{\rho}_t\hat{L}_j, \tag{4.4}$$

and by reordering terms we find

$$\partial_t\hat{\rho}_t = -\frac{1}{2}\Big\{\hat{L}^\dagger_j\hat{L}_j, \hat{\rho}_t\Big\} + q\langle\hat{L}^\dagger_j\hat{L}_j\rangle_t\hat{\rho}_t + (1-q)\hat{L}_j\hat{\rho}_t\hat{L}^\dagger_j. \tag{4.5}$$

[1] As seen in Sec. 2.1.3, different sites eventually provide mutually independent contributions to the Lindblad equation, and can thus be treated individually.

For measurements acting on all sites, since they act independently, we simply need to add a sum over the lattice index j on the right-hand side of Eq. (4.5). Finally, including also the coherent Hamiltonian evolution term, we obtain the master equation

$$\partial_t \hat{\rho}_t = \mathcal{L}_t \hat{\rho}_t, \tag{4.6a}$$

$$\mathcal{L}_t \bullet = -i\Big[\hat{H}, \bullet\Big] + \sum_{j=1}^{L} \left[(1-q)\hat{L}_j \bullet \hat{L}_j^\dagger - \frac{1}{2}\Big\{\hat{L}_j^\dagger \hat{L}_j, \bullet\Big\} + q\langle \hat{L}_j^\dagger \hat{L}_j \rangle_t \bullet \right], \tag{4.6b}$$

An alternative but equivalent interpretation that leads to Eq. (4.6) is the following. We assume that quantum trajectories are sampled regularly without any postselection, and we bias this process by discarding some realizations. For a randomly generated trajectory, we introduce a probability q to drop it whenever a click occurs, meaning it is completely disregarded and excluded from the ensemble over which observables are computed. This biased sampling protocol yields the same Liouvillian of the partial postselection paradigm, and constitutes an experimentally viable way to realize it. In both interpretations, the parameter q penalizes the relative probability of trajectories with many clicks, making them less likely to occur.

Properties of the Liouvillian – While apparently similar to a Lindblad master equation, Eq. (4.6) is not in the form of Eq. (2.11), mainly due to the factor $(1-q)$ in front of the quantum jump part of the dissipator. The evolution of the density matrix is formally non-linear, as it involves the expectation value $\langle \hat{L}_j^\dagger \hat{L}_j \rangle_t = \mathrm{Tr}\big(\hat{\rho}_t \hat{L}_j^\dagger \hat{L}_j\big)$. This term guarantees a trace-preserving evolution, and arises naturally from the derivation. However, the evolution can be made linear by discarding that term and renormalizing the density matrix at the final time.

The Liouvillian of Eq. (4.6b) is called quasi-free because the Hamiltonian is quadratic and the jump operators are linear in the fermionic operators. Notably, it can be solved exactly by diagonalizing it [2] through the formalism of third quantization [300–302]. Most importantly, it can be proven that the dynamics generated by quasi-free Liouvillians preserves the Gaussianity of the state [297], and thus $\hat{\rho}_t$ is fully characterized by its fermionic correlation matrix [116].

There are two notable limiting cases of the Liouvillian. For $q = 0$, Eq. (4.6) reduces to a regular Lindblad master equation, which describes the evolution obtained by averaging accross all possible, randomly generated, trajectories. In this case, it can be proven that the steady state can never be critical [303], and must have a finite correlation length. In the opposite limit of $q = 1$, each trajectory with one or more clicks is discarded, leaving only the no-click trajectory. This case is described by a deterministic pure state evolution, governed by a non-Hermitian Schrödinger equation [240, 243].

The no-click limit of this model coincides exactly with the one discussed in Sec. 3.2. Indeed, the monitoring protocols considered in this chapter and in the previous one differ only by the choice of the Kraus operator $\hat{A}_{1,j}$, which never plays a role in the no-click trajectory. Hence, all properties discussed previously are inherited in this setup, most importantly the phase diagram. For $|\mu| < 1$ and

[2] To be precise, its eigenoperators can be computed exactly, whereas its eigenvalues are determined up to the constant term $q\langle \hat{L}_j^\dagger \hat{L}_j \rangle_t$ that depends on the current state.

$\gamma < \gamma_c(\mu) = 4\sqrt{1-\mu^2}$ [56, 260, 263, 304], the system lies in an extended critical region with infinite-ranged correlations.

By tuning the parameter q we can interpolate between this state and the Lindblad limit. The main goal of our investigation is to understand whether the critical properties of the no-click limit are retained for $q < 1$. As detailed in the subsequent sections, we anticipate a negative answer: for all $q < 1$, we observe a finite correlation length and the absence of criticality, making the logarithmic phase unstable against imperfect detection.

4.2 Steady-State Correlation Matrix

We now move to the main focus of our study, which regards the investigation of the steady-state properties of Eq. (4.6). By exploiting the property that the Liouvillian $\mathcal{L}_t$ of Eq. (4.6b) preserves the Gaussianity of the state, we derive a Riccati equation that yields the exact correlation matrix of the steady state. We point out that Liouvillians similar to the one considered here have been recently studied in Ref. [297] with related techniques. The authors of that work characterize dynamical aspects of the model by computing quantities like the click waiting-time distribution and the no-click probability. In contrast, we work directly with the steady state to study its spatial correlations and entanglement properties.

4.2.1 The Riccati equation

From here on, it is convenient to work using the Majorana fermionic operators. Instead of using the $\hat{\gamma}_\mu$ introduced in Eq. (1.49), let us define $\hat{w}_{j,1} = (\hat{c}_j^\dagger + \hat{c}_j)/\sqrt{2} = \hat{\gamma}_{2j-1}/\sqrt{2}$, $\hat{w}_{j,2} = i(\hat{c}_j^\dagger - \hat{c}_j)/\sqrt{2} = \hat{\gamma}_{2j}/\sqrt{2}$, which satisfy the anticommutation relation $\{\hat{w}_{m,\mu}, \hat{w}_{n,\nu}\} = \delta_{m,n}\delta_{\mu,\nu}$. The Hamiltonian and jump operators are rewritten as

$$\hat{H} = \sum_{m,n=1}^{L} \sum_{\mu,\nu=1}^{2} \mathbb{H}_{(m,\mu),(n,\nu)} \hat{w}_{m,\mu} \hat{w}_{n,\nu}, \tag{4.7}$$

where $\mathbb{H} = -\mathbb{H}^T$ [3], and

$$\hat{L}_j = \sum_{m=1}^{L} \sum_{\mu=1}^{2} \ell_{m,\mu}^{(j)} \hat{w}_{m,\mu}. \tag{4.8}$$

For later convenience, let us introduce the so-called bath matrix

$$M_{(m,\mu),(n,\nu)} = \sum_{j=1}^{L} \ell_{m,\mu}^{(j)} \left(\ell_{n,\nu}^{(j)}\right)^*, \tag{4.9}$$

which is easily shown to be Hermitian. We are interested in computing the correlation matrix

$$\Gamma_{(m,\mu),(n,\nu)} = \frac{i}{2} \operatorname{Tr}\left(\hat{\rho}[\hat{w}_{m,\mu}, \hat{w}_{n,\nu}]\right) \tag{4.10}$$

[3] There are multiple equivalent ways to define $\mathbb{H}$. The requirement of $\mathbb{H} = -\mathbb{H}^T$ selects a unique one, and is convenient for later calculations.

in the steady state of the dynamics. To achieve this, we use the Liouville equation of Eq. (4.6) to obtain an equation of motion for Γ. In the process, one finds the appearance of expectation values of products of 4 Majorana operators. By exploiting the Gaussianity of the density matrix $\hat{\rho}_t$, we can apply Wick's theorem to reduce these fourth order terms, and obtain a closed equation for Γ. After a tedious but straightforward calculation, this leads to

$$\partial_t \Gamma_t = X\Gamma_t + \Gamma_t X^T + Y + \Gamma_t Z \Gamma_t, \tag{4.11}$$

where the matrices X, Y, and Z are given by

$$X = -2i\mathbb{H} - (1-q)\,\mathrm{Re}\,M, \tag{4.12a}$$
$$Y = (1-q/2)\,\mathrm{Im}\,M, \tag{4.12b}$$
$$Z = 2q\,\mathrm{Im}\,M. \tag{4.12c}$$

Equation (4.11) is known with the name of Riccati equation, and it appears in the field of optimal control theory.

We can exploit translational symmetry to simplify the problem by moving to momentum space. For $A \in \{\Gamma, X, Y, Z\}$, the matrix elements $A_{(m,\mu),(n,\nu)} = A_{\mu,\nu}(m-n)$ are functions of the distance $m-n$. Introducing the momentum-space matrices $\tilde{A}_{\mu,\nu}(k) = \sum_{x=1}^{L} e^{-ikx} A_{\mu,\nu}(x)$, Eq. (4.11) yields L independent equations for each k-mode. Finally, by imposing $\partial_t \tilde{\Gamma}_t(k) = 0$ we obtain the steady-state equation

$$\tilde{X}(k)\tilde{\Gamma}(k) + \tilde{\Gamma}(k)\tilde{X}^T(-k) + \tilde{Y}(k) + \tilde{\Gamma}(k)\tilde{Z}(k)\tilde{\Gamma}(k) = 0, \tag{4.13}$$

which has the form of a 2×2 algebraic Riccati equation (ARE).

4.2.2 Exact solution for the steady state

Despite its non-linearity, there exists a standard technique to solve the ARE. First, we introduce the block matrix

$$Q = \begin{pmatrix} \tilde{X}^T(-k) & \tilde{Z}(k) \\ -\tilde{Y}(k) & -\tilde{X}(k) \end{pmatrix}, \tag{4.14}$$

which allows us to rewrite the ARE in matrix form as

$$\begin{pmatrix} \tilde{\Gamma}(k) & -\mathbb{1} \end{pmatrix} Q \begin{pmatrix} \mathbb{1} \\ \tilde{\Gamma}(k) \end{pmatrix} = 0. \tag{4.15}$$

Consider the eigenvalue problem $QW = W\Lambda$, where $\Lambda = \mathrm{diag}\{\lambda_1, \lambda_2, \lambda_3, \lambda_4\}$ contains the eigenvalues of Q. The columns of the solution W are thus the right eigenvectors of Q. If we rewrite W as a block matrix

$$W = \begin{pmatrix} W_{1,1} & W_{1,2} \\ W_{2,1} & W_{2,2} \end{pmatrix}, \tag{4.16}$$

where each block $W_{m,n}$ has size 2×2, the solution of the ARE is given by

$$\tilde{\Gamma}(k) = W_{2,1} W_{1,1}^{-1}. \tag{4.17}$$

This can be checked by inserting this ansatz in Eq. (4.15) and using the identity $Q = W\Lambda W^{-1}$. Equation (4.17) involves only two columns of W, i.e., only two eigenvectors of Q. Any reordering of the eigenvectors provides a valid solution of the ARE. Since the number of inequivalent permutations is six, we conclude that there are these many solutions.

Most of these solutions must be unphysical. The correct one should satisfy the following two properties, which are immediately proved:

1. $\tilde{\Gamma}(k) = -\tilde{\Gamma}^\dagger(k)$ (anti-Hermitianity). This is easily seen by rewriting
$$(\tilde{\Gamma}^\dagger(k))_{\mu,\nu} = \tilde{\Gamma}^*_{\nu,\mu}(k) = \sum_m e^{ikx}\Gamma^*_{\nu,\mu}(m) = -\sum_m e^{ikx}\Gamma_{\mu,\nu}(-m) = -\tilde{\Gamma}_{\mu,\nu}(k), \tag{4.18}$$
where we used $\Gamma = -\Gamma^\dagger$, following directly from its definition.

2. $\tilde{\Gamma}_{1,1}(k) = -\tilde{\Gamma}_{2,2}(k)$ (tracelessness). This is a consequence of a symmetry of the Liouvillian under a swap of type-1 and type-2 Majorana operators plus an inversion of the lattice chain. Denoting by $\mathcal{L}[\{\hat{w}_{j,1}\},\{\hat{w}_{j,2}\}]$ the Liouvillian written in terms of the Majorana operators, it is easily checked that it satisfies $\mathcal{L}[\{\hat{w}_{j,1}\},\{\hat{w}_{j,2}\}] = \mathcal{L}[\{\hat{w}_{L-j,2}\},\{-\hat{w}_{L-j,1}\}]$. It follows that $\Gamma_{1,1}(x) = \Gamma_{2,2}(-x)$. Combining this with the identity $\Gamma_{\mu,\nu}(x) = -\Gamma_{\nu,\mu}(-x)$, which is a direct consequence of its definition, we obtain $\Gamma_{1,1}(x) = -\Gamma_{2,2}(x)$, and thus $\tilde{\Gamma}_{1,1}(k) = -\tilde{\Gamma}_{2,2}(k)$.

The most general traceless anti-Hermitian matrix can be parameterized as
$$\tilde{\Gamma}(k) = iA\begin{pmatrix} 1 & a+ib \\ a-ib & -1 \end{pmatrix}, \tag{4.19}$$
where $A, a, b \in \mathbb{R}$. By inserting this ansatz in the ARE we obtain three independent equations to determine these parameters, allowing to obtain their analytic expressions. This approach produces two solutions $\tilde{\Gamma}_\pm$ to the problem, corresponding to the parameters $\{A_\pm, a_\pm, b_\pm\}$. For our Liouvillian, we explicitly have
$$\tilde{X}(k) = \begin{pmatrix} -(1-q)\frac{\gamma}{2} & 2\mu - 2e^{-ik} \\ -2\mu + 2e^{ik} & -(1-q)\frac{\gamma}{2} \end{pmatrix}, \tag{4.20a}$$
$$\tilde{Y}(k) = -(1-\frac{q}{2})\frac{\gamma}{2}\begin{pmatrix} 0 & 1 \\ -1 & 0 \end{pmatrix}, \tag{4.20b}$$
$$\tilde{Z}(k) = -q\gamma\begin{pmatrix} 0 & 1 \\ -1 & 0 \end{pmatrix}. \tag{4.20c}$$
Defining for convenience
$$R = 2\mu - 2\cos k, \tag{4.21a}$$
$$I = 2\sin k, \tag{4.21b}$$
$$S = \sqrt{\gamma^4 + 16(R^2+I^2)^2 + 8\gamma^2[(1-4q+2q^2)I^2 + R^2]}, \tag{4.21c}$$
we find
$$a_\pm = \pm\frac{2\sqrt{2}R}{\sqrt{\gamma^2 - 4(R^2+I^2) + S}}, \tag{4.22a}$$

$$b_\pm = -\frac{1+a_\pm^2}{a_\pm}\frac{R}{I}, \tag{4.22b}$$

$$A_\pm = \frac{(1-q)\gamma a_\pm + 2R}{2q\gamma(1+a_\pm^2)R} I. \tag{4.22c}$$

At last, we need to pick the correct solution between the two. It is useful to consider the limits of $q \to 0$ and $q \to 1$. In the latter, the analytic expression of the correlation matrix is already available [1, 250, 260] by manipulating Eq. (3.14), and it coincides with $\tilde{\Gamma}_-$. We conclude that $\tilde{\Gamma}_-$ is the physically meaningful solution of the ARE describing the steady state. This is further established by looking at the limit of $q \to 0$, in which A_- behaves regularly while A_+ is singular, diverging as $1/q$. Thus, we now have access to the steady-state correlation matrix, enabling the calculation of all its physical properties.

4.3 Lengthscale of correlations

We now leverage the previous formalism to study the critical properties of our model. Using complex analysis tools, we are able to set an upper bound to the lengthscale ξ of the correlation functions, valid in the thermodynamic limit. This allows us to demonstrate that ξ is always finite for $q < 1$, which implies that any amount of partial averaging over trajectories forbids algebraically decaying correlations with the distance.

4.3.1 Analytic continuation approach

A useful approach to establish whether a correlation function decays as an exponential or as a power law consists in studying the singularities of its Fourier transform in the complex plane. We promote the momentum k to a complex variable $k \in \mathbb{C}$, and we look for non-analiticities of $\tilde{\Gamma}(k)$. Two examples are provided in Fig. 4.1, where $\mathrm{Im}\,\tilde{\Gamma}_{1,2}(k)$ is displayed (a) in the no-click limit ($q = 1$) for critical values of the parameters, and (b) for $q < 1$, with all the other parameters left unchanged.

The correlation matrix features lines of discontinuity rather than isolated poles. We denote by $\mathcal{C}$ the collection of these lines for $\mathrm{Im}\,k \geq 0$. For $q = 1$ the lines touch the real axis $\mathrm{Im}\,k = 0$, which is a necessary condition for a diverging correlation length, as shown later. In contrast, for $q < 1$ we observe that $\tilde{\Gamma}(k)$ is regular on the real axis. In this case, we can write the real-space correlation matrix $\Gamma(x)$ as a contour integral. After performing the change of variable $z = e^{ik}$, we obtain

$$\Gamma(x) = \frac{1}{2\pi i}\oint_{\mathcal{S}} z^{x-1}\tilde{\Gamma}(k(z))dz, \tag{4.23}$$

where $\mathcal{S}$ is the unit circle centered at the origin, encircling the singular lines $\mathcal{C}$ mapped to the new variable z. Proceeding as detailed in App. C, it is straightforward to prove that

$$|\Gamma(x)| \leq C \exp\left(-\min_{k\in\mathcal{C}}\{\mathrm{Im}\,k\}\, x\right), \tag{4.24}$$

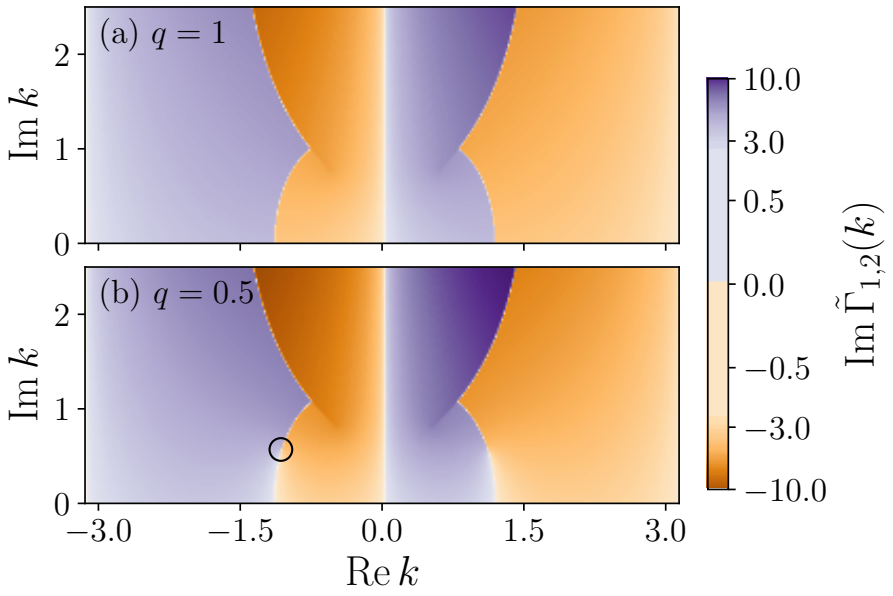

Figure 4.1: Profile of the correlation function $\mathrm{Im}\,\tilde{\Gamma}_{1,2}$ for complex argument k, using $\mu = 0.4$, $\gamma = 1$, and (a) $q = 1$, (b) $q = 0.5$. In the no-click limit (a) the discontinuous line extends to $\mathrm{Im}\,k = 0$, whereas in (b) it terminates at the point highlighted by the black circle.

where C is a constant and $\min_{k\in\mathcal{C}}\{\mathrm{Im}\,k\}$ is the imaginary part of the closest point of $\mathcal{C}$ to the real axis. This finally sets the upper bound

$$\xi \leq \xi_{\mathrm{up}} = \left(\min_{k\in\mathcal{C}}\{\mathrm{Im}\,k\}\right)^{-1}. \tag{4.25}$$

We can now study the correlation length of the Liouvillian steady state by looking for the singular lines $\mathcal{C}$ and computing their minimal distance from the real axis. Fig. 4.2 shows the upper lengthscale ξ_{up} as a function of q and γ, fixing the chemical potential μ. In general, we observe that the lengthscale is a monotonically increasing function of q for all parameter choices. This indicates that the less postselection is performed, the less information is retained on the long-range behavior of correlations. In particular, we observe that ξ_{up} can diverge only for $q = 1$, which demonstrates that the steady states for $q < 1$ are not critical (see the in-depth discussion below).

Finally, we also evaluated the true correlation length ξ by reconstructing $\Gamma(x)$ and fitting its decay [4]. Figure 4.3 shows a comparison between ξ_{up} and the fitted ξ. Despite the former being only an upper bound, we observe that it approximates quite well the true correlation length. At small values of q the estimation becomes noisy because we are fitting an exponential decay with very small lengthscale $\xi \sim 1$.

Almost perfect detection – Here we analyze the limit of almost perfect detection, where $1 - q \ll 1$. In this case, we can extract ξ_{up} analytically. First, let

[4] We assume the form $|\Gamma_{\mu,\nu}| \approx Ae^{-|x|/\xi}/|x|^{\alpha}$ and optimize the three parameters A, α, and ξ. We point out that the exact correlation functions manifest oscillations as well, but these are treated as noise around the previous decay profile.

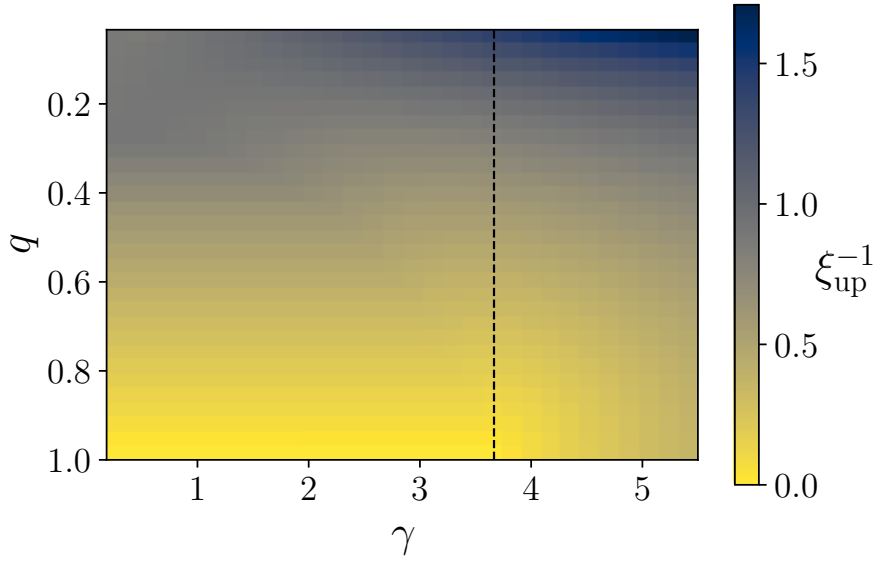

Figure 4.2: Inverse upper correlation length ξ_{up}^{-1} for $\mu = 0.4$, as a function of γ and q. The dashed line indicates the critical $\gamma_c(\mu)$ of the no-click limit. We observe $\xi_{\mathrm{up}}^{-1} > 0$ for any $q < 1$.

us prove rigorously that it cannot manifest singular behavior for $k \in \mathbb{R}$ if $q < 1$. It is convenient to analyze the no-click limit of $q = 1$ first. For $|\mu| < 1$, the term R defined in Eq. (4.21a) vanishes at momentum $k^* = \arccos \mu$. It is easy to check that A_-, a_-, and b_- are regular functions of k at k^* if $\gamma > \gamma_c(\mu) = 4\sqrt{1-\mu^2}$. In contrast, for $\gamma < \gamma_c(\mu)$ one can check that $a_- \sim \mathrm{Sign}(k-k^*)$, $b_- \sim |k-k^*|$, whereas A_- is still regular. These behaviors are responsible for the algebraic correlations observed in the no-click limit. In the case of $q < 1$, a_- can be singular only if its denominator vanishes at k^*. This yields the condition

$$\left[S^2 - \left(\gamma^2 - 4(R^2 + I^2)\right)^2\right]\Big|_{k^*} = 0, \tag{4.26}$$

which is satisfied only at $q = 1$. We thus conclude that a_- is regular at k^* for $q < 1$, and specifically we have $a_- \sim R$. From Eqs. (4.22b) and (4.22c) we then see that also b_- and A_- must be regular at k^*.

Beyond observing that $\xi_{\mathrm{up}}^{-1} > 0$ for $q < 1$, we can actually evaluate it explicitly for $1 - q \ll 1$. In this limit and for $\gamma < \gamma_c(h)$, the non-analitic (complex) k-point with smallest imaginary part will stay close to k^*. By assuming $k = k^* + dk$, where $dk = \mathcal{O}(1-q)$, and evaluating the denominator of Eq. (4.22a) at leading order in $1 - q$, we obtain

$$a_- \propto \frac{1}{\sqrt{(1-q)^2 + (dk)^2}}. \tag{4.27}$$

This function develops a jump discontinuity for $|dk| > 1 - q$, caused by the branch cut of the square root. Since this condition can be met only for $\mathrm{Im}(dk) > 1 - q$, we conclude that $\xi_{\mathrm{up}}^{-1} = 1 - q + \mathcal{O}((1-q)^2)$.

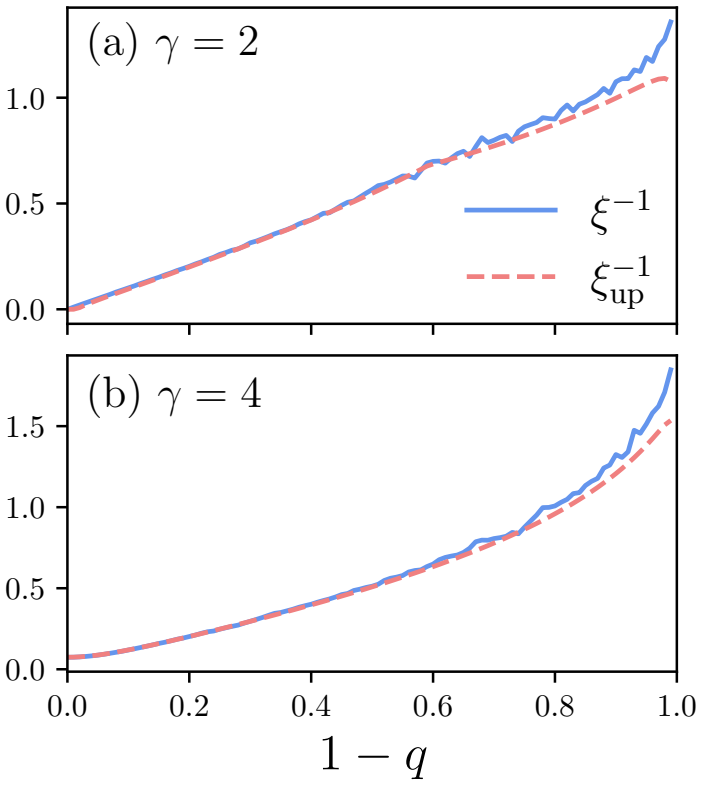

Figure 4.3: Decay of the correlation length induced by partial averaging, as a function of the detector inefficiency $1 - q$. We set $\mu = 0.4$ and (a) $\gamma = 2 < \gamma_c(\mu)$, (b) $\gamma = 4 > \gamma_c(\mu)$, corresponding to critical and off-critical no-click limits, respectively. ξ is fitted from the correlation matrix computed for a system size of $L = 2048$, whereas ξ_{up} is the theoretical upper bound of Eq. (4.25).

4.3.2 Entanglement negativity and Liouvillian gap

We complement the previous findings by computing additional quantities that are indicators of critical behavior. We start from the entanglement negativity [8, 9, 169–171] of the steady state, which is an good measure of entanglement even if the density matrix is mixed for $q < 1$. We then consider the Liouvillian gap of the spectrum of Eq. (4.6b), and observe that the model can becomes gapless only in the no-click limit of $q \to 1$.

As discussed in Sec. 1.1.2, since we are studying a fermionic system, it is appropriate to consider the logarithmic fermionic negativity [174–178] $\mathcal{N}_A = \log ||\hat{\rho}^{\tilde{T}_A}||$ defined in Eq. (1.57), which can be evaluated efficiently. In our case, we pick A to be a compact subsystem of length ℓ and B to be the rest of the chain. We show our results in Fig. 4.4. For $q = 1$ we observe an unbounded logarithmic growth, which is expected due to the critical nature of the state for the chosen parameters. In contrast, $\mathcal{N}_\ell$ eventually saturates to a constant for any $q < 1$. This is expected for states with a finite correlation length: the ground states of gapped one-dimensional models manifest an initial logarithmic growth $\sim \log \ell$ for $\ell \lesssim \xi$, and an eventual saturation to $\sim \log \xi$ at larger subsystem sizes [305]. The entanglement negativity

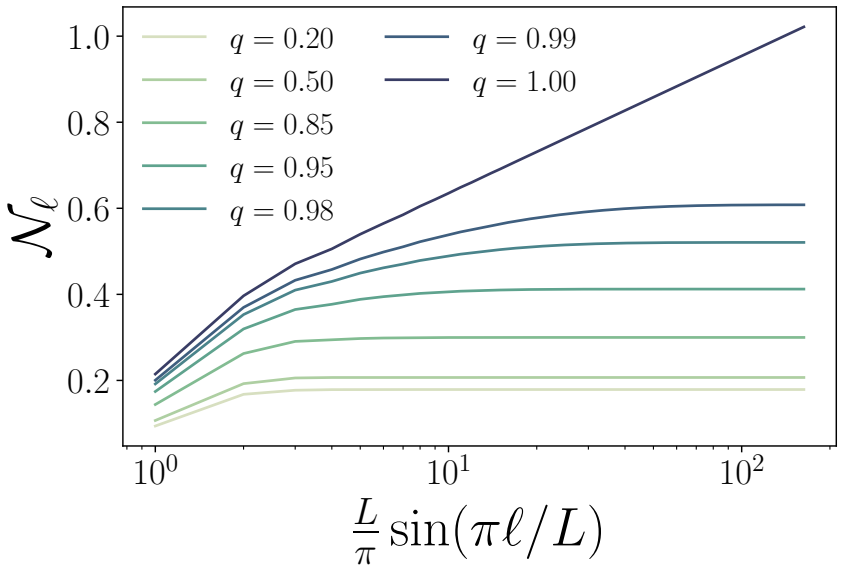

Figure 4.4: Scaling of the entanglement negativity $\mathcal{N}_\ell$ as a function of the chord length $\frac{L}{\pi}\sin(\pi\ell/L)$ [70]. Here we use $L = 512$, $\mu = 0.4$, and $\gamma = 1$.

shows that the steady state has quantum correlations, but these get smaller and smaller as more trajectories are considered in the averaging.

Phase transitions in open quantum systems can also be characterized through the Liouvillian spectral gap [43, 44, 306]. Denoting by λ_i, $i = 0, \dots, 4^N - 1$, the Liouvillian eigenvalues and ordering them such that $\mathrm{Re}\,\lambda_0 \geq \mathrm{Re}\,\lambda_1 \geq \cdots \geq \mathrm{Re}\,\lambda_{4^N-1}$, the Liouvillian gap is defined as $\Delta = \mathrm{Re}(\lambda_1 - \lambda_0)$ (see also Sec. 2.1.3). Since λ_0 corresponds to the slowest-decaying mode, the gap quantifies how quickly it is reached. The closure of the Liouvillian gap is often a signature of a phase transition. We can evaluate it numerically by diagonalizing the Liouvillian using the formalism of third quantization, which is discussed in App. D. In Fig. 4.5 we show Δ as a function of the parameters of our model. The gap closes only in the no-click limit of $q = 1$, thus confirming that no phase transition can occur for imperfect postselection corresponding to $q < 1$.

4.4 Conclusions

This chapter explores the impact of imperfect detection and partial postselection on quantum correlations in an analytically-solvable model of monitored dynamics. By computing the exact correlation matrix and employing complex analysis methods, we establish an upper bound to the correlation length of the system, which closely approximates the exact one. We reveal that trajectory averaging introduces an effective lengthscale for correlation functions, causing the entanglement phase transition observed in the fully postselected no-click limit to vanish for any degree of information loss ($q < 1$). This conclusion is further supported by our analysis of the entanglement negativity and the Liouvillian gap. Although non-trivial correlations persist at lengthscales below ξ, the latter diminishes rapidly as q decreases.

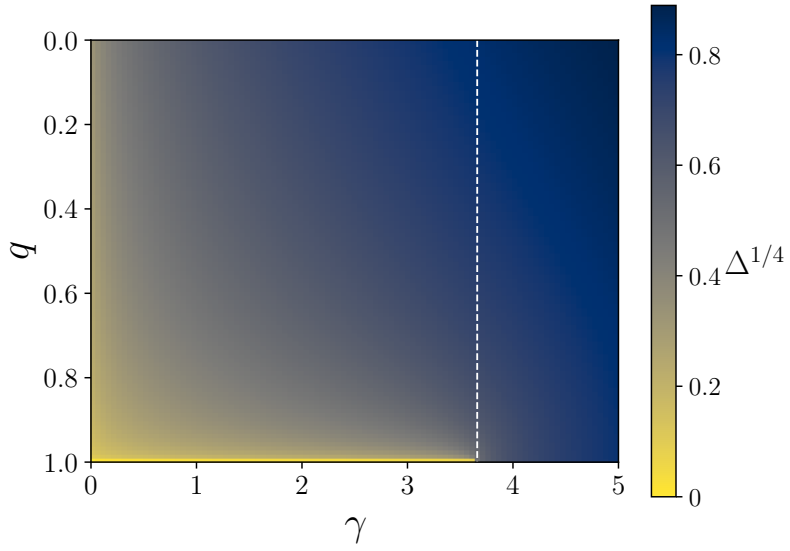

Figure 4.5: Liouvillian gap as a function of q and γ for $L = 128$ and $\mu = 0.4$. We display $\Delta^{1/4}$ instead of Δ to improve graphical visibility. The dashed line indicates the critical $\gamma_c(\mu)$ of the no-click limit. For any $q < 1$ the gap is always finite.

A crucial question following our findings is whether this result generalizes beyond our model. Our Liouvillian is integrable, and it may not be representative of generic monitored models. We expect that the appearance of a q-dependent correlation length holds quite generally, in line with the common understanding that decoherence destroys long-range quantum correlations. Still, there might exist models featuring an extended critical region with $\xi^{-1} = 0$ above some critical $q_c < 1$.

Future investigations could study the role of partial postselection in systems with Hamiltonian interactions or more complex jump operators, possibly producing non-Gaussian dynamics. Beyond Gaussianity, the problem becomes much harder to approach, as analytical tools are limited. At the same time, numerical simulations based on quantum trajectory unravelings are always restricted to finite system sizes, making it challenging to distinguishing between a very large ξ and a formally diverging one. In this context, the framework of the algebraic Riccati equation for the steady-state correlation matrix could be valuable for developing a perturbative approach in the presence of weak integrability-breaking terms.

Another important consideration is to what extent the instability of the no-click phase transition depends on the criterion used to discard quantum trajectories: in our study, partial postselection excludes trajectories with many jumps, but alternative criteria could be explored.

Finally, it would be interesting to investigate the role of dimensionality. Unlike fermions, monitored bosonic systems in two or more dimensions can exhibit criticality even without postselection [303]. In such cases, one might expect a non-trivial phase diagram at $0 < q < 1$, bridging the Lindbladian and no-click limits. These intriguing questions are left for future investigations.

Chapter 5

Measurement-altered Ising model

So far, we have focused on non-equilibrium protocols where measurements, together with unitary evolution, induce non-trivial dynamics and generate different kinds of entanglement structures at long times. More recently, the study of measurement-altered phases of matter has also been pursued in a *static* scenario, addressing the question of how a finite density of measurements affects the properties of a given quantum state. In detail, Refs. [307–312] investigate measurement-altered critical ground states, focusing on correlation functions and on the entanglement properties of Luttinger liquids and free-fermionic states. Compared to the dynamical setup of monitored systems [1, 55–57, 246–250, 313–318], this approach reveals equilibrium aspects of the underlying model, and constitutes a natural framework to explore the effect of measurements in many-body systems.

In this chapter, we expand the previous investigations beyond the gapless case to *non-critical* quantum Ising ground states, exploring the robustness of their quantum correlations and entanglement properties to a finite density $p \in [0, 1]$ of measurements. We develop a comprehensive picture by focusing on three entanglement witnesses of bipartite and multipartite quantum correlations: the entanglement entropy, the quantum Fisher information (QFI), and the two-body fermionic negativity. By considering both Born-rule and forced (postselected) measurements, we uncover how these protocols exhibit inequivalent phenomenology across the different phases of the Ising chain.

Our main result is that, contrary to common belief, local measurements do not necessarily reduce entanglement, but can even enhance it in atypical random realizations. This clarifies that the action of external monitoring goes beyond a simple disentangling role, and in fact affects the correlation structure of many-body systems in a non-trivial way. To understand this effect, we develop a perturbative theoretical approach and a network toy model that captures how quantum projections reshape the entanglement structure of a state. This clarifies that while measurements erase some correlations, they can generate new ones as well, potentially expanding the spatial reach of entanglement.

Finally, we extend our analysis to a measurement-altered non-Hermitian Ising chain, found in the no-click limits considered in the previous chapters. This approach aims at establishing to what extent non-Hermitian models can describe accurately the physics of the full ensemble of trajectories in MIPTs [1, 250, 304], and is partially motivated by the differences observed in Chapter 3 between the two. Our findings indicate that the scaling behaviors of entanglement witnesses are unchanged by the measurement protocol, thus indicating that any discrepancy between the non-

Hermitian description and the stochastic evolution must be a consequence of the interplay between dynamics and measurements.

The rest of this chapter is organized as follows. First, we define the framework of our study in Sec. 5.1, as well as the entanglement witnesses we consider. Afterward, we showcase numerical simulations in Sec. 5.2 and explain them using perturbation theory. Motivated by these results, in Sec. 5.3 we introduce a toy model of an entanglement network that describes the enhancement of correlations under measurements. Section 5.4 extends our investigation to the non-Hermitian case, where we characterize the impact of forced projections on the no-click limit of continuously monitored systems. A conclusive discussion of the results obtained is given in Sec. 5.5.

5.1 Model and Entanglement Witnesses

This section presents the paradigm of projected ensembles, generated by applying local measurements to a many-body system initially prepared in a given state $|\Psi_0\rangle$. We also introduce the key entanglement witnesses that we will use to characterize how quantum correlations are affected by this process. Specifically, we consider the ground state of the quantum Ising chain

$$\hat{H} = -\sum_j \hat{\sigma}_j^x \hat{\sigma}_{j+1}^x - h \sum_j \hat{\sigma}_j^z, \tag{5.1}$$

with periodic boundary conditions. The perturbation of this state with measurements has already been considered in Refs. [308, 312] in the critical case. Here we extend the study to generic choices of h, including non-Hermitian setups (cf. Sec. 5.4).

5.1.1 Projected ensembles

Starting from the state $|\Psi_0\rangle$, we are interested in studying the ensemble of states obtained by performing a finite density of local projective measurements of the observables $\hat{\sigma}_j^z$. For convenience, throughout this chapter we adopt the notation $|1_j\rangle \equiv |\uparrow_j\rangle$ or $|-1_j\rangle \equiv |\downarrow_j\rangle$ for the eigenstates of $\hat{\sigma}_j^z$. The details of the protocol are the following. Each lattice site j has a finite probability p of being addressed by a measurement, in such a way that pL spins are measured on average. To this purpose, for every qubit j we introduce a discrete random variable m_j such that $m_j = 0$ with probability $1-p$ and $m_j \neq 0$ with probability p, corresponding to a spin being measured or not, respectively. Whenever $m_j \neq 0$, it can assume the values $m_j = \pm 1$, which indicate the possible outcomes $|\pm 1_j\rangle$ of the projective measurement. Any post-observation state can be characterized by assigning the string $\mathbf{m} = (m_1, m_2, \ldots, m_L)$, and it is explicitly given by

$$|\Psi_{\mathbf{m}}\rangle = \frac{\hat{\Pi}_{\mathbf{m}}|\Psi_0\rangle}{||\hat{\Pi}_{\mathbf{m}}|\Psi_0\rangle||}, \quad \hat{\Pi}_{\mathbf{m}} = \prod_{j=1}^{L} \hat{A}_{m_j,j}, \tag{5.2}$$

where $\hat{A}_{0,j} = \sqrt{1-p}\mathbb{1}_j$, and $\hat{A}_{\pm 1,j} = \sqrt{p}\,|\pm 1_j\rangle\langle\pm 1_j|$ are the local Kraus operators.

When $m_j \neq 0$, the choice of the local post-measurement state $|m_j\rangle$ depends on the specific measurement protocol we adopt, which is one of the following:

(i) forced up measurements ($\mathcal{M}_{\text{up}}$), where the post-measurement state is $|1_j\rangle$;

(ii) forced down measurements ($\mathcal{M}_{\text{down}}$), where the post-measurement state is $|-1_j\rangle$;

(iii) Born-rule measurements ($\mathcal{M}_{\text{Born}}$), where the measurement outcomes are extracted randomly according to the Born rule, i.e., $|m_j\rangle$ is picked with probability $|\langle m_j|\Psi\rangle|^2$.

We point out that (i) and (ii) do not constitute proper quantum measurements, but rather they are exponentially unlikely post-selected realizations of (iii). Still, certain quantum-jump unravelings of Lindbladian dynamics can actually give rise to projections in a fixed direction, together with an effective non-Hermitian Hamiltonian evolution, like the no-click limit covered in the previous chapters [1, 248, 250, 319]. In this context, the investigation of forced jumps can be used to characterize the stability against sudden projections of the non-Hermitian physics produced by the Hamiltonian alone, which has been investigated in models of MIPTs (see Sec. 5.4). Moreover, as we demonstrate below, forced projections can affect entanglement in unexpected ways, thereby elucidating how quantum jumps perturb a state in general. Their investigation thus provides information on the behavior of atypical random realizations.

We frame our discussion in a unified perspective using the concept of *projected ensembles* [320–327] by introducing the outcome probability distributions

$$\mathcal{P}_{\mathcal{M}_{\text{up}}}(\mathbf{m}) = p^{\sum_j |m_j|}(1-p)^{\sum_j (1-|m_j|)} \prod_j (1-\delta_{m_j,-1}), \tag{5.3a}$$

$$\mathcal{P}_{\mathcal{M}_{\text{down}}}(\mathbf{m}) = p^{\sum_j |m_j|}(1-p)^{\sum_j (1-|m_j|)} \prod_j (1-\delta_{m_j,1}), \tag{5.3b}$$

$$\mathcal{P}_{\mathcal{M}_{\text{Born}}}(\mathbf{m}) = p^{\sum_j |m_j|}(1-p)^{\sum_j (1-|m_j|)} \langle\Psi_0|\,\hat{\Pi}_{\mathbf{m}}\,|\Psi_0\rangle \tag{5.3c}$$

for the different protocols. A measurement-altered system is described by the ensemble $\mathcal{E}_{\mathcal{M}}(|\Psi_0\rangle) = \{(\mathcal{P}_{\mathcal{M}}(\mathbf{m}), |\Psi_{\mathbf{m}}\rangle)\}$. The statistical properties of $\mathcal{E}_{\mathcal{M}}(|\Psi_0\rangle)$ contain more information than the average state $\hat{\rho}_1 = \sum_{\mathbf{m}} \mathcal{P}_{\mathcal{M}}(\mathbf{m})|\Psi_{\mathbf{m}}\rangle\langle\Psi_{\mathbf{m}}|$. Indeed, while $\hat{\rho}_1$ perfectly describes all linear functions of $|\Psi_{\mathbf{m}}\rangle\langle\Psi_{\mathbf{m}}|$ averaged over the distribution $\mathcal{P}_{\mathcal{M}}(\mathbf{m})$, it does not capture the typical properties of non-linear functionals of the density matrix. Such functionals include effects of the k-replicated density matrix

$$\hat{\rho}_k = \sum_{\mathbf{m}} \mathcal{P}_{\mathcal{M}}(\mathbf{m})(|\Psi_{\mathbf{m}}\rangle\langle\Psi_{\mathbf{m}}|)^{\otimes k}, \tag{5.4}$$

and reveal non-trivial beyond-average quantum correlations that are often witnesses of critical behavior in monitored many-body systems.

5.1.2 Entanglement witnesses

Entanglement measures and witnesses are examples of non-linear quantities, and they are the main focus of the present manuscript. Specifically, we consider the entanglement entropy and the QFI as functions of the measurement density p. Furthermore, we also investigate the fermionic negativity of spin pairs, from which we can extract the typical lengthscale of quantum correlations. Given our choice of the initial state and of the measurement operators, the problem can be studied efficiently using Gaussian states [116], using the methods presented in App. B. This makes the calculation of the entanglement witnesses efficient, allowing us to explore large system sizes.

As seen also in the previous chapters, the entanglement entropy [8, 26, 70, 71] between a compact interval A of ℓ spins and the complementary subsystem is defined as $S_\ell = -\operatorname{Tr}(\hat{\rho}_A \ln \hat{\rho}_A)$. We also remind the expression for the QFI [1, 135, 149, 162, 167, 193]. of a pure state $|\Psi\rangle$ with respect to an observable $\hat{O}[\{\mathbf{n}_j\}]$ in the form of Eq. (1.11), which is given by $F_Q[\hat{O}[\{\mathbf{n}_j\}]] = \sum_{\alpha,\beta}\sum_{i,j} n_i^\alpha n_j^\beta C_{i,j}^{\alpha,\beta}$, where $C_{i,j}^{\alpha,\beta} = \langle \hat{\sigma}_i^\alpha \hat{\sigma}_j^\beta \rangle - \langle \hat{\sigma}_i^\alpha \rangle \langle \hat{\sigma}_j^\beta \rangle$. As discussed previously, the density $f_Q = F_Q/L$ witnesses multipartite entanglement (see Sec. 1.1.3), and should be maximized with respect to the unit vectors $\mathbf{n}_j$ to do this effectively. In the following, we always perform the maximization using the same annealing algorithm used in the analysis of Chapter 3.

Finally, we study the fermionic logarithmic negativity [174–178, 328–335] discussed in Sec. 1.2.3, which properly measures entanglement in mixed states, differently for instance from the quantum mutual information [8, 168]. Given a tripartition of the system in distinct subsets A_1, A_2, and $\overline{A_1 \cup A_2}$, the negativity allows us to investigate the entanglement between A_1 and A_2 alone. Differently from how we used it in the previous chapter, in the following, we assume that A_1 and A_2 are single spins at positions i and j, and we investigate the decay of their negativity with the distance $|j-i|$. To do so, we first define $A = A_1 \cup A_2$, and we consider the reduced density matrix $\hat{\rho}_A$. The pair fermionic negativity is then given by

$$E_{i,j}^f = \log ||\hat{\rho}_A^{\tilde{T}_{A_1}}||, \tag{5.5}$$

where $\hat{\rho}_A^{\tilde{T}_{A_1}}$ is the twisted partial transpose of $\hat{\rho}_A$ with respect to subsystem A_1. The numerical calculation of the negativity is described in Sec. 1.2.3.

5.2 Numerical phenomenology and perturbative explanation

One of the main results of the present investigation is the demonstration that measurements do not simply degrade entanglement, but might actually strengthen it. In this section, we demonstrate this phenomenon using numerical simulations, and develop a qualitative theoretical explanation based on perturbation theory. We report numerical results for the quantities introduced in Sec. 5.1.2 using different measurement densities p and various protocols.

Before proceeding, let us illustrate a basic manifestation of entanglement growth produced by measurements with a simple example on the 3-qubit state

$$|\phi\rangle = \frac{1}{\sqrt{6}}\Big(2|-1_A, 1_B, 1_C\rangle + |1_A, -1_B, 1_C\rangle + |1_A, 1_B, -1_C\rangle\Big). \tag{5.6}$$

The entanglement entropy between C and the remainder is $S_C \approx 0.62$. Now, we perform a projective measurement on A. If the outcome is $|-1_A\rangle$, the post-measurement state is a product state $|\phi'_{-1}\rangle = |1_B 1_C\rangle$ with no entanglement, i.e., $S'_C|_{-1} = 0$. In contrast, if the outcome is $|1_A\rangle$, the post-measurement state is the Bell pair $|\phi'_1\rangle = (|1_B - 1_C\rangle + |-1_B 1_C\rangle)/\sqrt{2}$ and the post-observation entropy is $S'_C|_{+1} = \ln 2 \approx 0.69$. Therefore, depending on the outcome, the measurement of A can either destroy or enhance entanglement between B and C. This phenomenon is referred to as measurement-induced entanglement enhancement [336–338]. In the following, we investigate in which cases this effect appears in a many-body context.

In the following, we analyze the measurement-altered quantum Ising ground state considering both ordered and disordered phases, as well as the transition point $h = 1$. As anticipated, the model has been previously investigated in Ref. [177, 308–310] at criticality. These works demonstrate that the critical properties present crossover effects, with an effective central charge renormalized for forced up measurements and unaltered in the Born rule case. Here, we extend these considerations to the off-critical phase, and consider forced down measurements as well. Our main result is that the paramagnetic phase reveals an entanglement enhancement for the forced measurements $\mathcal{M}_{\text{down}}$, while a trivial crossover effect is observed for $\mathcal{M}_{\text{up/Born}}$. Instead, the ferromagnetic phase shows robustness to measurements, irrespective of the measurement-altering protocol.

5.2.1 Disordered phase $h > 1$

We begin our analysis by considering the paramagnetic disordered phase at $h > 1$. Fig. 5.1 summarizes our results for the representative choice of $h = 1.5$. In Fig. 5.1(a-c), we report the average entanglement entropy for varying p at different subsystem sizes. The protocols $\mathcal{M}_{\text{Born}}$ and $\mathcal{M}_{\text{up}}$ yield a similar size-independent behavior, monotonously decreasing with p. For Born measurements this is expected, as any entanglement monotone cannot increase on average under local operations [169, 339]. In contrast, we find that forced down projections result in larger entanglement as compared to the unperturbed state. In particular, S_ℓ develops a peak as a function of p, migrating toward $p = 1$ as ℓ is increased. This suggests that in the limit of $\ell \to \infty$ the entanglement entropy as a function of p tends to a limiting curve that saturates to a constant for $p \to 1$. Our numerics suggests that $\lim_{p\to 1} \lim_{\ell\to\infty} S_\ell$ is independent of ℓ, which implies that the enhanced entangled state still follows an area law.

Next, we analyze multipartite entanglement in Fig. 5.1(d-f). The average QFI density reveals a behavior similar to that of the entanglement entropy: for the protocols $\mathcal{M}_{\text{up/Born}}$, the QFI decreases when varying p, while forced down measurements yield enhanced QFI, with a peak value, saturated at large L, of $\overline{f_Q^{\max}} \simeq 4$. The maximal QFI is attained at around $p \simeq 0.45$, demonstrating that the measurements

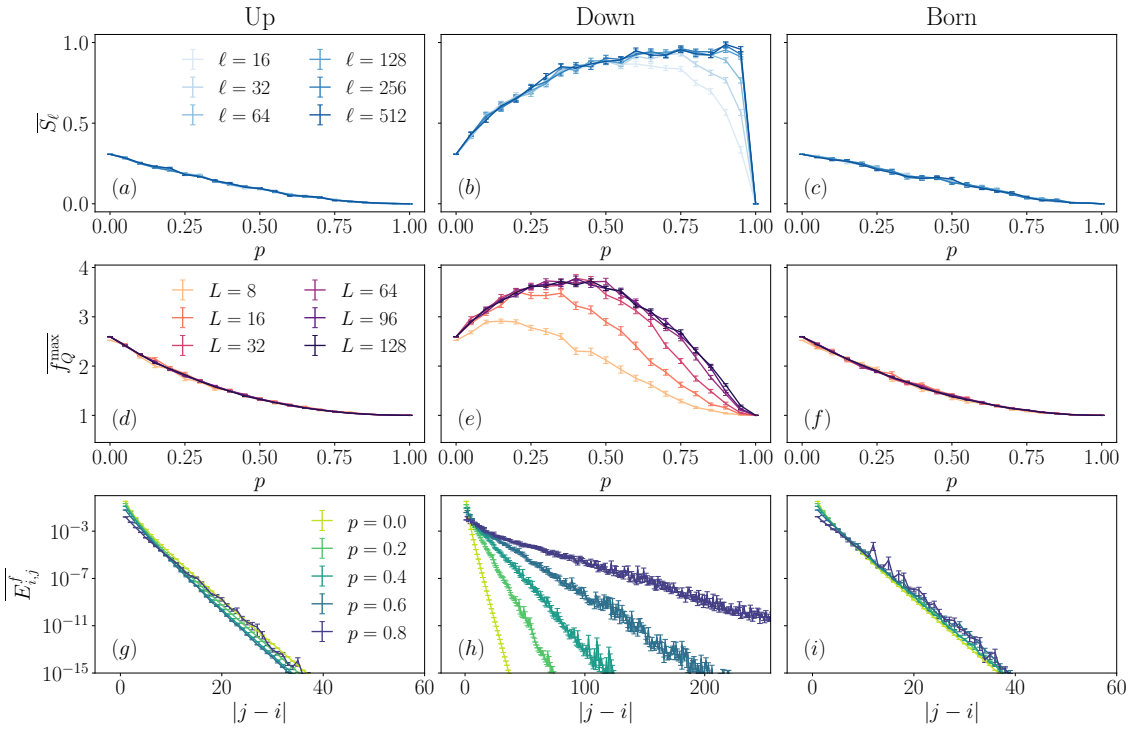

Figure 5.1: (a-c) Entanglement entropy, (d-f) maximal QFI density, and (g-i) pairwise fermionic negativity of the perturbed GS of the quantum Ising chain with $h = 1.5$. Left column: protocol $\mathcal{M}_{\text{up}}$. Center column: protocol $\mathcal{M}_{\text{down}}$. Right column: protocol $\mathcal{M}_{\text{Born}}$. We adopt $L = 1024$ for the entanglement entropy and $L = 512$ for the fermionic negativity.

affect inequivalently multipartite and bipartite quantum correlations. The saturating behavior of f_Q reveals bounded multipartiteness of entanglement.

Lastly, in Fig. 5.1(g-i) we report the average pairwise fermionic negativity $\overline{E^f_{i,j}}$ as a function of the distance $|j - i|$ for different measurement densities. The overall envelope of the decay is exponential, which is consistent with the presence of a finite length scale in the system, as demonstrated by the area-law entanglement previously discussed. Importantly, for $\mathcal{M}_{\text{up/Born}}$ the decay rate is independent of the measurement rate. Instead, for $\mathcal{M}_{\text{down}}$, the negativity features a renormalized length scale, which grows as the measurement density p increases. This reveals that the range of quantum correlations is effectively extended by the local measurements for $\mathcal{M}_{\text{down}}$, whereas for $\mathcal{M}_{\text{up/Born}}$ it remains unaffected. In Sec. 5.3, we develop a toy model to explain this effect qualitatively.

We stress that entanglement enhancement is a consequence of the monitoring alone, and no form of feedback is required. It is well known that many state-preparation protocols use measurements to realize long-range entangled states [340, 341], but these techniques also rely on entangling unitary gates, often conditioned to the measurement outcomes. Moreover, these paradigms usually operate on special simple states, whereas our observation of enhancement applies to complex many-body states. We point out, however, that the forced setups discussed in this chapter are impractical for the preparation of entangled states, as they rely on heavy post-

selection. In contrast, feedback operations enable countering the randomness of measurements and allow deterministic control of states.

Perturbative description – The observed phenomenology can be understood by considering the structure of the initial state $|\Psi_0\rangle$ within perturbation theory. For $h \gg 1$, we expand the ground state of the quantum Ising chain of Eq. (5.1) in powers of h^{-1} starting from the ground state for $h \to \infty$, which is simply the product state $|1_1 \dots 1_L\rangle$. Throughout the following calculations, the normalization of the state is disregarded, as it is irrelevant for the purposes of our discussion. For later convenience, let us label this state as $|vac\rangle$. Perturbative corrections consist of states with local defects, i.e., spins opposite orientations with respect to the rest of the chain. We denote a state with k defects at positions $j_1, \dots, j_k$ by $|j_1, \dots, j_k\rangle = (\prod_{m=1}^{k} \hat{\sigma}^x_{j_m}) |vac\rangle$. Using standard perturbation theory, the Ising ground state is expanded up to second order as

$$\begin{aligned} |\Psi_0\rangle = &|vac\rangle + \frac{1}{4h} \sum_i |i, i+1\rangle \\ &+ \frac{1}{16h^2} \sum_{j>i+1} |i, i+1, j, j+1\rangle + \frac{1}{8h^2} \sum_i |i, i+2\rangle + \mathcal{O}(h^{-3}). \end{aligned} \tag{5.7}$$

Notice that defects always appear in pairs, which is a crucial feature leading to entanglement enhancement.

Usually, an expansion like this is not particularly useful for many-body systems, as any finite truncation does not provide a good approximation of the true state. The way we will use Eq. (5.7) is to understand how measurements modify *all* perturbative orders collectively. As discussed below, this framework explains qualitatively all our numerical observations on the entanglement entropy and fermionic negativity for $h < 1$ and $h > 1$.

Let us focus on $\mathcal{M}_{\text{up}}$ first. When we apply $|1_n\rangle\langle 1_n|$ to $|\Psi_0\rangle$, some components of the expansion are filtered out, namely, all states with a difect at site n. We see from Eq. (5.7) that the leading 0th-order state is left unchanged, while $\mathcal{O}(L^{n-1})$ states are removed from each order $n > 0$. Since the population of each perturbative order is unaffected at leading order in L, the post-measurement state takes the form $|\Psi'\rangle = |1_j\rangle|\varphi\rangle$, where $|\varphi\rangle$ is a state of $(L-1)$ spins with analogous structure to $|\Psi_0\rangle$. Since the overlap $|\langle\Psi'|\Psi_0\rangle| \simeq 1$, we conclude that the projection represents a small perturbation to the hierarchical structure of the expansion. Furthermore, the weights of the different states in the superposition are modified only slightly by the renormalization of the wavefunction. For this reason, quantum correlations can only decrease, as one spin has been factorized while no properties of the rest of the chain have changed significantly.

Crucially, a very different phenomenology is present for the protocol $\mathcal{M}_{\text{down}}$, as applying $|-1_n\rangle\langle -1_n|$ to $|\Psi_0\rangle$ alters the state remarkably. In this case, the projected state reads

$$\begin{aligned} |\Psi'\rangle = &\frac{1}{4h} \left(|n-1, n\rangle + |n, n+1\rangle\right) + \frac{1}{16h^2} \sum_{i \neq n, n-1, n-2} |i, i+1, n-1, n\rangle \\ &+ \frac{1}{16h^2} \sum_{i \neq n, n\pm 1} |i, i+1, n, n+1\rangle + \frac{1}{8h^2} \left(|n-2, n\rangle + |n, n+2\rangle\right) + \mathcal{O}(h^{-3}). \end{aligned} \tag{5.8}$$

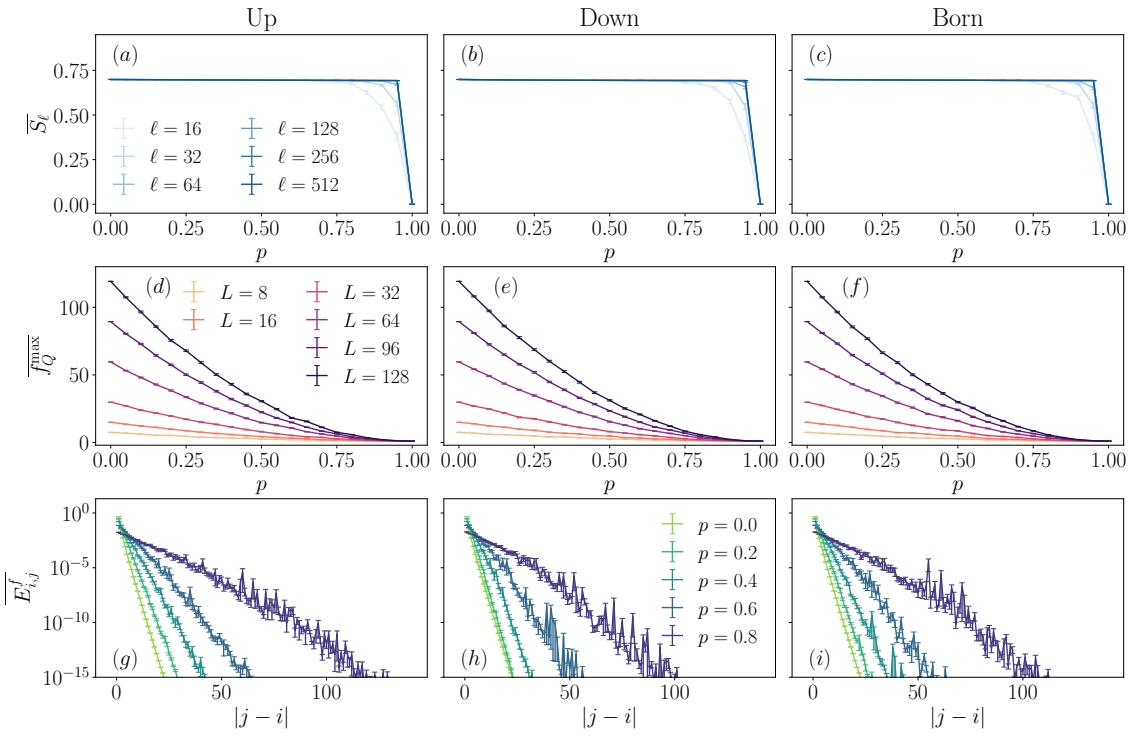

Figure 5.2: (a-c) Entanglement entropy, (d-f) maximal QFI density, and (g-i) pairwise fermionic negativity of the perturbed GS of the quantum Ising chain with $h = 0.5$. Left column: protocol $\mathcal{M}_{\rm up}$. Center column: protocol $\mathcal{M}_{\rm down}$. Right column: protocol $\mathcal{M}_{\rm Born}$. We adopt $L = 1024$ for the entanglement entropy and $L = 512$ for the fermionic negativity.

Therefore, the projection alters the structure of the state, shifting all orders by one. Most importantly, the populations of the various orders are renormalized. While the two leading orders of Eq. (5.7) contain one and L states, respectively, those of Eq. (5.8) contain twice as many (considering the leading power of L). As a consequence, more states participate to the superposition with relatively large amplitudes, and thus more entanglement is present. It is worth noting that the two new leading-order states of Eq. (5.7) form a Bell pair configuration for the spins on sites $n - 1$ and $n + 1$, further indicating an increase in entanglement. We stress, however, that entanglement enhancement cannot be reduced to the change of the leading-order, but rather it is an effect produced by the *collective renormalization* of populations of the various orders. In fact, the overlap of the full $|\Psi_0\rangle$ with the leading-order state only is exponentially small in L, and thus it cannot impact the entanglement properties alone. When multiple down projections are performed, one may expect that the populations of lower orders increase exponentially in the number of measured sites, possibly leading to entanglement growth despite the decimation of the measured spins.

Finally, the Born rule protocol represents an intermediate case between forced up and down projections. Since $|\langle 1_j|\Psi_0\rangle|^2 > |\langle -1_j|\Psi_0\rangle|^2$, entanglement enhancing jumps are rare, and the expected behavior is similar to the $\mathcal{M}_{\rm up}$ protocol.

5.2.2 Ordered phase $h < 1$

Different entanglement behavior is observed in the ordered ferromagnetic phase, as we show in Fig. 5.2 for the representative value of $h = 0.5$ [1]. In the following, we consider the symmetry unbroken ground state, namely, with no net longitudinal magnetization $\langle \hat{\sigma}_j^x \rangle = 0$. In Fig. 5.2(a-c) we show the average entanglement entropy. All projection protocol yield qualitatively similar results: thus, in contrast to the disordered phase, no enhancement is present for any $\mathcal{M}$. Additionally, for large subsystem sizes ℓ, the entanglement entropy appears to be approximately unaffected by the measurements, only decreasing when p is close to 1. As a consequence, the entanglement entropy for any $p < 1$ is qualitatively captured by the limit $p = 0$, i.e., by $|\Psi_0\rangle$, provided the subsystem size is sufficiently large.

We complement this analysis with the study of the QFI, reported in Fig. 5.2(d-f). Since the ordered phase features ferromagnetic long-range order, and we are considering a state with $\langle \hat{\sigma}_j^x \rangle = 0$, the correlator $C_{i,j}^{x,x}$ approaches a finite value for $|j - i| \to \infty$. As a consequence, the QFI density is extensive at $p = 0$. We observe that this remains true for all $p > 0$, and measurements renormalize the amplitude of the linear scaling. As for the entanglement entropy, all protocols yield qualitatively similar results.

Last, Fig. 5.2(g-i) shows the two-spin fermionic negativity. Despite the absence of entanglement entropy nor QFI enhancement, $\overline{E_{i,j}^f}$ decays exponentially with a length scale that grows with p, as in the case of $\mathcal{M}_{\text{down}}$ in the disordered phase. Interestingly, this result applies to all protocols we consider, consistent with the results of the other witnesses.

Perturbative description – Also in this case, we can develop an analytical understanding using perturbation theory. In the ferromagnetic phase, we expand the state around the symmetry-unbroken GHZ ground state for $h = 0$, obtaining

$$\begin{aligned} |\Psi_0\rangle = & \frac{|+_1 \cdots +_L\rangle + |-_1 \cdots -_L\rangle}{\sqrt{2}} \\ & + \frac{h}{4} \sum_i \frac{|+_1 \cdots -_i \cdots +_L\rangle + |-_1 \cdots +_i \cdots -_L\rangle}{\sqrt{2}} + \mathcal{O}(h^2), \end{aligned} \tag{5.9}$$

where $\hat{\sigma}^x |\pm\rangle = \pm |\pm\rangle$. States at order n in the expansion present n defects, corresponding to spin flips. Given that the spin states in Eq. (5.9) are in the x basis, both projectors $|1_n\rangle\langle 1_n|$ and $|-1_n\rangle\langle -1_n|$ impact the state in similar ways. The difference only relies in the phases acquired by the projected wavefunction, because $\langle 1|\pm\rangle = 1/\sqrt{2}$ while $\langle -1|\pm\rangle = \pm 1/\sqrt{2}$. As a consequence, it is not surprising to observe that the different protocols yield similar entanglement entropy [cf. Fig. 5.2(a-c)], even though $|\Psi_0\rangle$ has a finite transverse magnetization and thus the jump probabilities are asymmetric.

To explain the behavior of entanglement with p, let us assume the case of $\mathcal{M}_{\text{up}}$. For simplicity, let us consider the action of the projector $|1_1\rangle\langle 1_1|$ on the first lattice

[1] We consider L finite and then take the thermodynamic limit $L \to \infty$, following Ref. [342].

site. This yields a projected state $|\Psi'\rangle = |1_1\rangle\,|\varphi\rangle$, where

$$|\varphi\rangle = \left(1+\frac{h}{2\sqrt{2}}\right)\frac{|+_2\cdots+_L\rangle+|-_2\cdots-_L\rangle}{\sqrt{2}} + \frac{h}{4}\sum_{i=2}^{L}\frac{|+_2\cdots-_i\cdots+_L\rangle+|-_2\cdots+_i\cdots-_L\rangle}{\sqrt{2}}+\mathcal{O}(h^2). \tag{5.10}$$

Apart from subleading corrections to the amplitudes of each order, this state shares the same structure as $|\Psi_0\rangle$, with the difference that it involves only $L-1$ spins. As a consequence, the action of the projector approximately amounts to decimating a spin and mapping the remaining others to the Ising ground state with one less spin (and slightly modified parameters). Due to this chain renormalization, if we measure spin n, the entanglement between spins $i<n$ and $j>n$ after the projection is approximately the same as the entanglement between spins i and $j-1$ before the projection. This implies the growth of the average entanglement length scale shown in Fig. 5.2(d-f). Notice, however, that this mechanism simply shifts quantum correlations spatially, but does not grow their magnitude. As a consequence, as shown in Fig. 5.2(a-c), there can be no enhancement in the entanglement entropy. For large ℓ, S_ℓ is independent of p because the quantum correlations that cross the bipartition are still intact, even though they may have been translated spatially by the measurements. For small ℓ, instead, the entropy starts decreasing at large p, as most spins in the subsystem are decimated.

5.2.3 Critical point $h = 1$

Finally, in Fig. 5.3 we report the numerical results for the critical point $h = 1$. As we demonstrate in Fig. 5.3(a-c), overall bipartite entanglement decreases with p for all protocols $\mathcal{M}$. In particular, $\mathcal{M}_{\text{up/Born}}$ reproduce the results in the literature [308, 309], which are understood in terms of a defect perturbed field theory. Interestingly, for $\mathcal{M}_{\text{down}}$, the critical behavior is reminiscent to that of the off-critical phases, namely, the entropy appears to reach zero discontinuously for $p\to 1$. For all protocols, we observe that at any given $p<1$ the entanglement entropy maintains logarithmic dependence on ℓ, with a central charge $c_{\text{eff}}(p)$ renormalized by the external monitoring, consistently with previous results in the literature. Notice that for $\mathcal{M}_{\text{down}}$ it may appear that the curves corresponding to different values of ℓ converge to a limiting line for $\ell\to\infty$ at large p [see Fig. 5.3(b)]. This fact would indicate a transition to an area law. However, performing a finite-size analysis, we investigated this possibility by estimating the central charge $c_{\text{eff}}(p)$ using the largest values of ℓ available, and found that it reaches zero only at $p=1$.

Next, we analyze the QFI, summarizing our findings in Fig. 5.3(d-f). While $\mathcal{M}_{\text{up}}$ and $\mathcal{M}_{\text{Born}}$ yield a qualitatively similar decrease with the measurement density p, for the $\mathcal{M}_{\text{down}}$ protocol we observe enhanced multipartite entanglement. In detail, a small density of projections p can increase the QFI density. The peak position appears to shift towards larger p as L increases. Nevertheless, the effect of monitoring does not alter the scaling behavior of f_Q on L, analogously to the entanglement entropy.

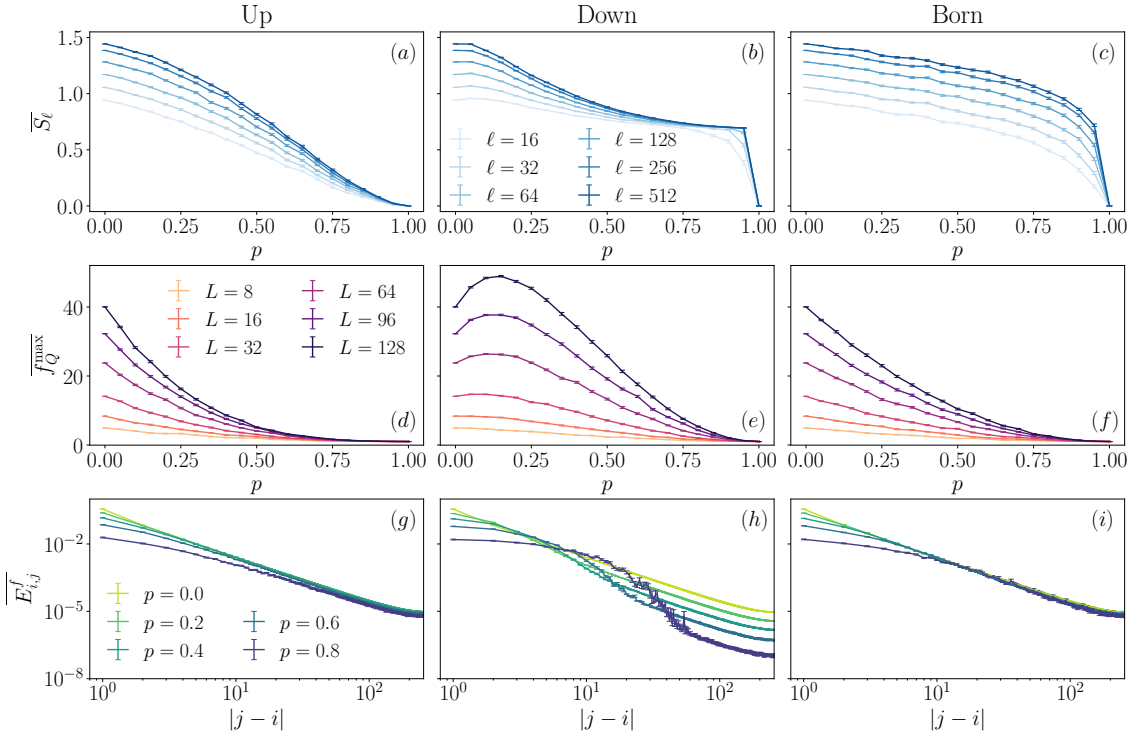

Figure 5.3: (a-c) Entanglement entropy, (d-f) maximal QFI density, and (g-i) pairwise fermionic negativity of the perturbed GS of the quantum Ising chain with $h = 1$. Left column: protocol $\mathcal{M}_{\rm up}$. Center column: protocol $\mathcal{M}_{\rm down}$. Right column: protocol $\mathcal{M}_{\rm Born}$. We adopt $L = 1024$ for the entanglement entropy and $L = 512$ for the fermionic negativity.

Finally, Fig. 5.3(g-i) highlights the pairwise negativity at the critical point. In this case, the decay is power law, and mirrors the divergence of the length scale of quantum correlations. All protocols maintain the same behavior and do not affect the exponent of the power law. However, for $\mathcal{M}_{\rm down}$ this holds only asymptotically in the distance $|j - i| \to \infty$, whereas a distinct behavior arises at short distances within a region whose size grows with p.

Our numerical findings show that a finite density of measurements can give rise to both bipartite and multipartite entanglement enhancement, as well as to a renormalization of the length scale of quantum correlations. In the next section, we describe this effect by means of a network toy model.

5.3 Entanglement network toy model

Our results on the pairwise fermionic negativity highlight that some measurement protocols can increase the typical length scale ξ of quantum correlations. Local projections disentangle a spin from the chain, and consequently break some local correlations within the scale ξ. Nevertheless, if the projected spin is partially correlated with some other, new quantum correlations can be developed among these additional degrees of freedom. Motivated by our numerical results, we formulate

a network toy model that captures the qualitative features of this phenomenon. It describes the action of measurements as cutting and sewing of quantum correlations, and, as we demonstrate below, it reproduces the key feature of entanglement enhancing, i.e., the renormalized average length scale of entanglement ξ. We anticipate that the model is not intended as a quantitative method, as it does not discriminate between different measurement protocols, nor it involves any notion of strength of entanglement. Rather, its purpose is to provide a simplified description of those quantum projections that alter the state significantly (as in the cases of $h > 1$ for $\mathcal{M}_{\text{down}}$ and $h < 1$ for all protocols), and develop a qualitative understanding of the microscopic mechanism that leads to the average growth of ξ.

In our toy model, we describe quantum correlations between two spins at positions i and j as bonds in a ring network with L vertices. The presence or absence of a bond is indicated by the binary variable $E_{i,j} = E_{j,i} = 0, 1$, whose values one and zero refer to the spins being entangled or not, respectively. This picture is a simplified version of the pairwise negativity (cf. Sec. 5.1). Heuristically, this description corresponds to a 0th-order negativity spectrum, a pathological limit that measures only the rank of $\hat{\rho}^{\tilde{T}_1}$ (cf. Sec. 5.1). We represent an initial state with finite entanglement length scale ξ_0 using the input state ansatz

$$E_{i,j} = \begin{cases} 1 & \text{if } |j - i| \leq \xi_0; \\ 0 & \text{otherwise.} \end{cases} \tag{5.11}$$

Quantum projections act on the network as follows. Let us denote by $E_{i,j}$ and $E'_{i,j}$ the network configurations before and after the measurement. Suppose that the measured spin is at site n. First, since the projection disentangles it from the chain, we must have

$$E'_{i,n} = 0 \quad \forall i. \tag{5.12}$$

In addition, we assume that the degrees of freedom that were initially entangled with site n develop new correlations by recoupling among themselves. (*En passant*, we note this procedure resembles methods of strong disorder decimations, cf. Ref. [343, 344].) In detail, for $i, j \neq n$ we impose

$$E'_{i,j} = \begin{cases} 1 & \text{if } E_{i,n} = E_{j,n} = 1; \\ E_{i,j} & \text{otherwise.} \end{cases} \tag{5.13}$$

In other words, the sub-network of spins initially coupled to n becomes all-to-all connected, whereas the rest of the system remains unaffected. Notice that these rules will generally lead to multiple bonds for each site: this distinguishes our approach, for instance, from the network model presented in Ref. [89] where only pairwise links are allowed.

We formulated this recoupling scheme by investigating how the true negativity $E^f_{i,j}$ is affected by individual quantum measurements, and found that this mechanism works reasonably well for a binary representation of quantum correlations. Moreover, we point out that the previous rules guarantee the commutativity of measurements, which must hold since projectors acting on different sites commute.

We implement numerically the toy model as follows. Starting from an initial configuration with small ξ_0, we select randomly a fraction p of the spins to project

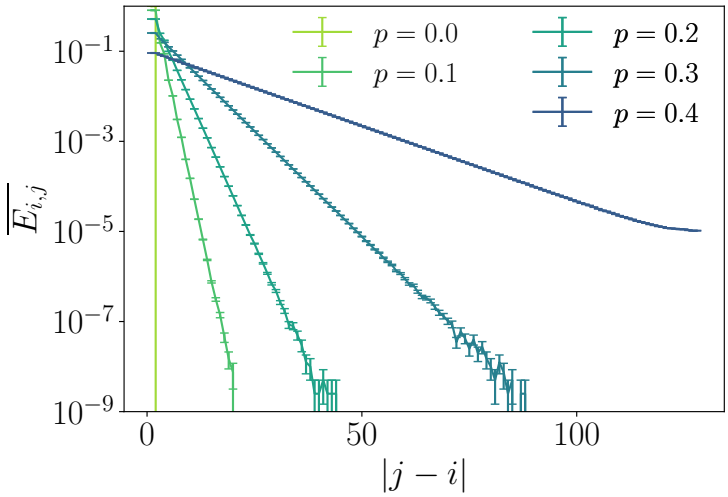

Figure 5.4: Average entanglement $\overline{E_{i,j}}$ of the toy model for $L = 256$ and $\xi_0 = 2$. The entanglement estimator decays exponentially, with a lengthscale that increases with p.

according to the previous network recoupling rule. We then repeat the procedure multiple times to compute the average $\overline{E_{i,j}}$. Figure 5.4 shows the results for $\xi_0 = 2$, representative of an area-law correlated state. We observe that bonds remain short-ranged on average, as $\overline{E_{i,j}}$ decays exponentially, but the length scale increases with p. This reproduces the entanglement enhancement observed in Sec. 5.2 for the pairwise fermionic negativity.

5.4 Stability test for the no-click limit of weak-measurement dynamics

Several works in the literature on monitored quantum dynamics discuss MIPTs in the no-click limit [1, 73, 250, 260, 304, 345, 346], already encountered in the previous chapters (see Sec. 3.2). The corresponding non-Hermitian Hamiltonian can often be approached theoretically to achieve analytical results. While it provides a simplified scenario to investigate the phenomenon, it is now understood that the no-click limit is unable to fully capture the more complex physics found in stochastic monitored dynamics, as the two manifest differences in phase boundaries [1, 265, 347] and critical exponents [296]. In the following, we leverage the framework of projected ensembles to investigate whether these discrepancies can be at least partially reproduced by perturbing the no-click limit with a layer of measurements, which is the simplest way to incorporate a key ingredient of the stochastic dynamics. Concretely, we repeat the analysis of the measurement-altered Ising chain for a different initial state $|\Psi_0\rangle$, which this time is the no-click stationary state. Since the monitored evolution does not include Born-rule measurements, we focus only on a single forced measurement protocol, corresponding to the quantum jumps of the stochastic dynamics.

Let us summarize the main properties of the no-click limit, reminding that a

complete treatment can be found in Sec. 3.2. We consider the pure steady state of the dynamics generated by the non-Hermitian Ising chain

$$\hat{H}_{\mathrm{NH}} = \hat{H} - i\frac{\gamma}{4}\sum_j \left(\hat{\sigma}_j^z - \langle\hat{\sigma}_j^z\rangle_t\right). \tag{5.14}$$

The no-click model features two distinct phases. For $|h| < 1$ and $\gamma < \gamma_c(h) = 4\sqrt{1-h^2}$, the entanglement entropy of the stationary state scales logarithmically with ℓ, whereas outside this region it saturates to an area law. A relationship between the measurement-induced transition, where no post-selection is present, and the non-Hermitian model has been recently proposed in Ref. [247]. However, it is not clear in which setups and up to what extent the non-Hermitian Hamiltonian describes quantitatively the properties of the system.

Let us now investigate how quantum jumps perturb the entanglement scaling properties of the no-click limit. In particular, we are interested in establishing whether the phase diagram is robust against measurements. For instance, it might occur that a state with logarithmic entropy scaling is unstable against measurements, which could degrade it to an area law. Choosing $|\Psi_0\rangle$ to be the stationary state of $\hat{H}_{\mathrm{NH}}$, we perturb it with a layer of forced up projections corresponding to the protocol $\mathcal{M}_{\mathrm{up}}$ of Eq. (5.3a), as this is the jump direction introduced by the stochastic Schrödinger equation of Eq. (3.3).

For $|\Psi_0\rangle$ in the area-law phase, all results on the entanglement witnesses are completely analogous to the case of the disordered Ising ground state (cf. Fig. 5.1). This is highlighted in the right column of Fig. (5.5), which shows numerical results for $\gamma > \gamma_c(h)$. The only difference between the Hermitian and non-Hermitian cases is that the roles of $\mathcal{M}_{\mathrm{up}}$ and $\mathcal{M}_{\mathrm{down}}$ are swapped. This is easily understood in terms of the transverse magnetization of $|\Psi_0\rangle$. For the Hermitian Ising chain at $h > 1$, the ground state has $\langle\hat{\sigma}_j^z\rangle > 0$, and quantum jumps produce entanglement enhancement only for measurements that oppose this magnetization, i.e., the protocol $\mathcal{M}_{\mathrm{down}}$. In contrast, the stationary state of Eq. (5.14) for $\gamma > 0$ has net magnetization $\langle\hat{\sigma}_j^z\rangle < 0$, and thus the enhancing protocol is $\mathcal{M}_{\mathrm{up}}$. In particular, forced up projections applied to the stationary state result in enhanced entanglement entropy and QFI, as well as in an enhanced length scale ξ of the pairwise fermionic negativity.

Regarding the logarithmic phase of the non-Hermitian model, we present our results in the left column of Fig. (5.5), which considers $\gamma < \gamma_c(h)$. The behaviors of the various witnesses are qualitatively similar to those of the critical Ising ground state of Fig. 5.3, provided swapping $\mathcal{M}_{\mathrm{up}}$ and $\mathcal{M}_{\mathrm{down}}$ as discussed above. The only notable difference is that the QFI density of Fig. 5.5(c) does not feature a peak, as opposed to Fig. 5.3(h). This is not surprising, as the Hermitian and non-Hermitian states $|\Psi_0\rangle$ considered do not feature identical entanglement structures. For instance, in both cases the QFI density at $p = 0$ scales as a power law, but the exponents are not the same.

Overall, the behaviors of the non-Hermitian model for $\gamma < \gamma_c(h)$ and $\gamma > \gamma_c(h)$ closely resemble what we found in the Hermitian case for $h = 1$ and $h > 1$, respectively. The scaling laws of all entanglement witnesses are unaffected by the measurement-altering scheme, proving that a single layer of measurements is not enough to affect them drastically and induce a crossover to the physics of the full

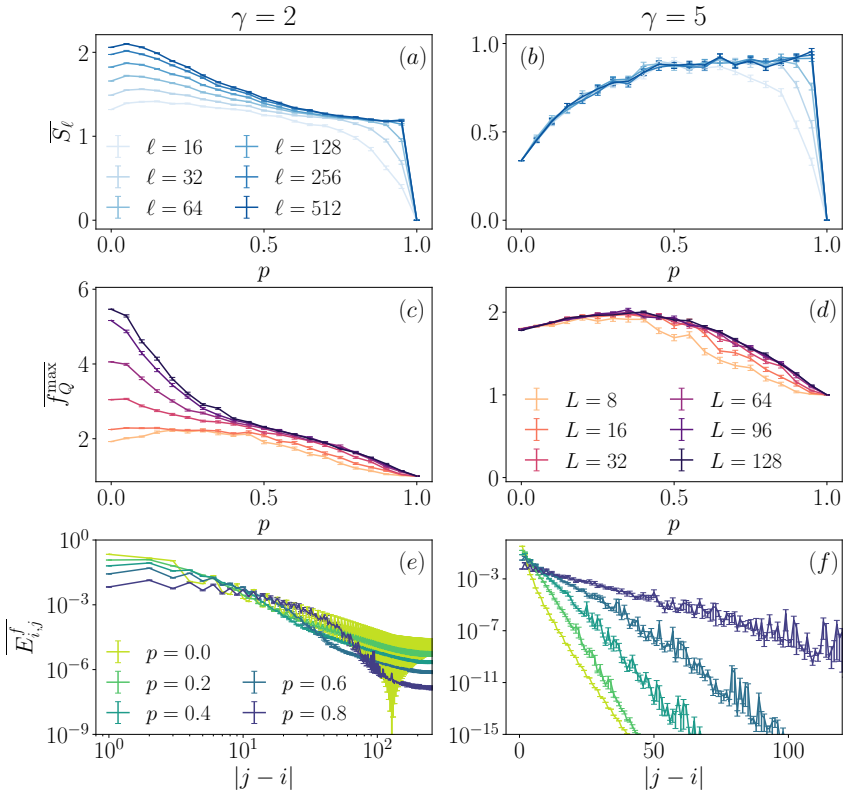

Figure 5.5: (a-b) Entanglement entropy, (c-d) maximal QFI density, and (e-f) pairwise fermionic negativity of the perturbed stationary state of the non-Hermitian Ising chain with $(h, \gamma) = (0.5, 2)$ (left column) and $(h, \gamma) = (0.5, 5)$ (right column), representative of other choices in the two phases. The protocol used is $\mathcal{M}_{\text{up}}$. We adopt $L = 1024$ for the entanglement entropy and $L = 512$ for the fermionic negativity.

monitored dynamics. We then conclude that the phenomenology generated by the full stochastic Schrödinger equation requires the interplay between random measurements and unitary evolution, and cannot be recovered by the simple description of a perturbed no-click limit considered here.

5.5 Conclusions

We investigated the entanglement properties of the measurement-altered Ising chain for different measurement protocols, measurement densities, and initial states. As our main result, we observe that local measurements alone may increase the system's entanglement for suitable outcomes. The principle beyond this effect is based on the monogamy of entanglement, and is exemplified in the perturbative analysis of Sec. 5.2 and in the toy model discussed in Sec. 5.3. This explicitly shows how postselected realizations of the monitoring can exhibit significant differences from the behavior of the full ensemble. In our investigation, enhancement is always intensive, implying that the measurement-altering protocol is unable to change the (non-)critical nature of the state.

The framework considered also provides insights into the relationship between the properties of non-Hermitian Hamiltonians and measurement-induced phases. Recalling that projections in forced directions arise naturally in quantum jump stochastic Schrödinger equations, we studied the stability of the non-Hermitian stationary state. The critical or non-critical nature of the starting state persists at all finite measurement densities, demonstrating its stability under this protocol. As a consequence, we conclude that any discrepancy between non-Hermitian physics and measurement-induced transitions must be looked for in the dynamical nature of latter.

It would be interesting to investigate the occurrence of entanglement enhancement in different models with distinct entanglement structure, as well as with interactions [348]. For instance, a natural question may be what happens to measurement-altered systems in two or more dimensions, where area-law entanglement entropy corresponds to a scaling S_ℓ. Another option not considered here regards the effects of different projection operators, e.g., local projectors in the longitudinal direction of spontaneous symmetry breaking, which likely change the phenomenology by destroying integrability. Lastly, one may expect even richer entanglement behavior in presence of entangling measurements, such as projections onto neighboring Bell pairs.

Chapter 6

Measurement-induced magic transitions in Gaussian dynamics

Quantum non-stabilizerness [81–88], a.k.a. magic, has recently emerged as a fundamental notion of quantum complexity whose relevance is comparable to that of entanglement. Conceptually, it constitutes a central resource for quantum computation, enabling the jump from the limited class of stabilizer states to the full Hilbert space. Although magic is more naturally defined in circuit models, both with and without measurements, over the last few years it has been used to characterize many-body phases in Hamiltonian settings as well. Remarkably, magic measures have been reported to manifest signatures of quantum phase transitions [205–209, 349], highlighting their usefulness as quantum information-based probes of critical behavior analogous to entanglement.

Recently, non-stabilizerness has also been investigated in monitored quantum dynamics, extending the paradigm of measurement-induced entanglement transitions to the broader framework of quantum complexity. Specifically, previous studies on hybrid Clifford circuits doped with non-stabilizer gates have highlighted critical behavior in magic measures, especially the stabilizer Rényi entropies (SREs). These quantities are challenging to compute directly for large systems [88, 234, 349–353], but recent advances in Majorana sampling techniques provide a powerful tool for handling fermionic Gaussian states, thus enabling the efficient computation of SREs even for systems with hundreds of lattice sites [354].

Motivated by this progress, in this chapter we address the problem of quantifying non-stabilizerness in the dynamics of free-fermionic systems. Specifically, our numerical investigation considers both the unitary and the monitored cases, looking for signatures of measurement-induced phase transitions (MIPTs) in magic. As discussed in Sec. 2.2.2, these models exhibit distinct entanglement phases depending on the particle number symmetry they exhibit, either $U(1)$ or $\mathbb{Z}_2$. For this reason, we explore the behavior of magic in both cases, aiming at understanding their discrepancies and, most importantly, the differences with respect to the behavior shown by the entanglement entropy. This consolidates the evidence that non-stabilizerness and entanglement generally exhibit distinct behavior in monitored dynamics, and their MIPTs do not necessarily match, as also highlighted in Ref. [278].

Unsurprisingly, in Hamiltonian models, the SREs always feature extensive behavior in all regimes, both with and without measurements. However, in monitored evolution, we highlight that critical behavior appears in the *subleading* corrections to the volume-law scaling. As our main result, the SREs exhibit logarithmic terms that disappear beyond a critical measurement rate, making them subtle yet striking

signatures of a novel form of MIPTs. Remarkably, this phenomenology is observed also in presence of $U(1)$ symmetry, thus highlighting its fundamental difference with entanglement which, instead, shows no MIPT in the corresponding monitored Gaussian model.

The chapter is organized in two parts. In Sec. 6.1, we investigate a chain of hopping fermions with $U(1)$ symmetry. We start by considering SREs in the unitary dynamics, and then shift to the monitored case. In contrast, Sec. 6.2 performs the same analysis on the quantum Ising chain, which can be mapped to a fermionic Kitaev chain with only $\mathbb{Z}_2$ symmetry. In the monitored case, instead of studying the full ensemble of quantum trajectories, we focus on the no-click limit considered in Chapter 3. Finally, we conclude with a discussion and outlook in Sec. 6.3.

6.1 Non-stabilizerness of hopping fermions

The first model we consider consists on spinless fermions hopping on a ring with periodic boundary conditions, described by the Hamiltonian

$$\hat{H} = -\frac{1}{2}\sum_{j=1}^{L}\left(\hat{c}_j^\dagger \hat{c}_{j+1} + \hat{c}_{j+1}^\dagger \hat{c}_j\right), \tag{6.1}$$

which preserves the total particle number $\hat{N}$. The dynamics is Gaussian due to the quadratic form of $\hat{H}$, and can be simulated efficiently as described in Sec. 1.2.2.

We consider the α-SREs

$$M_\alpha = \frac{1}{1-\alpha}\log_2\left(\sum_{\hat{P}\in\mathcal{P}_L}\frac{1}{2^L}\langle\psi|\hat{P}|\psi\rangle^{2\alpha}\right) \tag{6.2}$$

introduced in Eq. (1.83), particularly for $\alpha \to 1$ and $\alpha = 2$. For Gaussian states, these can be evaluated efficiently from the correlation matrix using the stochastic sampling algorithm of Ref. [354], which is presented in App. A. In the following, we study numerically the SREs in both the unitary case, which we refer to as plain dynamics, and the monitored one, where projective measurements of fermionic occupations are implemented randomly on all sites.

6.1.1 Plain dynamics

We begin our analysis by considering the purely unitary dynamics generated by the hopping Hamiltonian: the dynamics is fully deterministic, and the presence of a $U(1)$ symmetry in the model can significantly influence the stationary value of the non-stabilizerness reached at late times.

We consider two different initial conditions corresponding to distinct particle-number sectors, namely $N = L/2$ and $N = L/4$. These are prepared as generalized Néel states with fixed particle densities, i.e., $|1010\ldots\rangle$ and $|10001000\ldots\rangle$, respectively. The SREs M_α increase over time and eventually reach stationary values that scale linearly with the system size. The data are subject to fluctuations due to the probabilistic technique used in computing the SREs. In particular, they have been

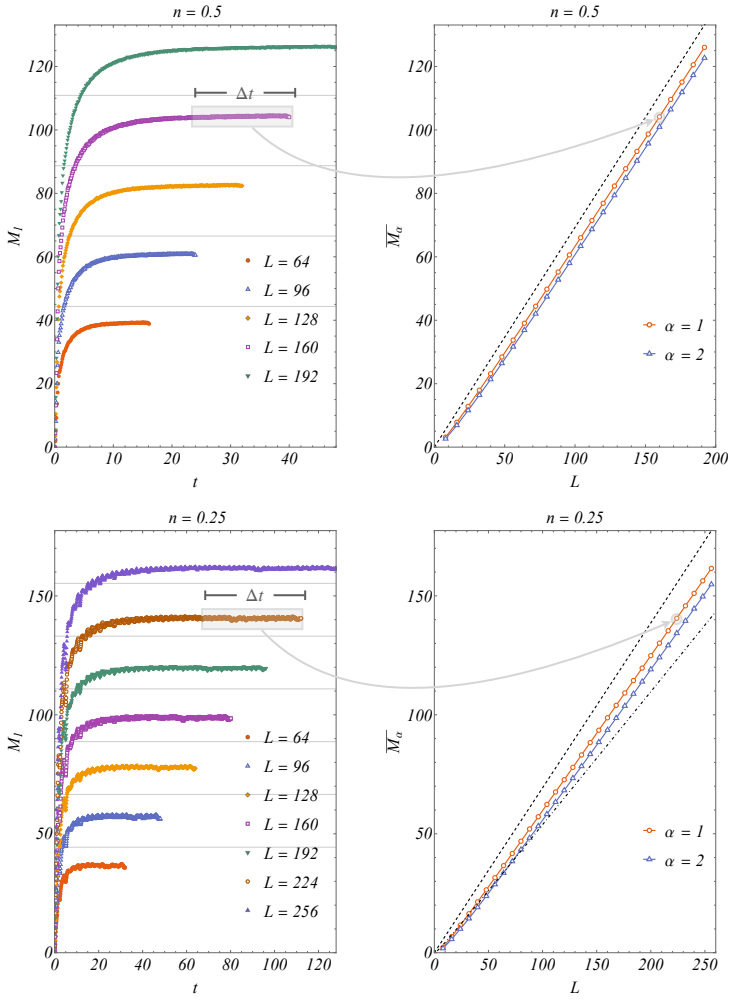

Figure 6.1: **Left panels**. Plain time evolution (no measurement, i.e. $\gamma = 0$) under the hopping Hamiltonian in Eq. (6.1) of the SRE M_1 after having initialized the system into the Néel state with particle density $n = N/L = 1/2$ (top) and $n = N/L = 1/4$ (bottom). Each point has been obtained by averaging over $\mathcal{S} = 1000$ Pauli strings. Gray horizontal lines correspond to $L\log(2)$. **Right panels**. Extensive behavior of the stationary stabilizer entropies averaged over a time window $\Delta t = [L/8, L/4]$ for $n = 1/2$, and $\Delta t = [L/4, L/2]$ for $n = 1/4$. The dashed line corresponds to $L\log(2)$ while, for $n = 1/4$ also $\log\binom{L}{L/4}$ is drawn (dot-dashed line).

computed by averaging over $\mathcal{S} = 1000$ samples. Notably, after performing a time average over a suitable window to suppress finite-time fluctuations (see Fig. 6.1, where we show the typical dynamics of M_1 for different system sizes), we observe that the stationary value of the magic exhibits, on top of the expected extensive behavior, sub-leading logarithmic corrections such that $\overline{M_\alpha(L)} \sim a_\alpha L - b_\alpha \log L - c_\alpha$. Here the coefficients $a_\alpha, b_\alpha, c_\alpha$ generally depend on both the Rényi index α and the initial conditions, i.e. the fixed particle density $n = N/L$ that characterizes the dynamical sector. For notational simplicity, we omit below the explicit dependence on n.

In Fig. 6.1, we display the leading behavior of the stationary values of the SREs for the two initial particle densities and for Rényi indices $\alpha = 1, 2$. At half filling,

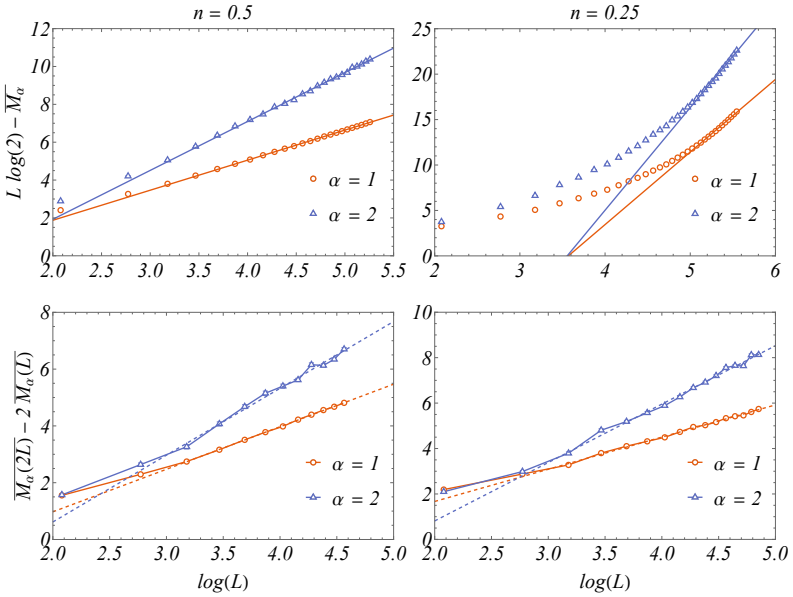

Figure 6.2: **Top panels**. Late-time SREs after a plain dynamics in the hopping fermions for $n = 1/2$ and $n = 1/4$, after subtracting the (non-symmetric) Haar average $L\log(2)$. **Bottom panels**. Logarithmic corrections to the non-stabilizerness, extracted via finite-size analysis (see main text for details).

the non-stabilizerness exhibits extensive behavior that asymptotically approaches the Haar average value of $L\log(2)$ In the large-L limit, the curves become nearly parallel to this reference, indicating convergence. This agreement becomes even more apparent when examining the subleading logarithmic corrections. This behavior aligns with what has been observed for random Gaussian states [354], even though is not clear which role is playing the $U(1)$ symmetry. In contrast, for the case with particle number $N = L/4$, the SREs do not appear to relax to the Haar value associated with the full Hilbert space. This may still occur, but, as expected for systems initialized with lower particle densities, reaching the thermodynamic limit likely requires significantly larger system sizes and longer times. Nonetheless, the SREs also deviate from the bound set by the Hilbert space dimension within the fixed-particle-number sector. In this case, the maximal scaling would be proportional to $\log\binom{L}{L/4}$, which disagrees with our numerical findings, as the numerics actually exceed this value. We find this interesting, as to the best of our knowledge, the non-stabilizerness uniformly averaged over a fixed particle-number sector is expected to be bounded from above by the logarithm of its dimension [355].

Subleading logarithmic corrections – As mentioned previously, the SREs are expected to exhibit sub-leading logarithmic corrections to the leading extensive behavior. In Fig. 6.2, we report a detailed analysis for both cases. As a first naive approach, we subtract from the stationary entropies the maximal Haar value, $L\log(2)$, and plot the residuals on a logarithmic scale, disregarding the presence of conserved quantities constraining the dynamics of non-stabilizerness. Remarkably, for the half-filling case $n = 1/2$, the remaining corrections display a striking logarithmic growth. This unambiguously confirms that the extensive coefficient of quantum magic under plain unitary dynamics, starting from a canonical Néel state,

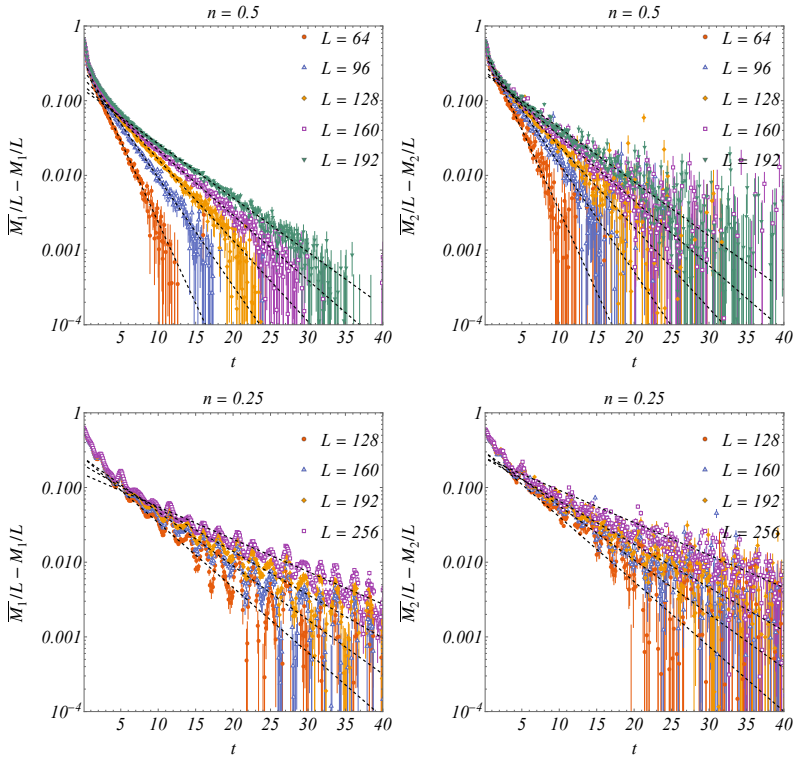

Figure 6.3: Log-linear plot of the relaxation dynamics of the SREs after having subtracted the best-fit finite-size stationary values $\overline{M_\alpha(L)} \sim a_\alpha L - b_\alpha \log L - c_\alpha$; dashed lines are size-dependent exponential decay drown as guide for the eyes.

indeed coincides with the Haar value. The quarter-filling case $n = 1/4$ shows a different behavior. After subtracting the Haar average, no clear logarithmic trend is observed, suggesting that the Haar value is not the appropriate leading term to subtract in this case.

To further investigate the logarithmic subleading corrections, without relying on any assumed leading extensive contribution, we analyze the finite-size difference $\overline{M_\alpha(2L)} - 2\overline{M_\alpha(L)}$. This combination cancels out any extensive linear scaling, allowing us to isolate potential logarithmic terms (see the bottom panels of Fig. 6.2).

This refined analysis enables us to extract the logarithmic coefficients for both particle densities and Rényi indices. Interestingly, the logarithmic corrections appear to be weakly dependent on the particle density, yet they depend on the Rényi index α. Our best-fit estimates yield the following coefficients:

$$n = 1/2,\ b_1 = 1.50(1),\ b_2 = 2.33(9),$$
$$n = 1/4,\ b_1 = 1.42(2),\ b_2 = 2.57(6).$$

Temporal dependence – We conclude our discussion of the plain unitary dynamics of hopping fermions by examining the time evolution of non-stabilizerness itself, i.e., how the SREs relax toward their stationary values. While our previous analysis focused on the asymptotic behavior, it is equally insightful to investigate the dynamical approach to stationarity. To this end, we consider the SRE density $M_\alpha(t, L)/L$, which depends on both time and system size, and focus on its behavior

at late times, $t \gg 1$. The limits $L \to \infty$ and $t \to \infty$ do not necessarily commute. In this section, although we analyze both the $n = 1/2$ and $n = 1/4$ cases, as well as the two Rényi indices $\alpha = 1, 2$, it is evident that the data are significantly more accurate for $n = 1/2$. This is due to reduced fluctuations and, most importantly, the necessity of knowing the extensive contribution to the SREs in the stationary regime with high precision. Consequently, one must exercise caution when interpreting relaxation dynamics in finite systems, especially when aiming to infer asymptotic scaling behavior.

The first question that naturally emerges is how the SREs approach their asymptotic form at large times. As a purely finite-size effect, and in line with observations from both random circuit dynamics and Gaussian evolutions [213, 354], the approach to stationarity may follow an exponential decay. As a preliminary analysis, we thus consider how the time-dependent data approach the finite-size stationary values. These stationary values have been carefully extracted from our best-fit analysis, which accounts for the extensive ($\sim L$), logarithmic ($\sim \log L$), and decaying ($\sim L^{-1}$) corrections, as already discussed. To this end, we study the quantity $(\overline{M_\alpha(L)} - M_\alpha(t, L))/L$ (see Fig. 6.3). This difference exhibits an exponential decay toward the finite-size stationary values, indicating that the $t \to \infty$ limit is taken first in this analysis. However, as the system size increases, the curves begin to bend on the log-linear scale and increasingly overlap in the early-time regime. This signals the emergence of a different universal behavior associated with the thermodynamic limit. This feature is particularly evident for the $\alpha = 1$, $n = 1/2$ case, where the data are especially clean and reliable.

A more systematic and conceptually sound analysis requires taking the thermodynamic limit ($L \to \infty$) before the long-time limit ($t \to \infty$). In this regime, the time-dependent behavior should become independent of L, and data from different system sizes are expected to collapse onto a universal thermodynamic scaling curve. As shown in Fig. 6.4, after shifting the data by a constant offset $\log(2)$ the SRE density $M_\alpha(t, L)/L$ displays an algebraic relaxation at intermediate times. However, once finite-size effects become relevant, i.e., beyond a characteristic crossover time $t^*(L)$, the dynamics transitions to the previously discussed exponential approach to the finite-size stationary value. Importantly, this exponential regime is delayed to progressively later times as the system size increases, and in the thermodynamic limit, it ultimately disappears, leaving the algebraic decay as the dominant relaxation behavior.

Since the model we consider is integrable, local properties relax to values that are described by Generalized Gibbs Ensembles [11, 186] at long times. This approach enables to determine stationary reduced density matrices exactly in the thermodynamic limit. We may leverage this formalism to analyze *subsystem* SREs. This analysis is presented in Appendix E.

6.1.2 Monitored dynamics

In the following, we investigate the unitary hopping dynamics interspersed with local projective measurements of occupation numbers $\hat{n}_j = \hat{c}_j^\dagger \hat{c}_j$, which are Gaussian

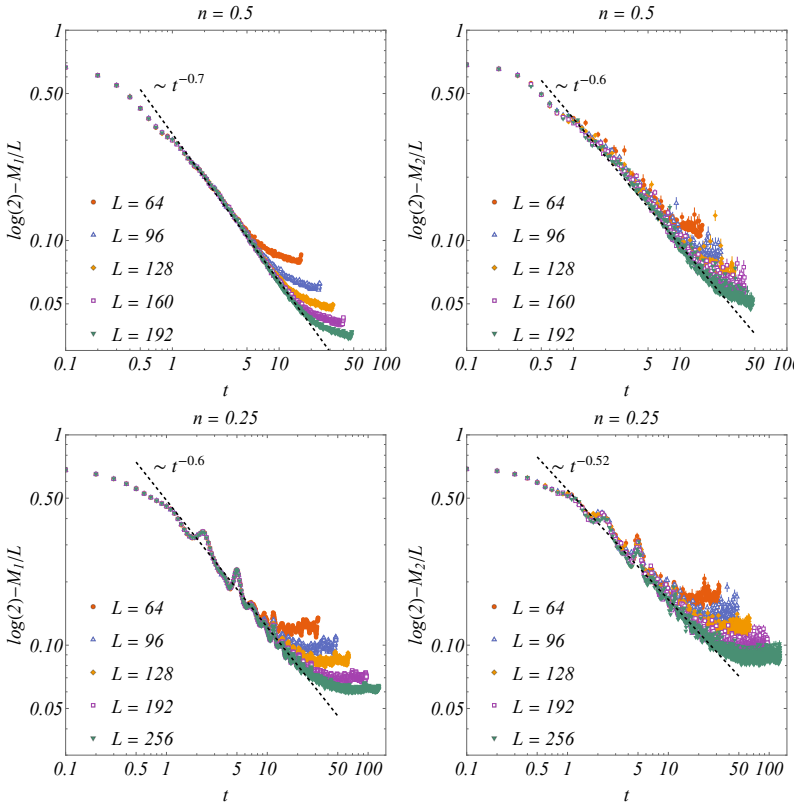

Figure 6.4: Time evolution of the SRE density approaching its thermodynamic limit for quenches with the Hopping Hamiltonian. The log-log plot highlights the thermodynamic scaling regime for times $t < t^*(L)$, where finite-size effects are negligible. The dashed line indicates the algebraic decay observed in this regime, as discussed in the main text.

operations. As such they preserve the Gaussianity of the problem. Specifically, after introducing a rate γ, we implement the monitoring protocol as in Ref. [57]: for each site j, we perform a measurement of $\hat{n}_j$ with probability γdt. If a measurement occurs, the outcome $n = 0, 1$ is drawn randomly according to the Born-rule probabilities. We restrict our analysis to the half-filling sector with particle density $n = 1/2$ where the system is initialized in the Néel state.

For each value of the system size L and measurement rate γ, we have collected $N_{\text{traj}} = 500$ independent quantum trajectories, each corresponding to a distinct random realization of local projective measurements. For each trajectory, the stabilizer Rényi entropies are evaluated via perfect sampling, using at least $\mathcal{S} \in [1000, 2000]$ configurations of Majorana string operators depending on the system size.

Our first analysis focuses on the impact of a finite measurement rate on the time-dependent behavior of the SREs. In particular, Fig. 6.5 illustrates the dynamics of non-stabilizerness for system sizes $L = 16, 32, 64, 128$ and for some representative values of the measurement rate $\gamma \in [0, 1]$. As expected, once the SREs are rescaled to their extensive component (i.e., plotting their density) the overall qualitative behavior remains robust across different measurement regimes. The relaxation towards the stationary value appears to retain an algebraic character, at least qualitatively.

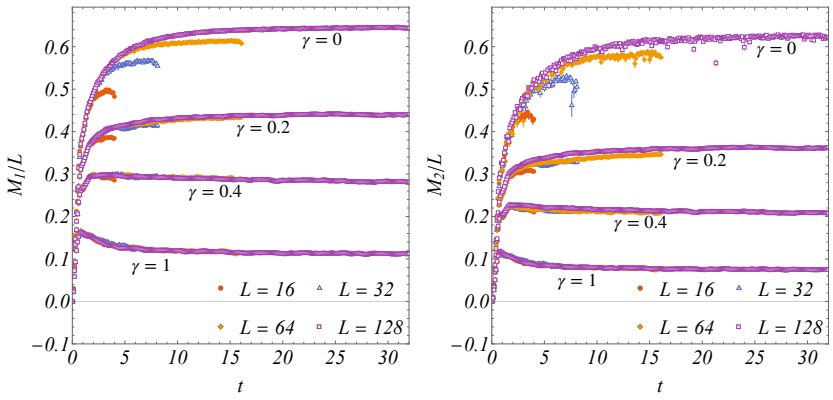

Figure 6.5: Time evolution of the SRE densities M_1/L (left panel) and M_2/L (right panel) under unitary free-fermionic dynamics interspersed with local projective measurements performed at various rates γ. The system is initialized in the Néel state at half filling ($n = 1/2$), and averages are taken over $N_{\text{traj}} = 500$ independent quantum trajectories. The rescaled entropies exhibit an overall extensive behavior, with finite-size corrections becoming increasingly suppressed as the measurement rate γ increases.

What is particularly notable is the behavior of the subleading finite-size corrections, visible as deviations from the thermodynamic-limit curves. These are more pronounced for small values of γ, but decrease and eventually become negligible as the measurement rate increases. This suggests that larger measurement rates suppress the features associated with finite-size effects, promoting faster convergence to the thermodynamic limit.

To characterize more accurately the leading behavior of non-stabilizerness in the stationary regime, we follow an approach analogous to that used in the case of purely unitary dynamics. Specifically, we compute the time average of the SREs over a suitable late-time window, and then analyze the scaling of these averaged values as a function of the total system size L.

The raw time-averaged data are shown in the left panels of Fig. 6.6, plotted as a function of the system size for several representative values of the measurement rate γ. The same data are displayed in the right panels as a function of γ, for various fixed system sizes. To extract the leading extensive contribution, we perform a linear fit in the range $L \in [16, 128]$. The resulting slope, which corresponds to the density of non-stabilizerness, is indicated by a solid black line in the right panels of Fig. 6.6.

Our results confirm that the extensive behavior of non-stabilizerness persists under projective measurements and evolves smoothly as a function of the measurement rate γ. Notably, no abrupt transition is observed in this scaling behavior, suggesting a continuous crossover rather than a sharp dynamical phase transition.

On the contrary, as already hinted at the level of the time-dependent data, and in line with recent observations on canonical participation entropies [61], the stationary quantum magic appears to exhibit an abrupt transition in its subleading corrections (here logarithmic), rather than in its leading extensive behavior. To further investi-

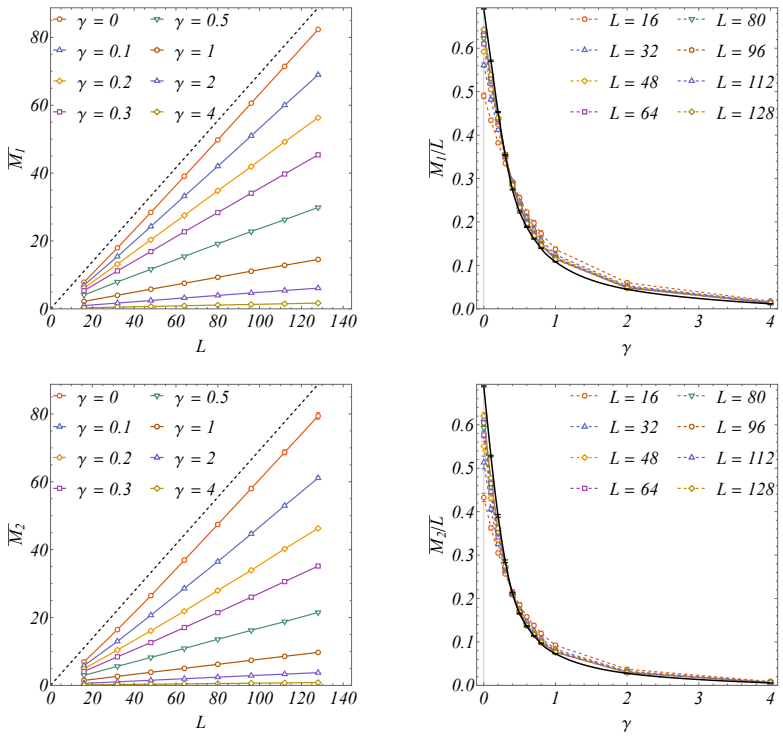

Figure 6.6: Scaling of the SRE densities M_1/L and M_2/L in the stationary regime for various values of the measurement rate γ. In each panel, the data points represent time-averaged values obtained from average time series (cfr. Fig. 6.5), computed over a suitable late-time window. **Left panels**. The entropy densities as functions of the system size L, highlighting their extensive scaling behavior (the dashed black line is $L\log(2)$). **Right panels**. The extracted leading coefficients (i.e., slopes from linear fits in $L \in [16, 128]$) as functions of γ (full black lines), demonstrating that the non-stabilizerness density varies smoothly with the measurement rate without exhibiting abrupt transitions.

gate this feature we once again analyze the finite-size difference $\overline{M_\alpha(2L)} - 2\,\overline{M_\alpha(L)}$, as done in the unitary case. We study the behavior of this quantity as a function of the measurement rate γ, shown in Fig. 6.7. From the numerical data, we extract the slope, which corresponds to the coefficient of the logarithmic correction in the thermodynamic limit. Although our system sizes are limited to $L \leq 128$, the results allow us to clearly identify a qualitative change in this coefficient as the measurement rate increases beyond a threshold value $\gamma^* \approx 0.4$. Specifically, upon rescaling the finite-size differences by $\log(L)$ and plotting them as a function of γ, the data become statistically compatible with zero above this threshold. This observation strongly indicates that the effect of measurements manifests itself predominantly in the sub-leading corrections to the non-stabilizerness of the monitored non-interacting hopping fermions, with a sharp suppression of the logarithmic contribution once $\gamma \gtrsim \gamma^*$.

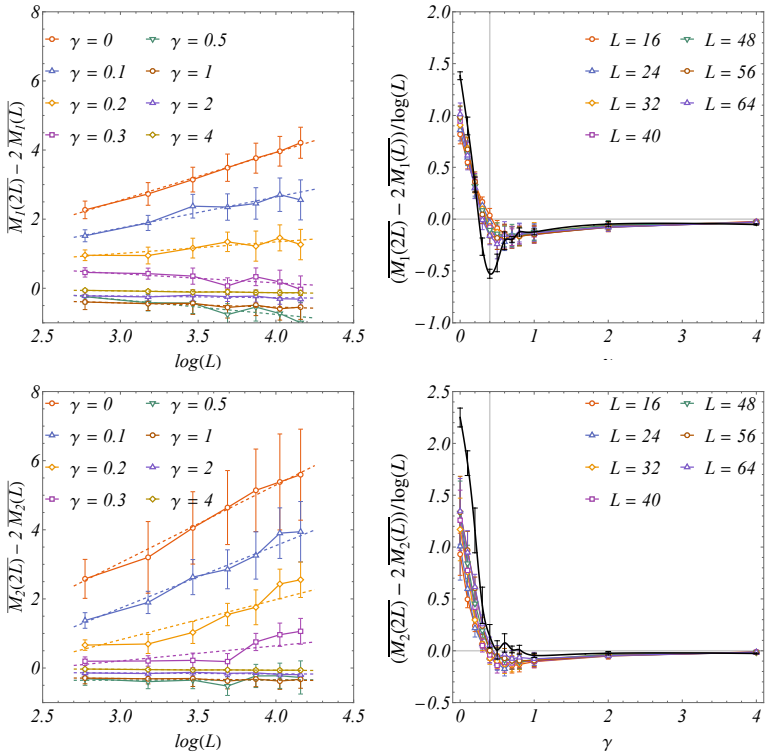

Figure 6.7: **Left panels**. Finite-size difference $\overline{M_\alpha(2L)} - 2\,\overline{M_\alpha(L)}$ as a function of $\log(L)$ for various values of the measurement rate γ. Dashed lines indicate the best linear fits, from which the logarithmic coefficients are extracted. **Right panels**. The same data, rescaled by $\log(L)$, are shown as a function of γ. Solid black lines denote the extrapolated values of the coefficient of the logarithmic corrections. Vertical gray lines mark the threshold $\gamma^* \approx 0.4$, above which the numerical data become statistically compatible with zero within 2σ.

6.2 Non-stabilizerness of the Quantum Ising chain

The second scenario we consider consists of a transverse field Ising model with periodic boundary conditions, given by

$$\hat{H} = -\sum_{j=0}^{L-1} \left(\hat{\sigma}_j^x \hat{\sigma}_{j+1}^x + h\, \hat{\sigma}_j^z \right). \tag{6.3}$$

As discussed in Sec. 1.2.1, the model can be exactly mapped to a system of free fermions through the Jordan-Wigner transformation, and further reformulated in terms of Majorana fermions. The dynamics is thus Gaussian and fully encoded by the Majorana covariance matrix.

We initialize the system in a fully polarized state along the z-direction $|\uparrow \dots \uparrow\rangle$, which in the fermionic language represents the vacuum state $|00\dots\rangle$, or in the Néel state $|\uparrow\downarrow\uparrow\downarrow\dots\rangle$ which corresponds to $|0101\dots\rangle$. Both initial states are Gaussian. As for the case of hopping fermions, we start our analysis from the case of plain unitary dynamics. We then proceed to investigate magic in the no-click limit discussed in Sec. 3.2.

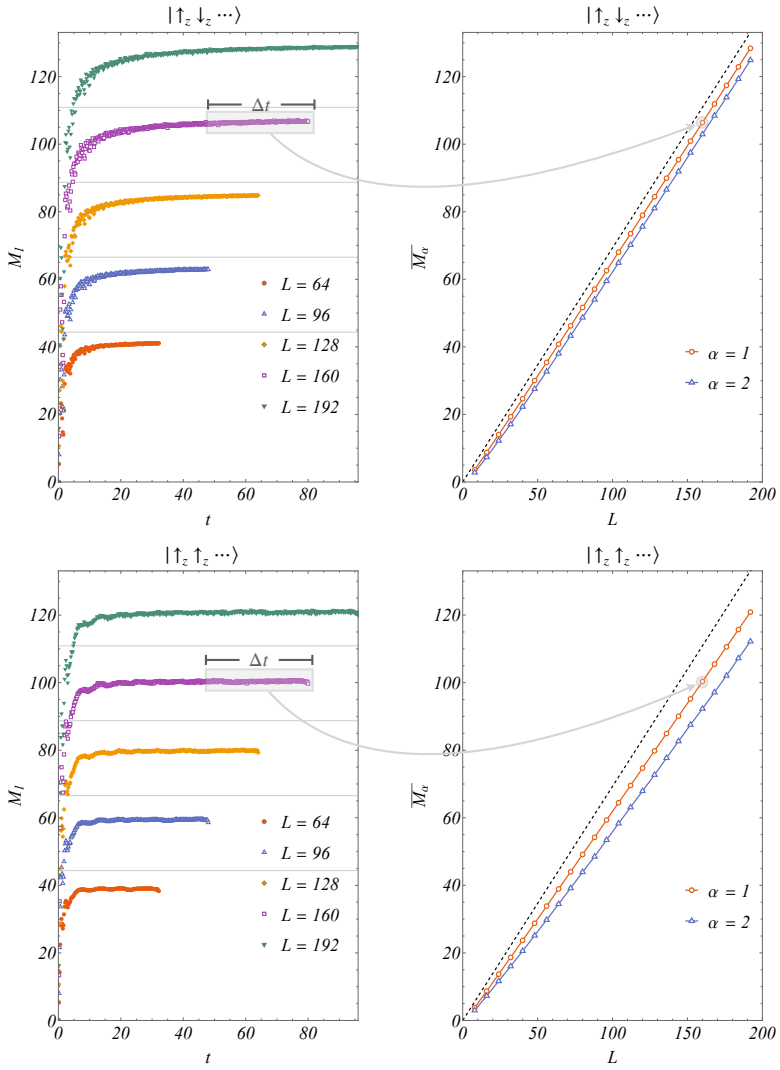

Figure 6.8: **Left panels**. Plain time evolution (no measurement) under the Ising Hamiltonian with $h = 0.5$ in Eq. (6.3) of the stabilizer Renyi entropy M_1 after having initialized the system in the Néel state (top), or in the fully polarized state (bottom). Each point has been obtained by averaging over $\mathcal{S} \in [1000, 24000]$ sample of Pauli strings, depending on the system size. Gray horizontal lines correspond to $L \log 2$. **Right panels**. Extensive behavior of the stationary stabilizer entropies averaged over a time window $\Delta t = [L/4, L/2]$. The dashed line corresponds to $L \log 2$.

6.2.1 Plain dynamics

Here we consider a quench dynamics generated by the Ising chain deeply within its ferromagnetic phase; specifically, we choose $h = 0.5$. In this setting, no trajectory averaging is involved, as no stochastic measurement events occur.

Also here, the SREs M_α increase over time and eventually saturate to stationary values that scale linearly with the system size. The numerical data exhibit fluctuations arising from the probabilistic nature of the computation, as the SREs are estimated via sampling. In particular, the averages are taken over $\mathcal{S} \in [1000, 24000]$ Majorana string configurations, depending on the system size.

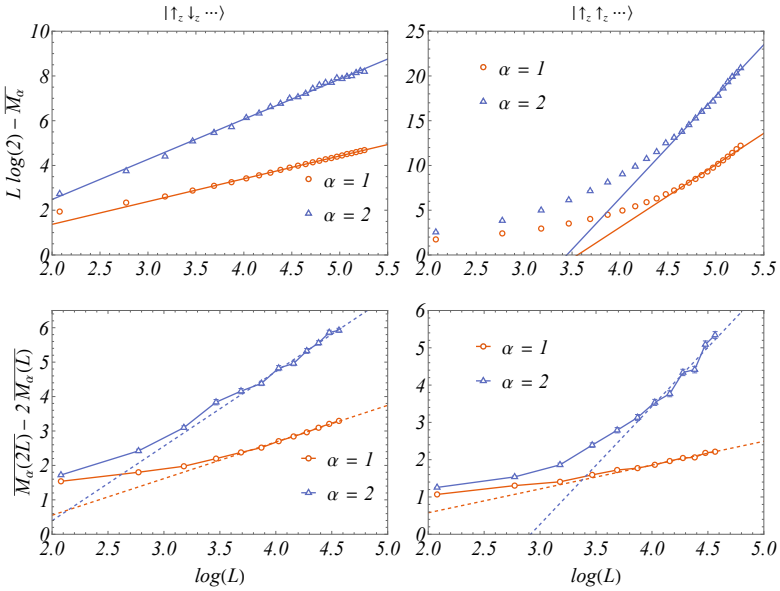

Figure 6.9: **Top panels**. Late-time SREs induced by a quench dynamics (without measurements) in the Ising Hamiltonian with $h = 0.5$, starting from the Néel and the vacuum initial states, after having subtracted the Haar average $L \log 2$. **Bottom panels**. Logarithmic corrections to the non-stabilizerness, obtained via finite-size analysis (see main text for details).

In Figure 6.8, we present representative time-series data for the SRE with index $\alpha = 1$. After averaging the data over a suitable late-time window, we extract the leading extensive behavior as a function of system size. When the dynamics starts from the Néel state, the stationary values approach the expected Haar limit $L \log 2$ at leading order, with subleading deviations similar to those observed in Fig. 6.1. Conversely, when starting from the vacuum state the system appears to equilibrate more rapidly in time. However, the subleading corrections to the extensive scaling can be more pronounced in this case, indicating that larger system sizes are necessary to unambiguously observe convergence toward the Haar average.

Subleading logarithmic corrections – Since we expect that $\overline{M_\alpha(L)} \sim a_\alpha L - b_\alpha \log L - c_\alpha$ also in this setup, as found for hopping fermions, we analyze the subleading logarithmic behavior. To this end, we subtract the maximal Haar value from the stationary SREs and plot the residuals on a logarithmic scale. The results reveal a strikingly clean logarithmic correction to the leading term in the case of the Néel state (Figure 6.9). In contrast, the results for the vacuum initial state display deviations from the expected Haar-like behavior. Given the absence of $U(1)$ symmetry, one might anticipate that the leading extensive scaling of the SREs follows the Haar form. However, significant finite-size effects are present: as shown in Fig. 6.8, the curves only begin to exhibit a parallel trend with the Haar prediction for very large system sizes. While this suggests a possible convergence toward the Haar slope, we cannot exclude the possibility that the true extensive coefficient in the thermodynamic limit differs from the Haar value.

To further probe this subleading structure, we once again examine the finite-size difference $\overline{M_\alpha(2L)} - 2\,\overline{M_\alpha(L)}$ to isolate possible logarithmic terms. The results are

displayed in the bottom panels of Figure 6.9. This refined analysis enables us to extract the logarithmic coefficients, whose best-fit estimates yield

$$\begin{aligned} \text{Néel state:} \quad & b_1 = 1.06(3),\ b_2 = 2.17(11), \\ \text{Vacuum state:} \quad & b_1 = 0.64(3),\ b_2 = 3.16(26)\ . \end{aligned}$$

Also in this case, the logarithmic corrections exhibit a clear dependence on the Rényi index α. Moreover, we observe a residual dependence on the choice of the initial state. Although such dependence might seem unexpected since we are probing the stationary properties of non-stabilizerness as a function of system size, and no explicit symmetry constraints the dynamics, this behavior can be attributed to finite-time effects and to the structure of the integrals of motion. Indeed, while the model lacks a $U(1)$ conservation law, it remains integrable, and the dynamics are tightly constrained by a complete set of conserved quantities. These are fixed by the initial conditions and differ substantially between the Néel and vacuum states. Consequently, the time-evolved stationary state inherits nontrivial signatures of the initial state. As already mentioned, the convergence behavior differs between the two preparations, and this may underlie the observed discrepancies in the subleading scaling corrections.

Temporal dependence – For any finite system size L, we have seen that the stationary values of the SREs display logarithmic corrections to the leading extensive behavior. This naturally prompts the question of how the SREs dynamically approach this asymptotic form at large times. Consistent with earlier findings from both random circuit dynamics and Gaussian evolutions [213, 354], the finite-size convergence to stationarity can follow an exponential decay.

Although we have observed that the dynamics from the vacuum state tend to approach their finite-size stationary values more rapidly, obtaining sufficiently accurate and converged results in that case would require higher precision and significantly longer simulations fro larger system sizes. For this reason, in the following time-dependent analysis, we only focus on the Néel initial state, where the stationary leading extensive behavior can be reliably inferred to follow $\overline{M}_\alpha \sim L \log(2)$.

To examine this, we analyze the difference between the time-dependent SREs and their best-fit stationary values, normalized by the system size, namely $(\overline{M_\alpha(L)} - M_\alpha(t, L))/L$ (see Fig. 6.10). The stationary values are extracted from fits accounting for extensive ($\sim L$), logarithmic ($\sim \log L$), and decaying corrections ($\sim L^{-1}$). The data show a clear exponential approach to the finite-size stationary values, confirming that the $t \to \infty$ limit is taken before the thermodynamic one.

However, as L increases, the curves progressively bend on a log-linear scale and begin to collapse in the early-time regime. This marks the onset of a different universal behavior associated with the thermodynamic limit, where $1 \ll t \ll L$. This transition in scaling is particularly visible for the case $\alpha = 1$.

6.2.2 No-click limit

We extend our analysis to the no-click limit of the quantum jump equation of Eq. 3.3. As explained in Sec. 3.2, this corresponds to a postselected realization of a weak monitoring protocol in which the dynamics is effectively ruled by a non-Hermitian

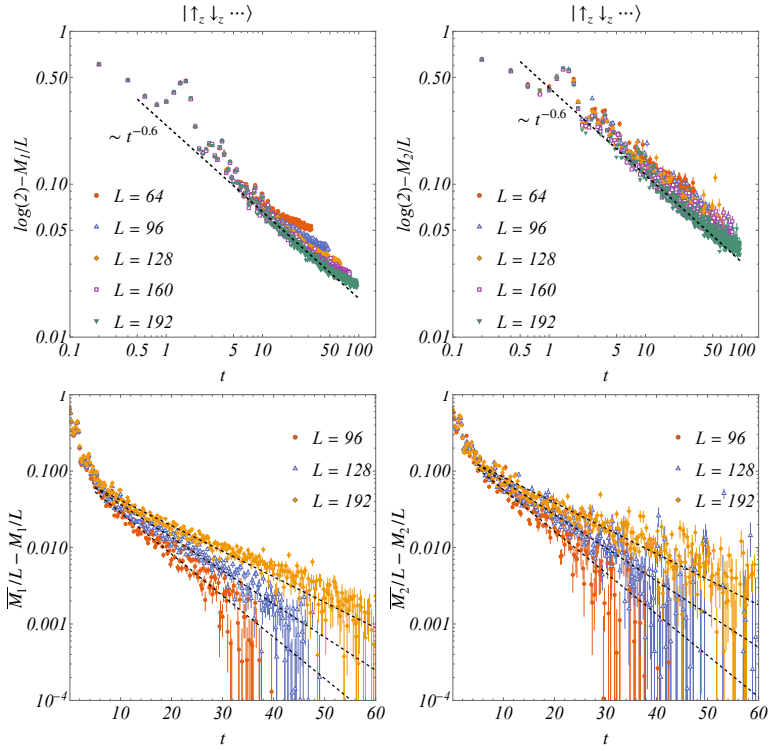

Figure 6.10: Time evolution of the SRE density approaching its thermodynamic limit after quenching the Néel state with the Ising Hamiltonian at $h = 0.5$. **Top panels**. The log-log plot highlights the thermodynamic scaling regime for times $t < t^*(L)$, where finite-size effects are negligible. The dashed line indicates the algebraic decay observed in this regime, as discussed in the main text. **Bottom panels**. Here, the log-linear plot highlights the exponential decay of the finite-size system towards its best-fit stationary values, given by $\overline{M_\alpha(L)} \sim a_\alpha L - b_\alpha \log L - c_\alpha$. The dashed lines represent size-dependent exponential fits, shown as guides to the eye.

Hamiltonian. This deterministic non-unitary evolution offers a complementary perspective to the projective measurement framework. For simplicity, in the following we consider the non-Hermitian quantum Ising Hamiltonian with no real transverse field ($h = 0$)

$$\hat{H}_{\text{eff}} = -\sum_{j=1}^{L-1} \hat{\sigma}_j^x \hat{\sigma}_{j+1}^x + i\frac{\gamma}{4} \sum_j \hat{\sigma}_j^z, \tag{6.4}$$

using open boundary conditions.

As in the case of hopping fermions, we consider both the fully polarized state $|\uparrow \ldots \uparrow\rangle$ and the Néel state $|\uparrow\downarrow\uparrow\downarrow \ldots\rangle$, and investigate how varying measurement rates γ impact the complexity of the system. For the numerical calculations, we implement the evolution generated by Eq. 6.4 using large-scale matrix-product state simulations, and non-stabilizerness is evaluated using the perfect sampling algorithm of Refs. [84, 349].

Figures 6.11 and 6.12 show the time evolution of the SRE M_1, respectively for the initial polarized state (Fig. 6.11) and for the Néel state (Fig. 6.12). Both fig-

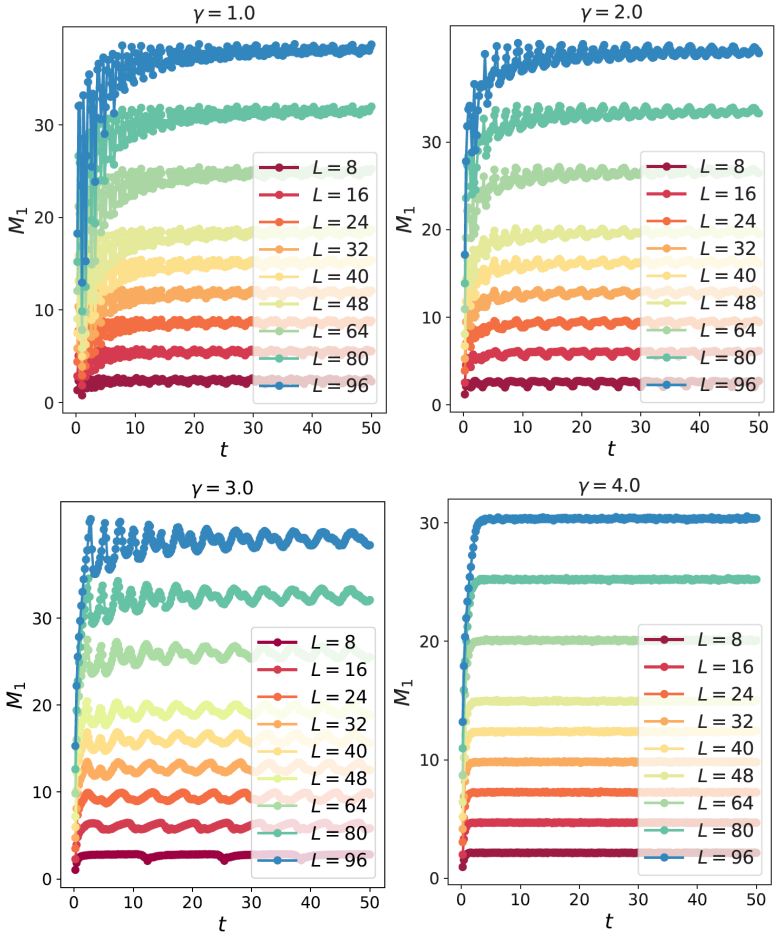

Figure 6.11: Time evolution of the SRE M_1 under non-unitary free-fermionic dynamics for different value of γ. The system is initialized in a fully polarized state $|\uparrow \ldots \uparrow\rangle$. The entropy M_1 exhibits a dependence on L for small and big values of γ.

ures clearly illustrate that, across different measurement rates γ, the SRE densities exhibit nontrivial size-dependent dynamics. For low measurement rates, the complexity growth is robust, saturating towards extensive stationary values. However, as γ increases, the measurements dominate, suppressing the overall complexity and reducing finite-size effects. These dynamics clearly demonstrate the intricate interplay between unitary complexity generation and measurement-induced complexity suppression.

In Figure 6.13, we investigate the relaxation dynamics by considering the deviation from stationary values $\Delta M_\alpha(t, L) = \overline{M_\alpha}(L) - M_\alpha(t, L)$ in a log-log scale. For all considered values of γ, an exponentially decay $e^{-\beta t}$ is observed, characterized by different decay exponents dependent on the measurement strength. This behavior highlights that the measurement-induced dynamics not only suppress stationary complexity but also alter relaxation rates.

Figure 6.14 summarizes the stationary regime by displaying the SRE entropies $\overline{M_1}$ and $\overline{M_2}$ as functions of system size L and measurement rate γ. Here the system is initialized in a fully polarized state $|\uparrow \ldots \uparrow\rangle$. For small but finite values of γ,

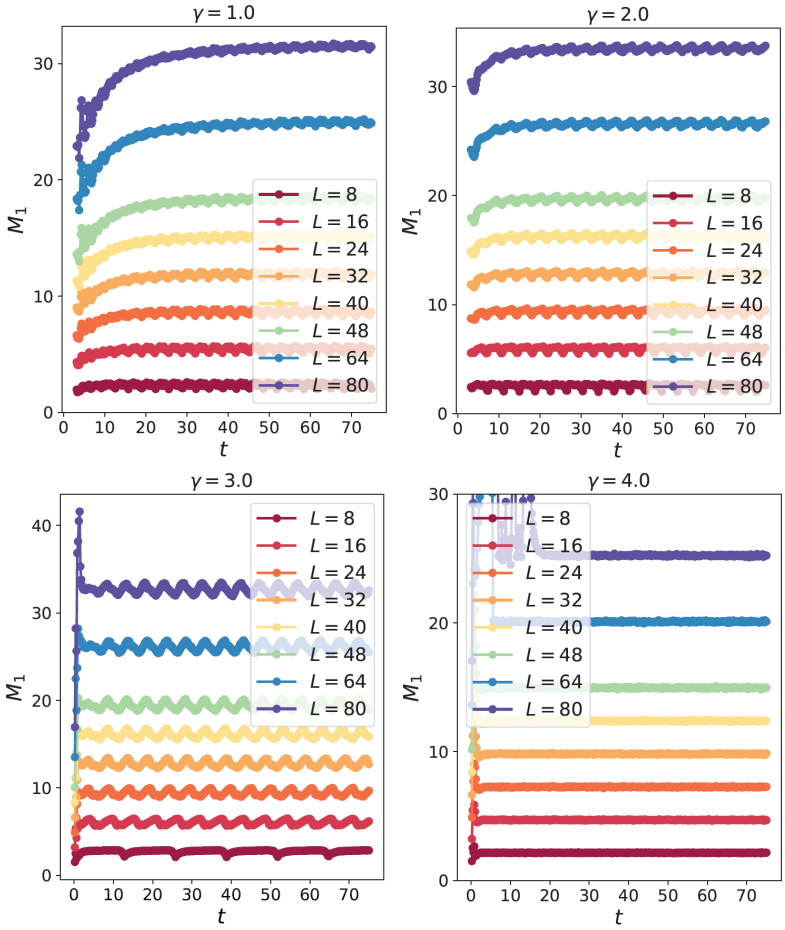

Figure 6.12: Time evolution of the SRE M_1 under no-click dynamics for different value of γ. The system is initialized in the Néel state $|\uparrow\downarrow\uparrow\downarrow\ldots\rangle$. The entropy M_1 exhibits a dependence on L for small and big values of γ.

the extensive coefficient of the SRE rises sharply, signaling a rapid enhancement in magic production. This is consistent with the fact that, in the absence of monitoring ($\gamma = 0$), the dynamics are governed by the classical Ising Hamiltonian and no transverse field. Although this Hamiltonian is non-diagonal in the computational basis, it generates trivial, non-entangling dynamics from product states and produces limited magic. Turning on γ introduces an effective imaginary transverse field via the no-click evolution, rendering the dynamics nontrivial and enabling efficient magic generation. However, as γ increases further, the effect of strong measurements in the Pauli basis dominates, progressively collapsing the wavefunction and thereby suppressing the generation of non-stabilizerness (right panels of Fig. 6.14). This results in a reduced magic density and a weakened dependence on system size in the stationary regime. Notably, this suppression is continuous, with no abrupt transitions in the leading extensive terms; instead, we observe a smooth crossover. Moreover, in the left panels of Fig. 6.14, we show the raw time-averaged data for different values of γ, demonstrating the extensive behavior of non-stabilizerness.

In contrast, as highlighted by the finite-size scaling analysis for the previous cases, the subleading logarithmic corrections exhibit sharp transitions at critical

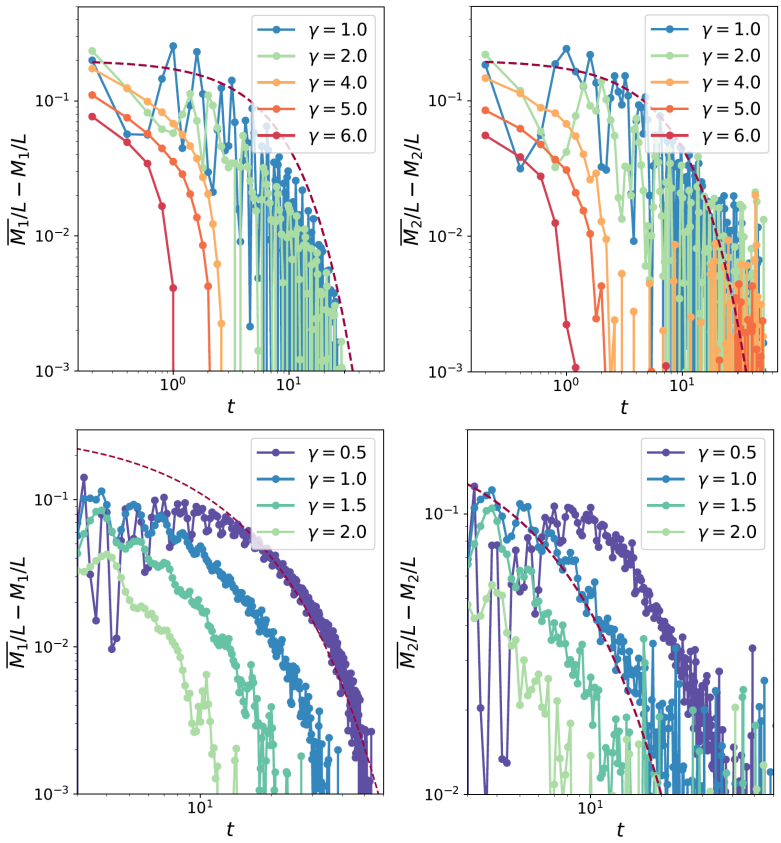

Figure 6.13: Log-log plot of the relaxation dynamics of the SREs M_1 and M_2 after having subtracted the best-fit finite-size stationary values $\overline{M_\alpha}(L)$. **Upper panels** correspond to quenches from the vacuum initial state, while **lower panels** show the results for quenches from the Néel initial state. In all cases, dashed lines indicate exponential decays $e^{-\beta t}$ drawn as guides to the eye.

measurement rates. This behavior signals subtle yet robust measurement-induced complexity transitions. To explore this further, we turn to a detailed analysis of the subleading scaling behavior under non-Hermitian evolution in the no-click limit, since we expect that, also in this monitored setup, the stationary SREs exhibit logarithmic corrections of the form $\overline{M}_\alpha = a_\alpha L - b_\alpha \log L - c_\alpha$. To probe this subleading structure, we again analyze the finite-size difference $\overline{M}_\alpha(2L) - 2\overline{M}_\alpha(L)$.

Figure 6.15 provides a detailed analysis of the subleading logarithmic corrections to the SRE for different measurement rate γ, comparing the vacuum (left panels) and Néel (right panels) initial states. Both panels show the finite-size differences plotted against L, clearly showing a $\log L$ dependence, for small measurement rates. This is strong evidence of persistent logarithmic corrections to the stationary non-stabilizerness in the weakly monitored regime. Crucially, as the measurement rate γ increases, the slope of these curves systematically decreases, signaling a suppression of logarithmic corrections. For both vacuum and Néel initial states, data show that the subleading logarithmic term vanishes sharply beyond a threshold measurement rate $\gamma > 3$, indicating an abrupt measurement-induced transition in the subleading scaling structure of complexity.

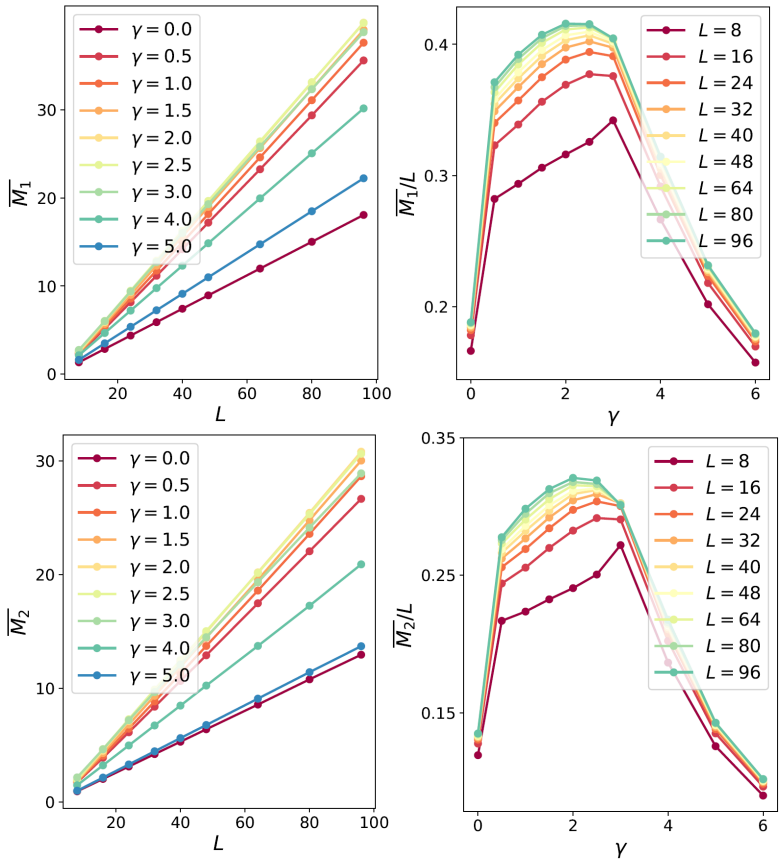

Figure 6.14: Scaling of the SRE densities $\overline{M_1}$ and $\overline{M_2}$ in the stationary regime for various values of γ. The system is initialized in a fully polarized state $|\uparrow \ldots \uparrow\rangle$. In each panel, the data points represent time-averaged values over a suitable late-time window. **Left panels**. The entropy densities as functions of the system size L, highlighting their extensive scaling behavior. **Right panels**. The extracted leading coefficients (i.e., slopes from linear fits in $L \in [8, 96]$) as functions of γ, demonstrating that the non-stabilizerness density varies smoothly with the measurement rate without exhibiting abrupt transitions.

6.3 Conclusions

We have investigated the dynamics of SREs as measures of quantum complexity in Gaussian fermionic systems. Our focus is on two paradigmatic free-fermionic models, namely, hopping fermions and the transverse-field Ising model. In both cases, unitary dynamics leads to a volume-law saturation of SREs. Behind this leading-order behavior, magic exhibits negative logarithmic corrections that depend on the symmetry of the model and on the initial state chosen. Such subleading terms appear to be characteristic of Gaussian states.

In the monitored case, our numerical results for hopping fermions indicate the existence of a MIPT in these logarithmic corrections, which vanish above a critical measurement rate. This is unexpected, as the conventionally-studied entanglement entropy does not exhibit any transition. This signals a subtle change in the scaling of

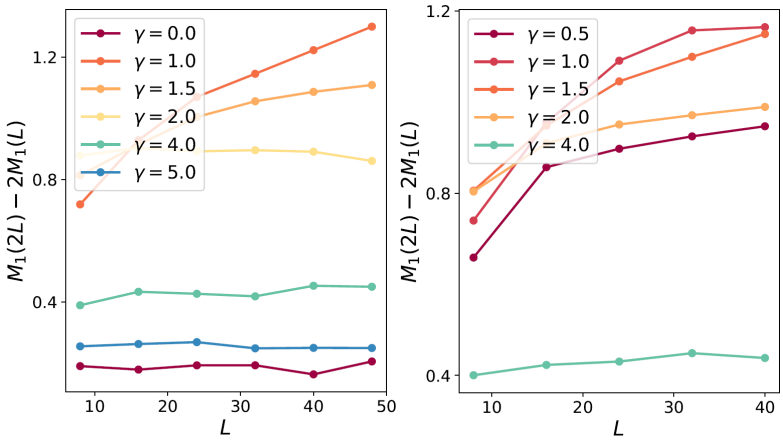

Figure 6.15: Finite-size analysis of the corrections to stationary SREs under non-Hermitian Hamiltonian evolution (no-click limit), contrasting vacuum (left panel), and Néel (right panel) initial states. Both panels show the finite-size difference $\overline{M}_1(2L) - 2\overline{M}_1(L)$ as a function of system size L, for different measurement rates γ. At small γ, data show a clear logarithmic growth with L, indicating robust logarithmic corrections to complexity. For $\gamma > 3$ the finite-size difference becomes independent of L, signaling the disappearance of logarithmic corrections and thus a simplification of the complexity structure.

complexity, demonstrating that in general monitoring can affect non-stabilizerness in ways that go beyond entanglement transitions alone. Consistent behavior is also observed in the case of the no-click Ising evolution.

Our analysis shows that although the SREs are always extensive at leading order, their full behavior is all but trivial, as manifested by subleading terms. Unfortunately, the numerical character of the present investigations limits the deep understanding of magic in Gaussian dynamics. For this reason, developing analytical frameworks to understand these logarithmic corrections and measurement-induced complexity transitions will be crucial for gaining a complete picture. In addition, it would be interesting to extend this study by doping the free-fermionic dynamics with non-Gaussian resources, providing a controlled framework to investigate the crossover towards Haar-random states.

Chapter 7

Entanglement structure from Gaussian to interacting circuits

Random quantum circuits offer a powerful framework for exploring many-body dynamics, enabling the analysis of the crossover from classically simulable to genuinely complex quantum evolution [50]. Restricting the set of quantum gates, either due to hardware limitations or resource-theoretic constraints, to a specific class can alter quantum dynamics dramatically. For example, as discussed in Chapter 1, both Gaussian and Clifford dynamics exhibit peculiar correlation structures and are unable to reproduce several features of Haar-random states. This chapter aims at clarifying how generic many-body entanglement properties emerge from free-fermionic states upon doping them with non-Gaussian resources [155, 258] that induce interactions. This sheds light on the role of quantum complexity in unlocking genuinely complex behavior, deviating from the class of efficiently simulable many-body systems.

Specifically, we focus on fermionic Gaussian circuits, or matchgates [112–114, 119], and dope them with tunable amounts of non-Gaussian gates. This guarantees control over the complexity of the resulting states, enabling the investigation of a gradual crossover from simple to complex regimes. The task presents an immediate theoretical difficulty: studying truly complex quantum dynamics is intrinsically hard, both analytically and in numerics. In order to make the problem tractable, we further constrain all gates considered to be Clifford, allowing us to perform efficient simulations. In other words, we explore the impact of non-Gaussianity on entanglement dynamics restricted to the set of stabilizer states.

In unitary dynamics, random matchgate circuits are known to exhibit diffusive entanglement growth $S_A(t) \sim \sqrt{t}$, in sharp contrast to the usual ballistic behavior $S_A(t) \sim t$ of generic models. As our first question, we investigate how injecting non-Gaussianity induces a crossover between these regimes. We highlight that an extensive total number of non-Gaussian gates is required to recover the conventional linear increase. In parallel, the fluctuations of entanglement gradually approach the Kardar-Parisi-Zhang (KPZ) scaling expected in generic random circuits.

We then shift our focus to monitored dynamics. As discussed in Sec. 2.2.2, the measurement-induced phase transition (MIPT) of free-fermionic systems is atypical, as it features a logarithmic entanglement phase rather than a volume-law one (in absence of $U(1)$ symmetry). We analyze how the scaling behavior of the entanglement entropy in this phase is affected by the introduction of non-Gaussianity. Depending on the complexity injection rate, we observe a power-law phase $S_\ell \sim \ell^\alpha$ (ℓ being the subsystem size), which eventually converges to the standard volume law with $\alpha = 1$ when an extensive number of non-Gaussian resources per circuit layer is used.

In both unitary and monitored cases, the fully Gaussian limit can be studied analytically through an exact mapping to a classical statistical model. This reveals exact results and fundamental insights on why free-fermionic systems behave differently from interacting ones.

The rest of this chapter is structured as follows. In Sec. 7.1 we introduce the general circuit model we consider. Then, Sec. 7.2 presents our results for doped unitary circuits, whereas Sec. 7.3 covers the monitored case. Finally, in Sec. 7.4 we discuss and summarize our findings.

7.1 Clifford matchgates and non-Gaussian doping

We now introduce the circuit model we study, realized with fermionic Gaussian and non-Gaussian gates. In our implementation, we constrain all unitaries to also belong to the Clifford group. This enables the efficient simulation of the problem, allowing us to explore how non-Gaussianity affects entanglement at very large system sizes. The dynamics of entanglement in Gaussian-Clifford circuits can be mapped exactly to a classical statistical model, enabling an analytical description of the evolution

7.1.1 Doped matchgate circuits

Given a system of N qubits, let $\mathcal{P}_N = \{\hat{\mathbb{1}}, \hat{\sigma}^x, \hat{\sigma}^y, \hat{\sigma}^z\}^{\otimes N}$ be the set of Pauli strings. Using the Jordan-Wigner mapping introduced in Sec. 1.2.1, we define the $2N$ Majorana operators $\hat{\gamma}_{2j-1} = \hat{\sigma}_1^z \cdots \hat{\sigma}_{j-1}^z \hat{\sigma}_j^x$, $\hat{\gamma}_{2j} = \hat{\sigma}_1^z \cdots \hat{\sigma}_{j-1}^z \hat{\sigma}_j^y$, satisfying the canonical anticommutation relations $\{\hat{\gamma}_\mu, \hat{\gamma}_\nu\} = 2\delta_{\mu\nu}$ [116, 117]. We consider the group $\mathcal{G}_N$ of Gaussian operations, containing all matchgates $\hat{U}$ that act linearly on Majorana operators, such as $\hat{U}^\dagger \hat{\gamma}_\mu \hat{U} = \sum_\nu Q_{\mu,\nu} \hat{\gamma}_\nu$ for a certain orthogonal transformation $Q \in \mathrm{SO}(2N)$. When acting on $|0\rangle^{\otimes N}$, these gates generate the fermionic Gaussian states [116, 117], which are completely characterized by their Majorana covariance matrix (see Sec. 1.2.2).

Matchgate circuits are not universal for quantum computation, as they lack the crucial resource given by non-Gaussianity [197]. This may be introduced either through the injection of specially prepared fermionic magic states [356], or by enabling operations beyond the matchgate framework, which act non-linearly on Majorana operators and effectively induce fermionic interactions [258] [1]. As a result, non-Gaussian unitaries enable entanglement structures and computational complexity that are fundamentally inaccessible to purely Gaussian dynamics.

For practical convenience, we constrain all gates (whether Gaussian or not) to lie within the Clifford group $\mathcal{C}_N$, the set of unitaries that map the Pauli group $\mathcal{P}_N$ onto itself up to phases. As detailed in Sec. 1.3.1, Clifford circuits generate stabilizer states $|\psi\rangle$, which are uniquely defined by N independent and commuting generators $\hat{g}_j \in \mathcal{P}_N$ satisfying $\hat{g}_j |\psi\rangle = \pm |\psi\rangle$ [2]. This structure enables efficient

[1] This closely parallels the role of non-stabilizer "magic states" or gates in promoting Clifford circuits to full quantum universality.

[2] For later convenience, throughout this chapter the generators are defined without the sign $\pm$. This is a slight difference compared to the discussion of Sec. 1.3.1, which however bears no

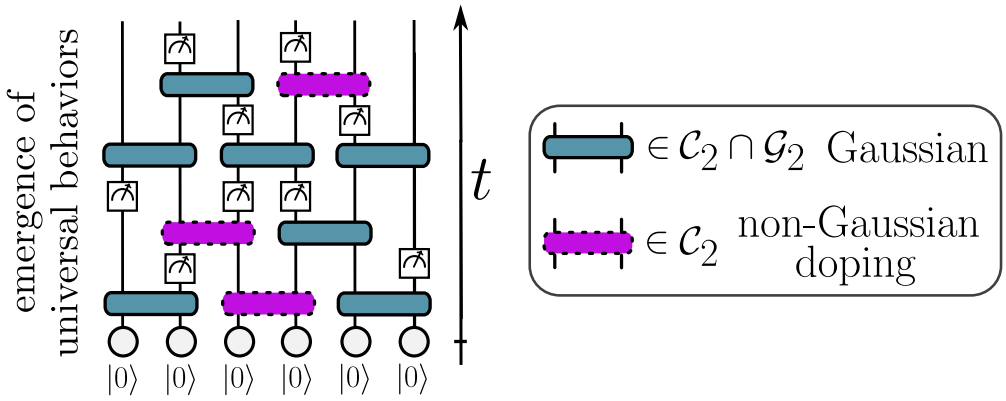

Figure 7.1: Schematic of the monitored circuits studied in this work, alternating layers of two-qubit gates and single-qubit projective measurements. Gates are either Gaussian (teal) or non-Gaussian (dotted purple), both drawn from the Clifford group. By tuning the density of non-Gaussian gates, we probe the onset of universal behavior beyond the free-fermionic limit.

classical simulation, allowing us to probe both Gaussian and non-Gaussian dynamics for system sizes of several hundred qubits. Hence, all numerical simulations in this chapter are performed using the stabilizer formalism [157, 357].

While the Clifford restriction might appear limiting, it is important to note that many non-linear properties closely mirror those of Haar-random circuits. In detail, the Clifford group $\mathcal{C}_N$ forms a unitary 3-design [358, 359] for the Haar ensemble [360], meaning that random unitaries sampled from these sets give rise to equal expectation values of observables acting on at most three replicas of the system. Similarly, the *Clifford-Gaussian* set $\mathcal{CG}_N = \mathcal{C}_N \cap \mathcal{G}_N$ forms a 3-design for $\mathcal{G}_N$ [361, 362]. Clifford circuits therefore provide a controlled framework to approximate the entanglement and dynamical properties of Gaussian and non-Gaussian states.

Figure 7.1 illustrates our setup: a system initialized in the vacuum $|\psi_0\rangle = |0\rangle^{\otimes N}$ evolves under a brickwall circuit composed of alternating layers of two-qubit gates and local measurements in the computational basis. In the latter, every qubit is measured in the computational basis with probability p, and left untouched with probability $1-p$. In the unitary layer, each gate U is drawn uniformly from $\mathcal{C}_2$ with probability q, and from the Gaussian matchgates $\mathcal{CG}_2$ with probability $1-q$. The resulting number of non-Gaussian gates per layer scales as $O(qN)$. By setting $q = \eta/N^\beta$, we enable control over this scaling: the number of non-Gaussian gates per layer is extensive for $\beta = 0$, sub-extensive for $0 < \beta < 1$, and intensive for $\beta = 1$. The quantity we focus in is the bipartite entanglement entropy $S_\ell = -\mathrm{Tr}(\rho_\ell \log_2 \rho_\ell)$ [3], where ρ_ℓ is the reduced density matrix for a subsystem $A = \{1, \ldots, \ell\}$.

implications.

[3] Notice that the entropy is defined using the base-2 logarithm throughout this chapter.

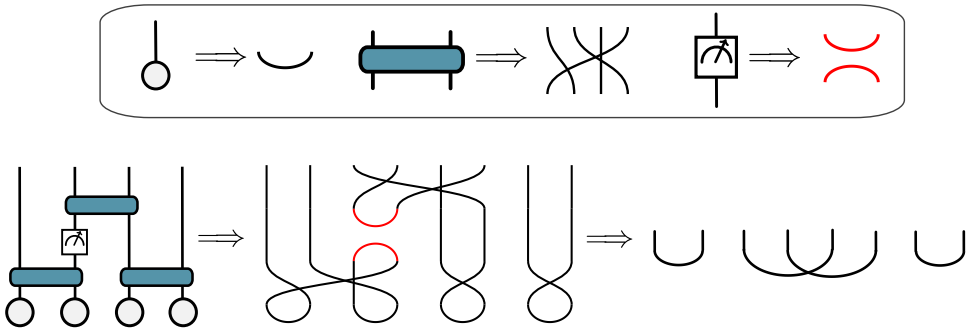

Figure 7.2: Sketch of the graphical representation of different circuit components in terms of the arc model. On the second line, we present an example applied to a given circuit configuration.

7.1.2 Mapping to an arc model

We note that any Clifford-Gaussian transformation $U \in \mathcal{CG}_N$ acts as a signed permutation $U^\dagger \hat{\gamma}_\mu U = \pm \hat{\gamma}_{\sigma(\mu)}$ on Majorana operators, where $\sigma \in S_{2N}$ is a permutation of $2N$ elements [4]. As we show below, this enables an exact mapping of the problem to a classical model of arcs that encodes all information on entanglement.

The initial state of the dynamics $|0\rangle^{\otimes N}$ is stabilized by the operators $\hat{g}_j = \hat{\sigma}^z_j = -i\hat{\gamma}_{2j-1}\hat{\gamma}_{2j}$, which we represent as a collection of arcs connecting adjacent "Majorana points" $(2j, 2j+1)$ along a $2N$-site chain. As observed above, Gaussian matchgates permute Majorana operators as $\hat{U}^\dagger \hat{g}_j \hat{U} = -i\hat{\gamma}_{\sigma(2j)}\hat{\gamma}_{\sigma(2j+1)}$, which amounts to permuting arc endpoints. These rules are illustrated in Fig. 7.2, together with an example showing how a circuit can be unrolled into an arc configuration.

Measurements of $\hat{\sigma}^z_j$ have a simple graphical representation as well. Consider the action of a computational basis measurement on the stabilizers generators. If $|\psi\rangle$ is stabilized by $i\hat{\gamma}_{2j-1}\hat{\gamma}_m$ and $i\hat{\gamma}_{2j}\hat{\gamma}_n$, then a measurement of $\hat{\sigma}^z_j$ replaces these with $i\hat{\gamma}_m\hat{\gamma}_n$ and $i\hat{\gamma}_{2j-1}\hat{\gamma}_{2j}$, regardless of the outcome. This operation "glues" the endpoints $2j-1$ and $2j$ of the original arcs, forming a new arc (m, n) as well as a local arc $(2j-1, 2j)$. Graphically, this rule is shown in Fig. 7.2.

Crucially, although the arc representation ignores the signs of the generators $\hat{g}_j$, it fully encodes the entanglement structure. For any subsystem bipartition in a subsystem A and its complement B, S_A equals half the number of arcs connecting A to B [89, 253]. The proof is simple, and follows from Eqs. (1.52) and (1.53). The entries of the covariance matrix $\Gamma_{\mu,\nu} = \frac{1}{2}\operatorname{Tr}(\hat{\rho}[\hat{\gamma}_\mu, \hat{\gamma}_\nu])$ are all zeros except for the pairs (μ, ν) corresponding to endpoints of an arc, in which case we have $\Gamma_{\mu,\nu} = \pm 1$. Let n be the number of arcs localized in A. It is immediately seen that an equal number n must be fully contained in B. For each arc within A, the matrix Γ_A of Eq. (1.52) will feature a non-zero entry in its upper triangle and a second in the lower one, specular with respect to the diagonal and with opposite sign. Arcs crossing the bipartition or inside B do not contribute to Γ_A. It follows that A will exhibit exactly n eigenvalue pairs $\pm i$, whereas the remaining $2|A| - 2n$ eigenvalues vanish. Then,

[4] Among the $|\mathcal{C}_2| = 11520$ gates, Clifford matchgates are only $|\mathcal{CG}_2| = 192$.

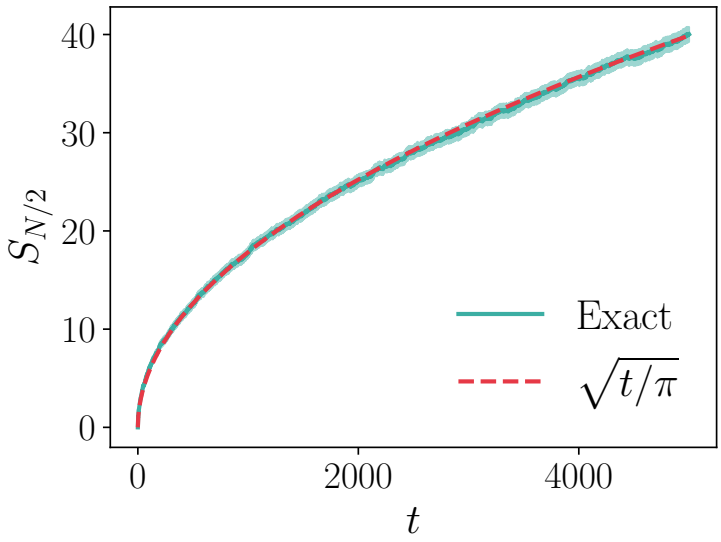

Figure 7.3: Diffusive growth of the entanglement entropy $S_{N/2}(t)$ under Clifford-Gaussian unitary dynamics. Data for $N = 512$, averaged over 200 random circuit realizations. The analytical prediction $S_{N/2}(t) \approx \sqrt{t/\pi}$ matches very well.

Eq. (1.53) yields the base-2 entanglement entropy $S_A = |A| - n$. Recalling that the total number of arcs is $2|A|$ and $2n$ of them do not cross the bipartition, the entropy is given by half the number of shared arcs between A and B.

7.2 Unitary dynamics

We start by analyzing the unitary dynamics without measurements, corresponding to $p = 0$. In this case, we are mainly interested in understanding how Gaussianity changes the functional form of entanglement growth from diffusive to ballistic, as well as the entanglement fluctuations. We also evaluate the entropy of random states, demonstrating a gradual convergence from the Clifford-Gaussian Page [363–366] curve to the stabilizer one. We start by presenting the Gaussian case, which can be treated analytically using the mapping to the arc model, and then show our numerical results with non-Gaussianity doping.

7.2.1 Diffusive Gaussian growth

Consider the purely Gaussian case of $\eta = 0$. As anticipated, entanglement manifests diffusive growth $S_{N/2} \sim \sqrt{t}$, which is typical of free-fermionic systems subject to noise or disorder [72, 195], as shown in Fig. 7.3. This behavior can be understood analytically from the mapping to the arc model, as we explain below.

Each Gaussian-Clifford gate implements a local permutation of 4 Majorana endpoints. Since the matchgates (and thus the corresponding permutations) are picked randomly, each arc endpoint moves stochastically. Let $P_t(x|x_0)$ denote the probability that an arc endpoint initially at x_0 reaches x after t steps. In the following calculations, we omit x_0 for brevity. First, we observe that for any

$t > 0$ we have $P_t(2n-1) = P_t(2n)$ for any physical site n, and thus we introduce $\mathcal{P}_t(n) = P_t(2n-1) + P_t(2n)$. This comes from the random permutations implemented by gates, which immediately make positions $2n$ and $2n+1$ equally likely as soon as the first unitary is applied.

Let us assume that $t = t_\mathrm{o}$ is odd, such that the last unitary layer applied couples each even physical site with its right neighbour. If n is even, the Majorana at x at time t must have come from either the physical site n or from $n+1$ at $t-1$; similarly, if n is odd then the physical site at the previous step must have been either $n-1$ or n. Since the gate implements a random permutation, all Majorana paths are equally likely and thus $\mathcal{P}_{t_\mathrm{o}}(n)$ is just the average of the probabilities of the two possible previous sites at $t_\mathrm{o}-1$. This gives us the recursion

$$\mathcal{P}_{t_\mathrm{o}}(n) = \frac{1}{2}\Big[\mathcal{P}_{t_\mathrm{o}-1}(2\lfloor n/2\rfloor) + \mathcal{P}_{t_\mathrm{o}-1}(2\lfloor n/2\rfloor + 1)\Big]. \tag{7.1}$$

Analogously, for even $t = t_\mathrm{e}$ we have: $\mathcal{P}_{t_\mathrm{e}}(n) = \frac{1}{2}[\mathcal{P}_{t_\mathrm{e}-1}(2\lfloor (n+1)/2\rfloor - 1) + \mathcal{P}_{t_\mathrm{e}-1}(2\lfloor (n+1)/2\rfloor)]$. These equations give rise to a binomial probability distribution that spreads over time. In detail, we obtain

$$P_t(n) = \begin{cases} \frac{1}{2^{t+1}} b(t-1, (t-1)/2 + \lfloor (x-1)/4\rfloor - \lfloor (x_0-1)/4\rfloor) & \text{for odd t,} \\ \frac{1}{2^{t+1}} b(t-1, t/2 - 1 + \lfloor (x+1)/4\rfloor - \lfloor (x_0-1)/4\rfloor) & \text{for even t,} \end{cases} \tag{7.2}$$

where $b(n,k)$ is the binomial coefficient $\binom{n}{k}$ for $0 \le k \le n$ and it is zero otherwise. It can be checked by explicit substitution that Eq. (7.2) satisfies the recursion relations with the correct initial condition. At long times, this distribution is well approximated by a Gaussian centered around $x = x_0$ with variance $4t$, i.e., $P_t(x|x_0) \approx \mathcal{N}(x; x_0, 4t)$.

As mentioned previously, the entanglement entropy is given by half the number of arcs that connect the two subsystems. For a half-chain bipartition, we need to count the average number of arcs with an endpoint in $[1, N]$ and the other in $[N+1, 2N]$. In the following, we consider the limit of $N \gg \sqrt{t} \gg 1$, in which case it is reasonable to assume that the two endpoints of an arc, starting from $x_0 = 2n$ and $x_0 = 2n+1$ at $t = 0$, are independently distributed at t. This yields

$$\overline{S_{N/2}(t)} = \frac{1}{2}\sum_{n=1}^{N}\left[\sum_{x=1}^{N} P_t(x|2n-1)\sum_{y=N+1}^{2N} P_t(y|2n) + \sum_{x=N+1}^{2N} P_t(x|2n-1)\sum_{y=1}^{N} P_t(y|2n)\right]. \tag{7.3}$$

Taking the continuum limit and using the Gaussian approximation of $P_t(x|x_0)$, after some straightforward passages we find

$$\overline{S_{N/2}(t)} = \sqrt{\frac{t}{2}}\int_0^A dx_0[\mathrm{erf}(A+x_0) - \mathrm{erf}(x_0)][\mathrm{erf}(A-x_0) + \mathrm{erf}(x_0)], \tag{7.4}$$

where $A = N/\sqrt{8t} \gg 1$. The final integral can be evaluated explicitly for $A \to \infty$ using $\mathrm{erf}(A+x_0) \approx 1$ and $\mathrm{erf}(A-x_0) \approx 1$ near $x_0 = 0$. The result is $\overline{S_{N/2}(t)} = \sqrt{t/\pi}$ at leading order, which matches well with our numerics, as shown in Fig. 7.3. The

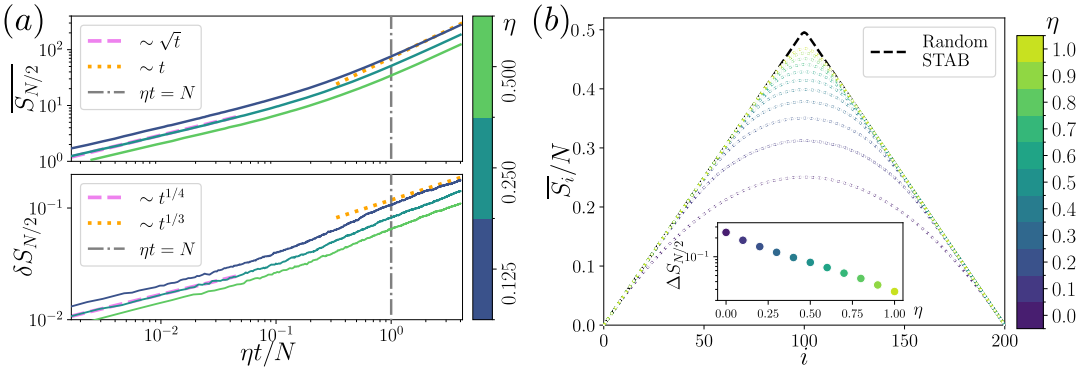

Figure 7.4: (a) Evolution of the half-chain entanglement entropy $\overline{S_{N/2}}$ (top) and its fluctuations $\delta S_{N/2}$ (bottom). We consider unitary dynamics ($p = 0$) and different rates of non-Gaussianity injection by varying η while fixing $\beta = 1$. Data for $N = 600$ averaged over 3000 random realizations. At late times, the injection of non-Gaussianity restores linear growth $\overline{S_{N/2}(t)} \sim t$ and KPZ-like fluctuations $\delta S_{N/2} \sim t^{1/3}$, characteristic of generic random circuits. (b) Page curve for increasing values of non-Gaussian doping, showing the entropy density $\overline{S_i}/N$ as a function of the subsystem length i. Data for $N = 200$ and $N_{\rm NG} = 5N\eta$ injected non-Gaussian gates, averaged over 3000 random realizations. The dashed black line represents the Page curve $\overline{S_i}|_{\mathcal{C}}$ of random stabilizer states. Inset: deviation $\Delta S_{N/2} = \overline{S_{N/2}}|_{\mathcal{C}} - \overline{S_{N/2}}$ as a function of η.

prefactor $1/\sqrt{t}$ is universal, and it differs from the one found in the diffusive pairing dynamics of Majorana defects [89].

At long times $t \sim \mathcal{O}(N^2)$, the arcs are completely delocalized and $P_t(x|x_0)$ approaches the uniform distribution, losing any memory of the starting condition. In this limit, the full circuit effectively implements a global permutation of the $2N$ Majorana operators. Assuming that $P_t(x|x_0)$ is uniform, we can immediately calculate the average steady-state saturation value $\overline{S_{N/2}} = N/4 + O(1)$, which exhibits a volume law.

7.2.2 Recovery of ballistic growth and KPZ fluctuations

We now introduce non-Gaussian gate in the circuit and explore how they affect the dynamics of entanglement. Specifically, we assume an intensive non-Gaussianity injection, corresponding to $\beta = 1$. We present our numerical results in Fig. 7.4(a). At early times, entanglement preserves the diffusive growth of free fermions, and gradually shifts toward a ballistic scaling typical of generic quantum dynamics. This transition occurs when the total number of non-Gaussian gates, $N_{\rm NG} \propto qNt = \eta t$, becomes extensive, i.e., $N_{\rm NG} \sim N$ (see dotted grey line in Fig. 7.4(a)).

In Fig. 7.4(a), we also analyze the fluctuations of the entanglement entropy, $\delta S_{N/2}$ across different circuit realizations. Initially, they scale as $t^{1/4}$, consistent with the variance of a binomial distribution with mean $\propto \sqrt{t}$. At late times, they shift to the $\sim t^{1/3}$ scaling characteristic of the KPZ universality class [72, 367], originally discovered in the context of stochastic surface growth [368]. As before, this crossover occurs once the number of non-Gaussian gates becomes extensive, $N_{\rm NG} \sim N$.

The long-time entanglement entropy achieved in unitary random circuits is known to follow the universal Page curve [363–366], which is different for Clifford [369] and Gaussian states [370–372]. We investigate the crossover between the two induced by non-Gaussian doping. Only for this study, we initialize the system in a random Gaussian stabilizer state (corresponding to a random arc configuration), and we evolve it with the doped unitary circuit for a time $T = 5N$ using variable rate η and fixing $\beta = 1$. This yields a total non-Gaussian content $N_{\mathrm{NG}}/N = 5\eta$. In Fig. 7.4(b) we show the average entanglement density $\overline{S}_i/N$ of a compact subsystem of length $i \in [1, N]$. As the doping increases, the Page curve converges smoothly from the Clifford-Gaussian page curve (derived from the arc model in App. H) to the stabilizer one (known analytically). The deviation at half-chain, $\Delta S_{N/2} = \overline{S_{N/2}}|_{\mathcal{C}} - \overline{S_{N/2}}$, decays approximately exponentially as $\Delta S_{N/2} \sim e^{-aN_{\mathrm{NG}}/N}$ with $a > 0$.

Our results indicate that injecting $N_{\mathrm{NG}} = O(N)$ non-Gaussian gates suffices to restore typical entanglement features. However, as we will see, this no longer holds true once measurements are introduced ($p > 0$).

7.3 Monitored dynamics

We now expand our investigation to hybrid quantum circuit containing measurements. As in the unitary case, we first discuss the Gaussian case, where we observe a MIPT from logarithmic to area-law scaling. The arc model can be leveraged to extract the scaling behavior at low measurement rates analytically. Then we present our results in presence of non-Gaussian doping, where we observe the emergence of a power-law phase $S_{N/2} \sim N^{\alpha}$.

7.3.1 Entanglement transition of hybrid Clifford matchgates

We now consider fully Gaussian monitored Clifford circuits without any doping ($\eta = 0$). Unlike the unitary case, where entanglement grows extensively, any nonzero measurement rate $p > 0$ destroys the volume-law scaling. In detail, under weak monitoring the long-time entanglement entropy scales logarithmically with system size, $\overline{S_{N/2}} \sim c_{\mathrm{eff}}/3 \log N$, and undergoes a transition to an area-law phase $\overline{S_{N/2}} \sim$ const. above a critical point $p_c|_{\mathcal{CG}} \approx 0.34$. This behavior, shown in Fig. 7.5, agrees with the known phenomenology of other free-fermionic systems without $U(1)$ symmetry, as discussed in Sec. 2.2.2. However, it stands in contrast with the entanglement transition of monitored Clifford circuits, which display a stable volume-law phase for $p < p_c|_{\mathcal{C}} \approx 0.16$ [53, 61].

The long-time entanglement scaling in presence of weak monitoring $p \ll 1$ can be reproduced by the arc model analytically. Specifically, we will now derive a classical master equation for the arc-length distribution $P_t(\ell)$, which can be solved exactly in the steady state. Given an arc with endpoints (μ, ν), let $x = \lfloor(\mu + 1)/2\rfloor$ and $y = \lfloor(\nu + 1)/2\rfloor$ the corresponding physical lattice sites. We are interested in their joint probability distribution. In presence of measurements, each timestep of the dynamics contains a unitary layer and a measurement layer, as shown in Fig. 7.1. Let $P_t(x, y)$ and $P_{t+1/2}(x, y)$ be the endpoint distributions after a unitary or measurement layer, respectively. At long times, it is reasonable to assume that

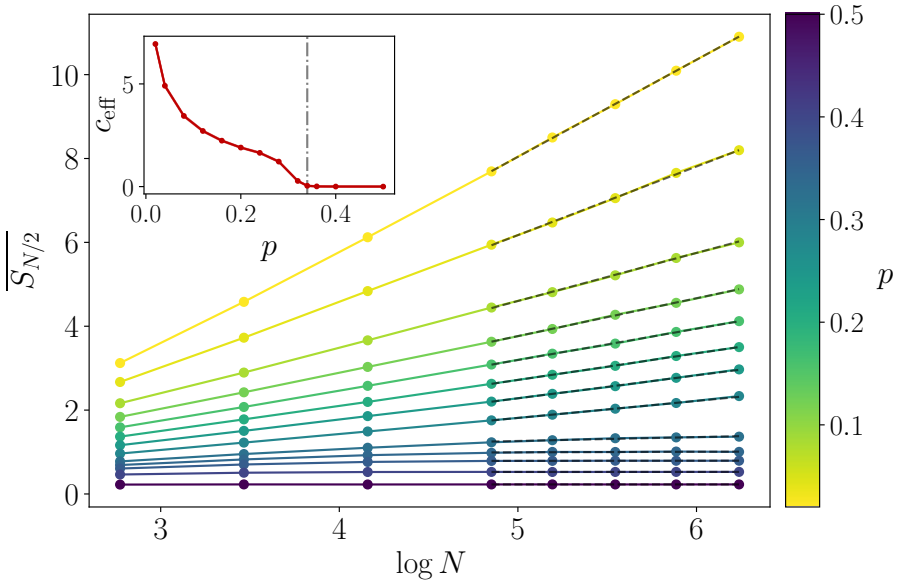

Figure 7.5: Entanglement transition in Clifford-Gaussian circuits. For small values of p, the system exhibits logarithmic scaling of the long-time entanglement entropy $\overline{S_{N/2}} \approx c_{\text{eff}}/3 \log N$. As p increases above a critical $p_c|_{\mathcal{CG}} \approx 0.34$, the entropy attains an area law, $\overline{S_{N/2}} \sim$ const. Inset: prefactor c_{eff} of the logarithmic scaling as a function of p. All data are averaged over 1000 random circuit realizations.

arcs delocalize, losing dependence on their center of mass position. As a consequence, we assume $P_t(x, y) = P_t(y - x)$ and $P_{t+1/2}(x, y) = P_{t+1/2}(y - x)$, where $y - x = \ell$ is the arc length, taken with the sign.

Let us consider the evolution of the probability distribution under a unitary step. As discussed in the unitary case, both x and y either remain unchanged or shift by ± 1. On average, each endpoint will cause the arc length to change by ± 1 with probability $1/4$ and to be unaffected otherwise. This yields the update rule

$$P_t(\ell) = \Big[f * (f * P_{t-1/2}) \Big] (\ell), \tag{7.5}$$

where $f(x) = (\delta_{x,-1} + 2\delta_{x,0} + \delta_{x,1})/4$, and $*$ denotes a convolution. Notice that the convolution is applied twice, once for each arc endpoint.

Next, consider the measurement layer. Here we assume a small measurement density $p \ll 1$, allowing us to safely neglect all processes in which an arc is affected by more than one measurement. As explained in Sec. 7.1.2, a measurement glues together two arcs of length ℓ and ℓ' into a composite arc of length $\ell + \ell'$, and creates a new localized arc of vanishing length (because its Majorana endpoints belong to the same physical site). This happens with a probability $1 - (1 - p)^2 \approx 2p$, because there are 2 endpoints that can be measured. Since we are keeping track of a single-arc distribution and this process involves two arcs simultaneously, we model a measurement as follows: half of the time, the original arc is mapped to the composite arc of length $\ell + \ell'$, whereas the other half it is mapped to the local arc of zero length. Overall, this yields the following possibilities:

1. No measurement: with probability $1 - 2p$, no measurement occurs, and an arc

of length ℓ remains unchanged.

2. Measurement, composite arc: with probability $2p \cdot 1/2$, the arc of length ℓ is originated by the composition of two arcs of lengths ℓ_1 and ℓ_2 such that $\ell = \ell_1 + \ell_2$. These sizes are picked randomly from their current distributions, i.e. $P_t(\ell_1)$,$P_t(\ell_2)$.

3. Measurement, localized arc: with probability $2p \cdot 1/2$, $\ell = 0$ is the local arc generated by a measurement.

Overall, we obtain

$$P_{t+1/2}(\ell) = (1-2p)P_t(\ell) + p\left[\delta_{\ell,0} + \sum_{\ell_1,\ell_2} P_t(\ell_1)P_t(\ell_2)\delta_{\ell,\ell_1+\ell_2}\right]. \tag{7.6}$$

By combining the update equations for the probability distribution, we find

$$P_{t+1}(\ell) = (1-2p)\left[f*(f*P_t)\right](\ell) + p(f*f)(\ell) + p\left[f*[f*(P_t*P_t)]\right](\ell), \tag{7.7}$$

which is a non-linear discrete master equation. Given the convolutions, the problem simplifies dramatically in momentum space (assuming translational symmetry). We thus introduce

$$\tilde{P}_t(k) = \sum_\ell e^{-ik\ell} P_t(\ell), \tag{7.8a}$$

$$\tilde{f}(k) = \sum_\ell e^{-ik\ell} f(\ell) = \cos^2(k/2), \tag{7.8b}$$

yielding

$$\tilde{P}_{t+1}(k) = \cos^4(k/2)\left[(1-2p)\tilde{P}_t(k) + p + p\tilde{P}_t^2(k)\right]. \tag{7.9}$$

Since we are interested in the steady state, we assume $\tilde{P}(k) = \lim_{t\to\infty}\tilde{P}_t(k) = \lim_{t\to\infty}\tilde{P}_{t+1}(k)$, which provides the final equation

$$p\tilde{P}^2(k) + [1-2p-\cos^{-4}(k/2)]\tilde{P}(k) + p = 0. \tag{7.10}$$

This is a quadratic equation that can be solved straightforwardly, giving [5]

$$\tilde{P}(k) = -\frac{1-2p-\cos^{-4}(k/2)}{2p} - \frac{\sqrt{[1-\cos^{-4}(k/2)][1-4p-\cos^{-4}(k/2)]}}{2p}. \tag{7.11}$$

Most importantly, the behavior of Eq. (7.11) for $|k| \ll 1$ determines the asymptotic decay of $P(\ell)$ in real space. After expanding, we find $\tilde{P}(k) \approx 1 - |k|\sqrt{2p}$. The inverse Fourier transform finally gives the asymptotic decay

$$P(\ell) = \int_{-\pi}^{\pi} \frac{dk}{2\pi} e^{ik\ell}\tilde{P}(k) \xrightarrow{\ell\gg 1} \frac{1}{\pi\sqrt{2p}\ell^2}, \tag{7.12}$$

[5] The second root of the quadratic equation is such that $\tilde{P}(k) > 1$, and is thus unphysical.

which is obtained by explicitly evaluating the contribution of $|k| \ll 1$ to the integral. Finally, the average half-chain entanglement entropy is related to the arc-length distribution by

$$\overline{S_{N/2}} = \frac{1}{2} \sum_{x=1}^{N/2} \sum_{y=N/2+1}^{2N} [P(x,y) + P(y,x)] \,. \tag{7.13}$$

After replacing the sums by integrals and inserting $P(\ell) \approx 1/\ell^2$, we obtain the logarithmic scaling $\overline{S_{N/2}} \sim \log N$.

Thus, the arc model provides a clear analytic explanation for the emergent logarithmic phase of monitored free fermions. The statistical description we developed closely resembles the diffusive dynamics of Majorana defects [89], but two-site interactions introduce crossings between Majorana worldlines, as in completely packed loop model with crossings (CPLC) [253, 274, 275, 277]. These models are reported to exhibit an additional $\sim \log^2 N$ contribution to the entanglement entropy, which becomes numerically visible only for very large system sizes $N \gtrsim 10^4$ [274]. This term also arises from renormalization-group arguments and field-theoretical calculations [91, 373]. We believe that a similar deviation could be present in the arc model considered here; however, the master equation we developed does not capture this contribution.

7.3.2 Doped monitored dynamics

Finally, we study the full entanglement phase diagram in the presence of both measurements ($p > 0$) and non-Gaussian doping $q = \eta/N^\beta > 0$. In Fig. 7.6(a), we show the late-time half-chain entanglement $\overline{S_{N/2}}$ versus p for various system sizes, fixing $\eta = 1$ and $\beta = 0.5$. The crossing of curves at different N signals the presence of a MIPT. Above the critical point we observe an area law, whereas for $p < p_c$ the entanglement entropy is sub-extensive, scaling as a power law $\overline{S_{N/2}} \sim N^\alpha$. This already highlights a key difference from the unitary case, where an intensive doping with $\beta = 1$ was sufficient to restore the properties of random Clifford circuits.

To probe the possibility of recovering the volume-law phase (i.e., $\alpha = 1$), we explore how steady-state entanglement is influenced by β. This is shown in Fig. 7.6(b) for fixed $\eta = 1$ and $p = 0.01$, where we observe that the entropy exhibits the power-law scaling $\sim N^\alpha$ for all choices of β, with the exponent α depending on β (and, in general, on p as well). Importantly, our analysis of the scaling behavior (accounting for logarithmic corrections expected in stabilizer circuits [53, 61]) highlights that volume-law entanglement is recovered only for $\beta = 0$ (see inset). Thus, an extensive non-Gaussianity injection per unit time is required to fully stabilize the volume-law phase of Clifford circuits. We interpret this as a consequence of the monitoring: measurements can destroy non-Gaussianity by projecting the system into locally Gaussian states, thus partially restoring Gaussian entanglement properties.

Near a transition point, the entanglement entropy is expected to exhibit a universal scaling behavior [48, 60, 374] of the form $\overline{S_{N/2}}(p) = a(p_c) \log N + F[(p - p_c)N^{1/\nu}]$, where F is a universal curve. Hence, we can extract the critical exponent ν by performing a scaling collapse analysis. At $\eta = 0$, the system belongs to the universality class of CPLC [253, 274, 275, 277]. Interestingly, for $\beta = 0$ we find that all choices

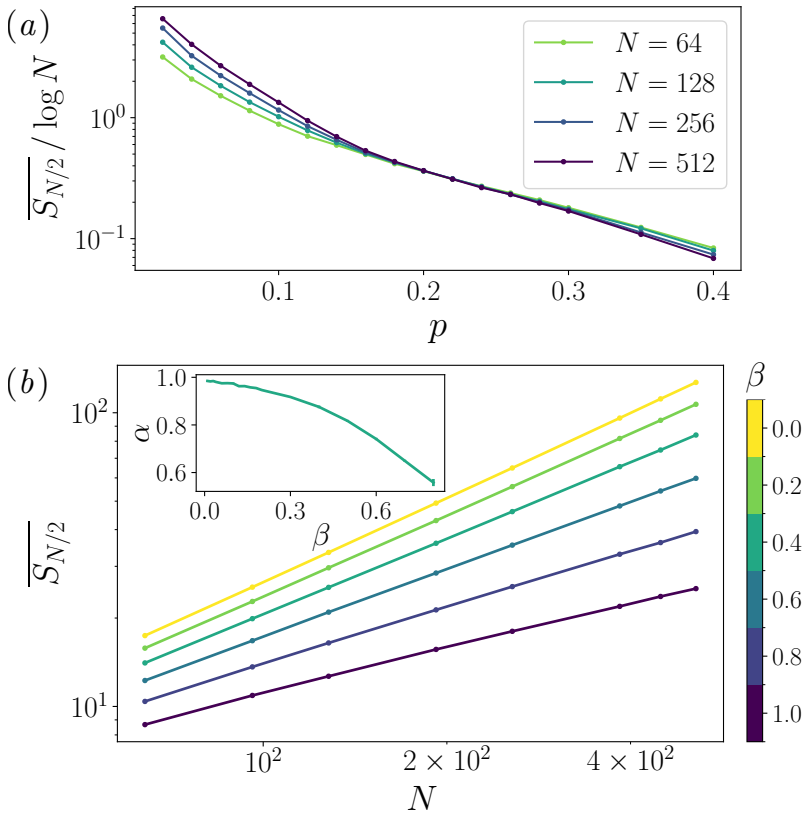

Figure 7.6: (a) Stationary entanglement for a monitored circuit with sub-extensive doping of non-Gaussian resources at $\eta = 1$, $\beta = 0.5$, as a function of the measurement rate. The crossing point $p_c \approx 0.21$ identifies a MIPT between a region with a super-logarithmic entanglement growth. (b) Half-chain entanglement entropy for different system sizes N and different doping exponents β, having fixed $p = 0.01$, $\eta = 1$. Every $\beta < 1$ results in a power-law with exponent $\alpha < 1$, as shown explicitly in the inset. Data obtained by averaging over 500 quantum trajectories.

of $\eta > 0$ yields equal critical behavior with $\nu \approx 1.3$, thus placing the model in the Clifford MIPT universality class [61].

7.4 Conclusions

We have investigated the role of non-Gaussianity in the emergence of generic dynamical entanglement behavior from random matchgate circuits. By restricting to the class of stabilizer states, we manage to explore large system sizes and develop a mapping to a classical arc model in the Gaussian case. This exact description captures both the diffusive entanglement growth and the emergence of logarithmic scaling under measurements, typical of free-fermionic systems. This constitutes a rare example of an analytically tractable MIPT, and clearly establishes the instability of the volume-law phase without relying on the complex formalism of non-linear sigma models [91, 92, 94].

By injecting an extensive number of non-Gaussian gates, we recover ballistic entanglement growth and KPZ-class fluctuations in unitary circuits in the unitary case.

In addition, the Gaussian Page curve gradually converges to the characteristic one of generic states. In the monitored setting, we uncover a MIPT between area-law and power-law entangled phases. Crucially, a genuine volume-law phase emerges only when the non-Gaussian doping is extensive per unit time. Our results quantify the minimal fermionic magic required to drive circuits beyond the non-interacting limit into a genuinely complex regime, establishing a direct connection between quantum complexity, as given by non-Gaussianity, and the structure of entanglement.

A topic of key interest for future research is the quantification of non-Gaussianity (see Sec. 1.2.4) as a resource and the study of its phase diagram, which may also feature critical behavior. In this direction, we ask whether it is possible to develop an analytic framework also in the presence of doping. Indeed, the dynamics considered remains always "simple", in the sense that it can be simulated efficiently using the stabilizer formalism. Related to this, it is important to understand how our choice of restricting to Clifford dynamics impacts our findings, as well as how removing this constraint can further unlock genuinely complex entanglement structures.

Chapter 8

Critical phenomena in magic-doped monitored Clifford circuits

Non-stabilizerness [81, 82, 85–87, 221] constitutes one of the main notions of quantum state complexity. In many-body systems, it has been applied as a probe of different phases of matter in both circuit [278, 279, 375–379] and Hamiltonian systems [206, 209, 222, 349], as we have also seen in Chapter 6. This approach consolidated the importance of studying quantum complexity beyond entanglement, as it can exhibit distinctive traces of quantum phase transitions. Despite much progress, the investigation of many-body non-stabilizerness remains computationally challenging: not only non-stabilizer states are hard to simulate in the first place, but also the known magic measures are exponentially expensive to evaluate [82, 83, 88]. While this problem can be mitigated using efficient non-stabilizerness estimation algorithms for matrix-product states (MPSs) [206, 208, 349, 379, 380] and Gaussian systems [222, 354], these limitations hinder the investigation of interacting regimes inaccessible to tensor network methods, such as very large system sizes, higher dimensionality, or highly-entangled states.

To address these challenges, in this chapter we develop a novel technique, which we name "Iterative Clifford Circuit Renormalization" (ICCR), to evaluate magic efficiently bypassing the aforementioned limitations. The method can be applied to states obtained from any given initial state through Clifford circuits doped with non-stabilizer gates and possibly measurements, in principle in arbitrary dimensionality. The main advantage of our approach is that we entirely avoid to evaluate the evolution generated by the circuit, which is the major computational bottleneck, by iteratively manipulating its geometry and renormalizing the initial state. In practice, we use a simple yet effective approximation method to follow the renormalization flow of the initial state, finding an optimal description as an MPS. Finally, magic can be computed efficiently with a stochastic sampling algorithm [349]. This approach allows for a systematic improvement of the approximation by simply increasing the bond dimension χ of the MPS. We further demonstrate that accurate non-stabilizerness estimates can be achieved with relatively low values of χ, much smaller than those required to fully reproduce the state or by conventional MPS methods.

The ICCR algorithm enables the exploration of system sizes as large as $N = 1000$. As a first application, we investigate hybrid Clifford circuits in one and more dimensions prepared in highly-non-stabilizer initial states, which are extremely challenging for conventional methods. Here, we report the emergence of measurement-induced phase transitions (MIPTs) [47–69] in the purification dynamics of magic, belong-

ing to the Clifford universality class [47, 51]. We then consider the more general and interesting case of doped Clifford dynamics, where the circuit layers contain non-stabilizer T gates as well. Here, the ICCR technique allows us to validate the observation of a measurement-induced magic phase transition reported by Ref. [278] at much larger system sizes, thus mitigating finite-size effects. Finally, we limit-test the power of the algorithm by considering the extremely challenging problem of magic-doped discrete Floquet dynamics.

The rest of this chapter is structured as follows. In Sec. 8.1 we briefly recap the notion of non-stabilizerness and its measures, introduced in Sec. 1.3.3. Then, Sec. 8.2 presents the ICCR algorithm to compute these measures efficiently, providing a step-by-step derivation and a discussion on its performance. We report several examples of application of this formalism in Sec. 8.3, which introduces the models we consider, our results, an analysis of the error of the approximation, and the benchmark of our method with tensor network simulations. Finally, we summarize our findings in Sec. 8.4.

8.1 Non-stabilizerness Measures

In this section we briefly review the concept of stabilizer states, magic, and its measures, repeating part of the discussion presented in Sec. 1.3.3 for convenience. Throughout this chapter, we denote Pauli operators by $\hat{X}$, $\hat{Y}$, and $\hat{Z}$. Moreover, the eigenstates of the Pauli operator $\hat{Z}$ will be denoted by $|+\rangle \equiv |\uparrow\rangle$ and $|-\rangle \equiv |\downarrow\rangle$.

Given a system of N qubits, we define the set of Pauli strings $\mathcal{P}_N = \{\hat{\mathbb{1}}, \hat{X}, \hat{Y}, \hat{Z}\}^{\otimes N}$. The class of stabilizers is the set of states $|\Psi\rangle$ for which there exist N commuting and independent Pauli strings $\hat{g}_j \in \{\pm 1\}\mathcal{P}_N$, $j = 1, \dots, N$, such that $\hat{g}_j |\Psi\rangle = + |\Psi\rangle$. The operators $\hat{g}_i$ generate the stabilizer group of $|\Psi\rangle$. The knowledge of the N generators completely defines the state. The Clifford group $\mathcal{C}_N$ is the set of unitaries that maps stabilizer states into other stabilizer states (and Pauli strings into other Pauli strings). This group is generated by only three elementary gates, namely the Hadamard gate $\hat{H}$, the phase gate $\hat{S}$, and the CNOT gate $\hat{\mathrm{CX}}$.

By applying a non-Clifford gate $\hat{U} \notin \mathcal{C}_N$ to a stabilizer state in general some or all the generators $\hat{g}_j$ will be mapped to $\hat{g}'_j = \hat{U}\hat{g}_j\hat{U}^\dagger \notin \{\pm 1\}\mathcal{P}_N$, thus making the state no longer a stabilizer. The amount of non-stabilizerness of a state can be quantified through different measures. A good measure $\mathcal{M}(|\Psi\rangle)$ should fulfill some properties, stemming from quantum resource theory [155, 156]:

- $\mathcal{M}(|\Psi_{\mathrm{stab}}\rangle) = 0$ if and only if $|\Psi_{\mathrm{stab}}\rangle$ is a stabilizer state, and $\mathcal{M}(|\Psi\rangle) > 0$ otherwise.
- $\mathcal{M}(\hat{U}_{\mathrm{Cliff}} |\Psi\rangle) = \mathcal{M}(|\Psi\rangle)$ for any Clifford operation $\hat{U}_{\mathrm{Cliff}} \in \mathcal{C}_N$.
- $\mathcal{M}(|\Psi_1\rangle \otimes |\Psi_2\rangle) = \mathcal{M}(|\Psi_1\rangle) + \mathcal{M}(|\Psi_2\rangle)$ (additivity).

Other properties, such as monotonicity under measurement, may be desirable [84].

In our analysis we investigate the non-stabilizerness measures already introduced in Sec. 1.3.3. First, we consider the stabilizer nullity ν, which is defined in terms of

the stabilizer dimension r. The stabilizer dimension of a state $|\Psi\rangle$ is given by the maximum integer R for which it is possible to write

$$|\Psi\rangle = \hat{U}_{\text{Cliff}} \left(|+\rangle^{\otimes R} \left| \Phi^{(N-R)} \right\rangle \right), \tag{8.1}$$

where $\hat{U}_{\text{Cliff}}$ is a suitable Clifford operator, and $\left| \Phi^{(N-R)} \right\rangle$ is a state of $N-R$ qubits. The dimension r coincides with the number of generators $\hat{g}_i \in \mathcal{P}_N$ of the stabilizer group of $|\Psi\rangle$, and it quantifies how many single-qubit stabilizer states it is possible to distill out of $|\Psi\rangle$ using only Clifford operations. The stabilizer nullity is then defined as $\nu = N - r$, and measures how many generators are missing to achieve a full stabilizer description. We also consider the stabilizer Rényi entropies (SREs) [83, 84, 205, 259, 349, 381] given by

$$M_n = \frac{1}{1-n} \log_2 \left(\sum_{\hat{P} \in \tilde{\mathcal{P}}_N} \frac{1}{2^N} \langle \Psi | \hat{P} | \Psi \rangle^{2n} \right). \tag{8.2}$$

Differently from the nullity, the SREs assume continuous values and they are proper monotones for $n \geq 2$ [84, 382]. The nullity is formally given by $\nu = \lim_{n\to\infty}(n-1)M_n$, upper bounds the other SREs M_n [208].

8.2 Iterative Clifford circuit renormalization

In this section we describe the ICCR technique we developed to study the dynamics of magic. This method can be applied to a wide class of perturbed Clifford circuits where the non-stabilizerness is either introduced in the initial state or directly injected through non-Clifford $\hat{T} = \text{diag}\{1, e^{i\pi/4}\}$ gates. We treat both possibilities in a unified framework, reducing both cases to a non-stabilizer initial state $|\Psi_0\rangle$ evolved with only Clifford operators and computational-basis measurements, as represented schematically in Fig. 8.1. This is achieved by making use of the so-called T gadget [383, 384], which allows us to translate a $\hat{T}$ gate into an equivalent circuit involving a projective measurement and an ancilla qubit prepared in a resource state. In detail, suppose we want to apply a $\hat{T}$ gate to a generic state $|\Psi_S\rangle$ of the system S. We introduce an ancilla qubit A prepared in the resource state $|T_A\rangle = (|+\rangle + e^{i\pi/4}|-\rangle)/\sqrt{2}$. The identity

$$(\hat{T}_S |\Psi_S\rangle) |+_A\rangle = \frac{1}{\sqrt{2}} \frac{\hat{\mathbb{1}} + \hat{Z}_A}{2} \hat{\text{CX}}_{S\to A} \Big(|\Psi_S\rangle |T_A\rangle \Big) \tag{8.3}$$

can be easily verified, and it is graphically represented in Fig. 8.2. Therefore, it is always possible to replace $\hat{T}$ gates by supplementing the system with ancillae and performing Clifford operations and projective measurements.

Below we provide a description of the ICCR method, schematized pictorially in Fig. 8.3. We start by providing a summary of the technique aimed at clarifying its conceptual procedure and physical intuition. We then explain the details needed for a practical implementation of the method. Finally, we comment on its computational cost and performance.

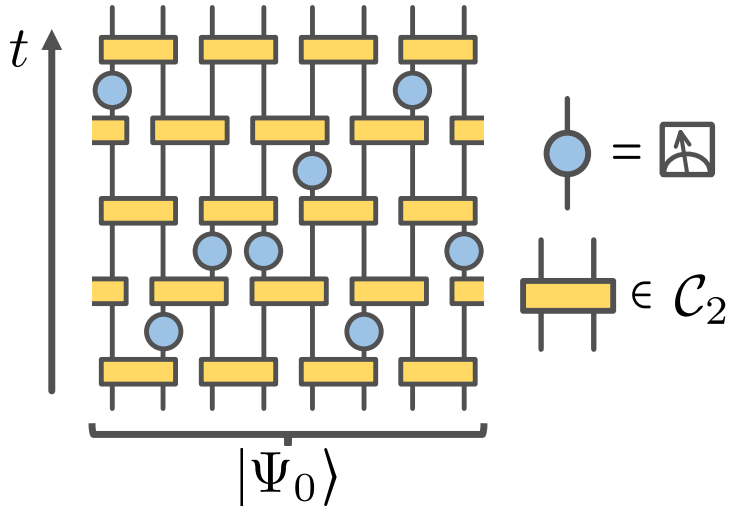

Figure 8.1: Example of Clifford circuit with measurements. Measurements of Pauli strings are represented by blue rounded boxes, unitary operators by yellow squared boxes.

8.2.1 ICCR in a nutshell

The concept underlying the ICCR algorithm is the following. Given a non-stabilizer initial state $|\Psi_0\rangle$ evolved with Clifford unitary gates and projective measurements, we want to obtain a renormalized initial state $|\Psi'\rangle$ and a measurement-free Clifford circuit $\hat{U}'$ such that $\hat{U}'|\Psi'\rangle$ outputs the same state as the original circuit. If successful, this approach enables direct evaluation of magic measures on $|\Psi'\rangle$, bypassing the need of simulating the entire time evolution. The ICCR algorithm performs the task iteratively, i.e. by removing one measurement at a time from the original circuit until none is left.

An iteration of the algorithm proceeds as follows. We consider the initial state $|\Psi_0\rangle$ and the portion of the unitary Clifford circuit $\hat{U}_0$ up to the first projective measurement (as in Fig. 8.3a), which we assume to be of $\hat{Z}_j$ at a certain position j. We swap measurement and unitary gate to obtain an equivalent circuit with a measurement acting directly on $|\Psi_0\rangle$. This transformation can always be accomplished efficiently, since $\hat{U}_0$ is Clifford. The result will yield a projective measurement of a new Pauli string $\hat{P}$ spread across multiple qubits.

The key idea of the ICCR method is to replace the new projector with an appropriate sequence of Clifford unitary gates $\hat{U}'$ acting on a renormalized initial state $|\Psi'\rangle$. In other words, denoting by $\hat{\Pi} = (\hat{\mathbb{1}} + s\hat{P})/2$ the projector associated to the measurement of $\hat{P}$ with outcome $s = \pm$, we want to rewrite

$$\hat{\Pi}\,|\Psi_0\rangle = \mathcal{N}\hat{U}'\,|\Psi'\rangle\,, \tag{8.4}$$

where $\mathcal{N}$ is the norm of the left-hand side. A key observation is that, regardless of the outcome s, the projected state obeys the constraint of being an eigenstate of $\hat{P}$, which effectively removes one qubit degree of freedom. This request can be always mimicked by taking $|\Psi'\rangle = |+\rangle\,|\Phi\rangle$ and $\hat{U}'$ as a sequence of CNOT gates entangling $|+\rangle$ with the remaining degrees of freedom (see Fig. 8.3d). The price to

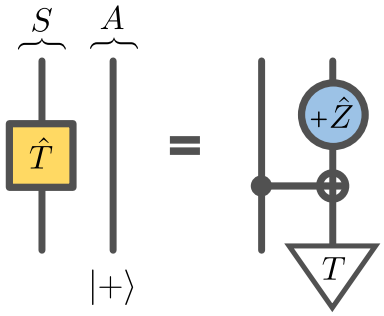

Figure 8.2: Graphical representation of the T gadget replacement. The blue circle represents a projective measurement of $\hat{Z}$ with positive outcome, as in Fig. 8.1.

pay is that $|\Phi\rangle$ is in general an unknown complex state. The key approximation would be to determine it variationally by minimizing the distance between $|+\rangle|\Phi\rangle$ and $(\hat{U}')^\dagger\hat{\Pi}|\Psi_0\rangle$.

8.2.2 Description of the implementation

We now explain step by step how to implement the ICCR method. A schematic description can be found in Algorithm 1. The basic iteration of the algorithm can be understood by considering an initial state $|\Psi_0\rangle$ with stabilizer dimension r that is evolved by a Clifford unitary $\hat{U}_0$ followed by a projective measurement of the operator $\hat{Z}_j$, as represented in Fig. 8.3a. Taking into account the definition of the stabilizer dimension (cf. Eq. (8.1)), we can assume without any loss of generality that

$$|\Psi_0\rangle = \bigotimes_{i=1}^{r} |\varphi_i\rangle \left|\Phi^{(N-r)}_{\text{non-stab}}\right\rangle, \tag{8.5}$$

i.e., the first r spins occupy single-qubit stabilizer states. We would like the projector to act directly on the initial state, so we swap it with the unitary $\hat{U}_0$ by introducing the Pauli string

$$\hat{P} = \hat{U}_0^\dagger \hat{Z}_j \hat{U}_0, \tag{8.6}$$

which allows us to rewrite

$$\frac{(\hat{\mathbb{1}} \pm \hat{Z}_j)}{2}\hat{U}_0|\Psi_0\rangle = \hat{U}_0\frac{(\hat{\mathbb{1}} \pm \hat{P})}{2}|\Psi_0\rangle, \tag{8.7}$$

as shown in Fig. 8.3b.

The next step to be taken depends on how $\hat{P}$ acts on $|\Psi_0\rangle$, i.e., whether it spreads over many qubits and which ones are involved. First of all, let us check if $\hat{P}$ acts trivially on the stabilizer qubits. Suppose that for $i \leq r$ the string contains the operator $\hat{p}_i \in \{\hat{X}_i, \hat{Y}_i, \hat{Z}_i\}$. If $|\varphi_i\rangle$ of Eq. (8.5) satisfies $\hat{p}_i|\varphi_i\rangle = \pm|\varphi_i\rangle$, then we can redefine $\hat{P}$ by updating $\hat{p}_i \to \pm\hat{\mathbb{1}}_i$. It might occur that in this process the string $\hat{P}$ is turned into the identity (modulo a sign): this means that the projective measurement leaves the state unaffected: we can thus drop the measurement from the circuit, and the ICCR step ends here.

In case the action of the projector is non-trivial, we first perform a local change of basis to turn $\hat{P}$ into a string of $\hat{Z}$ Pauli matrices. Let $\mathcal{S}$ be the support of $\hat{P}$, i.e.,

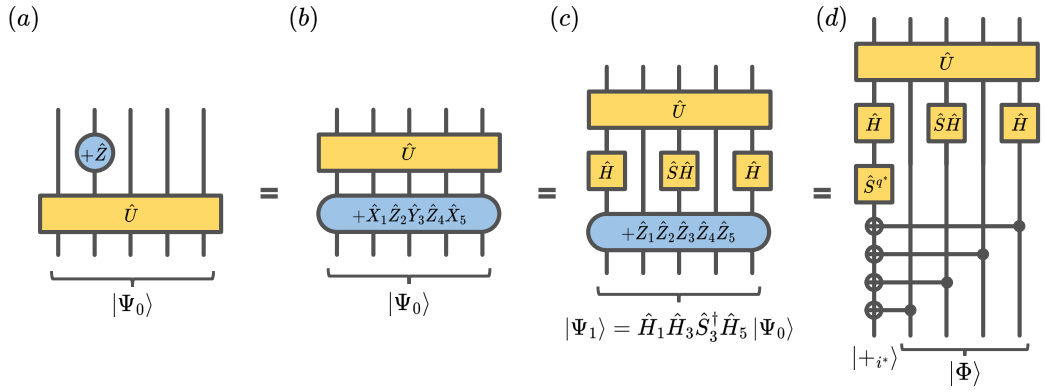

Figure 8.3: Schematic representation of the ICCR algorithm. Projectors on Pauli strings are represented by blue rounded boxes, unitary operators by yellow squared boxes. (a) The original circuit involves a unitary Clifford gate followed by a local projector, in this example corresponding to $\frac{(\hat{\mathbb{1}}\pm\hat{Z}_2)}{2}$. (b) The projector is moved through the Clifford gate resulting in a measurement of an extended Pauli string. (c) Single-qubit gates are applied to rotate the new Pauli string into one involving only $\hat{Z}$. (d) The projector is replaced by a cascade of CNOT and single-qubit gates, and the initial state is updated.

the set of sites on which it does not act as the identity. We can always find suitable single-qubit Clifford rotations $\hat{q}_i$ such that

$$\left(\prod_{i\in\mathcal{S}}\hat{q}_i\right)\hat{P}\left(\prod_{i\in\mathcal{S}}\hat{q}_i^\dagger\right)=\prod_{i\in\mathcal{S}}\hat{Z}_i. \tag{8.8}$$

The change of basis requires us to introduce a new initial state

$$|\Psi_1\rangle=\left(\prod_{i\in\mathcal{S}}\hat{q}_i\right)|\Psi_0\rangle=\bigotimes_{i=1}^{r}|\tilde{\varphi}_i\rangle\left|\tilde{\Phi}^{(N-r)}_{\text{non-stab}}\right\rangle \tag{8.9}$$

and a new unitary $\hat{U}_1=\hat{U}_0\left(\prod_{i\in\mathcal{S}}\hat{q}_i^\dagger\right)$ (see Fig. 8.3c). Let $s=\pm1$ be the outcome of the measurement. The previous change of basis consists in the rewriting

$$\hat{U}_0\frac{\hat{\mathbb{1}}+s\hat{P}}{2}|\Psi_0\rangle=\hat{U}_1\frac{\hat{\mathbb{1}}+s\prod_{i\in\mathcal{S}}\hat{Z}_i}{2}|\Psi_1\rangle\,. \tag{8.10}$$

Notice that the outcome is set to $s=+1$ for postselected measurements originated by T gadgets, whereas for other measurements it must be sampled randomly according to the Born rule by evaluating the expectation value $\langle\Psi_1|\prod_{i\in\mathcal{S}}\hat{Z}_i|\Psi_1\rangle$.

The fact that the projective measurement fixes the parity $\prod_{i\in\mathcal{S}}\hat{Z}_i$ to s allows us to represent its action on $|\Psi_1\rangle$ in terms of Clifford unitaries acting on a renormalized state. If we expand $|\Psi_1\rangle$ in the computational basis as

$$|\Psi_1\rangle=\sum_{\sigma_1,\ldots,\sigma_N=\pm1}a_{\sigma_1\ldots\sigma_N}|\sigma_1,\ldots,\sigma_N\rangle\,, \tag{8.11}$$

the projector destroys all terms in the linear combination that do not fulfill the constraint $\prod_{i\in\mathcal{S}}\sigma_i=s$. The constraint can be thought as reducing by one the free

Algorithm 1 ICCR iteration

Input: the initial state $|\Psi_0\rangle = \bigotimes_{i=1}^{r} |\varphi_i\rangle \left|\Phi_{\text{non-stab}}^{(N-r)}\right\rangle$, a Clifford unitary $\hat{U}_0$ and the measured operator $\hat{Z}_j$.

Compute $\hat{P} = \hat{U}_0^\dagger \hat{Z}_j \hat{U}_0$.
If possible, simplify $\hat{P}$ by checking its action on $|\varphi_i\rangle$.
if $\hat{P}|\Psi_0\rangle = \pm|\Psi_0\rangle$ **then**
    The measurement leaves the state unchanged, **break**.
end if
Find Cliffords $\hat{q}_i$ such that $(\prod_i \hat{q}_i)\,\hat{P}\left(\prod_i \hat{q}_i^\dagger\right) = \prod_{i\in\mathcal{S}} \hat{Z}_i$
Define $|\Psi_1\rangle = (\prod_i \hat{q}_i)|\Psi_0\rangle$ and $\hat{U}_1 = \hat{U}_0\left(\prod_i \hat{q}_i^\dagger\right)$.
If needed, pick a random outcome s using the Born rule.
Define $(i^*, q^*) = \text{argmax}\,\langle\Psi_1|\,\hat{\pi}_i(q)\,|\Psi_1\rangle$ (see Eq. (8.13)).
Initialize $|\Psi'\rangle = |\Psi_1\rangle$ and project qubit i^* to $|+_{i^*}\rangle$.
if $i^* > r$ (i^* was non-stabilizer) **then**
    Optimize variationally the non-stabilizer part of $|\Psi'\rangle$.
end if
Define $\hat{U}' = \hat{U}_1\hat{V}$ (see Eq.(8.15)).

Output: the renormalized initial state $|\Psi'\rangle$ and the equivalent unitary $\hat{U}'$ applied to it.

parameters in $\mathcal{S}$. We can mimick the effect of the projective measurement $\prod_{i\in\mathcal{S}} \hat{Z}_i$ with unitary operators by picking a qubit $i^* \in \mathcal{S}$ to be the target qubit of a CNOT gates cascade designed to enforce the parity constraint, as shown in Fig. 8.3d. While obviously any qubit in $\mathcal{S}$ can be picked as the target, the optimal choice consists of the qubit of $|\Psi_1\rangle$ that is closest to an eigenstate of $\hat{X}$ or $\hat{Y}$ [1]. Formally, we require that

$$(i^*, q^*) = \underset{i\in\mathcal{S},\, q\in\{0,1,2,3\}}{\text{argmax}} \langle\Psi_1|\,\hat{\pi}_i(q)\,|\Psi_1\rangle\ , \tag{8.12}$$

where

$$\hat{\pi}_i(q) = |\psi_i(q)\rangle\langle\psi_i(q)| \tag{8.13}$$

is a projector onto the local state $|\psi_i(q)\rangle = (|+_i\rangle + i^q|-_i\rangle)/\sqrt{2}$ $(q = 0, 1, 2, 3)$ that parameterizes $\hat{X}, \hat{Y}$ eigenstates on site i. Qubit i^* is the optimal target, whereas q^* determines which eigenstate of $\hat{X}_{i^*}$, $\hat{Y}_{i^*}$ it is closest to. If $\mathcal{S}$ overlaps with the stabilizer qubits we always find $i^* \leq r$ [2]. In this case we obtain the identity

$$\frac{\hat{\mathbb{1}} + s\prod_{i\in\mathcal{S}} \hat{Z}_i}{2}\,|\Psi_1\rangle = \mathcal{N}\hat{V}\,|\Psi'\rangle\ , \tag{8.14}$$

[1] As we shall see later, replacing the measurement with unitary gates can require a redefinition of the initial state of the circuit, and possibly an increase in its complexity. If the target qubit is in an eigenstate of $\hat{X}$ or $\hat{Y}$ the redefinition is trivial, and it does not bear any growth of complexity.

[2] We previously removed from $\mathcal{S}$ all sites $i \leq r$ corresponding to eigenstates of $\hat{Z}$. Hence, any $i \in \mathcal{S}$ with $i \leq r$ must correspond to an eigenstate of $\hat{X}$ or $\hat{Y}$.

where $\mathcal{N}$ is the norm of the left-hand side, $\hat{V}$ is the Clifford operator

$$\hat{V} = \hat{S}_{i^*}^{q^*} \left(\prod_{i \in \mathcal{S} \setminus \{i^*\}} \hat{\mathrm{CX}}_{i \to i^*} \right) \hat{X}_{i^*}^{\frac{1-s}{2}}, \tag{8.15}$$

and the state

$$|\Psi'\rangle = \bigotimes_{i=1}^{i^*-1} |\tilde{\varphi}_i\rangle \, |+_{i^*}\rangle \bigotimes_{i=i^*+1}^{r} |\tilde{\varphi}_i\rangle \left| \tilde{\Phi}_{\text{non-stab}}^{(N-r)} \right\rangle \tag{8.16}$$

is equal to $|\Psi_1\rangle$ apart from having qubit i^* set to $|+\rangle$. This result is proved in App. F. We successfully replaced the initial circuit with a measurementless one, characterized by the renormalized initial state $|\Psi'\rangle$ and the new Clifford unitary $\hat{U}' = \hat{U}_1 \hat{V}$. Notice that the non-stabilizer part of $|\Psi'\rangle$ is connected to that of the starting state $|\Psi_0\rangle$ by single-qubit rotations, and thus we conclude that the projective measurement does not modify the magic of the state.

A different scenario unfolds when $i^* > r$, in which case the projective measurement acts only on the non-stabilizer part of the state and impacts it in a non-trivial way. A final form like in Eq. (8.14) can still be obtained, but $|\Psi'\rangle$ will grow in complexity as compared to $|\Psi_1\rangle$ (see App. F). Even in the special case in which $\left|\Phi_{\text{non-stab}}^{(N-r)}\right\rangle$ of Eq. (8.5) is a tensor product of single-particle states, the action of the measurement typically results in an entangled renormalized initial state $|\Psi'\rangle$. The only approximation of this algorithm is made here: to keep the problem tractable, we use a variational approximation of $|\Psi'\rangle$ and we optimize it within a given class of states to minimize the distance between left and right-hand sides of Eq. (8.14). In Sec. 8.3 we implement an MPS approximation, showing that it performs well even with small bond dimension χ (as compared to those needed to explicitly represent the full state). Proceeding in this way, we finally have

$$|\Psi'\rangle \approx \bigotimes_{i=1}^{r} |\tilde{\varphi}_i\rangle \, |+_{i^*}\rangle \left| \tilde{\Phi}_{\text{non-stab}}^{(N-r-1)} \right\rangle, \tag{8.17}$$

where the state of non-stabilizer qubits $\left|\tilde{\Phi}_{\text{non-stab}}^{(N-r-1)}\right\rangle$ is obtained variationally. Notice that Eq. (8.17) is completely analogous to Eq. (8.16): the stabilizer states are the same as those of $|\Psi_1\rangle$, and the target qubit is set to $|+_{i^*}\rangle$. Notice however that in this case the stabilizer dimension has been explicitly increased by 1, manifestly changing the magic of the state.

8.2.3 Variational approximation of $|\Psi'\rangle$

As mentioned, the ICCR procedure can lead to a growth of complexity of the initial state, which requires to approximate the non-stabilizer part of Eq. (8.17). When using an MPS ansatz for $|\Psi'\rangle$, the approximation can be performed variationally with a standard MPS compression algorithm. In the following, we discuss in detail how this procedure is implemented.

The only case in which the non-stabilizer part $\left|\tilde{\Phi}_{\text{non-stab}}^{(N-r)}\right\rangle$ of the state $|\Psi_1\rangle$ (cf. Eq. (8.9)) must be updated is when the support $\mathcal{S}$ is entirely contained in the range $[r+1, \ldots, N]$. As a consequence, we can neglect the stabilizer qubits in Eq. (8.14)

and consider only the last $N-r$ ones. First, we assume that $\left|\tilde{\Phi}^{(N-r)}_{\text{non-stab}}\right\rangle$ is given as an MPS

$$\begin{aligned}\left|\tilde{\Phi}^{(N-r)}_{\text{non-stab}}\right\rangle &= \sum_{\sigma_{r+1},\ldots,\sigma_N=\pm 1} \mathbb{A}^{\sigma_{r+1}}_{r+1}\ldots\mathbb{A}^{\sigma_N}_{N}\left|\sigma_{r+1},\ldots,\sigma_N\right\rangle \\ &= \end{aligned} \quad , \tag{8.18}$$

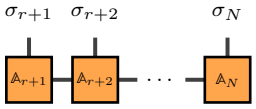

where we introduced standard tensor notation. In the previous equation, each $\mathbb{A}_i$ is a $\chi\times 2\times\chi$ tensor, except for the boundary matrices $\mathbb{A}_{r+1}$ and $\mathbb{A}_N$ that are $2\times\chi$ and $\chi\times 2$ tensors, respectively. The exact state that we want to approximate is given by

$$\left|\Psi_{\text{exact}}\right\rangle = \frac{1}{\mathcal{N}}\frac{\hat{\mathbb{1}}+s\prod_{i\in\mathcal{S}}\hat{Z}_i}{2}\left|\tilde{\Phi}^{(N-r)}_{\text{non-stab}}\right\rangle. \tag{8.19}$$

The variational ansatz we use is

$$\left|\Psi_{\text{approx}}\right\rangle = \hat{V}\left(\left|+_{i^*}\right\rangle\otimes\left|\tilde{\Phi}^{(N-r-1)}_{\text{non-stab}}\right\rangle\right), \tag{8.20}$$

where

$$\left|\tilde{\Phi}^{(N-r-1)}_{\text{non-stab}}\right\rangle = \tag{8.21}$$

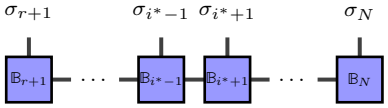

is the state appearing in Eq. (8.17) and it has bond dimension χ as well. Notice site i^* is missing from Eq. (8.21), and i^*-1 is directly linked to i^*+1.

Our goal is to optimize the choice of $|\beta_i\rangle$ to maximize the overlap

$$\left\langle\Psi_{\text{approx}}|\Psi_{\text{exact}}\right\rangle = \frac{\left(\left\langle+_{i^*}\right|\otimes\left\langle\tilde{\Phi}^{(N-r-1)}_{\text{non-stab}}\right|\right)\hat{O}\left|\tilde{\Phi}^{(N-r)}_{\text{non-stab}}\right\rangle}{2\mathcal{N}}, \tag{8.22}$$

where

$$\hat{O} = \hat{X}^{\frac{1-s}{2}}_{i^*}\left(\prod_{i\in\mathcal{S}\setminus\{i^*\}}\hat{\text{CX}}_{i\to i^*}\right)(\hat{S}^\dagger_{i^*})^{q^*}\left(\hat{\mathbb{1}}+s\prod_{i\in\mathcal{S}}\hat{Z}_i\right). \tag{8.23}$$

We notice that the projector $\hat{\mathbb{1}}+s\prod_{i\in\mathcal{S}}\hat{Z}_i$ destroys all computational basis states with parity different from s. Then, the sequence of CNOT gate forces the qubit i^* to the state $|s\rangle$. As a consequence, we can rewrite

$$\begin{aligned}\hat{O} &= \hat{X}^b_{i^*}\left|s_{i^*}\right\rangle\left(\left\langle+_{i^*}\right|+\left\langle-_{i^*}\right|\right)(\hat{S}^\dagger_{i^*})^{q^*}\left(\hat{\mathbb{1}}+s\prod_{i\in\mathcal{S}}\hat{Z}_i\right) \\ &= \left|+_{i^*}\right\rangle\left(\left\langle+_{i^*}\right|+i^{-q^*}\left\langle-_{i^*}\right|\right)\left(\hat{\mathbb{1}}+s\prod_{i\in\mathcal{S}}\hat{Z}_i\right).\end{aligned} \tag{8.24}$$

The matrix element of Eq. (8.22) is now given by the tensor contraction

$$\left\langle\Psi_{\text{approx}}|\Psi_{\text{exact}}\right\rangle = \frac{1}{2\mathcal{N}} \tag{8.25}$$

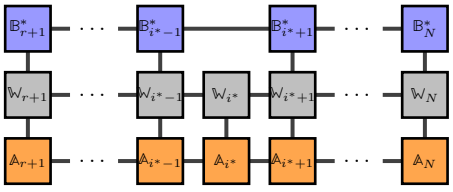

where we introduced a matrix-product operator (MPO) defined by

$$\mathbb{W}_i = \begin{pmatrix} \hat{\mathbb{1}} & 0 \\ 0 & \hat{M}_i \end{pmatrix} \quad \text{for } i \neq i^*, \tag{8.26a}$$

$$\mathbb{W}_{i^*} = \begin{pmatrix} \langle +_{i^*}| + \langle -_{i^*}| & 0 \\ 0 & s\left(\langle +_{i^*}| - \langle -_{i^*}|\right) \end{pmatrix}, \tag{8.26b}$$

where $\hat{M}_i = \hat{Z}$ if $i \in \mathcal{S}$ and $\hat{M}_i = \hat{\mathbb{1}}$ otherwise. In the previous equation, the boundary matrices $\mathbb{W}_{r+1}$ and $\mathbb{W}_N$ are understood to be row and column arrays respectively to contract correctly.

We set up the variational problem as follows. For each site $j \neq i^*$, we maximize the overlap as a function of $\mathbb{B}_j$ alone fixing all others and imposing the normalization constraint $\left\langle \tilde{\Phi}^{(N-r-1)}_{\text{non-stab}} \middle| \tilde{\Phi}^{(N-r-1)}_{\text{non-stab}} \right\rangle = 1$. This is easily done with standard methods [127] if we assume that $\left|\tilde{\Phi}^{(N-r-1)}_{\text{non-stab}}\right\rangle$ is put in mixed-canonical form centered around site j, in which case the solution of the variational step reads

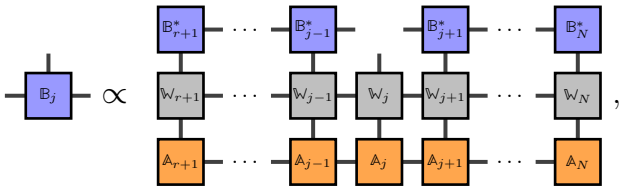

, (8.27)

where $\mathbb{B}_j$ is determined up to a prefactor that is determined by normalizing the MPS. We then repeat the procedure sweeping through all sites a few times until convergence is reached. Contracting the right-hand side of Eq. (8.27) has a computational cost that scales as $\mathcal{O}((N-r)\chi^3)$. Since we need to repeat this step multiple times for each site, the overall cost of the iterative optimization scales as $\mathcal{O}((N-r)^2\chi^3)$.

8.2.4 Computational cost

Here we discuss the efficiency of each step of the ICCR technique. The overall cost depends on the choice of the variational ansatz: in the following, we assume an MPS representation. In our implementations, we store in memory the stabilizer tableaus of unitary gates. Assuming that at the beginning of the procedure $\hat{U}_0$ consists of a single brick layer of Fig. 8.1, the cost to compose $N/2$ two-qubit gates is $\mathcal{O}(N^2)$. The evaluation of Eq. (8.6) is performed in $\mathcal{O}(N)$ operations using stabilizer-state methods [124]. Its simplification by checking how it acts on the states $|\varphi_i\rangle$ is also achieved in at most $\mathcal{O}(N)$ operations. Next, Eq. (8.9) involves applying $|\mathcal{S}|$ single-qubit unitaries, for a cost that scales as $\mathcal{O}(|\mathcal{S}|) \leq \mathcal{O}(N)$. Evaluating $\langle\Psi_1| \prod_{i\in\mathcal{S}} \hat{Z}_i |\Psi_1\rangle$ and finding i^* and q^* also have the same cost. The evaluation of $\hat{U}'$ amounts to composing $\hat{U}$ with $\mathcal{O}(|\mathcal{S}|)$ one or two-qubit gates, which costs $\mathcal{O}(N|\mathcal{S}|) \leq \mathcal{O}(N^2)$ operations. Finally, the cost of the optimization required to determine Eq. (8.17) is $\mathcal{O}((N-r)^2\chi^3) \leq \mathcal{O}(N^2\chi^3)$, as mentioned previously. In summary, the overall maximal cost of the algorithm is $\mathcal{O}(N^2\chi^3)$ per layer and per projective measurement. Assuming a total of M measurements, this brings the overall complexity to $\mathcal{O}(N^2\chi^3 M)$.

For circuits involving a number n_T of T gates a basic way to treat the problem is to replace each of them with a T gadget by introducing n_T ancilla qubits. The total number of qubits to simulate grows, thus increasing the complexity to $\mathcal{O}((N+n_T)^2\chi^3)$ per layer and per projective measurement in the worst case scenario. While the simulation is still efficient, it can become quite expensive for Clifford circuits doped with many T gates. In App. G we show that there is a better way of proceeding that keeps the computational cost at $\mathcal{O}(N^2\chi^3)$. The idea of this alternative approach is that the final state of the ancilla qubit of the T gadget is disentangled from the physical qubits, making it possible to remove its presence from both the effective initial state and the stabilizer tableau of the stored unitary gate. As a consequence, both $|\Psi\rangle$ and $\hat{U}$ are restored to being defined on N qubits.

8.2.5 Discussion on the approximation and its generalization

The ICCR algorithm provides a renormalization flow of the initial state $|\Psi\rangle$, which is however expensive to keep track of exactly and is thus approximated by restricting it to a variational class of states. A rather drastic approach is to take the latter as the class of product states, which has the advantage of simplifying the calculation of the SREs of Eq. (8.2) into a sum of single-qubit SREs due to the additivity property. While this approximation may seem dramatic, our numerical analysis presented in Sec. 8.3 shows that it already captures the qualitative properties of the dynamics of magic. The quality of the approximation is controlled by how close the target qubit i^* is to the eigenstates of $\hat{X}$ and $\hat{Y}$. If the size of the support $\mathcal{S}$ is large the choice of the target is broad and it is more likely to obtain a good approximation. In general, we expect errors to build up as the procedure is iterated, reasonably affecting the performance of the ICCR algorithm at long times.

Beyond this, one can play with the variational class replacing product states with MPSs with fixed bond dimension χ. Though naively analogous, this is very different from performing a full tensor network simulation of the problem, as our goal is still to avoid computing the dynamics. The idea is that while the initial state flow may build up some entanglement, it does not produce as much as the circuit evolution, and thus it can be efficiently captured with a low-χ MPS. The calculation of the SREs becomes more involved, but can still be done efficiently for low enough χ using the perfect sampling technique of Ref. [349], which involves extracting samples of Pauli strings and leveraging the outcomes to form statistical estimators. Unless otherwise specified, we sample 10^3 Pauli strings per SRE measurement. This generalization of the approximation also allows to verify the quality of the estimation by checking the convergence of the SREs as the bond dimension is increased. Indeed, in Sec. 8.3 we show that the accuracy improves with the bond dimension used, and the SREs converge to the exact values as $\sim \chi^{-1}$.

The ICCR step can be effectively viewed as an approach for approximating a generic quantum state using an MPS evolved with a Clifford unitary. This paradigm has been recently established under the name of Clifford enhanced (or augmented) MPSs by Ref. [385] in the context of quantum state designs [322, 360, 386], and by Refs. [387–390] from the perspective of increasing the numerical performance of

MPS algorithms. These works suggest a way to further improve the ICCR ansatz by optimizing variationally not only the MPS in Eq. (8.17), but also the Clifford operator $\hat{V}$ appearing in Eq. (8.14), rather than assuming the given form of Eq. (8.15). The implementation of this generalization is left for future studies. In particular, Ref. [390] uses Clifford-augmented MPSs to evaluate the growth of magic, which is closely related to our investigation. However, their focus is on characterizing how much entanglement can be extracted from an MPS using Clifford gates while maintaining an exact state representation. In this work, we instead relax the requirement to capture the state perfectly in order to accurately estimate non-stabilizerness at larger values of N. For this reason, we believe Ref. [390] and our study are complementary.

We expect that the ICCR estimates the stabilizer nullity very accurately, as the latter is insensitive to the specific definition of the non-stabilizer part of the state. Indeed, whether or not the stabilizer dimension increases by 1 depends only on the expression of the Pauli string $\hat{P}$ of Eq. (8.6) and on the stabilizer qubit states, and not on the details of $\left|\Phi^{(N-r)}_{\text{non-stab}}\right\rangle$. The nullity is also independent of the outcomes of the measurements, which are sampled from an approximation of the initial state [3]. There is however a very specific case in which the nullity is not estimated properly. While in our framework the stabilizer dimension can only increase by a unit as a result of a measurement, there exist non-stabilizer states for which it grows by more [391]. These processes are not captured by our framework, making our estimate of ν only an upper bound. Nevertheless, when comparing our method to exact diagonalization we found these instances to be extremely rare [4], making us confident that the ICCR estimates the stabilizer nullity very accurately.

8.3 Numerical results

In this section we present an example of application of the ICCR algorithm, as well as a benchmark of its performance. We consider a model of MIPTs considered in Refs. [47, 51], which consists of a 1D random Clifford circuit with projective measurements, as schematized in Fig. 8.1. Differently from these works, here we are interested in the dynamics of magic when the system is initially prepared in a non-stabilizer state $|\Psi_0\rangle$. We consider

$$|\Psi_0\rangle = [\cos(\pi/7)\,|+\rangle + \sin(\pi/7)\,|-\rangle]^{\otimes N}\,, \tag{8.28}$$

which has extensive non-stabilizerness. Neglecting the measurements, the unitary part of the dynamics forms a brick-wall circuit of depth T, where each two-qubit gate

[3] The difference between the two possible measurement outcomes only amounts to the presence or absence of an $\hat{X}$ gate in Eq. (8.15). This gate, being a π rotation, can at most affect the outcomes s of the following iterations.

[4] These events are rare in the sense that they typically require a fine-tuning of the properties of the state to occur. For instance, consider the state $|\Psi_0\rangle = |T\rangle^{\otimes 2}$ with stabilizer dimension $r = 0$, and perform a measurement of the Pauli operator $\hat{Z}_1\hat{Z}_2$. For both possible outcomes, the final state will be stabilizer, thus having $r = 2$. However, if $|\Psi_0\rangle$ is slightly perturbed, for instance by a small rotation generated by $\hat{Z}_1$, then both post-measurement states will have $r = 1$. Hence, it is indeed possible that r grows by more than a unit, but this requires a careful and fine-tuned choice of the state.

is picked randomly from the two-qubit Clifford group. We assume a ring geometry, so that the first and last qubits are connected by gates. Projective measurements in the Z basis are performed between layers of unitary operators with a density $0 < p < 1$, namely, each spin has a probability p of being measured after being subject to a unitary gate. The measurement outcomes are picked randomly according to the Born rule. As we show below, we observe that the magic features a measurement-induced transition when varying p.

8.3.1 Magic purification transition

We employ the ICCR method to study the dynamics of non-stabilizerness in the monitored Clifford circuit described above. This model is known to feature a MIPT [47, 51] in both entanglement and mixed-state purification dynamics with critical point at $p_c \approx 0.16$. To track the renormalization of the initial state, we use MPSs with bond dimension χ as the variational class. Figure 8.4 shows our numerical results for the densities of second SRE $m_2 = M_2/N$ and nullity ν/N for a system of $N = 1000$ qubits and depth $T = 2N$. We distinguish two phases separated by a critical measurement density p_c that coincides with that observed in previous works. For $p > p_c$, the measurements purify the magic of the system, leaving it in an almost-stabilizer state. In contrast, an extensive non-stabilizerness survives for $p < p_c$, meaning that the state is still non-trivial at times of order $\mathcal{O}(N)$.

As the bond dimension χ is increased, the renormalization of the initial state is followed more accurately, and thus we expect the non-stabilizerness estimates to converge to the exact results for $\chi \gg 1$. Interestingly, we notice that m_2 grows monotonically as χ is highered, indicating that computing the SRE at finite bond dimension systematically underestimates the true value. This numerical observation suggests that the ICCR method provides lower bounds to the magic measures, even though we were unable to prove it rigorously. In contrast, as argued previously, the stabilizer dimension is independent of χ.

The two phases are better distinguished by looking at how magic evolves as a function of the discrete time t of the circuit. For $p > p_c$, we show in Fig. 8.5 that the steady state with vanishing non-stabilizerness is reached with an exponential decay profile, with a typical relaxation time that depends on p and we find to be independent of N. In contrast, Fig. 8.6 shows the case of $p < p_c$, which features very slow dynamics given by $M_2(t) \approx N - A \ln t$ at long times. We observe that the prefactor A of the logarithmic growth is independent of N, and thus it takes an exponentially long time for m_1 to relax to zero. These results are consistent with the numerical investigation presented in Ref. [51], which considers the evolution of the von Neumann entropy $S(\hat{\rho}(t))$ of a density matrix $\hat{\rho}(t)$ initially prepared in $\hat{\rho}(0) = \hat{\mathbb{1}}/2^N$. For $p > p_c$ they observe that the entropy density relaxes to zero in a finite, N-independent time, whereas it remains finite for exponentially long times at small $p < p_c$, precisely as we find for magic measures. Indeed, the authors show that the entropy $S(\hat{\rho})$ actually coincides with the stabilizer nullity ν of $\hat{\rho}$ for the problem they consider. Our investigation thus confirms the findings of Ref. [51], and generalizes it to the case of a pure non-stabilizer initial state.

We now investigate the rate of convergence of the SRE estimates as the bond

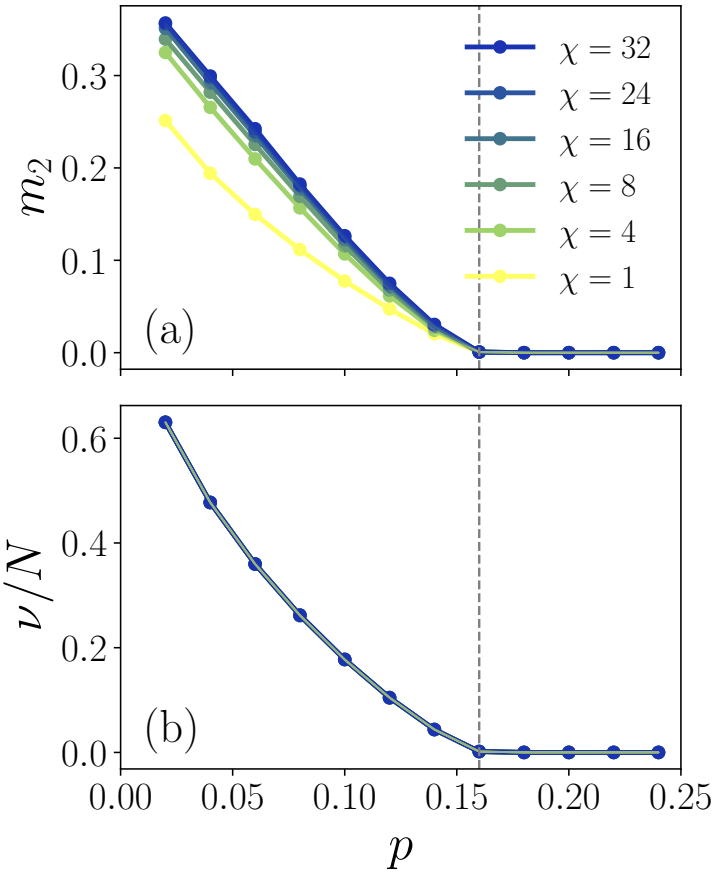

Figure 8.4: Long-time magic densities (a) m_2 and (b) ν/N, as functions of the measurement rate p, computed with the ICCR algorithm using different bond dimensions χ. Data for $N = 1000$, $T = 2000$, averaged over 200 realizations. All magic densities vanish for $p > p_c \approx 0.16$, whereas the system still features extensive non-stabilizerness below p_c.

dimension χ is increased. This allows us to quantify the bond dimension (and thus the amount of computational resources) needed to achieve a given accuracy. We focus on the phase $p < p_c$, because as shown above in the other region the SRE converges quickly with χ. We consider a system size of $N = 500$, a measurement density $p = 0.1$, and various possible depths $T = 250, 500, 1000$. For each of these, we evaluate $m_2(\chi)$ at different bond dimensions χ. We then estimate the variation $\delta m_2/\delta\chi \approx [m_2(\chi) - m_2(\chi - 5)]/5$, using a step $\delta\chi = 5$ to mitigate numerical error. Figure 8.7 shows our numerical results. We observe a power-law decay $\delta m_2/\delta\chi \sim \chi^{-2}$. This implies that the cumulative error $m_2(\infty) - m_2(\chi)$ is expected to scale as χ^{-1}, meaning that the bond dimension required to reach a given accuracy ϵ grows as ϵ^{-1}. We also point out that $\delta m_2/\delta\chi > 0$, which further indicates that finite-χ estimates $m_2(\chi)$ are lower bounds of the exact value.

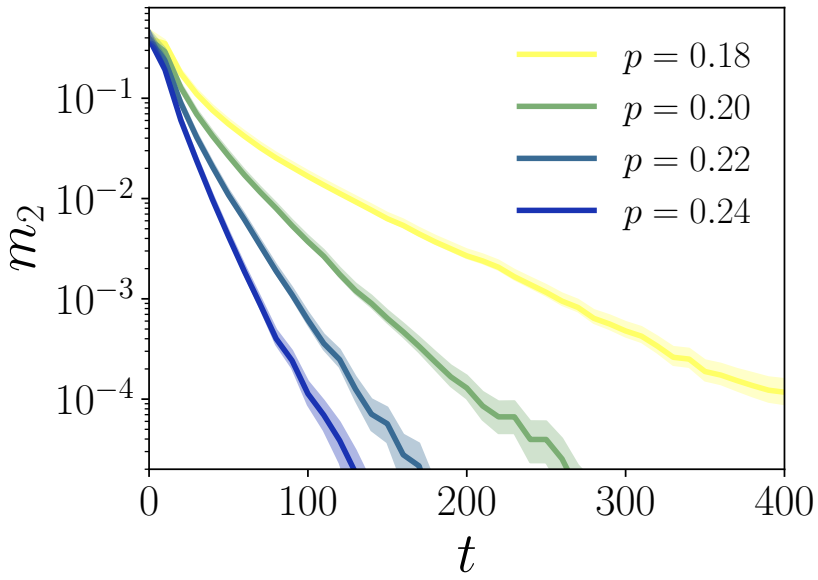

Figure 8.5: Dynamics of the second SRE density m_2 for $p > p_c$. Data for $N = 1000$ averaged over 200 realizations. We use $\chi = 32$, although other choices of χ produce qualitatively analogous behavior. The magic relaxes to zero in a finite time with an exponential time dependence.

8.3.2 Benchmark of the accuracy

To verify the correctness of the ICCR approach, we now compare the values of the SREs obtained using this technique with those obtained through standard tensor network methods. To this purpose, we perform an MPS simulation without resorting to the state renormalization techniques explained above, simply by contracting the quantum circuit using the time-evolving block decimation (TEBD) algorithm. We consider a system of size $N = 20$ and study the evolution of the SRE in a circuit of depth $T = 50$ with open boundary conditions. Importantly, at this system size we are able to follow the state exactly without truncating the TEBD bond dimension. Projective measurements were implemented in the MPS framework using standard techniques [392, 393]. The SRE of this simulation is evaluated using the perfect sampling algorithm [349], using a sampling of 10^3 Pauli strings.

In Fig. 8.8, we present the values of the SRE density m_2 obtained with the ICCR and TEBD approaches [5], for two different values of the projective measurements density $p = 0.1$ and $p = 0.22$. We observe an excellent agreement in the phase $p > p_c$ already with a product-state ansatz ($\chi = 1$), while in the phase $p < p_c$ we require a larger bond dimension to obtain matching values. This shows that the ICCR estimates are unbiased, and they will converge to the exact SRE when using a large enough bond dimension. As observed previously, also in this case the values obtained at small χ appear to lower bound the exact ones.

The different accuracy of the ICCR method in the two phases is reflected qualitatively in the error made by the approximation of Eq. (8.17). A possible way to

[5] For this comparison, we adopted the same trajectories (i.e., the same choices of Clifford gates and measurement outcomes) in the two methods.

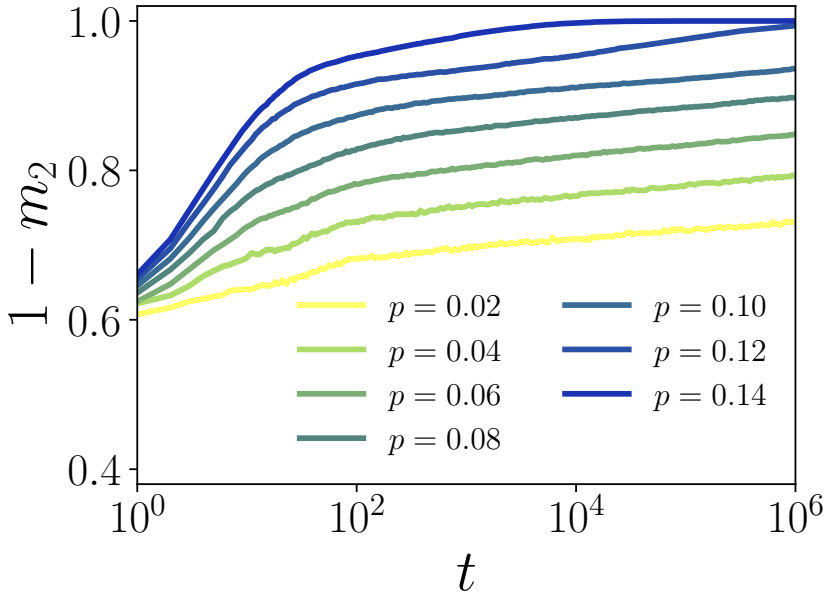

Figure 8.6: Dynamics of $1 - m_2$, the complementary of the second SRE density, for $p < p_c$. Data for $N = 140$ averaged over 100 realizations. We use $\chi = 16$, although other choices of χ produce qualitatively analogous behavior. Asymptotically, $1 - m_2$ grows logarithmically in time.

quantify it is by keeping track of the overlap between exact and approximate states at each ICCR iteration. Let $\left|\Psi'_{n,\text{exact}}\right\rangle$ be the state that solves Eq. (8.14) at the nth iteration of the ICCR algorithm, and let $\left|\Psi'_{n,\text{approx}}\right\rangle$ be its approximation obtained from Eq. (8.17) (see Sec. 8.2.3). We define the squared overlap

$$f_n = |\left\langle \Psi'_{n,\text{exact}} \middle| \Psi'_{n,\text{approx}} \right\rangle|^2. \tag{8.29}$$

Denoting by $M(t)$ the number of ICCR iterations performed up to a given circuit depth t, we introduce the cumulative fidelity

$$\mathcal{F}(t) = \prod_{n=1}^{M(t)} f_n \tag{8.30}$$

to estimate the drift of the iteratively approximated state from the exact one. In Fig. 8.9 we show its dynamics for measurement rates p in the two phases. As expected, a larger bond dimension χ implies more variational freedom in the approximation of the state, and as a result the fidelity is higher. The time dependence of $\ln \mathcal{F}$ appears to be logarithmic in time, indicating a power-law decay of the fidelity. For $p = 0.22 > p_c$ and $\chi = 1$, it saturates quickly to a constant $\mathcal{F} \approx 0.25$, which is very large especially considering the system size of $N = 140$; as χ is increased, the fidelity rapidly approaches 1. In contrast, for $p = 0.1 < p_c$ we observe two algebraic regimes: at short times the decay is faster, whereas it features a smaller exponent as longer times. The fidelity decreases much more in this phase, consistently with the worse performance of the ICCR method found in Fig. (8.8).

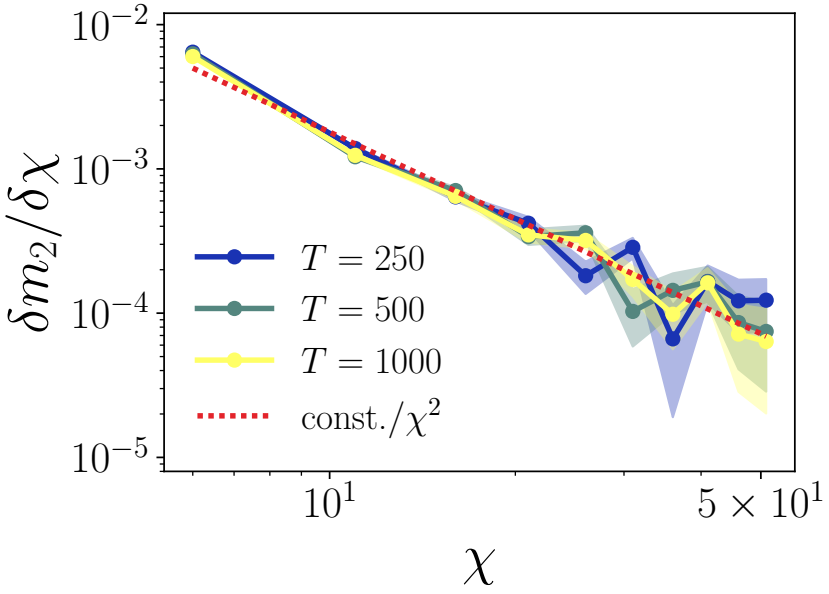

Figure 8.7: Estimate of $\delta m_2/\delta\chi$ evaluated at different circuit depths T. Data for $N = 500$ and $p = 0.1$ averaged over 2500 realizations.

The connection between the fidelity and the quality of the SRE estimation is only qualitative, as it clearly emerges from our results that m_2 converges much quicker than $\mathcal{F}$. In other words, while m_2 can be captured quite accurately even using fairly low values of χ, the state itself is not reproduced equally well necessarily, and the fidelity can still be very small due to accumulated errors from the iterative approximation. This is completely reasonable, because the expectation of capture all properties of a state with a variational approximation that depends on a polynomial amount of parameters is unrealistic. Yet, the more modest goal of computing non-stabilizerness (rather than the full state) can be achieved with limited computational resources.

8.3.3 Other circuit geometries

The ICCR algorithm does not depend on the geometry of the Clifford circuit, and can thus be used to study the non-stabilizerness dynamics in more than one dimension. In the following, we extend the previous investigation to other Clifford gate structures, focusing on (i) a 2D and (ii) a long-range geometry. We reproduce analogue phase diagrams to the one presented in Fig. 8.4, and we study the convergence of the SRE as the bond dimension is increased.

First, we consider a 2D geometry where qubits are arranged on a square grid of size $N_x \times N_x$, so that the overall number of sites is $N = N_x^2$. The unitary circuit is obtained by cycling over four layers of (randomly sampled) 2-qubit gates, covering (in order) horizontal even neighboring bonds, horizontal odd ones, vertical even ones, and vertical odd ones. We assume periodic boundary conditions. The starting state of the dynamics is still the same as in Eq. (8.28), and measurements are again applied after each unitary layer with a probability p per site. Figure 8.10a shows our numerical results for the long-time magic density. The transition is qualitatively

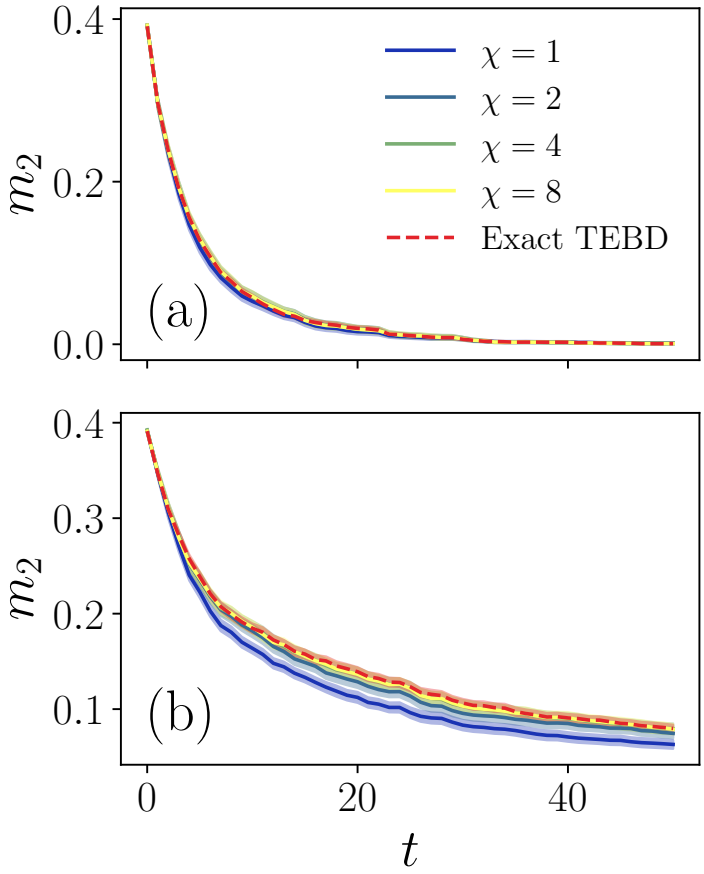

Figure 8.8: Average SRE density m_2 computed using the ICCR algorithm with various bond dimensions χ (solid lines) and exact TEBD (dashed red line). Data for $N = 20$ and (a) $p = 0.22$, (b) $p = 0.1$, averaged over 50 random realizations.

the same as in the 1D case, but the critical point is shifted to $p_c \approx 0.3$. While accurately quantifying p_c is not the primary aim of our study, we note that this value is consistent with the one reported in Ref. [59], which studied the meausurement-induced entanglement transition of 2D random Clifford circuits.

Next, we investigate the SRE convergence in this setting by computing the variation $\delta m_2/\delta\chi$ (as in Sec. 8.3.2). Our results for the 2D system are shown in Fig. 8.10b. We still observe a power-law convergence of the SRE, but the decay of $\delta m_2/\delta\chi$ appears to be slightly slower than the 1D case, roughly as $\sim \chi^{-1.7}$ instead of $\sim \chi^{-2}$. This suggests that the convergence of m_2 to its exact value might be slower, yet the approximation can still be improved efficiently with a power-law increase of χ.

We now move to the case of a long-range geometry, in which qubits at arbitrary distances are coupled by Clifford gates. In detail, each layer consists of $N/2$ random unitaries applied on randomly selected pairs of sites. We show the long-time m_2 in Fig. 8.11a, where we again observe two distinct purification phases. The critical point $p_c \approx 0.32$ appears to be shifted to an even larger value than the 2D one. This may indicate that magic is scrambled more effectively in higher dimensions, and thus a higher measurement density is required to purify it efficiently.

Finally, we study once again the variation $\delta m_2/\delta\chi$, presented in Fig. 8.11b, for

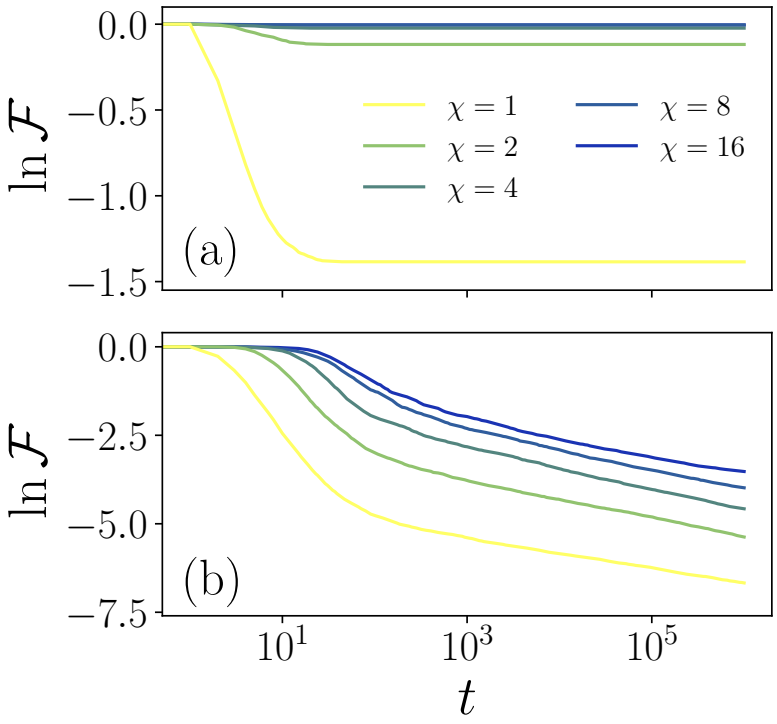

Figure 8.9: Dynamics of the logarithmic cumulative fidelity $\ln \mathcal{F}$ in the two phases: (a) $p = 0.22$, and (b) $p = 0.1$. Data for $N = 140$ averaged over 200 realizations.

the long-range geometry. This time we observe a much slower convergence, which we estimate to be compatible with $\sim \chi^{-1}$. While a precise characterization of the exponent is not possible with the data available, we point out that this result would imply that $m_2(\chi)$ approaches the exact value logarithmically, potentially requiring an exponential scaling of the bond dimension to systematically improve the accuracy. Hence, we expect the ICCR method to perform worse in this scenario, at least when evaluating m_2. This is likely due to our choice to represent the initial state as an MPS, which has an intrinsically one-dimensional structure and struggles to incorporate long-range operations effectively. Hence, while the ICCR method itself is independent of dimensionality, the quality of the approximation of m_2 appears to be affected by it. We remark, however, that the calculation of the nullity is independent of χ, and thus its evaluation (which is enough to obtain the phase diagram) remains feasible also for long-range geometries.

8.3.4 Monitored dynamics with T gates

We now discuss the case in which magic is not stored in the initial state, but injected dynamically using T gates throughout the time evolution. In detail, we study a variation of the protocol schematized in Fig. 8.1, where after each layer of measurements we add an additional layer containing n_T T gates on random sites, and we assume that the system is initially prepared in the stabilizer state $|\Psi_0\rangle = |+\rangle^{\otimes N}$ instead of Eq. (8.28). This setup has first been considered in Ref. [278], highlighting distinct measurement-induced transitions in entanglement entanglement entropy and

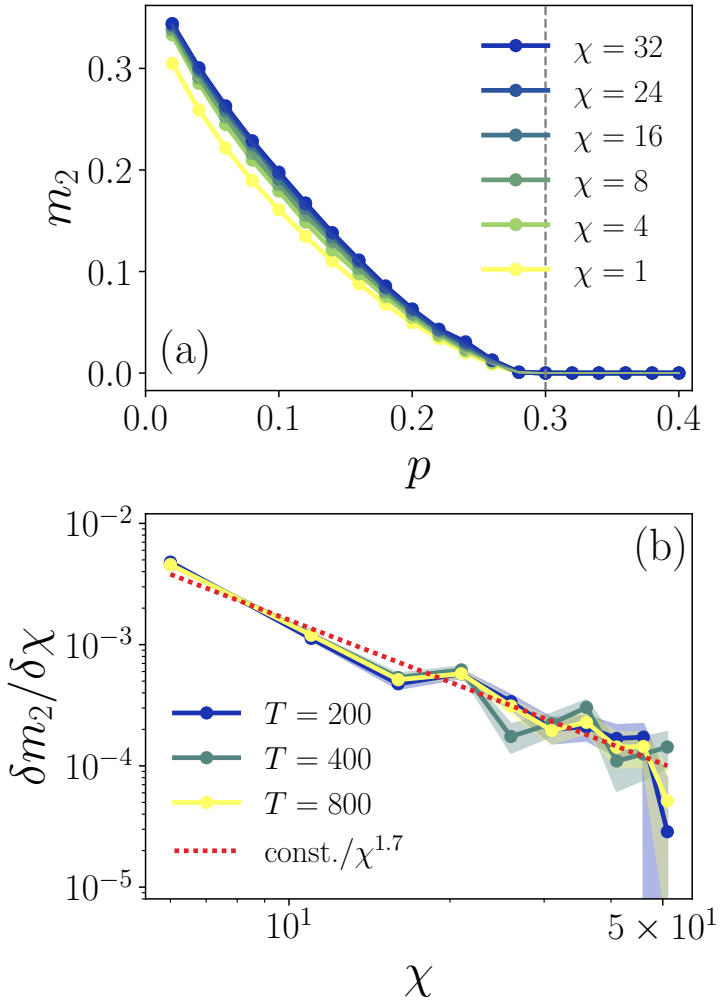

Figure 8.10: Long-time m_2 and its convergence upon increasing χ for the 2D geometry, evaluated for $N_x = 20$ ($N = 400$). (a) Dependence of m_2, evaluated at $T = 800$, on p. Data averaged over 200 realizations. (b) Estimate of $\delta m_2/\delta\chi$ evaluated at different circuit depths T. Data for $p = 0.1$ averaged over 2500 realizations.

non-stabilizerness. This is observed when taking $n_T = \mathcal{O}(1)$, corresponding to an intensive density of T gates per unitary and measurement layer. Here, we employ the ICCR algorithm to enhance the investigation to larger system sizes, corroborating their results on the existence of 3 phases of magic.

In this protocol, magic starts from zero at $t = 0$, and grows linearly until saturation. We show this in Fig. 8.12, where we assume a single T gate per layer. The convergence of m_2 upon increase of χ seems much faster as compared to Fig. 8.4: it appears that only the lowest-level approximation with $\chi = 1$ underestimates the SRE notably, and only for small enough measurement rates. We then proceeded to study the scaling properties of the saturation values reached at $t \gg 1$. In Fig. 8.13 we present our results for both the long-time M_2 and its density m_2. On the one hand, M_2 manifests scaling behavior below $p_c \approx 0.2$, whereas it is intensive at larger measurement rates. On the other hand, however, Fig. 8.13b indicates that $m_2 \to 0$ as $N \to \infty$ already for $p > p_c' \approx 0.1$. This observation suggests the existence of two

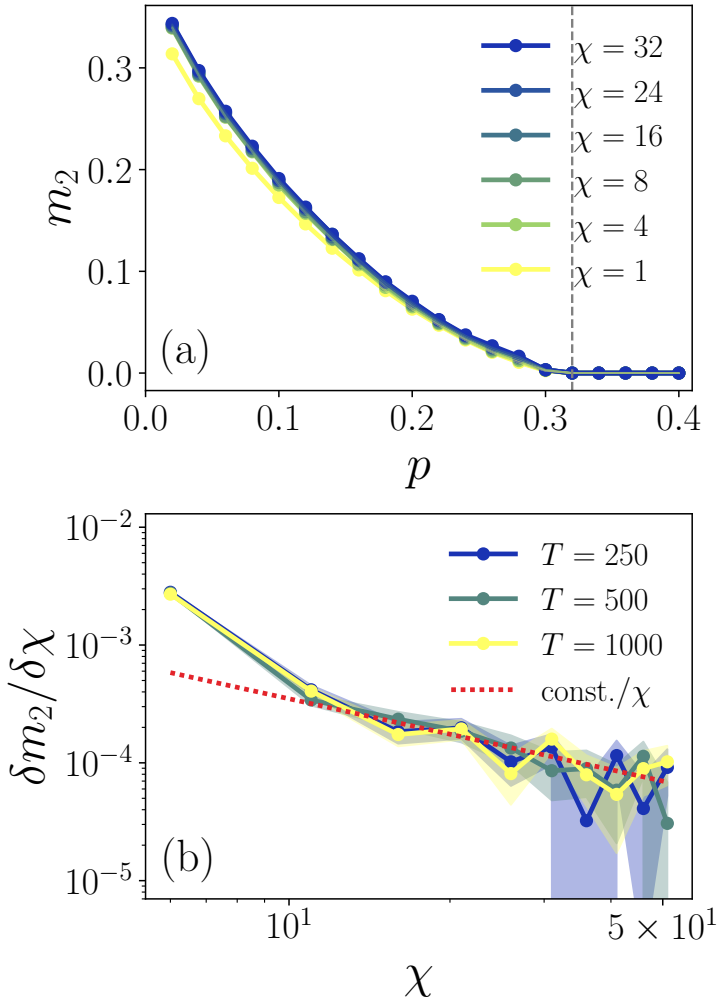

Figure 8.11: Long-time m_2 and its convergence upon increasing χ for the long-range geometry, evaluated for $N = 500$. (a) Dependence of m_2, evaluated at $T = 1000$, on p. Data averaged over 200 realizations. (b) Estimate of $\delta m_2/\delta\chi$ evaluated at different circuit depths T. Data for $p = 0.1$ averaged over 2500 realizations.

separate critical points. At $p < p_c'$, the SRE features a volume law $M_2 \sim N$. For $p_c' < p < p_c$ we instead have a sub-extensive phase with $M_2 \sim N^\gamma$, where $0 < \gamma < 1$. Finally, the SRE is intensive for $p > p_c$. Besides demonstrating the usefulness of ICCR even in presence of T gates, our conclusions confirm the results of Ref. [278].

8.3.5 Floquet unitary circuit

Lastly, we investigate the performance of ICCR in a fully unitary circuit where an extensive amount of magic is injected at each layer through non-Clifford rotations. We consider a translationally invariant Floquet circuit built by alternating a Clifford layer $\hat{C}$ with a non-Clifford rotation layer $\hat{R}(\varphi)$, such that the time evolution after t steps is given by the unitary operator $(\hat{R}(\varphi)\hat{C})^t$. For the Clifford layer we choose $\hat{C} = (\prod_{i=1}^N \hat{H}_i)(\prod_{i=1}^N \hat{CZ}_{i\to i+1})$, where $\hat{CZ}_{i\to i+1}$ is the controlled Z gate between neighboring qubits, and we impose closed boundary conditions. For

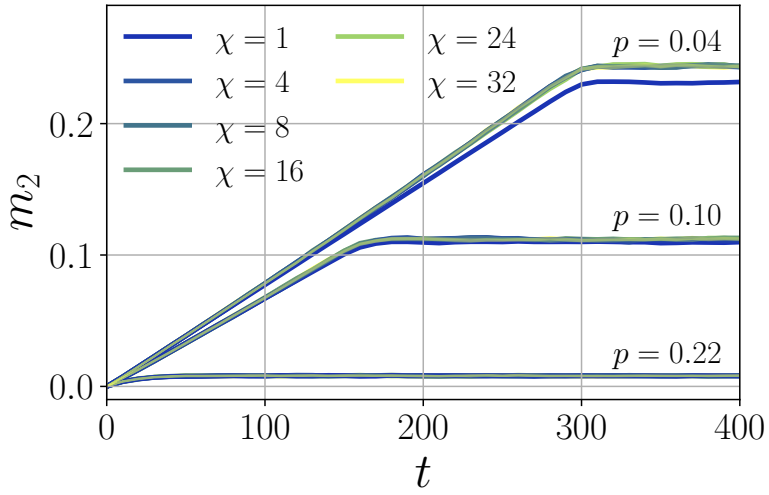

Figure 8.12: Dynamics of m_2 starting from a stabilizer product state, assuming $n_T = 1$ T gates per layer, and various measurement rates p. Data for $N = 500$ averaged over 100 realizations. The SRE shows linear growth before saturating. The non-stabilizerness estimates converge very rapidly with χ.

the rotation layer we instead use $\hat{R}(\varphi) = \prod_{j=1}^{N} e^{-i\varphi\hat{Y}_j/2}$, allowing us to tune the amount of injected magic through the parameter φ. These gates can be implemented using a straightforward generalization of the T gadget [6]. Finally, we take $|\Psi_0\rangle = \left(\frac{|+\rangle+i|-\rangle}{\sqrt{2}}\right)^{\otimes N}$ as the initial state.

We use the ICCR algorithm to evaluate the SRE m_2 as a function of t, i.e., after each rotation layer. In Fig. 8.14 we present our results for a small rotation angle $\varphi = \pi/40$, which show an approximately linear growth of non-stabilizerness in time. At early times m_2 is captured accurately even with small bond dimensions, but the quality of the estimates deteriorates as t increases, requiring progressively larger values of χ. This is further illustrated in Fig. 8.14, which shows that m_2 converges to limiting values as χ increases, although the convergence becomes slower at later times

We also consider the case of a large rotation angle $\varphi = \pi/4$, presented in Fig. 8.15. For this choice, the SRE grows rapidly and appears to saturate at long times. However, analyzing the dependence of m_2 on the bond dimension reveals that convergence is not achieved, indicating that the magic estimates are not quantitatively accurate.

These observations suggest that ICCR may lose accuracy as increasing amounts of non-stabilizerness are injected into the system, eventually making the SRE estimation only qualitative. Indeed, each non-Clifford gate potentially requires a variational optimization step within the algorithm, which inevitably introduces some error. This is consistent with the findings of Ref. [390], which show that magic can no longer be stored by a low-χ Clifford-augmented MPS beyond an extensive

[6] First, we use Clifford gates to rewrite the Y rotation in terms of a Z rotation as $e^{-i\varphi\hat{Y}/2} = \hat{H}\hat{S}^\dagger e^{-i\varphi\hat{Z}/2}\hat{S}\hat{H}$. Next, the Z rotation by the angle φ is implemented analogously to the T gate, using the ancilla resource state $|\varphi_A\rangle = (|+\rangle + e^{-i\varphi/2}|-\rangle)/\sqrt{2}$ in place of $|T_A\rangle$ in Eq. (8.3)

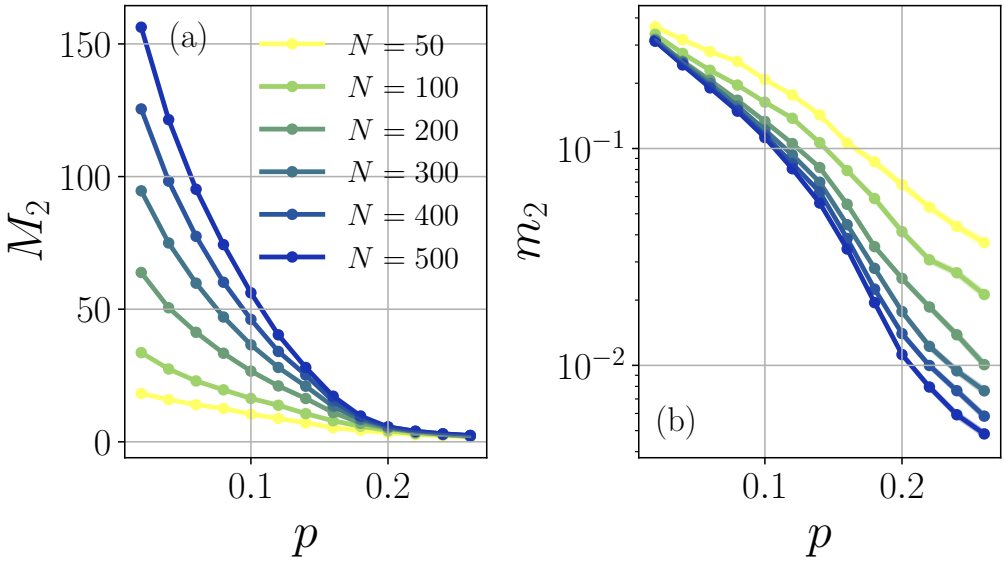

Figure 8.13: Steady-state (a) M_2 and (b) m_2 as functions of p and N, starting from a stabilizer product state and assuming $n_T = 1$ T gates per layer. Data for $\chi = 32$ (sufficient for convergence), averaged over 100 realizations.

threshold number of T gates. Therefore, although the performance of the algorithm should be tested case-by-case, we generally expect that circuits with an extensive number of non-Clifford unitaries per layer are more challenging to study, and the ICCR method remains quantitatively accurate only at low enough circuit depths.

8.4 Conclusions

We developed the new ICCR algorithm to face the challenging problem of evaluating magic in quantum circuits. The main advantage of this technique is that it entirely bypasses the explicit calculation of the dynamics of the state, resulting in a computational cost that scales only polynomially in the number of degrees of freedom. This result is achieved through an iterative manipulation of the structure of the circuit and of the initial state, exploiting the property that Clifford unitary gates preserve non-stabilizerness. The ICCR method significantly extends the range of system sizes accessible by conventional tools, thus enabling the large-scale simulation of magic behavior in a broad class of protocols.

We showcase several applications of ICCR for systems of up to $N = 1000$ qubits. We start by studying circuits involving projective measurements in one and more dimensions, showing that they exhibit measurement-induced transitions in the rate of magic purification. For the 1D and 2D cases, the estimated error on the SRE scales as a power law of the bond dimension χ of the MPS ansatz used to capture the initial state, whereas it appears to be more severe for a long-range circuit connectivity. Nonetheless, we successfully evaluate the phase diagram in all cases, and we observe numerically that results at finite χ lower bound the exact magic values. We then extend our investigation to T-doped monitored Clifford circuits, demonstrat-

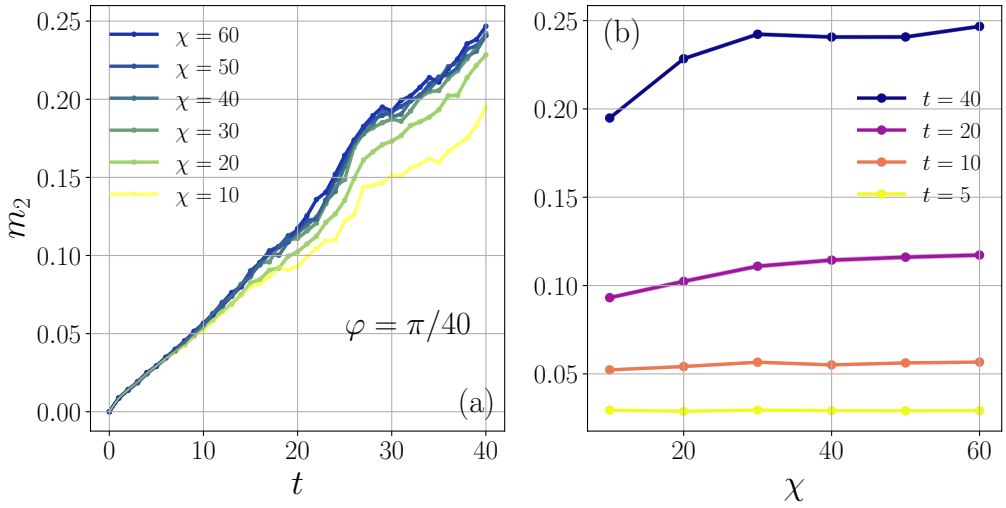

Figure 8.14: Dynamics of non-stabilizerness in the Floquet circuit, using $N = 100$ and $\varphi = \pi/40$. (a) Time evolution of $m_2(t)$. (b) m_2 as a function of the bond dimension χ, fixing some choices of t. Here the SRE is evaluated with a sample of 5000 Pauli strings.

ing strong ICCR performance and identifying three distinct measurement-induced magic phases. Finally, we address the most challenging case of a Floquet circuit containing an extensive number of non-Clifford rotations per layer, showing that the accuracy of the SRE estimates decreases as more magic gates are applied.

As we have demonstrated, the ICCR method can in principle be applied to any quantum circuit decomposed in terms of Clifford unitaries, non-Clifford gates, and measurements. Nonetheless, we highlight two main scenarios where we expect the accuracy of the algorithm to be limited. First, as emerged from our study of Clifford circuits with long-range gates, the variational MPS ansatz may not be best suited to study high-dimensional geometries, which feature a potentially inefficient scaling of the computational resources needed to achieve convergence in the SRE estimates. Second, our analysis in Sec. 8.3.5 indicates that the ICCR performance worsens in circuits doped with an extensive number of non-Clifford gates per layer, as low-χ MPSs augmented with Clifford gates have been shown to be insufficient to capture the state faithfully [390]. Nevertheless, quantitatively accurate results can still be achieved for shallow circuits, and beyond that it may still be possible to extract the behavior of magic at least qualitatively. Moreover, even in these challenging cases the evaluation of the nullity remains efficient, as it is insensitive to the variational approximation.

We believe that ICCR is a powerful and versatile tool to investigate a variety of problems involving non-stabilizerness dynamics, such as those considered in Refs. [279, 376, 377] on hybrid quantum circuits, at very large system sizes. We expect the ICCR method to reproduce the results of these works with lower computational cost, as we demonstrated by investigating the setup presented in Ref. [278], allowing for an in-depth study of the phase transitions observed. An interesting question left for future studies would be to characterize the performance of ICCR combined with other classes of states for the variational approximation. For instance,

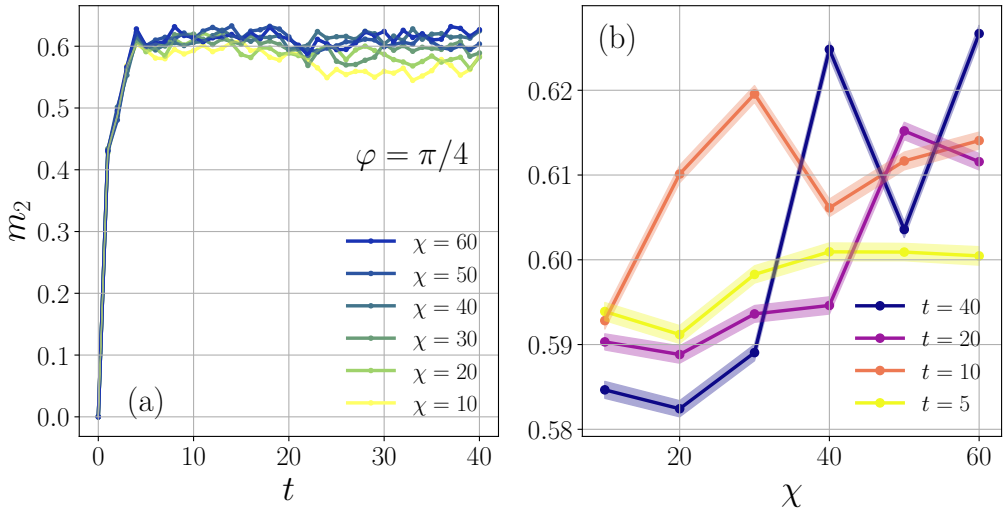

Figure 8.15: Dynamics of non-stabilizerness in the Floquet circuit, using $N = 100$ and $\varphi = \pi/4$. (a) Time evolution of $m_2(t)$. (b) m_2 as a function of the bond dimension χ, fixing some choices of t. Here the SRE is evaluated with a sample of 5000 Pauli strings.

while using an MPS appears to work reasonably well for a 2D circuit geometry, a projected entangled pair state (PEPS) ansatz could be more suited and effective. Finally, a relevant question to explore regards the behavior of magic in Clifford circuits with particular structures, instead of random ones, such as gate arrangements corresponding to practically-useful quantum computing protocols.

Chapter 9

Memory loss and measurement-induced transitions in the PXP model

In monitored dynamics, the choice of the initial state is typically irrelevant, as measurements gradually erase the memory of the starting conditions. An interesting yet still unexplored question is whether this mechanism holds in localized [24–26] or ergodicity-breaking [140–144] systems, which are known to elude thermalization in the absence of measurements. To address this, in this chapter we explore the impact of monitoring in the PXP spin chain [145–152], an effective model for Rydberg atom arrays that exhibits non-ergodic behavior. Specifically, for some choices of the initial state, such as the Néel state, the dynamics does not relax to a thermal steady state, and instead exhibits long-time revivals [36, 394, 395]. This anomalous behavior is a consequence of quantum many-body scars [140–144], a special class of energy eigenstates that violate the Eigenstate Thermalization Hypothesis (ETH).

In our analysis, we first examine the PXP dynamics under a conventional projective protocol, where local measurements are applied at random times. We compare the evolution of the Néel state to the uniform one, which instead thermalizes in the unitary case. We observe that measurements drive both of them toward a common steady state, featuring the same average entanglement. Throughout the monitored evolution, the initially scar-dominated Néel state gradually shifts toward the ETH part of the spectrum, thus losing its characteristic non-ergodicity. Still, some differences between the two states are still retained in the transient regime preceding saturation.

Next, focusing on the Néel state, we implement a periodic monitoring protocol where measurements are synchronized with the unitary state revivals, instead of being performed randomly. Here, we demonstrate a measurement-induced fidelity enhancement relative to the unmeasured evolution. Surprisingly, although the measurements are local, their effects propagate over long distances, which we attribute to the large multipartite entanglement generated by the PXP dynamics. Finally, we approach this revival enhancement from the perspective of many-body scars, revealing that measurements resynchronize quantum scarred eigenstates, counteracting their natural dephasing. Overall, our analysis highlights a dual phenomenology of monitored scarred systems, where measurements can either disrupt or enhance collective non-ergodic dynamics depending on how they are implemented.

The rest of this chapter is organized as follows. In Sec. 9.1 we introduce the PXP Hamiltonian and summarize the properties of its quantum scars. Section 9.2 presents our results for the dynamics with random-in-time measurements. Next, in Sec. 9.3 we introduce the periodic monitoring protocol and discuss the corresponding

phenomenology, featuring an enhancement in state revivals. Finally, we summarize and comment our findings in Sec. 9.4.

9.1 PXP model

Let us now introduce the PXP Hamiltonian and its main features. Throughout this chapter, we denote the down and up eigenstates of $\hat{\sigma}^z$ by $|\circ\rangle$ and $|\bullet\rangle$, respectively, following commonly used notation. The PXP model [145, 146] for a system of N qubits is defined by

$$\hat{H} = \sum_{j=1}^{N} \hat{P}_{j-1}\hat{\sigma}_j^x\hat{P}_{j+1}, \tag{9.1}$$

where $\hat{P}_j = (\hat{\mathbb{1}} - \hat{\sigma}_j^z)/2 = |\circ\rangle_j \langle\circ|_j$ is the projector onto the down state, and either open or periodic boundary conditions (OBC or PBC, respectively) are assumed [1]. This Hamiltonian allows for a spin flip on a given site only if its neighbors contain no excitations $|\bullet\rangle$. As a consequence, assuming that the system is initially prepared in a state that does not contain pairs of neighboring excitations of type $|\bullet\bullet\rangle$, these cannot be generated by the dynamics. In the following, we consider two choices of initial states that satisfy this requirement, namely, the uniform state $\left|\Psi_0^{\text{unif}}\right\rangle = \otimes_{j=1}^{N} |\circ\rangle_j$ and the Néel state $\left|\Psi_0^{\text{Néel}}\right\rangle = \otimes_{j=1}^{N/2} |\bullet\rangle_{2j-1} |\circ\rangle_{2j}$. For the monitoring, we will consider local measurements of the operator $\hat{\sigma}_j^z$, which are unable to create adjacent excitations. As a result, the system only explores a portion of the full Hilbert space called Fibonacci cube (for OBC) or Lucas cube (for PBC), spanned by all computational basis states without neighboring excitations [145, 146]. The sizes of these spaces scale asymptotically as $\sim \varphi^N$, where $\varphi = (1+\sqrt{5})/2$ is the golden ratio.

A well known property of the non-integrable model of Eq. (9.1) is the presence of quantum scars. In detail, the spectrum hosts N eigenstates with unexpected properties, such as an entanglement entropy that scales logarithmically with N instead of extensively. Figure 9.1 presents the half-chain entanglement entropy $S_{N/2}$ of PXP many-body eigenstates as a function of their energy E. Quantum scars correspond to the clearly visible line of points with anomalously low entanglement as compared to the rest. Other particular properties of scars include large multipartite entanglement, given by a super-extensive quantum Fisher information [131, 132, 149], high overlap with the Néel state, and violation of ETH. Such features are often associated to semiclassical behavior, and give rise to atypical entanglement and relaxation dynamics.

These scarred states are responsible for the anomalous time evolution of $\left|\Psi_0^{\text{Néel}}\right\rangle$. When prepared in this state and evolved under the Hamiltonian of Eq. (9.1), the system exhibits imperfect periodic revivals at times $t = nT$, $n \in \mathbb{N}$, where $T \approx 4.72$ is the period [146] (extracted from numerical simulations). This behavior is explained by considering that scars are approximately equally spaced in energy with a separation $\Delta E \approx 2\pi/T \approx 1.33$, as can be seen from Fig. 9.1. As a consequence,

[1] For OBC, the boundary terms take the form $\hat{\sigma}_1^x\hat{P}_2 + \hat{P}_{N-1}\hat{\sigma}_N^x$.

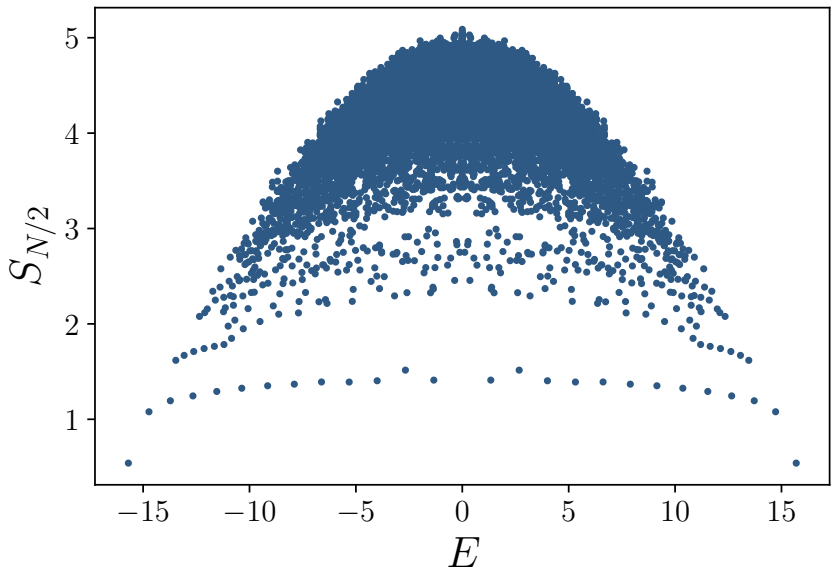

Figure 9.1: Scatter plot of the entanglement entropy $S_{N/2}$ versus the energy E of many-body eigenstates of the PXP Hamiltonian, for $N = 26$. Data obtained through exact diagonalization in the symmetry sector containing the Néel state. The aligned points at the bottom correspond to quantum scars.

these scarred states approximately get in phase every multiple of T. As also discussed below, the Néel state has very large overlap with the scar subspace, and thus the almost coherent oscillations of scars cause approximate fidelity revivals. Since the scar energy spectrum is slightly anharmonic, the recurrences are not perfect and dephasing makes them decay slowly.

9.2 Standard monitored dynamics

We investigate the evolution of the uniform and Néel states under the PXP Hamiltonian interspersed with projective measurements of $\hat{\sigma}^z_j$. Each site is monitored independently and at random times, assuming a constant probability per unit time γ. This is the standard framework of measurement-induced criticality considered also in previous chapters, where the parameter γ tunes a phase transition in the long-time entanglement attained by the system.

9.2.1 Entanglement dynamics and memory loss

The dynamics of entanglement in the presence of measurements depends crucially on the initial state. In Fig. 9.2 we present our numerical results for the half-chain entanglement entropy $S_{N/2}$ averaged over multiple random realizations of the measurement protocol. Simulations are performed with matrix-product states (MPSs) using OBC, implementing a standard TEBD algorithm [125, 127]. In detail, we Trotter-decompose the evolution over a short duration dt into a sequence of local gates $\exp\left(-idt\hat{P}_{j-1}\hat{\sigma}^x_j\hat{P}_{j+1}\right)$, which are then applied to the MPS. The non-thermalizing

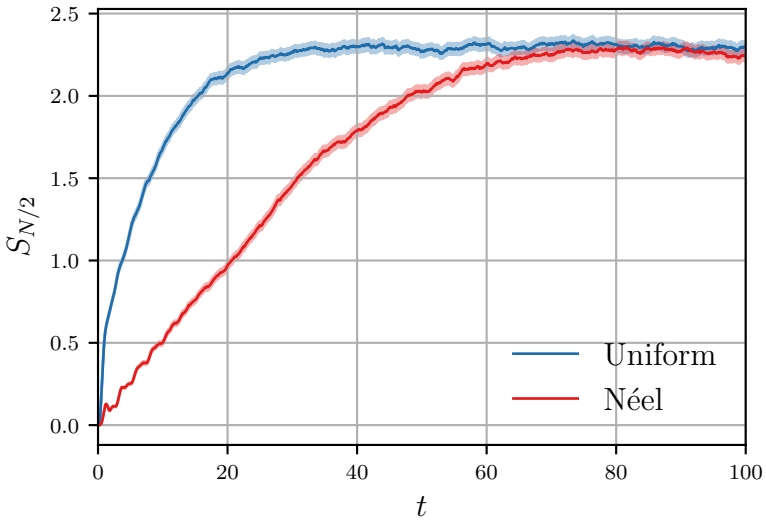

Figure 9.2: Half-chain entanglement entropy dynamics for the two initial states, using $N = 28$, $\gamma = 0.04$, and assuming OBC. Data is averaged over 500 random realizations. The entropy growth rate depends on the initial conditions, but the saturation value is unique. Measurements enhance the amplitude of revivals, while at the same time reducing the entanglement built up by the system.

nature of the Néel state is manifested by a slower entanglement growth compared to the uniform state, which reaches the steady state quicker. Notice however that the stationary state appears to be the same for both cases, indicating that measurements indeed erase memory of the initial conditions. A related study [396] recently investigated a dissipative constrained model, finding that memory can instead be preserved in the presence of degenerate steady states.

The slow dynamics of the Néel state is a consequence of scars, which constitute a significant portion of $\left|\Psi_0^{\text{Néel}}\right\rangle$. Throughout the dynamics, measurements change the overlap of the state with the scar subspace. In particular, since the operator $\hat{\sigma}_j^z$ does not commute with $\hat{H}$, each measurement will partially "reshuffle" the linear combination of the state in the basis of energy eigenstates $|E_n\rangle$, inducing transitions from each $|E_n\rangle$ to all the others. Since the ETH eigenstates exponentially outnumber the scars, it is extremely likely that this process results in a net depopulation of the latter in favor of the former. As a consequence, the monitoring deteriorates the scar overlap in a finite time. The saturation observed starting from the Néel initial condition can thus be understood as a gradual transfer of weight from the scar to the ETH subspaces.

9.2.2 Change in the entanglement velocity

In unitary dynamics, the uniform and Néel state feature significantly different rate of growth of entanglement [147]. In detail, the dynamics of the Néel state takes longer to build up entanglement as compared to the case of the uniform initial state. This is another consequence of scars: the Néel state has a significant weight over the scar subspace, which does not undergo regular scrambling dynamics, but rather evolves

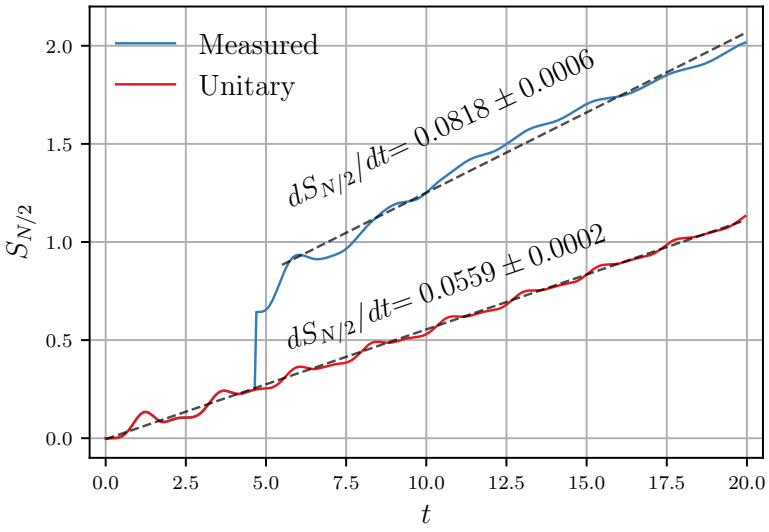

Figure 9.3: Half-chain entanglement entropy computed for the unitary dynamics (red) and in presence of a single local projection to $|\bullet\rangle_{N/2}$ applied at $t = T$ (blue). Data for $N = 32$ and OBC, starting from the Néel state. The measurement deteriorates the overlap with the scar subspace, and this is reflected by an increased entanglement growth rate (estimated with a linear fit).

in an almost coherent way by displaying approximate revivals.

Following this interpretation, one would expect that a depletion of the scar subspace induced by measurements is paired with an increase in the entanglement velocity $dS_{N/2}/dt$. To test this hypothesis, we evolve $\left|\Psi_0^{\text{Néel}}\right\rangle$ with the PXP Hamiltonian and disrupt the dynamics with a single postselected measurement to $|\bullet\rangle_{N/2}$ performed at time $t = T$. Before the measurement, the approximate Néel revival implies that site $N/2$ is close to $|\circ\rangle_{N/2}$ (for even $N/2$); as a consequence, by projecting to $|\bullet\rangle_{N/2}$ we significantly alter the structure of the state. Later, we will demonstrate explicitly that this specific projection disrupts the scar overlap significantly.

In Fig. 9.3 we show the entanglement growth after the measurement and we compare it to the case of regular unitary dynamics. As expected, we observe that the measurement produces an increase in the slope $dS_{N/2}/dt$. This further confirms that measurements performed at generic times decrease the scar overlap of the state, thus erasing the coherent revival dynamics and eventually leading the system to a fully scrambled state.

We considered other protocols as well, changing the measurement time and implementing multiple local measurements. Qualitatively, we observe the same result: the entanglement velocity grows as a consequence of perturbing the scar-dominated dynamics. The magnitude of the slope increase depends on the details of the measurement protocol in general, and is not monotonic in the number of monitored sites.

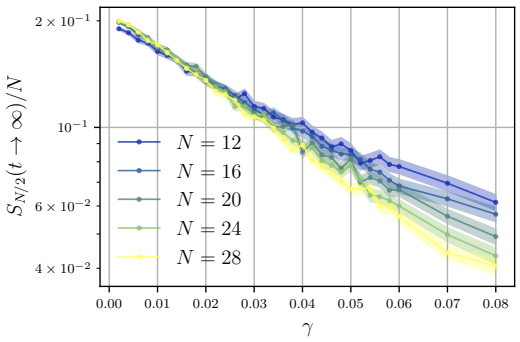

Figure 9.4: Long-time entropy density $S_{N/2}(t \to \infty)/N$ as a function of the measurement rate γ, for multiple system sizes N. We observe a crossover between a volume law and an area law around $\gamma \approx 0.015$.

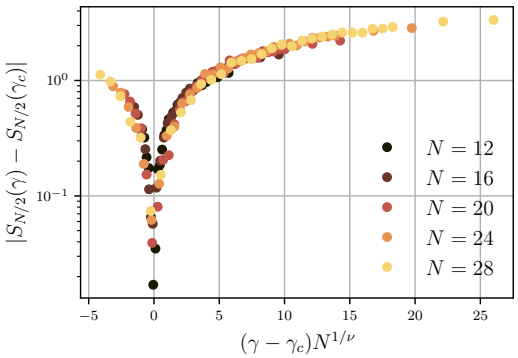

Figure 9.5: Finite-size scaling analysis of the long-time entanglement entropy, using $N = 12, 16, 20, 24, 28$. The fitted parameters are $\gamma_c = 0.013 \pm 0.002$ and $\nu = 0.56 \pm 0.02$, where the uncertainties are estimated by bootstrapping.

9.2.3 Entanglement transition

We also observe a measurement-induced phase transition (MIPT) in the scaling properties of the saturation value $S_{N/2}(t \to \infty)$. In Fig. 9.4, we show the entanglement density $S_{N/2}(t \to \infty)/N$ as a function of the measurement rate γ. The steady-state entropy is evaluated as a long-time average, performed over the time window $t \in [60, 80]$. For $\gamma \lesssim 0.015$, the entropy density appears to converge to a constant as N is increased, indicating volume-law scaling. In contrast, at large γ we notice $S_{N/2}(t \to \infty)/N \to 0$, compatible with the anticipated area law. This agrees with the standard phenomenology of monitored non-integrable Hamiltonians (see the discussion of Sec. 2.2.2).

At the transition point, the system is expected to manifest scale invariance and universal behavior. To better characterize the transition and estimate the critical point, we performed a finite-size scaling analysis. We adopt the ansatz

$$|S_{N/2}(\gamma) - S_{N/2}(\gamma_c)| = F((\gamma - \gamma_c)N^{1/\nu}), \tag{9.2}$$

where F is an unknown universal function, whereas γ_c and ν are parameters to be optimized. This scaling form proved to be appropriate for other monitored models [48, 60, 374]. The critical entropies $S_{N/2}(\gamma_c)$ appearing in Eq. (9.2) are estimated by linear interpolation using data of the closest values of γ available. The parameter optimization is performed using a variation of the algorithm proposed in Ref. [397], which uses a Bayesian inference technique. The optimal data collapse is shown in Fig. 9.5. We obtain a finite critical point $\gamma_c = 0.013 \pm 0.002$, indeed suggesting that the MIPT is genuine.

The low value of γ_c as compared to other monitored Hamiltonian models, such as the Ising chain of Chapter 3, is due to the local PXP constraint forbidding neighboring excitations. Whenever a measurement with outcome $|\bullet\rangle_j$ occurs, the adjacent spins must necessarily be projected to $|\circ\rangle_{j\pm1}$, thus disentangling 3 qubits instead of a single one. As a consequence, measurements in the PXP model disrupt

entanglement much more effectively than in other systems, and thus the volume phase appears only at very low values of γ.

9.3 Periodic monitoring

Instead of measuring at random times, let us now consider the impact of a periodic monitoring on the dynamics. The approximate revivals of the Néel state make it periodically return to an almost computational-basis state. As we show below, local measurements can be used to correct the imperfect fidelity and strengthen the revivals. We highlight that the mechanism behind this effect is a rephasing of quantum scars induced by the periodic monitoring, which partially corrects the dephasing of the unitary evolution.

9.3.1 Measurement-enhanced revivals

Starting from the initial state $\left|\Psi_0^{\text{Néel}}\right\rangle$, we implement the periodically monitored dynamics by alternating a unitary evolution for a duration T and a single projective measurement performed on the boundary spin with $j = 1$, assuming OBC. Rather than the steady state properties, we are now interested in the intermediate-time regime where athermal behavior can still be observed. We consider Born rule measurements, where the outcome is sampled randomly, as well as postselected projections to $|\bullet\rangle_1$, which is the state that would be recovered if the revival was perfect. We compute the fidelity

$$\mathcal{F}(t) = \left|\left\langle \Psi_t \middle| \Psi_0^{\text{Néel}} \right\rangle\right|^2, \tag{9.3}$$

where $|\Psi_t\rangle$ is the evolved state at time t under the hybrid dynamics.

Our numerical results, again obtained with TEBD simulations, are shown in Fig. 9.6a. As expected, the postselected measurements strengthen the revivals, as they explicitly project the boundary spin to a local state compatible with $\left|\Psi_0^{\text{Néel}}\right\rangle$. More surprisingly an enhancement from the second peak onward [2] can be observed even for Born rule measurements, where the first spin has a chance to be projected to $|\circ\rangle_1$, instantly deleting the overlap with the Néel state. This shows that measurements counter the revival decay, extending the duration of coherent behavior shown by the system. A similar observation was made in Ref. [398], where measurements were employed to correct errors dynamically. We point out that the probability of the postselected trajectory decays exponentially yet slowly in the number of measurements, with each postselected outcome having a probability $\gtrsim 90\%$ (evaluated numerically) in the time window $t \in [0, 40]$ considered; hence, it can be accessed in realistic implementations.

It is interesting to also analyze the entanglement growth of the periodically monitored dynamics. In absence of measurements, entanglement shows oscillatory behavior but an overall linear increase. Not surprisingly, measurements reduce the

[2] Since the Néel state is an eigenstate of the measured operator $\hat{\sigma}_1^z$, the expected value of the fidelity after a Born-rule measurement is unaffected by it. Nevertheless, the measurement does change the structure of the state in a way that leads to a fidelity increase of future revivals.

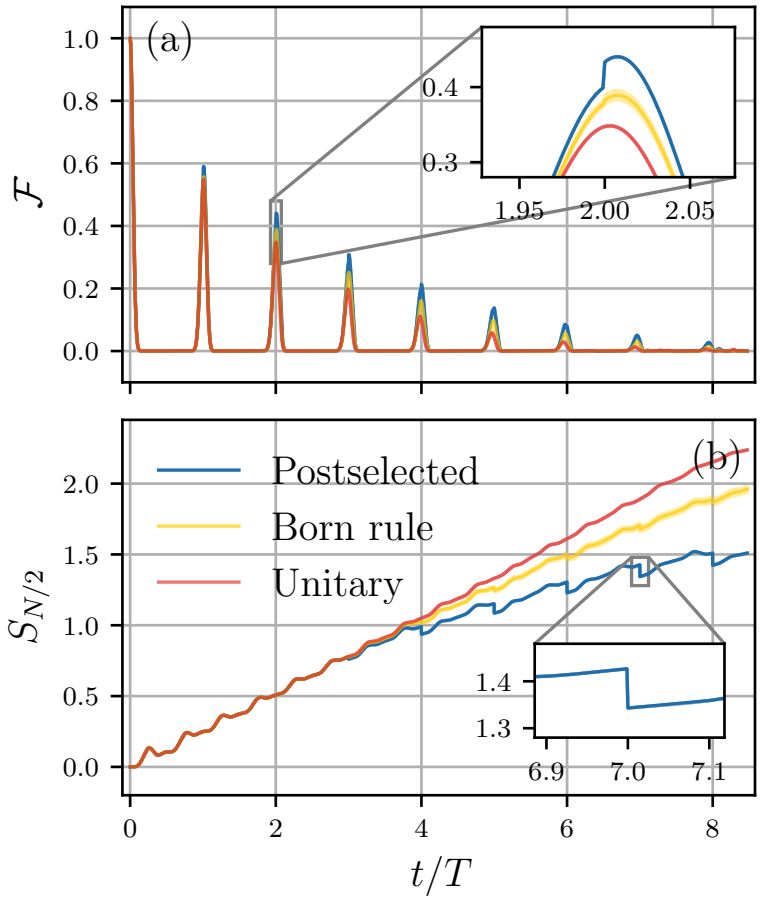

Figure 9.6: Dynamics of (a) fidelity $\mathcal{F}$ and (b) half-chain entanglement entropy $S_{N/2}$ under a periodic monitoring of the left-most site, starting from the Néel state and using $N = 32$. We compare the unmeasured unitary case to both Born rule measurements (for which we average over 500 random realizations) and postselected $|\bullet\rangle_1$ projections.

total entanglement, as we observe in Fig. 9.6b for $t \gtrsim 10$. We point out that the three curves coincide at shorter times because we are evaluating the half-chain entanglement entropy, and thus the effects of a measurement on the boundary take time to propagate through a distance $N/2$.

At longer times, we observe that the entropy shows sudden jumps (see inset), indicating that the measurement on the first site instantaneously impacts the bulk. In other words, despite the measurement being local, it causes a macroscopic collapse of the state that causes long-range effects at extensive distances $\sim N$. This is an explicit manifestation of the large multipartite entanglement [8, 131, 132] generated by the PXP evolution, which has been highlighted in a previous study [149]. In detail, the system develops long-range correlations that mediate a non-local action of the measurements, similar to how measuring locally a GHZ state $(\otimes_{j=1}^{N} |\circ\rangle_j + \otimes_{j=1}^{N} |\bullet\rangle_j)/\sqrt{2}$ affects all qubits instantly. This also explains why measuring even a single, boundary spin can result in an exponential enhancement of the fidelity.

Other periodic monitoring protocols – Besides the boundary qubit moni-

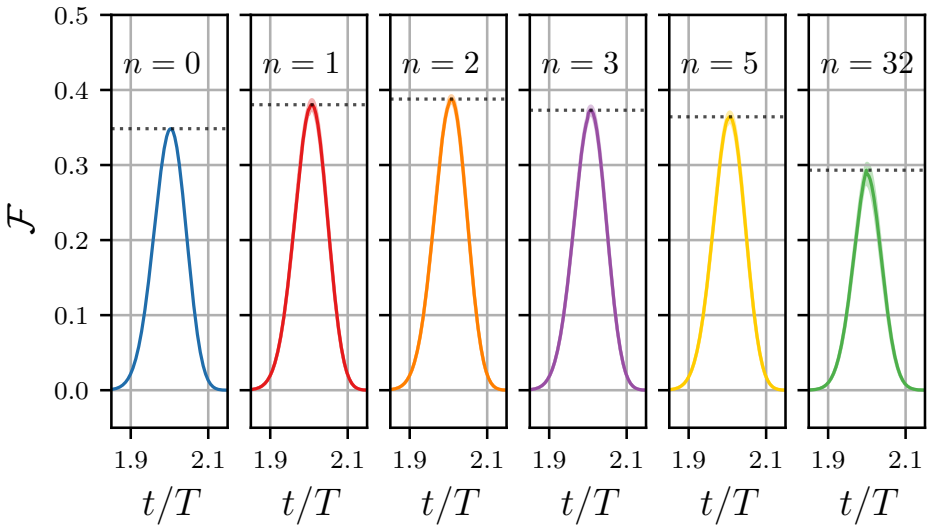

Figure 9.7: Fidelity revivals under Born rule periodic monitoring of the n left-most sites of the chain, starting from the Néel state and using $N = 32$ and different n. Data is zoomed around the second peak at $t \approx 2T$, and averaged over 1000 random realizations.

toring, we also considered measurements of bulk spins, obtaining analogous results. A more interesting case is that when multiple sites are measured at the same time. Specifically, we alternate a step of unitary evolution for a duration T with a step of measurements of $\hat{\sigma}_j^z$ on the sites $j \in [1, n]$, i.e., the n left-most spins of the chain.

If we postselect measurements to reproduce the pattern $|\bullet \circ \bullet \circ \ldots\rangle$, the fidelity grows monotonically with n. This is not surprising, as measurements are gradually resetting the state precisely to the Néel one. In contrast, in the Born rule case we observe a different phenomenology. Figure 9.7 shows our results for different choices of n. In order to compare the different curves, the curves presented are zoomed around the second fidelity peak. We observe that the enhancement is still present for $n > 1$ but gets weaker upon increase of n (a slight increase is observed for $n = 2$, though). Eventually, as more and more sites are measured, the monitoring decreases the fidelity instead of enhancing it, as hinted by our results for $n = 32$.

This phenomenology can be explained as a tradeoff between fidelity gain and probability loss of the most likely outcome. As commented above, the fidelity must increase if the measurement outcomes are $|\bullet \circ \bullet \circ \ldots\rangle$ (up to site n), which has the largest probability of occurring. Nevertheless, this probability decays with the number of monitored sites n. As a consequence, despite the larger fidelity gains, measuring more sites suppresses the probability of obtaining the Néel pattern, yielding an overall net fidelity decrease as compared to lower values of n.

9.3.2 Quantum scar resynchronization

Quantum scars constitute the fundamental ingredient for fidelity revivals. We now explore how measurements impact the scar superposition of the Néel state. Not only we observe that periodic measurements leave the overall overlap with the scar

subspace almost unchanged, but we highlight that the key mechanism underlying the revival enhancement is a measurement-induced realignment of the scar phases.

Let us denote the scar states by $|\psi_s\rangle$, $s = 1, \dots N$. These can be obtained through exact diagonalization, as described in Ref. [146], by looking for the energy eigenstates with lowest entanglement entropy in Fig. 9.1. In the following, we assume PBC. First, we are interested in understanding how projective measurements modify the overlap of the evolved state $|\Psi_t\rangle = e^{-i\hat{H}t}\left|\Psi_0^{\text{Néel}}\right\rangle$ with the scar subspace. Naturally, such an overlap is left invariant by the unitary evolution, and only measurements can change it. We thus assume to measure $\hat{\sigma}_1^z$ on $|\Psi_t\rangle$ postselecting the outcome to $|\bullet\rangle_1$ [3], yielding the post-measurement state

$$\left|\Psi_t^{\text{proj}}\right\rangle = \frac{(\hat{\mathbb{1}} - \hat{P}_1)\,|\Psi_t\rangle}{\sqrt{1 - \langle\Psi_t|\,\hat{P}_1\,|\Psi_t\rangle}}. \tag{9.4}$$

We then introduce the scar weight

$$W = \sum_{s=1}^{N} \left|\left\langle\psi_s\middle|\Psi_t^{\text{proj}}\right\rangle\right|^2, \tag{9.5}$$

which measures the overlap with the scar subspace after performing a measurement at time t. Figure 9.8 shows the time-dependence of W. As expected, at almost all times the projection decreases the weight, bringing the state toward the ETH part of the spectrum. However, we observe that by finely tuning the measurement time to match multiples of the period T, the measurement leaves W practically unaffected, if not slightly increased. This result is surprising, because no individual scar $|\psi_s\rangle$ is an eigenstate of the projector $\hat{\mathbb{1}} - \hat{P}_1$. This means that the specific superposition structure of the state causes the measurement to reshuffle scars without changing their overall weight.

Motivated by this observation, we analyze more in detail how measurements performed at $t = T$ modify the individual coefficients of scars appearing in the state superposition. Any arbitrary state $|\Psi\rangle$ can be written as

$$|\Psi\rangle = \sqrt{1 - W}\,|\Psi_{ETH}\rangle + \sum_{s=1}^{N} a_s e^{i\varphi_s}\,|\psi_s\rangle\,, \tag{9.6}$$

highlighting the scar and ETH contributions. Here $a_s > 0$ satisfy $\sum_{s=1}^{N} a_s^2 = W$, where W is the total scar weight. Since each $|\psi_s\rangle$ is defined up to a phase, we conventionally set it such that the Néel state has $\varphi_s = 0$. In order to understand how measurements change the phases, we first consider the state $|\Psi_T\rangle = e^{-i\hat{H}T}\left|\Psi_0^{\text{Néel}}\right\rangle$ evolved by one period, which clearly has $\varphi_s = E_s T$, where E_s are the scar energies. We then perform projective measurements on a compact set of n neighboring qubits (i.e., from $j = 1$ to $j = n$), postselecting the outcomes to be $|\bullet\rangle_{2j-1}$ for odd sites and $|\circ\rangle_{2j}$ for even ones, such that they gradually impose the Néel ordering. Finally, we evaluate the post-measurement phases φ_s.

The results of this calculation are presented in Fig. 9.9a. First, the unmeasured state ($n = 0$) manifests different phases for the various scars, which happens because

[3] Notice that choosing any odd site provides equivalent results, since we are using PBC.

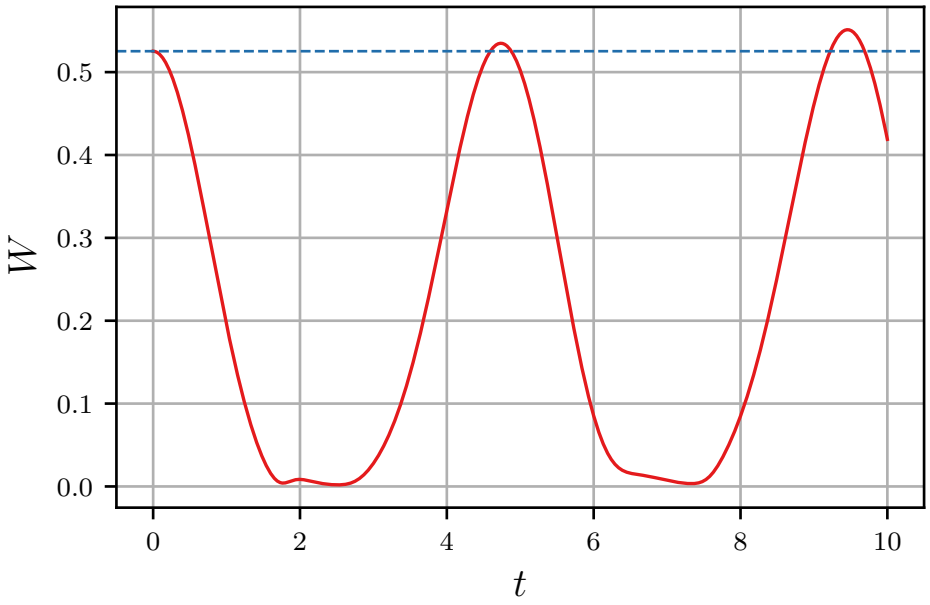

Figure 9.8: Post-measurement scar subspace weight W as a function of the measurement time t, using $N = 26$ and PBC. Measurements performed at times $t = nT$ leave the weight almost unchanged, whereas they deteriorate the scar overlap when acting at other times.

the energy spacings of E_s are not perfectly homogeneous. Indeed, explicitly we have $\varphi_s|_{n=0} = E_s T$, which are only approximately integer multiples of 2π. We observe that the different φ_s are gradually brought back in phase as more and more sites are measured, thus mitigating the original dephasing. In the process, the individual amplitudes a_s^2 remain approximately constant, as shown in Fig. 9.9b. This suggests that measurements have little effect on the scar populations, acting mainly on their phases instead. We thus conclude that postselected measurements at $t = T$ implement a rephasing mechanism that realigns scar states without significantly affecting their weights, thus countering the dephasing responsible for the revival decay.

9.4 Conclusions

The dynamics of the PXP model under local monitoring exhibits a dual phenomenology: measurements can either destroy coherent revivals or enhance them depending on their temporal structure. Despite the non-ergodic nature of the Néel state evolution in the unitary case, measurements performed at random times erase memory of the initial conditions, leading the system to an ETH-dominated steady state. Nevertheless, signatures of the scar dynamics are visible in the transient regime, where the Néel state takes longer to relax as compared to the uniform one. In contrast, periodic measurements synchronized with the Néel state revivals enhance the coherent scar dynamics rather than destroying it. While this effect is expected in the case of postselected measurements, we surprisingly observe that it persists also

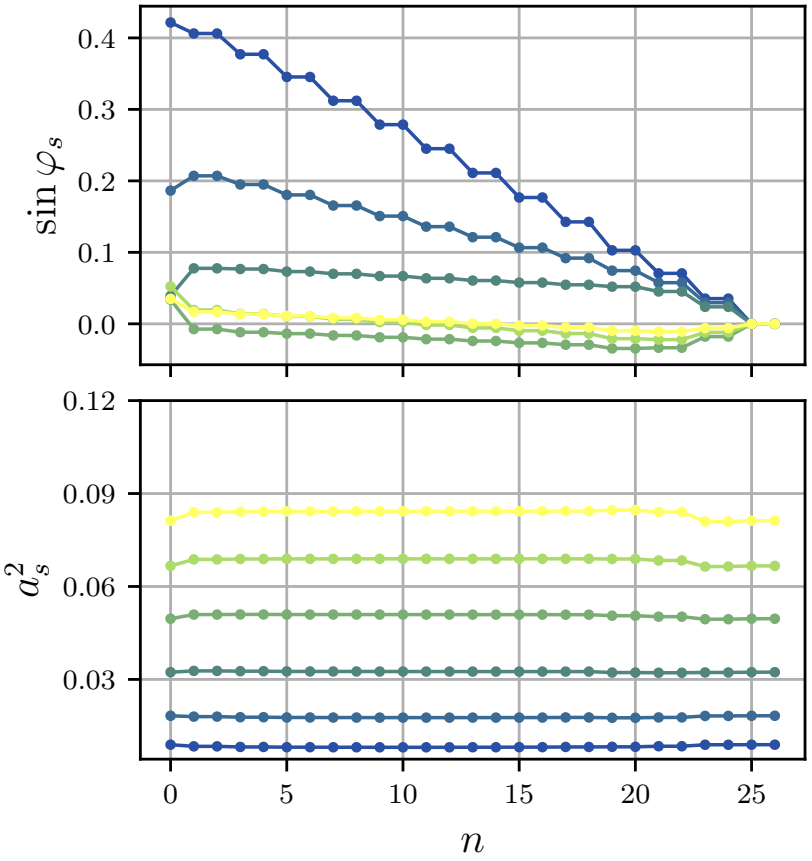

Figure 9.9: Changes of (a) $\sin\varphi_s$ and (b) a_s as functions of the number n of measured sites on the state $|\Psi_T\rangle$, using $N = 26$. $n = 0$ corresponds to the unmeasured state, for which $\varphi_s = E_s T$. Different colors correspond to different scar indices s, and only scars with $a_s^2|_{n=0} > 0.005$ and $\sin\varphi_s|_{n=0} > 0$ are shown (the phases appear in pairs $\pm\varphi_s$ due to the spectrum E_s being symmetric around zero).

in the Born rule case. We further notice that local measurements cause non-local effects mediated by large multipartite correlations, allowing a single-site monitoring to impact the full system entirely. Finally, we uncover that the periodic monitoring unexpectedly acts as a rephasing process that counters the natural scar dephasing.

Our findings shed light on the physics of monitored non-thermalizing models, which are yet widely unexplored, and on memory loss of initial conditions in MIPTs. Moreover, we highlight that measurements can surprisingly be employed to strengthen coherent effects and correct dephasing. Exploring these mechanisms has key relevance for manipulating Rydberg atom arrays, where a structured monitoring could potentially constitute a viable tool to improve control and coherence. In parallel, our results clearly indicate that random decoherence can quickly destroy non-ergodic behavior by obscuring the scar dynamics.

When comparing the uniform and Néel initial states, we observed that entanglement approaches the common steady state over distinct timescales. While not considered in the present analysis, it is reasonable to expect that this difference in the relaxation applies to conventional observables as well. Thus, it would be inter-

esting to investigate whether signatures of this effect can be seen from a Lindbladian approach, possibly being related to a notion of open-system scars that decay slowly.

Another question left for future studies is whether an external monitoring can help to fully stabilize the state revivals in other scarred models where measurements can be implemented continuously in times, without being constrained to multiples of a period T. If so, measurements could potentially be used to protect coherent effects from noise and decoherence. In addition, it might also allow to leverage the quantum Zeno effect to further stabilize the scar dynamics.

Chapter 10

Conclusive remarks and future directions

The work presented in this thesis addresses key questions concerning the understanding and characterization of monitored many-body dynamics. As we have demonstrated, measurement-induced phase transitions (MIPTs) are not limited to the behavior of the entanglement entropy, but also emerge in other indicators of quantum complexity, such as multipartite correlations, magic, and non-Gaussianity. This highlights the intrinsically quantum informational nature of these transitions, in full agreement with their absence in conventional Lindbladian observables. As a consequence, the need for more refined theoretical frameworks to characterize MIPTs remains a central challenge, leaving several fundamental aspects still unresolved.

A natural direction for future research concerns the potential application of measurement-induced phases to practical tasks. As discussed in this thesis, monitored dynamics can generate unique correlation structures and large multipartite entanglement. Can these properties be harnessed in quantum protocols, such as metrology, to enhance their performance? Of course, a major difficulty lies in the stochastic nature of states, which complicates the preparation of repeated copies of them. Nevertheless, monitored dynamics may offer a valuable resource for quantum tasks and control.

The study of MIPTs has also sparked significant interest in non-Hermitian quantum mechanics, which arises naturally in the no-click limit of continuously monitored systems. This setting has been widely explored across a variety of models, revealing critical phenomena that resemble the conventional quantum phase transitions in ground states. For instance, in the quantum Ising chain, criticality can be linked to the closure of a spectral gap, mirroring the Hermitian case. However, this analogy has yet to be proven rigorously, and a full theoretical characterization of non-unitary stationary regimes emerging from postselected monitored dynamics is still missing.

One of the major experimental challenges remains the difficulty of observing MIPTs directly in the laboratory, due to the need for postselection of quantum trajectories. While removing this requirement entirely may be too ambitious, there might still be ways to mitigate it. Our results show that averaging observables over random realizations progressively blurs any signature of the transition. A promising strategy to address this issue could involve harnessing the information stored in the measurement outcomes that identify quantum trajectories, which are usually discarded. For instance, by correlating these records with observables, one could construct non-linear functionals of the density matrix that remain sensitive to the underlying phase diagram.

Finally, a promising direction of investigation is the development of a quantum

thermodynamic characterization of the transition. The volume-law and area-law phases of the entanglement entropy reflect regimes in which different amounts of quantum correlations are destroyed by measurements. As established by Landauer's principle [17], quantum information has physical concreteness, and its erasure is inevitably linked to heat dissipation. This naturally raises the question of whether this mechanism plays a role in MIPTs, possibly distinguishing between the two phases. Such a perspective could bridge the gap between monitored quantum dynamics and conventional thermodynamics, offering a new theoretical lens for characterizing measurement-induced transitions using the conventional tools of statistical physics.

Bibliography

[1] A. Paviglianiti and A. Silva. *"Multipartite entanglement in the measurement-induced phase transition of the quantum Ising chain"*. Phys. Rev. B **108**, 184302 (2023).

[2] A. Paviglianiti, X. Turkeshi, M. Schirò, et al. *"Enhanced Entanglement in the Measurement-Altered Quantum Ising Chain"*. Quantum **8**, 1576 (2024).

[3] A. Paviglianiti, G. Lami, M. Collura, et al. *"Estimating Nonstabilizerness Dynamics Without Simulating It"*. PRX Quantum **6**, 030320 (2025).

[4] A. Paviglianiti, G. D. Fresco, A. Silva, et al. *"Breakdown of Measurement-Induced Phase Transitions Under Information Loss"*. Quantum **9**, 1781 (2025).

[5] A. Paviglianiti and A. Silva. *"Enhancing Revivals via Projective Measurements in a Quantum Scarred System"*. Phys. Rev. Lett. **135**, 090402 (2025).

[6] E. Tirrito, L. Lumia, A. Paviglianiti, et al. *Magic phase transitions in monitored gaussian fermions*. 2025. ArXiv: 2507.07179 (quant-ph).

[7] A. Paviglianiti, L. Lumia, E. Tirrito, et al. *Emergence of Generic Entanglement Structure in Doped Matchgate Circuits*. 2025. ArXiv: 2507.12526 (quant-ph).

[8] L. Amico, R. Fazio, A. Osterloh, et al. *"Entanglement in many-body systems"*. Reviews of Modern Physics **80**, 517–576 (2008).

[9] R. Horodecki, P. Horodecki, M. Horodecki, et al. *"Quantum entanglement"*. Reviews of Modern Physics **81**, 865–942 (2009).

[10] J. M. Deutsch. *"Quantum statistical mechanics in a closed system"*. Phys. Rev. A **43**, 2046–2049 (1991).

[11] M. Rigol, V. Dunjko, and M. Olshanii. *"Thermalization and its mechanism for generic isolated quantum systems"*. Nature **452**, 854–858 (2008).

[12] L. D'Alessio, Y. Kafri, A. Polkovnikov, et al. *"From quantum chaos and eigenstate thermalization to statistical mechanics and thermodynamics"*. Advances in Physics **65**, 239–362 (2016).

[13] C. Gogolin and J. Eisert. *"Equilibration, thermalisation, and the emergence of statistical mechanics in closed quantum systems"*. Reports on Progress in Physics **79**, 056001 (2016).

[14] A. M. Kaufman, M. E. Tai, A. Lukin, et al. *"Quantum thermalization through entanglement in an isolated many-body system"*. Science **353**, 794–800 (2016).

[15] T. Langen, S. Erne, R. Geiger, et al. *"Experimental observation of a generalized Gibbs ensemble"*. Science **348**, 207–211 (2015).

[16] M. Ueda. *"Quantum equilibration, thermalization and prethermalization in ultracold atoms"*. Nature Reviews Physics **2**, 669–681 (2020).

[17] R. Landauer. *"Irreversibility and Heat Generation in the Computing Process"*. IBM Journal of Research and Development **5**, 183–191 (1961).

[18] M. Campisi, P. Hänggi, and P. Talkner. *"Colloquium: Quantum fluctuation relations: Foundations and applications"*. Rev. Mod. Phys. **83**, 771–791 (2011).

[19] J. Goold, M. Huber, A. Riera, et al. *"The role of quantum information in thermodynamics—a topical review"*. Journal of Physics A: Mathematical and Theoretical **49**, 143001 (2016).

[20] A. Polkovnikov, K. Sengupta, A. Silva, et al. *"Colloquium: Nonequilibrium dynamics of closed interacting quantum systems"*. Rev. Mod. Phys. **83**, 863–883 (2011).

[21] M. Heyl. *"Dynamical quantum phase transitions: a review"*. Rep. Prog. Phys. **81**, 054001 (2018).

[22] P. W. Anderson. *"Absence of Diffusion in Certain Random Lattices"*. Phys. Rev. **109**, 1492–1505 (1958).

[23] J. H. Bardarson, F. Pollmann, and J. E. Moore. *"Unbounded Growth of Entanglement in Models of Many-Body Localization"*. Phys. Rev. Lett. **109** (2012).

[24] R. Nandkishore and D. Huse. *"Many-Body Localization and Thermalization in Quantum Statistical Mechanics"*. Annual Review of Condensed Matter Physics **6** (2014).

[25] E. Altman and R. Vosk. *"Universal Dynamics and Renormalization in Many-Body-Localized Systems"*. Annual Review of Condensed Matter Physics **6**, 383–409 (2015).

[26] N. Laflorencie. *"Quantum entanglement in condensed matter systems"*. Phys. Rep. **646**, 1–59 (2016).

[27] R. P. Feynman. *"Simulating physics with computers"*. International Journal of Theoretical Physics **21**, 467–488 (1982).

[28] M. A. Nielsen and I. L. Chuang. *Quantum Computation and Quantum Information: 10th Anniversary Edition*. Cambridge University Press, 2010.

[29] I. M. Georgescu, S. Ashhab, and F. Nori. *"Quantum simulation"*. Reviews of Modern Physics **86**, 153–185 (2014).

[30] C. Monroe, W. C. Campbell, L.-M. Duan, et al. *"Programmable quantum simulations of spin systems with trapped ions"*. Rev. Mod. Phys. **93**, 025001 (2021).

[31] J. Preskill. *"Quantum Computing in the NISQ era and beyond"*. Quantum **2**, 79 (2018).

[32] K. Temme, S. Bravyi, and J. M. Gambetta. *"Error Mitigation for Short-Depth Quantum Circuits"*. Phys. Rev. Lett. **119**, 180509 (2017).

[33] J. Fraxanet, T. Salamon, and M. Lewenstein. "The Coming Decades of Quantum Simulation". In: *Sketches of Physics*. Springer International Publishing, 2023, 85–125.

[34] K. Kim, S. Korenblit, R. Islam, et al. *"Quantum simulation of the transverse Ising model with trapped ions"*. New Journal of Physics **13**, 105003 (2011).

[35] J. Simon, W. Bakr, R. Ma, et al. *"Quantum Simulation of Antiferromagnetic Spin Chains in an Optical Lattice"*. Nature **472**, 307–12 (2011).

[36] H. Bernien, S. Schwartz, A. Keesling, et al. *"Probing many-body dynamics on a 51-atom quantum simulator"*. Nature **551**, 579–584 (2017).

[37] J. Zhang, G. Pagano, P. W. Hess, et al. *"Observation of a many-body dynamical phase transition with a 53-qubit quantum simulator"*. Nature **551**, 601–604 (2017).

[38] Y. Bando, Y. Susa, H. Oshiyama, et al. *"Probing the universality of topological defect formation in a quantum annealer: Kibble-Zurek mechanism and beyond"*. Phys. Rev. Res. **2**, 033369 (2020).

[39] H.-P. Breuer and F. Petruccione. *The Theory of Open Quantum Systems*. Oxford University Press, 2007.

[40] A. J. Daley. *"Quantum trajectories and open many-body quantum systems"*. Advances in Physics **63**, 77–149 (2014).

[41] ´A. Rivas and S. F. Huelga. *Open Quantum Systems: An Introduction*. Springer Berlin Heidelberg, 2012.

[42] S. Diehl, A. Micheli, A. Kantian, et al. *"Quantum states and phases in driven open quantum systems with cold atoms"*. Nature Physics **4**, 878–883 (2008).

[43] E. M. Kessler, G. Giedke, A. Imamoglu, et al. *"Dissipative phase transition in a central spin system"*. Phys. Rev. A **86**, 012116 (2012).

[44] F. Minganti, A. Biella, N. Bartolo, et al. *"Spectral theory of Liouvillians for dissipative phase transitions"*. Phys. Rev. A **98**, 042118 (2018).

[45] G. Lindblad. *"On the Generators of Quantum Dynamical Semigroups"*. Commun. Math. Phys. **48**, 119 (1976).

[46] V. Gorini, A. Kossakowski, and E. C. G. Sudarshan. *"Completely positive dynamical semigroups of N-level systems"*. Journal of Mathematical Physics **17**, 821–825 (1976).

[47] Y. Li, X. Chen, and M. P. A. Fisher. *"Quantum Zeno effect and the many-body entanglement transition"*. Physical Review B **98**, 205136 (2018).

[48] B. Skinner, J. Ruhman, and A. Nahum. *"Measurement-Induced Phase Transitions in the Dynamics of Entanglement"*. Physical Review X **9**, 031009 (2019).

[49] X. Cao, A. Tilloy, and A. De Luca. *"Entanglement in a fermion chain under continuous monitoring"*. SciPost Physics **7**, 024 (2019).

[50] M. P. Fisher, V. Khemani, A. Nahum, et al. *"Random Quantum Circuits"*. Annual Review of Condensed Matter Physics **14**, 335–379 (2023).

[51] M. J. Gullans and D. A. Huse. *"Dynamical Purification Phase Transition Induced by Quantum Measurements"*. Physical Review X **10**, 041020 (2020).

[52] S. Choi, Y. Bao, X.-L. Qi, et al. *"Quantum Error Correction in Scrambling Dynamics and Measurement-Induced Phase Transition"*. Phys. Rev. Lett. **125**, 030505 (2020).

[53] Y. Li, X. Chen, and M. P. A. Fisher. *"Measurement-driven entanglement transition in hybrid quantum circuits"*. Physical Review B **100**, 134306 (2019).

[54] Y. Bao, S. Choi, and E. Altman. *"Theory of the phase transition in random unitary circuits with measurements"*. Physical Review B **101**, 104301 (2020).

[55] O. Alberton, M. Buchhold, and S. Diehl. *"Entanglement Transition in a Monitored Free-Fermion Chain: From Extended Criticality to Area Law"*. Physical Review Letters **126**, 170602 (2021).

[56] X. Turkeshi, A. Biella, R. Fazio, et al. *"Measurement-induced entanglement transitions in the quantum Ising chain: From infinite to zero clicks"*. Physical Review B **103**, 224210 (2021).

[57] M. Coppola, E. Tirrito, D. Karevski, et al. *"Growth of entanglement entropy under local projective measurements"*. Physical Review B **105**, 094303 (2022).

[58] A. Zabalo, M. J. Gullans, J. H. Wilson, et al. *"Critical properties of the measurement-induced transition in random quantum circuits"*. Physical Review B **101**, 060301(R) (2020).

[59] O. Lunt, M. Szyniszewski, and A. Pal. *"Measurement-induced criticality and entanglement clusters: A study of one-dimensional and two-dimensional Clifford circuits"*. Phys. Rev. B **104**, 155111 (2021).

[60] S. Sharma, X. Turkeshi, R. Fazio, et al. *"Measurement-induced criticality in extended and long-range unitary circuits"*. SciPost Physics Core **5**, 023 (2022).

[61] P. Sierant, M. Schirò, M. Lewenstein, et al. *"Measurement-induced phase transitions in $(d+1)$-dimensional stabilizer circuits"*. Physical Review B **106**, 214316 (2022).

[62] M. Block, Y. Bao, S. Choi, et al. *"Measurement-Induced Transition in Long-Range Interacting Quantum Circuits"*. Physical Review Letters **128**, 010604 (2022).

[63] C.-M. Jian, Y.-Z. You, R. Vasseur, et al. *"Measurement-induced criticality in random quantum circuits"*. Physical Review B **101**, 104302 (2020).

[64] A. C. Potter and R. Vasseur. "Entanglement Dynamics in Hybrid Quantum Circuits". In: *Entanglement in Spin Chains*. Springer International Publishing, 2022, 211–249.

[65] S. Sang and T. H. Hsieh. *"Measurement-protected quantum phases"*. Physical Review Research **3**, 023200 (2021).

[66] T. Minato, K. Sugimoto, T. Kuwahara, et al. *"Fate of Measurement-Induced Phase Transition in Long-Range Interactions"*. Phys. Rev. Lett. **128**, 010603 (2022).

[67] P. Sierant and X. Turkeshi. *"Entanglement and Absorbing State Transitions in (d+1)-Dimensional Stabilizer Circuits"*. Acta Phys. Pol. A **144**, 474–485 (2023).

[68] P. Sierant, M. Schirò, M. Lewenstein, et al. *"Entanglement Growth and Minimal Membranes in (d+1) Random Unitary Circuits"*. Phys. Rev. Lett. **131**, 230403 (2023).

[69] Z. Li, A. Delmonte, X. Turkeshi, et al. *Monitored long-range interacting systems: spin-wave theory for quantum trajectories*. 2024. ArXiv: 2405.12124 (quant-ph).

[70] P. Calabrese and J. Cardy. *"Entanglement entropy and quantum field theory"*. J. Stat. Mech. **2004**, P06002 (2004).

[71] P. Calabrese and J. Cardy. *"Entanglement entropy and conformal field theory"*. J. Phys. A **42**, 504005 (2009).

[72] A. Nahum, J. Ruhman, S. Vijay, et al. *"Quantum Entanglement Growth under Random Unitary Dynamics"*. Phys. Rev. X **7**, 031016 (2017).

[73] S. Gopalakrishnan and M. J. Gullans. *"Entanglement and Purification Transitions in Non-Hermitian Quantum Mechanics"*. Physical Review Letters **126**, 170503 (2021).

[74] Y. Kuno, T. Orito, and I. Ichinose. *"Purification and scrambling in a chaotic Hamiltonian dynamics with measurements"*. Physical Review B **106**, 214304 (2022).

[75] S. P. Kelly, U. Poschinger, F. Schmidt-Kaler, et al. *Coherence requirements for quantum communication from hybrid circuit dynamics*. 2022.

[76] U. Agrawal, A. Zabalo, K. Chen, et al. *"Entanglement and Charge-Sharpening Transitions in U(1) Symmetric Monitored Quantum Circuits"*. Physical Review X **12**, 041002 (2022).

[77] F. Barratt, U. Agrawal, S. Gopalakrishnan, et al. *"Field Theory of Charge Sharpening in Symmetric Monitored Quantum Circuits"*. Physical Review Letters **129**, 120604 (2022).

[78] H. Oshima and Y. Fuji. *"Charge fluctuation and charge-resolved entanglement in a monitored quantum circuit with $U(1)$ symmetry"*. Phys. Rev. B **107**, 014308 (2023).

[79] X. Feng, N. Fishchenko, S. Gopalakrishnan, et al. *"Charge and Spin Sharpening Transitions on Dynamical Quantum Trees"*. Quantum **9**, 1692 (2025).

[80] G. Martín-Vázquez, T. Tolppanen, and M. Silveri. *Phase transitions induced by standard and predetermined measurements in transmon arrays*. 2023.

[81] S. Bravyi and A. Kitaev. *"Universal quantum computation with ideal Clifford gates and noisy ancillas"*. Phys. Rev. A **71**, 022316 (2005).

[82] V. Veitch, S. A. H. Mousavian, D. Gottesman, et al. *"The resource theory of stabilizer quantum computation"*. New Journal of Physics **16**, 013009 (2014).

[83] L. Leone, S. F. Oliviero, and A. Hamma. *"Stabilizer Rényi Entropy"*. Phys. Rev. Lett. **128**, 050402 (2022).

[84] T. Haug and L. Piroli. *"Stabilizer entropies and nonstabilizerness monotones"*. Quantum **7**, 1092 (2023).

[85] J. R. Seddon, B. Regula, H. Pashayan, et al. *"Quantifying Quantum Speedups: Improved Classical Simulation From Tighter Magic Monotones"*. PRX Quantum **2**, 010345 (2021).

[86] M. Howard and E. Campbell. *"Application of a Resource Theory for Magic States to Fault-Tolerant Quantum Computing"*. Phys. Rev. Lett. **118**, 090501 (2017).

[87] Z.-W. Liu and A. Winter. *"Many-Body Quantum Magic"*. PRX Quantum **3**, 020333 (2022).

[88] T. Haug and M. Kim. *"Scalable Measures of Magic Resource for Quantum Computers"*. PRX Quantum **4**, 010301 (2023).

[89] A. Nahum and B. Skinner. *"Entanglement and dynamics of diffusion-annihilation processes with Majorana defects"*. Phys. Rev. Res. **2**, 023288 (2020).

[90] A. Nahum, S. Roy, B. Skinner, et al. *"Measurement and Entanglement Phase Transitions in All-To-All Quantum Circuits, on Quantum Trees, and in Landau-Ginsburg Theory"*. PRX Quantum **2**, 010352 (2021).

[91] M. Fava, L. Piroli, T. Swann, et al. *"Nonlinear Sigma Models for Monitored Dynamics of Free Fermions"*. Physical Review X **13**, 041045 (2023).

[92] I. Poboiko, P. Pöpperl, I. V. Gornyi, et al. *"Theory of Free Fermions under Random Projective Measurements"*. Phys. Rev. X **13** (2023).

[93] M. Fava, L. Piroli, D. Bernard, et al. *"Monitored fermions with conserved $U(1)$ charge"*. Phys. Rev. Res. **6**, 043246 (2024).

[94] E. Starchl, M. H. Fischer, and L. M. Sieberer. *"Generalized Zeno Effect and Entanglement Dynamics Induced by Fermion Counting"*. PRX Quantum **6**, 030302 (2025).

[95] I. Poboiko, I. V. Gornyi, and A. D. Mirlin. *"Measurement-Induced Phase Transition for Free Fermions above One Dimension"*. Phys. Rev. Lett. **132**, 110403 (2024).

[96] I. Poboiko, P. Pöpperl, I. V. Gornyi, et al. *"Measurement-induced transitions for interacting fermions"*. Phys. Rev. B **111**, 024204 (2025).

[97] M. Paris and J. Rehacek. *Quantum State Estimation*. 1st. Springer Publishing Company, Incorporated, 2010.

[98] T. Brydges, A. Elben, P. Jurcevic, et al. *"Probing Rényi entanglement entropy via randomized measurements"*. Science **364**, 260–263 (2019).

[99] J. M. Koh, S.-N. Sun, M. Motta, et al. *"Measurement-induced entanglement phase transition on a superconducting quantum processor with mid-circuit readout"*. Nat. Phys. **19**, 1314–1319 (2023).

[100] C. Noel, P. Niroula, D. Zhu, et al. *"Measurement-induced quantum phases realized in a trapped-ion quantum computer"*. Nature Physics **18**, 760–764 (2022).

[101] U. Agrawal, J. Lopez-Piqueres, R. Vasseur, et al. *"Observing Quantum Measurement Collapse as a Learnability Phase Transition"*. Phys. Rev. X **14**, 041012 (2024).

[102] J. C. Hoke, M. Ippoliti, E. Rosenberg, et al. *"Measurement-induced entanglement and teleportation on a noisy quantum processor"*. Nature **622**, 481–486 (2023).

[103] H. Kamakari, J. Sun, Y. Li, et al. *"Experimental Demonstration of Scalable Cross-Entropy Benchmarking to Detect Measurement-Induced Phase Transitions on a Superconducting Quantum Processor"*. Phys. Rev. Lett. **134**, 120401 (2025).

[104] J.-S. Caux and F. H. L. Essler. *"Time Evolution of Local Observables After Quenching to an Integrable Model"*. Phys. Rev. Lett. **110**, 257203 (2013).

[105] B. Bertini, M. Collura, J. De Nardis, et al. *"Transport in Out-of-Equilibrium XXZ Chains: Exact Profiles of Charges and Currents"*. Phys. Rev. Lett. **117**, 207201 (2016).

[106] L. Vidmar and M. Rigol. *"Generalized Gibbs ensemble in integrable lattice models"*. Journal of Statistical Mechanics: Theory and Experiment **2016**, 064007 (2016).

[107] O. A. Castro-Alvaredo, B. Doyon, and T. Yoshimura. *"Emergent Hydrodynamics in Integrable Quantum Systems Out of Equilibrium"*. Phys. Rev. X **6**, 041065 (2016).

[108] V. Alba and P. Calabrese. *"Entanglement and thermodynamics after a quantum quench in integrable systems"*. Proceedings of the National Academy of Sciences **114**, 7947–7951 (2017).

[109] J. De Nardis, D. Bernard, and B. Doyon. *"Hydrodynamic Diffusion in Integrable Systems"*. Phys. Rev. Lett. **121**, 160603 (2018).

[110] E. Fradkin. *Field Theories of Condensed Matter Physics*. 2nd ed. Cambridge University Press, 2013.

[111] E. Knill. *Fermionic Linear Optics and Matchgates*. 2001. ArXiv: quant-ph/0108033.

[112] L. G. Valiant. "Quantum computers that can be simulated classically in polynomial time". In: *Proc. Annu. ACM Symp. Theory Comput.* New York, NY, USA: Association for Computing Machinery, 2001, 114–123.

[113] B. M. Terhal and D. P. DiVincenzo. *"Classical simulation of noninteracting-fermion quantum circuits"*. Phys. Rev. A **65** (2002).

[114] R. Jozsa and A. Miyake. *"Matchgates and classical simulation of quantum circuits"*. Proc. R. Soc. A Math. Phys. Eng. Sci. **464**, 3089–3106 (2008).

[115] B. Dias and R. Koenig. *"Classical simulation of non-Gaussian fermionic circuits"*. Quantum **8**, 1350 (2024).

[116] J. Surace and L. Tagliacozzo. *"Fermionic Gaussian states: an introduction to numerical approaches"*. SciPost Phys. Lect. Notes , 54 (2022).

[117] G. B. Mbeng, A. Russomanno, and G. E. Santoro. *"The quantum Ising chain for beginners"*. SciPost Phys. Lect. Notes 82 (2024).

[118] O. Reardon-Smith, M. Oszmaniec, and K. Korzekwa. *"Improved simulation of quantum circuits dominated by free fermionic operations"*. Quantum **8**, 1549 (2024).

[119] A. Mocherla, L. Lao, and D. E. Browne. *Extending Matchgate Simulation Methods to Universal Quantum Circuits*. 2024. ArXiv: 2302.02654 (quant-ph).

[120] D. Gottesman. *"Stabilizer Codes and Quantum Error Correction"*. ArXiv: quant-ph/9705052 (1997).

[121] D. Gottesman. *"Theory of fault-tolerant quantum computation"*. Phys. Rev. A **57**, 127–137 (1998).

[122] D. Gottesman. *"The Heisenberg Representation of Quantum Computers"*. ArXiv: quant-ph/9807006 (1998).

[123] S. Aaronson and D. Gottesman. *"Improved simulation of stabilizer circuits"*. Phys. Rev. A **70**, 052328 (2004).

[124] C. Gidney. *"Stim: a fast stabilizer circuit simulator"*. Quantum **5**, 497 (2021).

[125] G. Vidal. *"Efficient Simulation of One-Dimensional Quantum Many-Body Systems"*. Phys. Rev. Lett. **93**, 040502 (2004).

[126] M. B. Hastings. *"An area law for one-dimensional quantum systems"*. Journal of Statistical Mechanics: Theory and Experiment **2007**, P08024–P08024 (2007).

[127] U. Schollwöck. *"The density-matrix renormalization group in the age of matrix product states"*. Annals of Physics **326**, 96–192 (2011).

[128] P. Silvi, F. Tschirsich, M. Gerster, et al. *"The Tensor Networks Anthology: Simulation techniques for many-body quantum lattice systems"*. SciPost Phys. Lect. Notes , 8 (2019).

[129] J. Biamonte. *Lectures on Quantum Tensor Networks*. 2020. ArXiv: 1912.10049 (quant-ph).

[130] M. Hofmann, A. Osterloh, and O. Gühne. *"Scaling of genuine multiparticle entanglement close to a quantum phase transition"*. Physical Review B **89**, 134101 (2014).

[131] G. Tóth. *"Multipartite entanglement and high-precision metrology"*. Phys. Rev. A **85**, 022322 (2012).

[132] P. Hyllus, W. Laskowski, R. Krischek, et al. *"Fisher information and multiparticle entanglement"*. Physical Review A **85**, 022321 (2012).

[133] P. Hauke, M. Heyl, L. Tagliacozzo, et al. *"Measuring multipartite entanglement through dynamic susceptibilities"*. Nature Physics **12**, 778–782 (2016).

[134] L. Pezzé, M. Gabbrielli, L. Lepori, et al. *"Multipartite Entanglement in Topological Quantum Phases"*. Physical Review Letters **119**, 250401 (2017).

[135] M. Brenes, S. Pappalardi, J. Goold, et al. *"Multipartite Entanglement Structure in the Eigenstate Thermalization Hypothesis"*. Physical Review Letters **124**, 040605 (2020).

[136] B. Swingle. *"Unscrambling the physics of out-of-time-order correlators"*. Nature Phys. **14**, 988–990 (2018).

[137] P. Richerme, Z.-X. Gong, A. Lee, et al. *"Non-local propagation of correlations in quantum systems with long-range interactions"*. Nature **511**, 198–201 (2014).

[138] S. Xu and B. Swingle. *"Locality, Quantum Fluctuations, and Scrambling"*. Phys. Rev. X **9**, 031048 (2019).

[139] R. J. Lewis-Swan, A. Safavi-Naini, A. M. Kaufman, et al. *"Dynamics of quantum information"*. Nature Reviews Physics **1**, 627–634 (2019).

[140] M. Schecter and T. Iadecola. *"Weak Ergodicity Breaking and Quantum Many-Body Scars in Spin-1 XY Magnets"*. Phys. Rev. Lett. **123**, 147201 (2019).

[141] M. Serbyn, D. A. Abanin, and Z. Papi'c. *"Quantum many-body scars and weak breaking of ergodicity"*. Nature Physics **17**, 675–685 (2021).

[142] F. M. Surace, M. Votto, E. G. Lazo, et al. *"Exact many-body scars and their stability in constrained quantum chains"*. Phys. Rev. B **103**, 104302 (2021).

[143] F. M. Surace, M. Dalmonte, and A. Silva. *"Quantum local random networks and the statistical robustness of quantum scars"*. SciPost Phys. **14**, 174 (2023).

[144] L. Logari ć, S. Dooley, S. Pappalardi, et al. *"Quantum Many-Body Scars in Dual-Unitary Circuits"*. Phys. Rev. Lett. **132**, 010401 (2024).

[145] C. J. Turner, A. A. Michailidis, D. A. Abanin, et al. *"Weak ergodicity breaking from quantum many-body scars"*. Nature Physics **14**, 745–749 (2018).

[146] C. J. Turner, A. A. Michailidis, D. A. Abanin, et al. *"Quantum scarred eigenstates in a Rydberg atom chain: Entanglement, breakdown of thermalization, and stability to perturbations"*. Phys. Rev. B **98**, 155134 (2018).

[147] W. W. Ho, S. Choi, H. Pichler, et al. *"Periodic Orbits, Entanglement, and Quantum Many-Body Scars in Constrained Models: Matrix Product State Approach"*. Phys. Rev. Lett. **122**, 040603 (2019).

[148] C. J. Turner, J.-Y. Desaules, K. Bull, et al. *"Correspondence Principle for Many-Body Scars in Ultracold Rydberg Atoms"*. Phys. Rev. X **11**, 021021 (2021).

[149] J.-Y. Desaules, F. Pietracaprina, Z. Papi ć, et al. *"Extensive Multipartite Entanglement from su(2) Quantum Many-Body Scars"*. Phys. Rev. Lett. **129**, 020601 (2022).

[150] C.-J. Lin and O. I. Motrunich. *"Exact Quantum Many-Body Scar States in the Rydberg-Blockaded Atom Chain"*. Phys. Rev. Lett. **122**, 173401 (2019).

[151] G. Giudici, F. M. Surace, and H. Pichler. *"Unraveling PXP Many-Body Scars through Floquet Dynamics"*. Phys. Rev. Lett. **133**, 190404 (2024).

[152] D. Yuan, S.-Y. Zhang, Y. Wang, et al. *"Quantum information scrambling in quantum many-body scarred systems"*. Phys. Rev. Res. **4**, 023095 (2022).

[153] C. H. Bennett, G. Brassard, C. Crépeau, et al. *"Teleporting an unknown quantum state via dual classical and Einstein-Podolsky-Rosen channels"*. Phys. Rev. Lett. **70**, 1895–1899 (1993).

[154] J. Bardeen, L. N. Cooper, and J. R. Schrieffer. *"Theory of Superconductivity"*. Phys. Rev. **108**, 1175–1204 (1957).

[155] E. Chitambar and G. Gour. *"Quantum resource theories"*. Reviews of Modern Physics **91**, 025001 (2019).

[156] G. Gour. *Resources of the Quantum World*. 2024. ArXiv: 2402.05474 (quant-ph).

[157] A. Hamma, R. Ionicioiu, and P. Zanardi. *"Ground state entanglement and geometric entropy in the Kitaev model"*. Phys. Lett. A **337**, 22–28 (2005).

[158] A. Kitaev and J. Preskill. *"Topological Entanglement Entropy"*. Physical Review Letters **96**, 110404 (2006).

[159] M. Levin and X.-G. Wen. *"Detecting Topological Order in a Ground State Wave Function"*. Physical Review Letters **96**, 110405 (2006).

[160] V. Alba and P. Calabrese. *"Entanglement dynamics after quantum quenches in generic integrable systems"*. SciPost Phys. **4**, 017 (2018).

[161] P. Calabrese and J. Cardy. *"Evolution of entanglement entropy in one-dimensional systems"*. J. Stat. Mech. **2005**, P04010 (2005).

[162] S. Pappalardi, A. Russomanno, B. Žunkovič, et al. *"Scrambling and entanglement spreading in long-range spin chains"*. Phys. Rev. B **98** (2018).

[163] A. Aspect, P. Grangier, and G. Roger. *"Experimental Tests of Realistic Local Theories via Bell's Theorem"*. Phys. Rev. Lett. **47**, 460–463 (1981).

[164] R. Islam, R. Ma, P. M. Preiss, et al. *"Measuring entanglement entropy in a quantum many-body system"*. Nature **528**, 77–83 (2015).

[165] *"Direct Estimations of Linear and Nonlinear Functionals of a Quantum State, author = Ekert, Artur K. and Alves, Carolina Moura and Oi, Daniel K. L. and Horodecki, Michał and Horodecki, Paweł and Kwek, L. C."* Phys. Rev. Lett. **88**, 217901 (2002).

[166] L. Pezzé and A. Smerzi. *Quantum theory of phase estimation*. 2014.

[167] L. Pezzé, A. Smerzi, M. K. Oberthaler, et al. *"Quantum metrology with non-classical states of atomic ensembles"*. Reviews of Modern Physics **90**, 035005 (2018).

[168] B. Groisman, S. Popescu, and A. Winter. *"Quantum, classical, and total amount of correlations in a quantum state"*. Phys. Rev. A **72**, 032317 (2005).

[169] G. Vidal and R. F. Werner. *"Computable measure of entanglement"*. Phys. Rev. A **65**, 032314 (2002).

[170] M. B. Plenio. *"Logarithmic Negativity: A Full Entanglement Monotone That is not Convex"*. Phys. Rev. Lett. **95**, 090503 (2005).

[171] P. Calabrese, J. Cardy, and E. Tonni. *"Entanglement Negativity in Quantum Field Theory"*. Phys. Rev. Lett. **109** (2012).

[172] A. Peres. *"Separability Criterion for Density Matrices"*. Phys. Rev. Lett. **77**, 1413–1415 (1996).

[173] C. H. Bennett, D. P. DiVincenzo, J. A. Smolin, et al. *"Mixed-state entanglement and quantum error correction"*. Phys. Rev. A **54**, 3824–3851 (1996).

[174] H. Shapourian, K. Shiozaki, and S. Ryu. *"Partial time-reversal transformation and entanglement negativity in fermionic systems"*. Phys. Rev. B **95**, 165101 (2017).

[175] H. Shapourian, P. Ruggiero, S. Ryu, et al. *"Twisted and untwisted negativity spectrum of free fermions"*. SciPost Phys. **7**, 037 (2019).

[176] S. Murciano, R. Bonsignori, and P. Calabrese. *"Symmetry decomposition of negativity of massless free fermions"*. SciPost Phys. **10**, 111 (2021).

[177] S. Murciano, V. Vitale, M. Dalmonte, et al. *"Negativity Hamiltonian: An Operator Characterization of Mixed-State Entanglement"*. Phys. Rev. Lett. **128**, 140502 (2022).

[178] F. Rottoli, S. Murciano, E. Tonni, et al. *"Entanglement and negativity Hamiltonians for the massless Dirac field on the half line"*. J. Stat. Mech. **2023**, 013103 (2023).

[179] D. Bertsimas and J. Tsitsiklis. *"Simulated Annealing"*. Statistical Science **8**, 10–15 (1993).

[180] S. Ledesma, G. Aviña, and R. Sanchez. "Practical Considerations for Simulated Annealing Implementation". In: *Simulated Annealing*. Rijeka: IntechOpen, 2008. Chap. 20.

[181] S. Sachdev and J. Ye. *"Gapless spin-fluid ground state in a random quantum Heisenberg magnet"*. Phys. Rev. Lett. **70**, 3339–3342 (1993).

[182] J. Maldacena and D. Stanford. *"Remarks on the Sachdev-Ye-Kitaev model"*. Phys. Rev. D **94**, 106002 (2016).

[183] C. Liu, X. Chen, and L. Balents. *"Quantum entanglement of the Sachdev-Ye-Kitaev models"*. Phys. Rev. B **97**, 245126 (2018).

[184] T. Kinoshita, T. Wenger, and D. S. Weiss. *"A quantum Newton's cradle"*. Nature **440**, 900–903 (2006).

[185] P. Calabrese and J. Cardy. *"Time Dependence of Correlation Functions Following a Quantum Quench"*. Phys. Rev. Lett. **96**, 136801 (2006).

[186] F. H. L. Essler and M. Fagotti. *"Quench dynamics and relaxation in isolated integrable quantum spin chains"*. Journal of Statistical Mechanics: Theory and Experiment **2016**, 064002 (2016).

[187] A. Mitra. *"Quantum Quench Dynamics"*. Annual Review of Condensed Matter Physics **9**, 245–259 (2018).

[188] M. Rigol, V. Dunjko, V. Yurovsky, et al. *"Relaxation in a Completely Integrable Many-Body Quantum System: An Ab Initio Study of the Dynamics of the Highly Excited States of 1D Lattice Hard-Core Bosons"*. Phys. Rev. Lett. **98**, 050405 (2007).

[189] W. G. Brown and L. Viola. *"Convergence Rates for Arbitrary Statistical Moments of Random Quantum Circuits"*. Phys. Rev. Lett. **104**, 250501 (2010).

[190] A. Nahum, S. Vijay, and J. Haah. *"Operator Spreading in Random Unitary Circuits"*. Phys. Rev. X **8**, 021014 (2018).

[191] C. W. von Keyserlingk, T. Rakovszky, F. Pollmann, et al. *"Operator Hydrodynamics, OTOCs, and Entanglement Growth in Systems without Conservation Laws"*. Phys. Rev. X **8**, 021013 (2018).

[192] T. Guhr, A. Müller–Groeling, and H. A. Weidenmüller. *"Random-matrix theories in quantum physics: common concepts"*. Physics Reports **299**, 189–425 (1998).

[193] S. Pappalardi, A. Russomanno, A. Silva, et al. *"Multipartite entanglement after a quantum quench"*. Journal of Statistical Mechanics: Theory and Experiment **2017**, 053104 (2017).

[194] R. Vosk and E. Altman. *"Many-Body Localization in One Dimension as a Dynamical Renormalization Group Fixed Point"*. Phys. Rev. Lett. **110**, 067204 (2013).

[195] G. Roósz, R. Juhász, and F. Iglói. *"Nonequilibrium dynamics of the Ising chain in a fluctuating transverse field"*. Phys. Rev. B **93** (2016).

[196] P. Marian and T. A. Marian. *"Relative entropy is an exact measure of non-Gaussianity"*. Phys. Rev. A **88**, 012322 (2013).

[197] P. Sierant, P. Stornati, and X. Turkeshi. *Fermionic Magic Resources of Quantum Many-Body Systems*. 2025. ArXiv: 2506.00116 (quant-ph).

[198] E. R. Caianiello and S. Fubini. *"On the Algorithm of Dirac spurs"*. Il Nuovo Cimento **9**, 1218–1226 (1952).

[199] E. Barouch and B. M. McCoy. *"Statistical Mechanics of the XY Model. II. Spin-Correlation Functions"*. Phys. Rev. A **3**, 786–804 (1971).

[200] A. Kitaev. *"Fault-tolerant quantum computation by anyons"*. Annals of Physics **303**, 2–30 (2003).

[201] A. G. Fowler, M. Mariantoni, J. M. Martinis, et al. *"Surface codes: Towards practical large-scale quantum computation"*. Phys. Rev. A **86**, 032324 (2012).

[202] D. A. Lidar and T. A. Brun. *Quantum Error Correction*. 2013.

[203] L. Fidkowski, J. Haah, and M. B. Hastings. *"How Dynamical Quantum Memories Forget"*. Quantum **5**, 382 (2021).

[204] J. Odavić, T. Haug, G. Torre, et al. *"Complexity of frustration: A new source of non-local non-stabilizerness"*. SciPost Phys. **15**, 131 (2023).

[205] S. F. E. Oliviero, L. Leone, and A. Hamma. *"Magic-state resource theory for the ground state of the transverse-field Ising model"*. Phys. Rev. A **106**, 042426 (2022).

[206] P. S. Tarabunga, E. Tirrito, T. Chanda, et al. *"Many-Body Magic Via Pauli-Markov Chains—From Criticality to Gauge Theories"*. PRX Quantum **4**, 040317 (2023).

[207] X. Turkeshi, A. Dymarsky, and P. Sierant. *"Pauli spectrum and nonstabilizerness of typical quantum many-body states"*. Phys. Rev. B **111**, 054301 (2025).

[208] P. S. Tarabunga. *"Critical behaviors of non-stabilizerness in quantum spin chains"*. Quantum **8**, 1413 (2024).

[209] M. Frau, P. S. Tarabunga, M. Collura, et al. *"Nonstabilizerness versus entanglement in matrix product states"*. Phys. Rev. B **110**, 045101 (2024).

[210] P. S. Tarabunga and E. Tirrito. *Magic transition in measurement-only circuits*. 2024. ArXiv: 2407.15939 (quant-ph).

[211] M. Hoshino, M. Oshikawa, and Y. Ashida. *Stabilizer Rényi Entropy and Conformal Field Theory*. 2025. ArXiv: 2503.13599 (quant-ph).

[212] M. Frau, P. S. Tarabunga, M. Collura, et al. *"Stabilizer disentangling of conformal field theories"*. SciPost Phys. **18**, 165 (2025).

[213] X. Turkeshi, E. Tirrito, and P. Sierant. *"Magic spreading in random quantum circuits"*. Nature Communications **16** (2025).

[214] Y. Zhang and Y. Gu. *Quantum magic dynamics in random circuits*. 2024. ArXiv: 2410.21128 (quant-ph).

[215] Z.-Y. Hou, C. Cao, and Z.-C. Yang. *Stabilizer Entanglement as a Magic Highway*. 2025. ArXiv: 2503.20873 (quant-ph).

[216] G. C. Santra, A. Windey, S. Bandyopadhyay, et al. *Complexity transitions in chaotic quantum systems*. 2025. ArXiv: 2505.09707 (quant-ph).

[217] E. Tirrito, X. Turkeshi, and P. Sierant. *Anticoncentration and magic spreading under ergodic quantum dynamics*. 2024. ArXiv: 2412.10229 (quant-ph).

[218] D. Szombathy, A. Valli, C. P. Moca, et al. *Independent stabilizer Rényi entropy and entanglement fluctuations in random unitary circuits*. 2025. ArXiv: 2501.11489 (quant-ph).

[219] D. Szombathy, A. Valli, C. P. Moca, et al. *Spectral Properties Versus Magic Generation in T-doped Random Clifford Circuits*. 2025. ArXiv: 2412.15912 (quant-ph).

[220] D. Sticlet, B. Dóra, D. Szombathy, et al. *Non-stabilizerness in open XXZ spin chains: Universal scaling and dynamics*. 2025. ArXiv: 2504.11139 (quant-ph).

[221] L. Leone, S. F. E. Oliviero, Y. Zhou, et al. *"Quantum Chaos is Quantum"*. Quantum **5**, 453 (2021).

[222] E. Tirrito, P. S. Tarabunga, D. S. Bhakuni, et al. *Universal Spreading of Nonstabilizerness and Quantum Transport*. 2025. ArXiv: 2506.12133 (quant-ph).

[223] X. Turkeshi. *"Coherent errors make magic"*. Nature Phys. **20**, 1696–1697 (2024).

[224] B. Magni, A. Christopoulos, A. D. Luca, et al. *Anticoncentration in Clifford Circuits and Beyond: From Random Tensor Networks to Pseudo-Magic States*. 2025. ArXiv: 2502.20455 (quant-ph).

[225] B. Magni and X. Turkeshi. *Quantum Complexity and Chaos in Many-Qudit Doped Clifford Circuits*. 2025. ArXiv: 2506.02127 (quant-ph).

[226] T. Haug, L. Aolita, and M. Kim. *"Probing quantum complexity via universal saturation of stabilizer entropies"*. Quantum **9**, 1801 (2025).

[227] A. G. Catalano, J. Odavić, G. Torre, et al. *Magic phase transition and nonlocal complexity in generalized W State*. 2024. ArXiv: 2406.19457 (quant-ph).

[228] G. Passarelli, R. Fazio, and P. Lucignano. *"Nonstabilizerness of permutationally invariant systems"*. Phys. Rev. A **110**, 022436 (2024).

[229] G. Passarelli, P. Lucignano, D. Rossini, et al. *"Chaos and magic in the dissipative quantum kicked top"*. Quantum **9**, 1653 (2025).

[230] G. Passarelli, A. Russomanno, and P. Lucignano. *Nonstabilizerness of a Boundary Time Crystal*. 2025. ArXiv: 2503.05243 (quant-ph).

[231] B. Jasser, J. Odavic, and A. Hamma. *Stabilizer Entropy and entanglement complexity in the Sachdev-Ye-Kitaev model*. 2025. ArXiv: 2502.03093 (quant-ph).

[232] J. Odavić, M. Viscardi, and A. Hamma. *Stabilizer entropy in non-integrable quantum evolutions*. 2025. ArXiv: 2412.10228 (quant-ph).

[233] S. Bera and M. Schirò. *Non-Stabilizerness of Sachdev-Ye-Kitaev Model*. 2025. ArXiv: 2502.01582 (quant-ph).

[234] A. Sinibaldi, A. F. Mello, M. Collura, et al. *Non-stabilizerness of Neural Quantum States*. 2025. ArXiv: 2502.09725 (quant-ph).

[235] S. Zhou, Z.-C. Yang, A. Hamma, et al. *"Single T gate in a Clifford circuit drives transition to universal entanglement spectrum statistics"*. SciPost Phys. **9**, 087 (2020).

[236] F. B. Trigueros and J. A. M. Guzmán. *Nonstabilizerness and Error Resilience in Noisy Quantum Circuits*. 2025. ArXiv: 2506.18976 (quant-ph).

[237] N. D. Varikuti, S. Bandyopadhyay, and P. Hauke. *Impact of Clifford operations on non-stabilizing power and quantum chaos*. 2025. ArXiv: 2505.14793 (quant-ph).

[238] M. Heinrich and D. Gross. *"Robustness of Magic and Symmetries of the Stabiliser Polytope"*. Quantum **3**, 132 (2019).

[239] K. M. R. Audenaert and M. B. Plenio. *"Entanglement on mixed stabilizer states: normal forms and reduction procedures"*. New Journal of Physics **7**, 170–170 (2005).

[240] H. M. Wiseman. *"Quantum trajectories and quantum measurement theory"*. Quantum and Semiclassical Optics: Journal of the European Optical Society Part B **8**, 205–222 (1996).

[241] H. Carmichael. *Statistical Methods in Quantum Optics 1*. Springer Berlin, Heidelberg, 1999.

[242] C. Gardiner and P. Zoller. *Quantum Noise*. Springer Berlin, Heidelberg, 2004.

[243] K. Jacobs and D. A. Steck. *"A straightforward introduction to continuous quantum measurement"*. Contemp. Phys. **47**, 279–303 (2006).

[244] T. A. Brun. *"A simple model of quantum trajectories"*. Am. J. Phys. **70**, 719–737 (2002).

[245] H. M. Wiseman and G. J. Milburn. *Quantum Measurement and Control*. Cambridge University Press, 2009.

[246] X. Turkeshi, L. Piroli, and M. Schiró. *"Enhanced entanglement negativity in boundary-driven monitored fermionic chains"*. Phys. Rev. B **106**, 024304 (2022).

[247] X. Turkeshi, M. Dalmonte, R. Fazio, et al. *"Entanglement transitions from stochastic resetting of non-Hermitian quasiparticles"*. Phys. Rev. B **105**, L241114 (2022).

[248] G. Piccitto, A. Russomanno, and D. Rossini. *"Entanglement transitions in the quantum Ising chain: A comparison between different unravelings of the same Lindbladian"*. Physical Review B **105**, 064305 (2022).

[249] A. Russomanno, G. Piccitto, and D. Rossini. *"Entanglement transitions and quantum bifurcations under continuous long-range monitoring"*. Phys. Rev. B **108**, 104313 (2023).

[250] C. Zerba and A. Silva. *"Measurement phase transitions in the no-click limit as quantum phase transitions of a non-hermitean vacuum"*. SciPost Phys. Core **6**, 051 (2023).

[251] P. Sierant, G. Chiriacò, F. M. Surace, et al. *"Dissipative Floquet Dynamics: from Steady State to Measurement Induced Criticality in Trapped-ion Chains"*. Quantum **6**, 638 (2022).

[252] M. Ippoliti, M. J. Gullans, S. Gopalakrishnan, et al. *"Entanglement Phase Transitions in Measurement-Only Dynamics"*. Physical Review X **11**, 011030 (2021).

[253] K. Klocke and M. Buchhold. *"Majorana Loop Models for Measurement-Only Quantum Circuits"*. Phys. Rev. X **13**, 041028 (2023).

[254] K. Chahine and M. Buchhold. *"Entanglement phases, localization, and multifractality of monitored free fermions in two dimensions"*. Phys. Rev. B **110**, 054313 (2024).

[255] P. Sierant and X. Turkeshi. *"Universal Behavior beyond Multifractality of Wave Functions at Measurement-Induced Phase Transitions"*. Phys. Rev. Lett. **128**, 130605 (2022).

[256] T. Müller, S. Diehl, and M. Buchhold. *"Measurement-Induced Dark State Phase Transitions in Long-Ranged Fermion Systems"*. Phys. Rev. Lett. **128**, 010605 (2022).

[257] P. Sierant and X. Turkeshi. *"Controlling Entanglement at Absorbing State Phase Transitions in Random Circuits"*. Physical Review Letters **130**, 120402 (2023).

[258] L. Lumia, E. Tirrito, R. Fazio, et al. *"Measurement-induced transitions beyond Gaussianity: A single particle description"*. Phys. Rev. Res. **6**, 023176 (2024).

[259] E. Tirrito, A. Santini, R. Fazio, et al. *"Full counting statistics as probe of measurement-induced transitions in the quantum Ising chain"*. SciPost Phys. **15**, 096 (2023).

[260] X. Turkeshi and M. Schiró. *"Entanglement and correlation spreading in non-Hermitian spin chains"*. Phys. Rev. B **107**, L020403 (2023).

[261] Z. Li, A. Delmonte, X. Turkeshi, et al. *"Monitored long-range interacting systems: spin-wave theory for quantum trajectories"*. Nature Communications **16**, 4329 (2025).

[262] H.-Z. Li, J.-X. Zhong, and X.-J. Yu. *Measurement-Induced Entanglement Phase Transition in Free Fermion Systems*. 2025. ArXiv: 2503.21427 (quant-ph).

[263] G. Di Fresco, B. Spagnolo, D. Valenti, et al. *"Metrology and multipartite entanglement in measurement-induced phase transition"*. Quantum **8**, 1326 (2024).

[264] Y. L. Gal, X. Turkeshi, and M. Schirò. *"Volume-to-area law entanglement transition in a non-Hermitian free fermionic chain"*. SciPost Phys. **14**, 138 (2023).

[265] Y. Le Gal, X. Turkeshi, and M. Schirò. *"Entanglement Dynamics in Monitored Systems and the Role of Quantum Jumps"*. PRX Quantum **5**, 030329 (2024).

[266] V. Ravindranath, Y. Han, Z.-C. Yang, et al. *"Entanglement steering in adaptive circuits with feedback"*. Phys. Rev. B **108**, L041103 (2023).

[267] L. Piroli, Y. Li, R. Vasseur, et al. *"Triviality of quantum trajectories close to a directed percolation transition"*. Phys. Rev. B **107**, 224303 (2023).

[268] M. Ippoliti and V. Khemani. *"Postselection-Free Entanglement Dynamics via Spacetime Duality"*. Phys. Rev. Lett. **126**, 060501 (2021).

[269] G. Passarelli, X. Turkeshi, A. Russomanno, et al. *"Many-Body Dynamics in Monitored Atomic Gases without Postselection Barrier"*. Phys. Rev. Lett. **132** (2024).

[270] Y. Li, Y. Zou, P. Glorioso, et al. *"Cross Entropy Benchmark for Measurement-Induced Phase Transitions"*. Phys. Rev. Lett. **130**, 220404 (2023).

[271] Y. Li and M. P. A. Fisher. *"Decodable hybrid dynamics of open quantum systems with $\mathbb{Z}_2$ symmetry"*. Phys. Rev. B **108**, 214302 (2023).

[272] S. J. Garratt and E. Altman. *"Probing Postmeasurement Entanglement without Postselection"*. PRX Quantum **5**, 030311 (2024).

[273] X. Turkeshi. *"Measurement-induced criticality as a data-structure transition"*. Physical Review B **106**, 144313 (2022).

[274] S. Sang, Y. Li, T. Zhou, et al. *"Entanglement Negativity at Measurement-Induced Criticality"*. PRX Quantum **2**, 030313 (2021).

[275] J. Merritt and L. Fidkowski. *"Entanglement transitions with free fermions"*. Phys. Rev. B **107**, 064303 (2023).

[276] B. Fan, C. Yin, and A. M. García-García. *Entanglement dynamics of monitored non-interacting fermions on Graphic-Processing-Units*. 2025. ArXiv: 2508.18468 (quant-ph).

[277] A. Nahum, P. Serna, A. M. Somoza, et al. *"Loop models with crossings"*. Phys. Rev. B **87**, 184204 (2013).

[278] G. E. Fux, E. Tirrito, M. Dalmonte, et al. *"Entanglement – nonstabilizerness separation in hybrid quantum circuits"*. Phys. Rev. Res. **6**, L042030 (2024).

[279] M. Bejan, C. McLauchlan, and B. Béri. *"Dynamical Magic Transitions in Monitored Clifford+T Circuits"*. PRX Quantum **5**, 030332 (2024).

[280] A. Lira-Solanilla, X. Turkeshi, and S. Pappalardi. *"Multipartite Entanglement Structure of Monitored Quantum Circuits"*. Phys. Rev. Lett. **135**, 080401 (2025).

[281] M. J. Gullans and D. A. Huse. *"Scalable Probes of Measurement-Induced Criticality"*. Phys. Rev. Lett. **125**, 070606 (2020).

[282] X. Turkeshi, R. Fazio, and M. Dalmonte. *"Measurement-induced criticality in $(2+1)$-dimensional hybrid quantum circuits"*. Physical Review B **102**, 014315 (2020).

[283] Q. Tang and W. Zhu. *"Measurement-induced phase transition: A case study in the nonintegrable model by density-matrix renormalization group calculations"*. Physical Review Research **2**, 013022 (2020).

[284] T. Boorman, M. Szyniszewski, H. Schomerus, et al. *"Diagnostics of entanglement dynamics in noisy and disordered spin chains via the measurement-induced steady-state entanglement transition"*. Physical Review B **105**, 144202 (2022).

[285] M. Szyniszewski, O. Lunt, and A. Pal. *Disordered monitored free fermions*. 2022.

[286] T. Botzung, S. Diehl, and M. Müller. *"Engineered dissipation induced entanglement transition in quantum spin chains: From logarithmic growth to area law"*. Physical Review B **104**, 184422 (2021).

[287] F. Carollo and V. Alba. *"Entangled multiplets and spreading of quantum correlations in a continuously monitored tight-binding chain"*. Physical Review B **106**, L220304 (2022).

[288] S. E. Ahnert and M. C. Payne. *"General implementation of all possible positive-operator-value measurements of single-photon polarization states"*. Physical Review A **71**, 012330 (2005).

[289] B. Svensson. *"Pedagogical review of quantum measurement theory with an emphasis on weak measurements"*. Quanta **2**, 18–49 (2013).

[290] L. P. García-Pintos, D. Tielas, and A. del Campo. *"Spontaneous Symmetry Breaking Induced by Quantum Monitoring"*. Physical Review Letters **123**, 090403 (2019).

[291] J. Dalibard, Y. Castin, and K. Mølmer. *"Wave-function approach to dissipative processes in quantum optics"*. Physical Review Letters **68**, 580–583 (1992).

[292] J. M. Hickey, S. Genway, I. Lesanovsky, et al. *"Time-integrated observables as order parameters for full counting statistics transitions in closed quantum systems"*. Physical Review B **87**, 184303 (2013).

[293] P. M. Poggi and M. H. Muñoz-Arias. *"Measurement-induced multipartite-entanglement regimes in collective spin systems"*. Quantum **8**, 1229 (2024).

[294] F. Minganti, A. Miranowicz, R. W. Chhajlany, et al. *"Hybrid-Liouvillian formalism connecting exceptional points of non-Hermitian Hamiltonians and Liouvillians via postselection of quantum trajectories"*. Phys. Rev. A **101** (2020).

[295] G. Kells, D. Meidan, and A. Romito. *"Topological transitions in weakly monitored free fermions"*. SciPost Phys. **14**, 031 (2023).

[296] C. Y. Leung, D. Meidan, and A. Romito. *"Theory of Free Fermions Dynamics under Partial Postselected Monitoring"*. Phys. Rev. X **15**, 021020 (2025).

[297] M. Coppola, D. Karevski, and G. T. Landi. *"Conditional no-jump dynamics of noninteracting quantum chains"*. Phys. Rev. B **110**, 094315 (2024).

[298] S. Gupta, H. K. Yadalam, M. Kulkarni, et al. *"Quantum jumps in driven-dissipative disordered many-body systems"*. Phys. Rev. A **109**, L050201 (2024).

[299] Y.-G. Liu and S. Chen. *"Lindbladian dynamics with loss of quantum jumps"*. Phys. Rev. B **111**, 024303 (2025).

[300] T. Prosen. *"Third quantization: a general method to solve master equations for quadratic open Fermi systems"*. New J. Phys. **10**, 043026 (2008).

[301] T. Prosen. *"Spectral theorem for the Lindblad equation for quadratic open fermionic systems"*. J. Stat. Mech. **2010**, P07020 (2010).

[302] T. Barthel and Y. Zhang. *"Solving quasi-free and quadratic Lindblad master equations for open fermionic and bosonic systems"*. J. Stat. Mech. **2022**, 113101 (2022).

[303] Y. Zhang and T. Barthel. *"Criticality and Phase Classification for Quadratic Open Quantum Many-Body Systems"*. Phys. Rev. Lett. **129**, 120401 (2022).

[304] A. Biella and M. Schiró. *"Many-Body Quantum Zeno Effect and Measurement-Induced Subradiance Transition"*. Quantum **5**, 528 (2021).

[305] P. Calabrese, J. Cardy, and E. Tonni. *"Entanglement negativity in extended systems: a field theoretical approach"*. J. Stat. Mech. **2013**, P02008 (2013).

[306] B. Horstmann, J. I. Cirac, and G. Giedke. *"Noise-driven dynamics and phase transitions in fermionic systems"*. Phys. Rev. A **87**, 012108 (2013).

[307] S. J. Garratt, Z. Weinstein, and E. Altman. *"Measurements Conspire Nonlocally to Restructure Critical Quantum States"*. Phys. Rev. X **13**, 021026 (2023).

[308] Z. Weinstein, R. Sajith, E. Altman, et al. *"Nonlocality and entanglement in measured critical quantum Ising chains"*. Phys. Rev. B **107**, 245132 (2023).

[309] J. Y. Lee, C.-M. Jian, and C. Xu. *"Quantum Criticality Under Decoherence or Weak Measurement"*. PRX Quantum **4**, 030317 (2023).

[310] Z. Yang, D. Mao, and C.-M. Jian. *"Entanglement in a one-dimensional critical state after measurements"*. Phys. Rev. B **108**, 165120 (2023).

[311] X. Sun, H. Yao, and S.-K. Jian. *New critical states induced by measurement*. 2023. ArXiv: 2301.11337 (quant-ph).

[312] S. Murciano, P. Sala, Y. Liu, et al. *"Measurement-Altered Ising Quantum Criticality"*. Phys. Rev. X **13**, 041042 (2023).

[313] M. Buchhold, Y. Minoguchi, A. Altland, et al. *"Effective Theory for the Measurement-Induced Phase Transition of Dirac Fermions"*. Phys. Rev. X **11**, 041004 (2021).

[314] B. Ladewig, S. Diehl, and M. Buchhold. *"Monitored open fermion dynamics: Exploring the interplay of measurement, decoherence, and free Hamiltonian evolution"*. Phys. Rev. Res. **4**, 033001 (2022).

[315] X. Turkeshi, L. Piroli, and M. Schirò. *"Density and current statistics in boundary-driven monitored fermionic chains"*. Phys. Rev. B **109**, 144306 (2024).

[316] C.-M. Jian, H. Shapourian, B. Bauer, et al. *Measurement-induced entanglement transitions in quantum circuits of non-interacting fermions: Born-rule versus forced measurements*. 2023. ArXiv: 2302.09094 (cond-mat.stat-mech).

[317] S.-K. Jian, C. Liu, X. Chen, et al. *"Measurement-Induced Phase Transition in the Monitored Sachdev-Ye-Kitaev Model"*. Phys. Rev. Lett. **127**, 140601 (2021).

[318] H. Lóio, A. De Luca, J. De Nardis, et al. *"Purification timescales in monitored fermions"*. Phys. Rev. B **108**, L020306 (2023).

[319] J. A. Maki, A. Berti, I. Carusotto, et al. *"Monte Carlo matrix-product-state approach to the false vacuum decay in the monitored quantum Ising chain"*. SciPost Phys. **15**, 152 (2023).

[320] W. W. Ho and S. Choi. *"Exact Emergent Quantum State Designs from Quantum Chaotic Dynamics"*. Phys. Rev. Lett. **128**, 060601 (2022).

[321] P. W. Claeys and A. Lamacraft. *"Emergent quantum state designs and biunitarity in dual-unitary circuit dynamics"*. Quantum **6**, 738 (2022).

[322] M. Ippoliti and W. W. Ho. *"Solvable model of deep thermalization with distinct design times"*. Quantum **6**, 886 (2022).

[323] M. Ippoliti and W. W. Ho. *"Dynamical Purification and the Emergence of Quantum State Designs from the Projected Ensemble"*. PRX Quantum **4**, 030322 (2023).

[324] M. Lucas, L. Piroli, J. De Nardis, et al. *"Generalized deep thermalization for free fermions"*. Phys. Rev. A **107**, 032215 (2023).

[325] P. Łyd żba, M. Mierzejewski, M. Rigol, et al. *"Generalized Thermalization in Quantum-Chaotic Quadratic Hamiltonians"*. Phys. Rev. Lett. **131**, 060401 (2023).

[326] J. Choi, A. L. Shaw, I. S. Madjarov, et al. *"Preparing random states and benchmarking with many-body quantum chaos"*. Nature **613**, 468–473 (2023).

[327] J. S. Cotler, D. K. Mark, H.-Y. Huang, et al. *"Emergent Quantum State Designs from Individual Many-Body Wave Functions"*. PRX Quantum **4**, 010311 (2023).

[328] J. Eisert, V. Eisler, and Z. Zimborás. *"Entanglement negativity bounds for fermionic Gaussian states"*. Phys. Rev. B **97**, 165123 (2018).

[329] A. Neven, J. Carrasco, V. Vitale, et al. *"Symmetry-resolved entanglement detection using partial transpose moments"*. npj Quantum Inf. **7**, 152 (2021).

[330] V. Vitale, A. Elben, R. Kueng, et al. *"Symmetry-resolved dynamical purification in synthetic quantum matter"*. SciPost Phys. **12**, 106 (2022).

[331] X. Turkeshi, P. Ruggiero, and P. Calabrese. *"Negativity spectrum in the random singlet phase"*. Phys. Rev. B **101**, 064207 (2020).

[332] P. Ruggiero and X. Turkeshi. *"Quantum information spreading in random spin chains"*. Phys. Rev. B **106**, 134205 (2022).

[333] V. Alba and F. Carollo. *"Spreading of correlations in Markovian open quantum systems"*. Phys. Rev. B **103**, L020302 (2021).

[334] V. Alba and F. Carollo. *"Logarithmic negativity in out-of-equilibrium open free-fermion chains: An exactly solvable case"*. SciPost Phys. **15**, 124 (2023).

[335] F. Rottoli, S. Murciano, and P. Calabrese. *"Finite temperature negativity Hamiltonians of the massless Dirac fermion"*. J. High Energy Phys. **2023**, 139 (2023).

[336] C.-J. Lin, W. Ye, Y. Zou, et al. *"Probing sign structure using measurement-induced entanglement"*. Quantum **7**, 910 (2023).

[337] Z. Cheng, R. Wen, S. Gopalakrishnan, et al. *"Universal structure of measurement-induced information in many-body ground states"*. Phys. Rev. B **109**, 195128 (2024).

[338] Y. Zhang and S. Gopalakrishnan. *"Nonlocal growth of quantum conditional mutual information under decoherence"*. Phys. Rev. A **110**, 032426 (2024).

[339] M. Plenio and S. Virmani. *"An introduction to entanglement measures"*. Quantum Information and Computation **7**, 001–051 (2005).

[340] L. Piroli, G. Styliaris, and J. I. Cirac. *"Quantum Circuits Assisted by Local Operations and Classical Communication: Transformations and Phases of Matter"*. Phys. Rev. Lett. **127**, 220503 (2021).

[341] N. Tantivasadakarn, A. Vishwanath, and R. Verresen. *"Hierarchy of Topological Order From Finite-Depth Unitaries, Measurement, and Feedforward"*. PRX Quantum **4**, 020339 (2023).

[342] X.-G. Wen. *Quantum Field Theory of Many-Body Systems: From the Origin of Sound to an Origin of Light and Electrons*. Oxford University Press, 2007.

[343] F. Iglói and C. Monthus. *"Strong disorder RG approach of random systems"*. Phys. Rep. **412**, 277–431 (2005).

[344] F. Iglói and C. Monthus. *"Strong disorder RG approach – a short review of recent developments"*. Euro. Phys. J. B **91**, 290 (2018).

[345] E. Granet, C. Zhang, and H. Dreyer. *"Volume-Law to Area-Law Entanglement Transition in a Nonunitary Periodic Gaussian Circuit"*. Phys. Rev. Lett. **130**, 230401 (2023).

[346] B. Barch, N. Anand, J. Marshall, et al. *"Scrambling and operator entanglement in local non-Hermitian quantum systems"*. Phys. Rev. B **108**, 134305 (2023).

[347] X. Turkeshi, M. Dalmonte, R. Fazio, et al. *"Erratum: Entanglement transitions from stochastic resetting of non-Hermitian quasiparticles [Phys. Rev. B 105, L241114 (2022)]"*. Phys. Rev. B **107**, 079901 (2023).

[348] B. Xing, X. Turkeshi, M. Schiró, et al. *"Interactions and integrability in weakly monitored Hamiltonian systems"*. Phys. Rev. B **109**, L060302 (2024).

[349] G. Lami and M. Collura. *"Nonstabilizerness via Perfect Pauli Sampling of Matrix Product States"*. Phys. Rev. Lett. **131**, 180401 (2023).

[350] L. Chen, R. J. Garcia, K. Bu, et al. *"Magic of random matrix product states"*. Phys. Rev. B **109**, 174207 (2024).

[351] G. Lami and M. Collura. *"Unveiling the Stabilizer Group of a Matrix Product State"*. Phys. Rev. Lett. **133**, 010602 (2024).

[352] P. S. Tarabunga, E. Tirrito, M. C. Bañuls, et al. *"Nonstabilizerness via Matrix Product States in the Pauli Basis"*. Phys. Rev. Lett. **133**, 010601 (2024).

[353] P. S. Tarabunga and T. Haug. *Efficient mutual magic and magic capacity with matrix product states*. 2025. ArXiv: 2504.07230 (quant-ph).

[354] M. Collura, J. D. Nardis, V. Alba, et al. *The quantum magic of fermionic Gaussian states*. 2025. ArXiv: 2412.05367 (quant-ph).

[355] A. Russomanno, G. Passarelli, D. Rossini, et al. *Efficient evaluation of the nonstabilizerness in unitary and monitored quantum many-body systems*. 2025. ArXiv: 2502.01431 (quant-ph).

[356] M. Hebenstreit, R. Jozsa, B. Kraus, et al. *"All Pure Fermionic Non-Gaussian States Are Magic States for Matchgate Computations"*. Phys. Rev. Lett. **123**, 080503 (2019).

[357] A. Hamma, R. Ionicioiu, and P. Zanardi. *"Bipartite entanglement and entropic boundary law in lattice spin systems"*. Phys. Rev. A **71**, 022315 (2005).

[358] Z. Webb. *The Clifford group forms a unitary 3-design*. 2016. ArXiv: 1510.02769 (quant-ph).

[359] H. Zhu. *"Multiqubit Clifford groups are unitary 3-designs"*. Phys. Rev. A **96**, 062336 (2017).

[360] A. A. Mele. *"Introduction to Haar Measure Tools in Quantum Information: A Beginner's Tutorial"*. Quantum **8**, 1340 (2024).

[361] K. Wan, W. J. Huggins, J. Lee, et al. *"Matchgate Shadows for Fermionic Quantum Simulation"*. Commun. Math. Phys. **404**, 629–700 (2023).

[362] P. Braccia, N. L. Diaz, M. Larocca, et al. *Optimal Haar random fermionic linear optics circuits*. 2025. ArXiv: 2505.24212 (quant-ph).

[363] D. N. Page. *"Average entropy of a subsystem"*. Phys. Rev. Lett. **71**, 1291–1294 (1993).

[364] S. K. Foong and S. Kanno. *"Proof of Page's conjecture on the average entropy of a subsystem"*. Phys. Rev. Lett. **72**, 1148–1151 (1994).

[365] J. Sánchez-Ruiz. *"Simple proof of Page's conjecture on the average entropy of a subsystem"*. Phys. Rev. E **52**, 5653–5655 (1995).

[366] S. Sen. *"Average Entropy of a Quantum Subsystem"*. Phys. Rev. Lett. **77**, 1–3 (1996).

[367] T. Zhou and A. Nahum. *"Emergent statistical mechanics of entanglement in random unitary circuits"*. Phys. Rev. B **99**, 174205 (2019).

[368] M. Kardar, G. Parisi, and Y.-C. Zhang. *"Dynamic Scaling of Growing Interfaces"*. Phys. Rev. Lett. **56**, 889–892 (1986).

[369] O. Dahlsten and M. B. Plenio. *Exact entanglement probability distribution of bi-partite randomised stabilizer states*. 2007. ArXiv: quant-ph/0511119 (quant-ph).

[370] E. Bianchi, L. Hackl, and M. Kieburg. *"Page curve for fermionic Gaussian states"*. Phys. Rev. B **103**, L241118 (2021).

[371] L. Vidmar, L. Hackl, E. Bianchi, et al. *"Entanglement Entropy of Eigenstates of Quadratic Fermionic Hamiltonians"*. Physical Review Letters **119** (2017).

[372] D. Bernard and L. Piroli. *"Entanglement distribution in the quantum symmetric simple exclusion process"*. Physical Review E **104** (2021).

[373] A. Tiutiakina, H. Lóio, G. Giachetti, et al. *"Field theory for monitored Brownian SYK clusters"*. Quantum **9**, 1794 (2025).

[374] R. Modak, D. Rakshit, and U. Sen. *Finite-size scalings in measurement-induced dynamical phase transition*. 2021. ArXiv: 2107.14647 (quant-ph).

[375] S. F. E. Oliviero, L. Leone, A. Hamma, et al. *"Measuring magic on a quantum processor"*. npj Quantum Information **8**, 148 (2022).

[376] P. Niroula, C. D. White, Q. Wang, et al. *"Phase transition in magic with random quantum circuits"*. Nat. Phys. **20**, 1786–1792 (2024).

[377] X. Turkeshi and P. Sierant. *"Error-Resilience Phase Transitions in Encoding-Decoding Quantum Circuits"*. Phys. Rev. Lett. **132**, 140401 (2024).

[378] A. F. Mello, G. Lami, and M. Collura. *Retrieving non-stabilizerness with Neural Networks*. 2024. ArXiv: 2403.00919 (quant-ph).

[379] G. Lami and M. Collura. *Learning the stabilizer group of a Matrix Product State*. 2024. ArXiv: 2401.16481 (quant-ph).

[380] T. Haug and L. Piroli. *"Quantifying nonstabilizerness of matrix product states"*. Phys. Rev. B **107**, 035148 (2023).

[381] D. Rattacaso, L. Leone, S. F. E. Oliviero, et al. *"Stabilizer entropy dynamics after a quantum quench"*. Phys. Rev. A **108**, 042407 (2023).

[382] L. Leone and L. Bittel. *"Stabilizer entropies are monotones for magic-state resource theory"*. Phys. Rev. A **110**, L040403 (2024).

[383] S. Bravyi and D. Gosset. *"Improved Classical Simulation of Quantum Circuits Dominated by Clifford Gates"*. Phys. Rev. Lett. **116**, 250501 (2016).

[384] X. Zhou, D. W. Leung, and I. L. Chuang. *"Methodology for quantum logic gate construction"*. Phys. Rev. A **62**, 052316 (2000).

[385] G. Lami, T. Haug, and J. D. Nardis. *Quantum State Designs with Clifford Enhanced Matrix Product States*. 2024. ArXiv: 2404.18751 (quant-ph).

[386] D. Gross, K. Audenaert, and J. Eisert. *"Evenly distributed unitaries: On the structure of unitary designs"*. Journal of Mathematical Physics **48**, 052104 (2007).

[387] X. Qian, J. Huang, and M. Qin. *"Augmenting Density Matrix Renormalization Group with Clifford Circuits"*. Phys. Rev. Lett. **133**, 190402 (2024).

[388] A. F. Mello, A. Santini, and M. Collura. *"Hybrid Stabilizer Matrix Product Operator"*. Phys. Rev. Lett. **133**, 150604 (2024).

[389] J. Huang, X. Qian, and M. Qin. *Non-stabilizerness Entanglement Entropy: a measure of hardness in the classical simulation of quantum many-body systems*. 2024. ArXiv: 2409.16895 (quant-ph).

[390] G. E. Fux, B. Béri, R. Fazio, et al. *Disentangling unitary dynamics with classically simulable quantum circuits*. 2024. ArXiv: 2410.09001 (quant-ph).

[391] M. Beverland, E. Campbell, M. Howard, et al. *"Lower bounds on the non-Clifford resources for quantum computations"*. Quantum Science and Technology **5**, 035009 (2020).

[392] E. M. Stoudenmire and S. R. White. *"Minimally entangled typical thermal state algorithms"*. New Journal of Physics **12**, 055026 (2010).

[393] A. J. Ferris and G. Vidal. *"Perfect sampling with unitary tensor networks"*. Phys. Rev. B **85**, 165146 (2012).

[394] S. Choi, C. J. Turner, H. Pichler, et al. *"Emergent SU(2) Dynamics and Perfect Quantum Many-Body Scars"*. Phys. Rev. Lett. **122**, 220603 (2019).

[395] A. Hudomal, J.-Y. Desaules, B. Mukherjee, et al. *"Driving quantum many-body scars in the PXP model"*. Phys. Rev. B **106**, 104302 (2022).

[396] A. Marché, G. Morettini, L. Mazza, et al. *Exceptional stationary state in a dephasing many-body open quantum system*. 2025. ArXiv: 2412.13820 (quant-ph).

[397] K. Harada. *"Bayesian inference in the scaling analysis of critical phenomena"*. Phys. Rev. E **84**, 056704 (2011).

[398] M. M. Wauters, E. Ballini, A. Biella, et al. *"Symmetry-protection Zeno phase transition in monitored lattice gauge theories"*. Phys. Rev. B **111**, 094315 (2025).

[399] C. Launay, B. Galerne, and A. Desolneux. *"Exact sampling of determinantal point processes without eigendecomposition"*. Journal of Applied Probability **57**, 1198–1221 (2020).

[400] A. Kulesza. *"Determinantal Point Processes for Machine Learning"*. Foundations and Trends in Machine Learning **5**, 123–286 (2012).

Appendix A

Stabilizer Rényi Entropies of Gaussian states

We present in detail the procedure to evaluate the SREs of fermionic Gaussian states from the knowledge of their Majorana covariance matrix $\Gamma_{\mu,\nu} = \frac{1}{2}\operatorname{Tr}(\hat{\rho}[\hat{\gamma}_\mu, \hat{\gamma}_\nu])$, introduced in Sec. 1.2.3. We follow the algorithm proposed in Ref. [354], and in the following we assume that $\hat{\rho}$ is pure. Let $D = 2^L$ be the Hilbert space dimension, and let $\mathcal{P}_L = \{\hat{\mathbb{1}}, \hat{\sigma}^x, \hat{\sigma}^y, \hat{\sigma}^z\}^{\otimes L}$ be the set of Pauli strings. For $n > 0$, the n-Rényi entropy of Eq. (1.83) can be written as [83]

$$M_n = \frac{1}{1-n} \log \left(\sum_{\hat{P} \in \mathcal{P}_L} \pi^n(\hat{P}) \right) - \log D, \tag{A.1}$$

which, up to an additive constant, coincides with the n-Rényi entropy of the distribution

$$\pi(\hat{P}) = \frac{1}{D} \operatorname{Tr}\Big(\hat{\rho}\hat{P}\Big)^2. \tag{A.2}$$

For $n \to 1$, the SRE reduces to the Shannon entropy $M_1 = -\sum_{\hat{P}\in\mathcal{P}_L} \pi(\hat{P}) \log \pi(\hat{P}) - \log D$. SREs are useful in characterizing the distribution π_ρ and measuring non-stabilizerness.

Focusing on Gaussian states simplifies drastically the calculation of the SRE. We start by observing that Majorana and Pauli strings are in one-to-one correspondence. Specifically, using the Jordan-Wigner map each $\hat{P} \in \mathcal{P}_L$ can be expressed (apart from a phase) as a Majorana string $\hat{\gamma}^{\mathbf{x}} = \hat{\gamma}_1^{x_1} \dots \hat{\gamma}_L^{x_{2L}}$, where $\mathbf{x} = (x_1, \dots, x_L)$ is an array of binary exponents $x_j = 0, 1$. As a consequence, the probability distribution $\pi(\hat{P})$ is equivalently rewritten as

$$\pi(\mathbf{x}) = \frac{1}{D} |\operatorname{Tr}(\hat{\rho}\,\hat{\gamma}^{\mathbf{x}})|^2, \tag{A.3}$$

which is now defined as a function of $\mathbf{x}$. By applying Wick's theorem, we can further express it as [1]

$$\pi(\mathbf{x}) = \det[i\Gamma|_{\mathbf{x}}], \tag{A.4}$$

where $\Gamma|_{\mathbf{x}}$ denotes the submatrix of Γ restricted to the support of $\mathbf{x}$, i.e., obtained by discarding all rows and columns j such that $x_j = 0$ [116]. This result follows from Wick's theorem, which allows us to write $\operatorname{Tr}(\hat{\rho}\,\hat{\gamma}^{\mathbf{x}})$ as a Pfaffian (see Sec. 1.2.3), combined with the property that its square is a determinant.

[1] Notice the presence of an extra factor i compared to Ref. [354]. This is due to a difference in the convention adopted to define Γ.

The SREs can be evaluated by sampling $\mathcal{S}$ bitstrings $\mathbf{x}^{(m)}$, $m = 1, \dots \mathcal{S}$, from the distribution $\pi(\mathbf{x})$ and estimating the average

$$\mathbb{E}[\pi(\mathbf{x})^{n-1}] \approx \frac{1}{\mathcal{S}} \sum_{m=1}^{\mathcal{S}} \pi(\mathbf{x}^{(m)})^{n-1}. \tag{A.5}$$

The n-SRE can then be computed as

$$M_n = \frac{1}{1-n} \log \left(\mathbb{E}[\pi(\mathbf{x})^{n-1}] \right) - \log D. \tag{A.6}$$

The sampling is typically challenging because the number of Majorana string is $D^2 = 4^L$. This difficulty can be overcome by decomposing the full probability into a product of conditional probabilities

$$\pi(\mathbf{x}) = \pi(x_1)\pi(x_2|x_1) \dots \pi(x_{2L}|x_1, \dots, x_{2L-1}), \tag{A.7}$$

and sampling the distribution iteratively, one bit at a time. This is possible because the conditional probabilities $\pi(x_\mu|x_1, \dots, x_{\mu-1})$ can be computed efficiently for Gaussian states. To this end, the marginal probabilities $\pi(x_1, \dots, x_\mu)$ are obtained by summing $\pi(\mathbf{x})$ over all unspecified bits, which, using Eq. (A.4), reduces to a determinant formula involving the covariance matrix. Explicitly, we obtain [354, 399, 400]

$$\pi(x_1, \dots, x_\mu) = \det\Big[(\mathbb{1}_{[\mu+1,2L]} + i\Gamma)|_{(x_1,\dots,x_\mu,1,\dots,1)} \Big], \tag{A.8}$$

where $\mathbb{1}_{[\mu+1,2L]}$ is the diagonal matrix whose diagonal entries are 1 for indices in the interval $[\mu+1, 2L]$ and zero otherwise.

Lastly, this approach can readily be extended to the case when $\hat{\rho}$ does not describe the pure state of the full system, but instead corresponds to any any contiguous subsystem of qubits starting from the first lattice site. Indeed, any Pauli substring supported on a connected subsystem $[1, \ell]$ maps to a Majorana substring defined on the corresponding Majorana sublattice $[1, 2\ell]$. Moreover, since the reduced density matrix of a Gaussian ensemble remains Gaussian, the same formula for the marginal probabilities applies. One simply needs to evaluate Eq. (A.8) using the covariance matrix restricted to the subsystem under consideration.

Appendix B

Quantum jump dynamics in the Gaussian formalism

The quantum jump dynamics generated by the stochastic Schrödinger equation of Eq. (3.3) starting from any initial Gaussian states, such as $|\psi_0\rangle = |0\rangle^{\otimes L}$, preserves Gaussianity at all times. As a consequence, the evolution of the system can be fully characterized in terms of its fermionic covariance matrix. Here, we present how to implement this in practice, generalizing the unitary update rules of Eq. (1.48).

Consider the matrices $C_{m,n}(t) = \langle\psi_t|\,\hat{c}_m\hat{c}_n^\dagger\,|\psi_t\rangle$ and $F_{m,n}(t) = \langle\psi_t|\,\hat{c}_m\hat{c}_n\,|\psi_t\rangle$. In the absence of jumps, the state $|\psi_t\rangle$ evolves according to a deterministic Schrödinger equation, governed by the Hamiltonian $\hat{H}$ of Eq. (3.4). In terms of the matrices $C(t)$ and $F(t)$, the dynamics can still be formulated in terms of first-order differential equations, which are derived in the following way. We explicitly compute the time derivatives

$$\partial_t C_{m,n}(t) = i\,\langle\psi_t|\left(\hat{H}^\dagger\hat{c}_m\hat{c}_n^\dagger - \hat{c}_m\hat{c}_n^\dagger\hat{H}\right)|\psi_t\rangle\,, \tag{B.1a}$$

$$\partial_t F_{m,n}(t) = i\,\langle\psi_t|\left(\hat{H}^\dagger\hat{c}_m\hat{c}_n - \hat{c}_m\hat{c}_n\hat{H}\right)|\psi_t\rangle\,. \tag{B.1b}$$

It is fundamental to include also the constant term $i\frac{\gamma}{4}\sum_j\langle\psi_t|\,\hat{\sigma}_j^z\,|\psi_t\rangle$, as it enforces the conservation of the norm $\langle\psi_t|\psi_t\rangle = 1$ at all times. The right-hand sides of Eqs. (B.1a) and (B.1b) can be worked out explicitly using Wick's theorem, yielding

$$\partial_t C(t) = -2i\left([\mathbb{H}_1, C(t)] + \mathbb{H}_2F^\dagger(t) + F(t)\mathbb{H}_2\right) + \gamma\left(C(t)^2 - F(t)F^\dagger(t) - C(t)\right), \tag{B.2a}$$

$$\begin{aligned}\partial_t F(t) = &-2i\left[\{\mathbb{H}_1, F(t)\} + \mathbb{H}_2(\mathbb{1} - C^T(t)) - C(t)\mathbb{H}_2\right]\\ &+\gamma\left[C(t)F(t) - F(t)(\mathbb{1} - C^T(t))\right],\end{aligned} \tag{B.2b}$$

where $\mathbb{H}_{1,2}$ are $L\times L$ matrices with non-zero elements

$$(\mathbb{H}_1)_{m,m+1} = (\mathbb{H}_1)_{m+1,m} = -\frac{1}{2}, \tag{B.3a}$$

$$(\mathbb{H}_1)_{L,1} = (\mathbb{H}_1)_{1,L} = \frac{1}{2}, \tag{B.3b}$$

$$(\mathbb{H}_1)_{m,m} = h, \tag{B.3c}$$

and

$$(\mathbb{H}_2)_{m,m+1} = -(\mathbb{H}_2)_{m+1,m} = -\frac{1}{2}, \tag{B.4}$$

$$(\mathbb{H}_2)_{L,1} = -(\mathbb{H}_2)_{1,L} = \frac{1}{2}. \tag{B.5}$$

These matrices encode the contribution of the Hermitian Hamiltonian $\hat{H}_0$, which can be written (apart from a constant) as

$$\hat{H}_0 = \begin{pmatrix} \hat{c}_1^\dagger & \dots & \hat{c}_L^\dagger & \hat{c}_1 & \dots & \hat{c}_L \end{pmatrix} \begin{pmatrix} \mathbb{H}_1 & \mathbb{H}_2 \\ -\mathbb{H}_2 & -\mathbb{H}_1 \end{pmatrix} \begin{pmatrix} \hat{c}_1 \\ \dots \\ \hat{c}_L \\ \hat{c}_1^\dagger \\ \dots \\ \hat{c}_L^\dagger \end{pmatrix}. \tag{B.6}$$

For $\gamma = 0$, we recover Eq. (1.48). The continuous monitoring adds non-linear contributions to the differential equations. This is expected, since the Hamiltonian already contains the expectation values $\langle\psi_t|\,\hat{\sigma}_j^z\,|\psi_t\rangle$ evaluated on the current state.

The discontinuous evolution produced by quantum jumps is implemented as follows. Suppose the jump occurs on site j. The starting state $|\psi\rangle$ is projected onto $|\psi'\rangle = \frac{\hat{L}_j|\psi\rangle}{\sqrt{\langle\psi|\hat{L}_j|\psi\rangle}}$, where $\hat{L}_j = \hat{\mathbb{1}} - \hat{n}_j$ given our definition of Eq. (1.22). It follows that the correlation functions C and F are updated to

$$C'_{m,n} = \frac{\langle\psi|\,\hat{L}_j^\dagger \hat{c}_m \hat{c}_n^\dagger \hat{L}_j\,|\psi\rangle}{\langle\psi|\,\hat{L}_j^\dagger \hat{L}_j\,|\psi\rangle}, \tag{B.7a}$$

$$F'_{m,n} = \frac{\langle\psi|\,\hat{L}_j^\dagger \hat{c}_m \hat{c}_n \hat{L}_j\,|\psi\rangle}{\langle\psi|\,\hat{L}_j^\dagger \hat{L}_j\,|\psi\rangle}, \tag{B.7b}$$

which can be evaluated using Wick's theorem. After a tedious but straightforward calculation, we finally obtain

$$C'_{m,n} = C_{m,n} - \frac{C_{m,j}C_{j,n}}{C_{j,j}} + \frac{F_{m,j}F_{j,n}^\dagger}{C_{j,j}} + \delta_{j,m}\delta_{j,n}, \tag{B.8a}$$

$$F'_{m,n} = F_{m,n} - \frac{C_{m,j}F_{j,n}}{C_{j,j}} + \frac{F_{j,m}C_{n,j}}{C_{j,j}}. \tag{B.8b}$$

It is worth noting that the jth rows and columns of both C and F are updated to $C'_{m,j} = C'_{j,m} = \delta_{m,j}$ and $F'_{m,j} = F'_{j,m} = 0$, independent of their previous values. In our implementation, we impose such conditions explicitly instead of using Eqs. (B.8a) and (B.8b) for these specific rows and columns, because we observed that this improves numerical stability.

For the simulations presented in Chapter 3, we discretize time in intervals of duration δt. At each step, we implement the non-unitary evolution by integrating the coupled differential equations for $C(t)$ and $F(t)$ using a Runge-Kutta algorithm of 5^{th} order. We then check whether a quantum jump randomly occurs or not, following the method adopted in Ref. [56]. The expected number of jumps on each site j is equal to its jump probability $p_j = \gamma\delta t\,\langle\psi_t|\,\hat{L}_j\,|\psi_t\rangle$, and thus the total expected number of jumps is $P = \sum_j p_j$. For sufficiently small δt, $P < 1$ can be interpreted as the probability to have a jump on one of the lattice sites. We thus extract a random number $0 \leq r \leq 1$ and we compare it to P. If $r > P$, no jump occurs. In

contrast, for $r \leq P$ we implement a jump on a site m, which is chosen randomly among all sites using p_j as relative probabilities. We point out that an alternative (but equivalent) implementation consists of checking if a jump occurs on each single site independently, which allows for multiple jumps within the same time step. If δt is small enough, the two methods coincide, because processes involving n jumps happen with probability proportional to $(\delta t)^n$. Regardless, both implementations produce the same average number of jumps P, which is the physically relevant quantifier of how frequently entanglement is reduced by a projective measurement. We checked numerically that these two approaches produce no notable difference in the quantities we investigated.

As an additional check, we evaluated the average dynamics of the total number of fermions $\hat{N}$, and compared it to the simulations found using a different stochastic measurement protocol that yields the same Lindblad evolution of the disorder-averaged density matrix, as discussed in Ref. [248]. We found that the two implementations produced compatible numerical results.

Appendix C

Correlation length from analytic continuation

In this Appendix, we derive the correlation length bound of Eq. (4.24). First, let us rewrite the correlation matrix in terms of a contour integral. From the definition of $\tilde{\Gamma}(k)$, the inverse Fourier transform is given by

$$\Gamma(x) = \frac{1}{L}\sum_k e^{ikx}\tilde{\Gamma}(k), \tag{C.1}$$

where the sum runs over the Brillouin defined by $k = \pm\frac{2m-1}{L}\pi$, $m = 1, \ldots, L$, for periodic boundary conditions. For $L \to \infty$ the previous expression becomes the integral

$$\Gamma(x) = \frac{1}{2\pi}\int_{-\pi}^{\pi} e^{ikx}\tilde{\Gamma}(k)dk. \tag{C.2}$$

After introducing the complex variable $z = e^{ik}$ we obtain the contour integral

$$\Gamma(x) = \frac{1}{2\pi i}\oint_{\mathcal{S}} z^{x-1}\tilde{\Gamma}(k(z))dz, \tag{C.3}$$

where $\mathcal{S}$ is the unit circle with counterclockwise orientation. This rewriting is possible assuming that $\tilde{\Gamma}(k)$ is analytic for $k \in \mathbb{R}$, which is the case of non-critical steady states. In all regions where $\tilde{\Gamma}(k(z))$ is regular the contour can be safely deformed. In particular, we can shrink $\mathcal{S}$ to a new contour $\mathcal{K}$ that encircles tightly the non-analiticities of the correlation matrix. This is represented in Fig. C.1. With the introduction of $\mathcal{K}$ we finally obtain

$$\Gamma(x) = \frac{1}{2\pi i}\oint_{\mathcal{K}} z^{x-1}\tilde{\Gamma}(k(z))dz. \tag{C.4}$$

At last, we derive the upper bound to the correlation length. Let us parameterize the closed path $\mathcal{K}$ by a function $\kappa(s)$ of real variable $s \in [0, 1)$, so that

$$\Gamma(x) = \frac{1}{2\pi i}\int_0^1 \kappa(s)^{x-1}\tilde{\Gamma}(k(\kappa(s)))\kappa'(s)ds. \tag{C.5}$$

We then have

$$\begin{aligned} |\Gamma(x)| &\leq \frac{1}{2\pi}\int_0^1 |\kappa(s)|^{x-1}\left|\tilde{\Gamma}(k(\kappa(s)))\kappa'(s)\right|ds \\ &\leq \frac{1}{2\pi}\left(\max_{s\in[0,1)}\{|\kappa(s)|\}\right)^{x-1}\int_0^1 \left|\tilde{\Gamma}(k(\kappa(s)))\kappa'(s)\right|ds. \end{aligned} \tag{C.6}$$

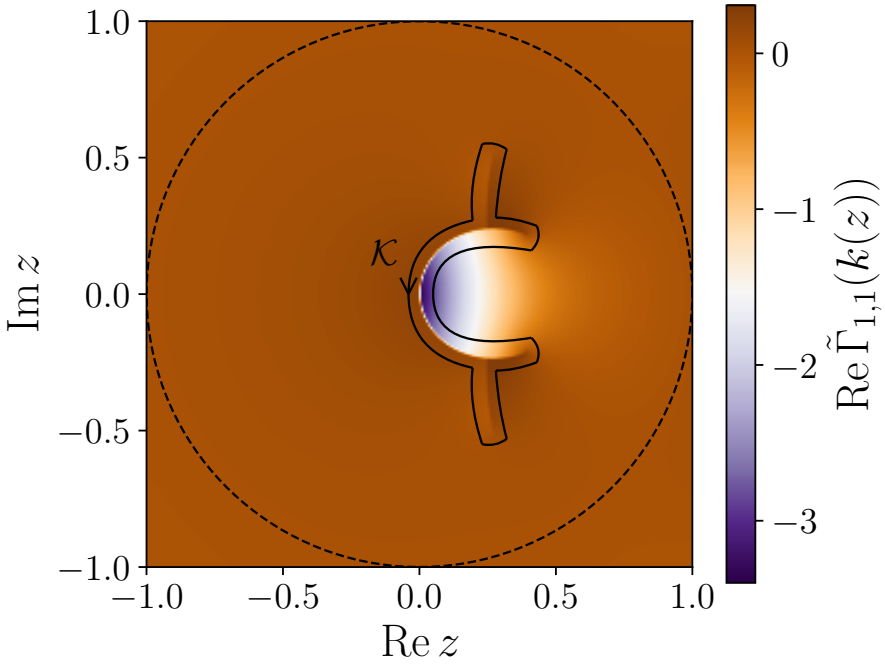

Figure C.1: Correlation function $\mathrm{Re}\,\tilde{\Gamma}_{1,1}$ after the change of variable $z = e^{ik}$, using $\mu = 0.4$, $\gamma = 1$, and $q = 0.5$. A sketch of the integration contour $\mathcal{K}$, encircling the discontinuity lines, is presented.

Since we take the contour $\mathcal{K}$ to be at an infinitesimal distance from the discontinuities of $\tilde{\Gamma}$, the maximum of $|\kappa(s)|$ is achieved at the point of non-analiticity that is further away from the origin. Recalling that $z = e^{ik}$, the maximum modulus of z corresponds to the minimum imaginary part of k, and thus

$$\max_{s\in[0,1)} \{|\kappa(s)|\} = \exp\left(-\min_{k\in\mathcal{C}} \{\mathrm{Im}\, k\}\right). \tag{C.7}$$

This yields the bound of Eq. (4.24).

Appendix D

Third quantization

We now describe how to generalize the formalism of third quantization introduced in Refs. [300, 301] to diagonalize Eq. (4.6b). From now on we drop the constant term needed for trace preservation because it simply adds a shift to the Liouvillian spectrum, and we thus consider

$$\mathcal{L}\bullet = -i\big[\hat{H},\bullet\big] + \sum_{j=1}^{L}\left((1-q)\hat{L}_j \bullet \hat{L}_j^\dagger - \frac{1}{2}\big\{\hat{L}_j^\dagger\hat{L}_j,\bullet\big\}\right). \tag{D.1}$$

The procedure is completely analogous to the one presented in Ref. [300], and thus we will cover it only briefly.

The space of operators acting on the 2^L-dimensional Hilbert space can be seen as a 4^L-dimensional Hilbert space itself, whose elements $\hat{A}$ will be relabeled as $\big|\hat{A}\big\rangle$, when supplemented with the inner product $\big\langle\hat{A}\big|\hat{B}\big\rangle = \mathrm{Tr}\left(\hat{A}^\dagger\hat{B}\right)/4^L$. The set of strings of Majorana operators

$$\hat{P}_{\boldsymbol{\alpha}} = \hat{w}_1^{\alpha_1}\hat{w}_2^{\alpha_2}\ldots\hat{w}_{2L}^{\alpha_{2L}}, \tag{D.2}$$

where $\boldsymbol{\alpha} = (\alpha_1,\ldots,\alpha_{2L})$ with $\alpha_j = 0,1$, forms a basis of the space of operators, and the states $\big|\hat{P}_{\boldsymbol{\alpha}}\big\rangle$ can be thought as Fock states. We introduce a set of annihilation and creation linear operators $\hat{f}_j$ and $\hat{f}_j^\dagger$, $j = 1,\ldots,2L$, defined by

$$\hat{f}_j\big|\hat{P}_{\boldsymbol{\alpha}}\big\rangle = \delta_{\alpha_j,1}\big|\hat{w}_j\hat{P}_{\boldsymbol{\alpha}}\big\rangle, \tag{D.3a}$$

$$\hat{f}_j^\dagger\big|\hat{P}_{\boldsymbol{\alpha}}\big\rangle = \delta_{\alpha_j,0}\big|\hat{w}_j\hat{P}_{\boldsymbol{\alpha}}\big\rangle. \tag{D.3b}$$

It is easily checked that $\hat{f}_j$ and $\hat{f}_j^\dagger$ fulfill canonical anticommutation relations. For convenience, let us introduce the $4L$ Majorana operators $\hat{a}_{2j-1} = \left(\hat{f}_j + \hat{f}_j^\dagger\right)/\sqrt{2}$, $\hat{a}_{2j} = -i\left(\hat{f}_j^\dagger - \hat{f}_j\right)/\sqrt{2}$. We remark that these operators are actually super-operators with respect to the original Hilbert space of physical states. Any Liouvillian $\mathcal{L}$ can be represented as a sum of strings of Majorana operators. In practice, this is done by evaluating how it acts on the basis states $\big|\hat{P}_{\boldsymbol{\alpha}}\big\rangle$. For the model of Eq. (D.1) we obtain

$$\mathcal{L} = \sum_{m,n=1}^{2L}\mathbb{A}_{m,n}\hat{a}_m\hat{a}_n - A_0 \tag{D.4}$$

where

$$\mathbb{A} = \begin{pmatrix} -2i\mathbb{H} + 2i\,\mathrm{Im}\,M & 2i\,(1-q)\,M \\ -2i\,(1-q)\,M^T & -2i\mathbb{H} - 2i\,\mathrm{Im}\,M \end{pmatrix}. \tag{D.5}$$

Here $\mathbb{H}$ and M are the Hamiltonian and the bath matrices introduced in Eqs. (4.7) and (4.9), and $A_0 = 2\,\mathrm{Tr}\,M$.

Assuming that $\mathbb{A}$ is diagonalizable, it can be decomposed as

$$\mathbb{A} = V^T \begin{pmatrix} 0 & \beta_1 & 0 & 0 & \dots \\ -\beta_1 & 0 & 0 & 0 & \dots \\ 0 & 0 & 0 & \beta_2 & \dots \\ 0 & 0 & -\beta_2 & 0 & \dots \\ \vdots & \vdots & \vdots & \vdots & \ddots \end{pmatrix} V, \tag{D.6}$$

where

$$VV^T = \begin{pmatrix} 0 & 1 & 0 & 0 & \dots \\ 1 & 0 & 0 & 0 & \dots \\ 0 & 0 & 0 & 1 & \dots \\ 0 & 0 & 1 & 0 & \dots \\ \vdots & \vdots & \vdots & \vdots & \ddots \end{pmatrix}. \tag{D.7}$$

The β_m are called rapidities, and we can sort them in such a way that $\mathrm{Re}\,\beta_1 \geq \mathrm{Re}\,\beta_2 \geq \ldots \geq \mathrm{Re}\,\beta_{2L} \geq 0$. This allows us to introduce a set of normal master modes $\hat{b}_m = \sum_{n=1}^{4L} V_{2m-1,n}\hat{a}_n$, $\hat{b}'_m = \sum_{n=1}^{4L} V_{2m,n}\hat{a}_n$ that satisfy the almost-canonical anti-commutation relations $\left\{\hat{b}_m, \hat{b}_n\right\} = \left\{\hat{b}'_m, \hat{b}'_n\right\} = 0$, $\left\{\hat{b}_m, \hat{b}'_n\right\} = \delta_{m,n}$. The Liouvillian can then be rewritten in diagonal form as

$$\mathcal{L} = -2\sum_{j=1}^{2L} \beta_j \hat{b}'_j \hat{b}_j - B_0, \tag{D.8}$$

where $B_0 = A_0 - \sum_{j=1}^{2L} \beta_j$. The non-equilibrium steady state corresponds to the Liouvillian eigenoperator whose eigenvalue has the largest real part, and it thus coincides with the vacuum state of the normal modes satisfying $\mathcal{L}\hat{\rho}_{\mathrm{NESS}} = -B_0\hat{\rho}_{\mathrm{NESS}}$. It also follows, as in Ref. [300], that the Liouvillian gap is given by $\Delta = -2\,\mathrm{Re}\,\beta_{2L}$.

Appendix E

Stationary Magic within the Generalized Gibbs Ensemble

A well-known result in the study of quench dynamics of isolated many-body integrable systems is that, at late times, local observables can (formally) be computed as if the system were described by a Generalized Gibbs Ensemble (GGE) (see the review Ref. [186] and references therein).

In the case of a non-interacting fermionic theory, the GGE takes the particularly simple form [11]

$$\hat{\rho}_{\mathrm{GGE}} = \frac{1}{Z} \exp\left(\sum_k \lambda_k \hat{n}_k\right), \tag{E.1}$$

with $Z = \mathrm{Tr}\left(e^{\sum_k \lambda_k \hat{n}_k}\right)$, where $\hat{n}_k$ are the mode occupation number operators corresponding to the single-particle eigenmodes that diagonalize the post-quench Hamiltonian, and λ_k are the associated Lagrange multipliers fixed by the initial conditions.

This description implies that, for any local observable $\hat{O}_\ell$ supported on a subsystem of size ℓ, the long-time limit (when it exists) coincides with its time average and can be computed using the GGE. In other words,

$$\lim_{t\to\infty} \langle \hat{O}_\ell(t) \rangle = \mathrm{Tr}\left(\hat{O}_\ell\, \hat{\rho}_{\mathrm{GGE}}\right). \tag{E.2}$$

Eventually, when considering the thermodynamic limit, one may also take the subsystem size ℓ to scale accordingly. In this extended setting, the above relation is expected to hold in a thermodynamic sense, albeit with some caveats. Specifically, in the previous equation, the limit $L \to \infty$ was taken first, meaning that all quantities were already evaluated in the thermodynamic regime. However, sending $\ell \to \infty$ afterward, while keeping $\ell \ll L$, is not generally equivalent to taking $\ell = L$ from the outset and then letting $L \to \infty$. These two procedures may lead to qualitatively different behaviors. Thus, the setting we consider here explores a different regime compared to that discussed in Chapter 6: we now focus on large but finite subsystems embedded in the thermodynamic bulk, rather than on the global properties of the entire system.

In the absence of measurements, the plain unitary dynamics of hopping fermions initialized in a generalized Néel state with fixed density n leads, at late times, to a GGE. For any subsystem of size ℓ, the reduced density matrix approaches a form described by the following restricted Majorana covariance matrix

$$i\Gamma_\ell = \mathbb{1}_\ell \otimes \begin{pmatrix} 0 & 1-2n \\ 2n-1 & 0 \end{pmatrix}, \tag{E.3}$$

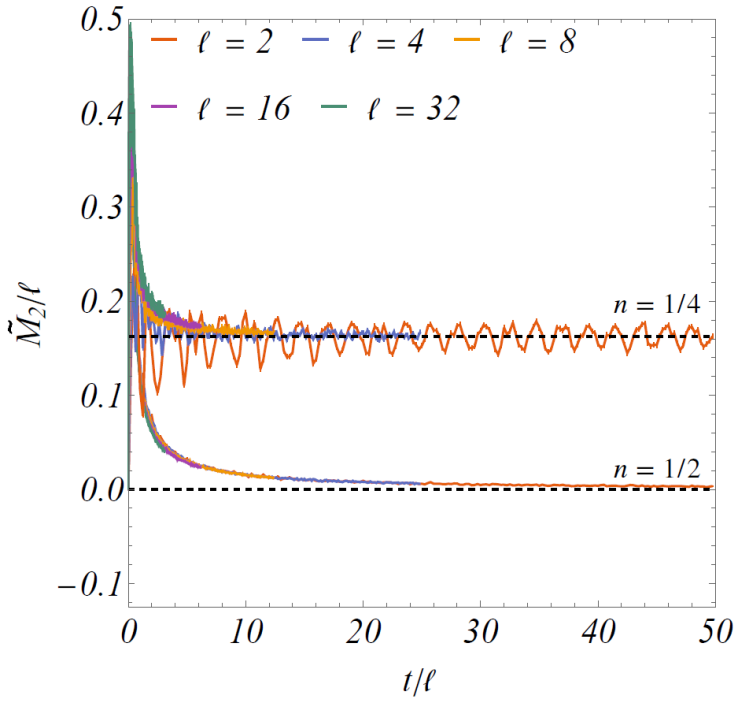

Figure E.1: Time evolution of the subsystem SRE density $\tilde{M}_2/\ell$ under unitary free-fermionic dynamics. The full system of size $L = 256$ is initialized in the Néel state at filling $n = 1/2, 1/4$. As a function of the rescaled time t/ℓ all curves tend to an ℓ-independent evolution which approaches the infinite-time stationary value (black dashed lines) computed with the GGE.

where $\mathbb{1}_\ell$ is the identity matrix on the ℓ-site subsystem.

From this structure, it is straightforward to compute $\pi(\mathbf{x})$ associated with a given Majorana string operator $\hat{\gamma}^{\mathbf{x}}$. Notice that for mixed states this is no longer a probability distribution, as it is not normalized properly. A suitable normalization should be implemented to evaluated SREs stochastically as described in App. A. Nevertheless, we will carry out the full calculation analytically, and thus this step is unnecessary for the current case. $\pi(\mathbf{x})$ depends only on the number $m_{\mathbf{x}}$ of contiguous pairs of Majorana operators appearing in the string for which the determinant of the corresponding submatrix is non-vanishing. All other configurations yield no contribution. For the non-vanishing cases, we find

$$\pi(\mathbf{x}) = \frac{1}{2^\ell}(1-2n)^{2m_{\mathbf{x}}}. \tag{E.4}$$

The SREs can then be computed directly from the definition by summing over all such valid contributions. Specifically, one obtains

$$M_\alpha(\ell) = \frac{1}{1-\alpha}\log\left(\frac{1}{2^\ell}\sum_{m=0}^{\ell}\binom{\ell}{m}(1-2n)^{2\alpha m}\right) = \frac{\ell}{1-\alpha}\log\left(\frac{1+(1-2n)^{2\alpha}}{2}\right). \tag{E.5}$$

Next, to evaluate $\tilde{M}_2$ of Eq. 1.86 we also need the second Rényi entropy $S^{(2)}$, which

is given by

$$S^{(2)} = -\log\left(\mathrm{Tr}\left(\hat{\rho}^2\right)\right) = -\log\left(\sum_{\mathbf{x}} \pi(\mathbf{x})\right) = -\ell \log\left(\frac{1+(1-2n)^2}{2}\right). \tag{E.6}$$

Finally, we obtain

$$\tilde{M}_2 = M_2 - S^{(2)} = -\log\left(\frac{1+(1-2n)^4}{1+(1-2n)^2}\right) \tag{E.7}$$

In Fig. E.1, we present the time evolution of the SREs for subsystems embedded within a larger system of size $L = 256$. We focus on the dynamical regime defined by $\ell \ll t \ll L$, where a GGE description is expected to hold locally within the subsystem. After a very short transient (of the order of the subsystem size) during which the subsystem non-stabilizerness increases similarly to the full system (not visible in the figures), the long-time dynamics reveals a qualitatively different trend. In this scaling limit, the SREs of the subsystem decrease toward the GGE value predicted by Eq. (E.5). Furthermore, the relaxation toward this stationary value appears to follow an algebraic decay, approximately as $\sim (t/\ell)^{-1}$.

Appendix F

Proof of the ICCR step replacement

We prove the identities of Eqs. (8.14), (8.15), (8.16), and we provide the formal exact expression of $|\Psi'\rangle$ of Eq. (8.17).

First, assume we can find $i^* \leq r$ with $|\tilde{\varphi}_{i^*}\rangle = (|+\rangle + i^{q^*}|-\rangle)/\sqrt{2}$ (cf. Eq. (8.9)). Let us perform a computational-base expansion of $|\Psi_1\rangle$. We have

$$\begin{aligned} |\Psi_1\rangle &= \sum_{\sigma_1,\ldots,\sigma_N=\pm 1} a_{\sigma_1,\ldots,\sigma_N} |\sigma_1,\ldots,\sigma_N\rangle \\ &= \sum_{\sigma_i \,:\, i\in\mathcal{S}} |\sigma_i \;:\; i\in\mathcal{S}\rangle \sum_{\sigma_i \,:\, i\notin\mathcal{S}} a_{\sigma_1,\ldots,\sigma_N} |\sigma_i \;:\; i\notin\mathcal{S}\rangle \\ &= \sum_{\sigma_i \,:\, i\in\mathcal{S}} |\sigma_i \;:\; i\in\mathcal{S}\rangle\, A_{\{\sigma_i \,:\, i\in\mathcal{S}\}} \left|\psi_{\{\sigma_i \,:\, i\in\mathcal{S}\}}\right\rangle, \end{aligned} \tag{F.1}$$

where we isolated the contribution of spins contained in $\mathcal{S}$ by grouping all others in the states $\left|\psi_{\{\sigma_i \,:\, i\in\mathcal{S}\}}\right\rangle$. The latter are normalized to 1, and thus the amplitudes $A_{\{\sigma_i \,:\, i\in\mathcal{S}\}}$ appear in the expansion. Let us introduce a string $\boldsymbol{\sigma} = \{\sigma_i \;:\; i\in\mathcal{S}\setminus\{i^*\}\}$ of length $|\mathcal{S}|-1$ containing all qubits in $\mathcal{S}$ except for the one at i^*. $|\Psi_1\rangle$ can be rewritten compactly as

$$|\Psi_1\rangle = \sum_{\boldsymbol{\sigma}} \sum_{\sigma_{i^*}} A_{\boldsymbol{\sigma},\sigma_{i^*}} |\boldsymbol{\sigma}\rangle |\sigma_{i^*}\rangle |\psi_{\boldsymbol{\sigma},\sigma_{i^*}}\rangle . \tag{F.2}$$

Using the fact that qubit i^* is in the known product state $|\tilde{\varphi}_{i^*}\rangle$, the amplitudes factorize as $A_{\boldsymbol{\sigma},\sigma_{i^*}} = \tilde{A}_{\boldsymbol{\sigma}} (i^{q^*})^{\frac{1-\sigma_{i^*}}{2}}/\sqrt{2}$ and the states $|\psi_{\boldsymbol{\sigma},\sigma_{i^*}}\rangle$ are independent of σ_{i^*}, thus yielding

$$|\Psi_1\rangle = \sum_{\boldsymbol{\sigma}} \tilde{A}_{\boldsymbol{\sigma}} |\boldsymbol{\sigma}\rangle \sum_{\sigma_{i^*}} \frac{(i^{q^*})^{\frac{1-\sigma_{i^*}}{2}}}{\sqrt{2}} |\sigma_{i^*}\rangle |\psi_{\boldsymbol{\sigma}}\rangle . \tag{F.3}$$

We now evaluate the action of the projector $(\hat{\mathbb{1}} + s\prod_{i\in\mathcal{S}} \hat{Z}_i)/2$ on this state. The projector preserves all components of the superposition satisfying $\prod_{i\in\mathcal{S}} \sigma_i = s$, and destroys all others. As a consequence, defining $\bar{\sigma} = \prod_{i\in\mathcal{S}\setminus\{i^*\}} \sigma_i$, for any given $\boldsymbol{\sigma}$ only states with $\sigma_{i^*} = s\bar{\sigma}$ are not annihilated, yielding

$$\frac{\hat{\mathbb{1}} + s\prod_{i\in\mathcal{S}} \hat{Z}_i}{2} |\Psi_1\rangle = \sum_{\boldsymbol{\sigma}} \tilde{A}_{\boldsymbol{\sigma}} \frac{(i^{q^*})^{\frac{1-s\bar{\sigma}}{2}}}{\sqrt{2}} |\boldsymbol{\sigma}\rangle |s\bar{\sigma}\rangle |\psi_{\boldsymbol{\sigma}}\rangle . \tag{F.4}$$

The state $|s\bar{\sigma}\rangle$ can be achieved by preparing qubit i^* in $|s\rangle$ and controlling it with $|\mathcal{S}|-1$ CNOT gates applied from the spins in $\mathcal{S}\setminus\{i^*\}$. The phase $(i^{q^*})^{\frac{1-s\bar{\sigma}}{2}}$ is

reproduced with the gate $\hat{S}_{i^*}^{q^*}$, namely,

$$\frac{\hat{\mathbb{1}} + s\prod_{i\in\mathcal{S}}\hat{Z}_i}{2}|\Psi_1\rangle = \frac{1}{\sqrt{2}}\hat{S}_{i^*}^{q^*}\left(\prod_{i\in\mathcal{S}\setminus\{i^*\}}\hat{\mathrm{CX}}_{i\to i^*}\right)\sum_{\boldsymbol{\sigma}}\tilde{A}_{\boldsymbol{\sigma}}|\boldsymbol{\sigma}\rangle|s\rangle|\psi_{\boldsymbol{\sigma}}\rangle\,. \tag{F.5}$$

Notice that the state on the last line of the previous equation is closely related to Eq. (F.3), as it differs only by having $|s\rangle$ instead of $|\tilde{\varphi}_{i^*}\rangle$ on site i^*. Using the identity $|s\rangle = \hat{X}^{\frac{1-s}{2}}|+\rangle$, we finally obtain Eq. (8.14) with $\mathcal{N} = 1/\sqrt{2}$.

Let us now assume that the target qubit i^* is non-stabilizer. The simplification of Eq. (F.2) to Eq. (F.3) is no longer possible, the amplitudes $A_{\boldsymbol{\sigma},\sigma_{i^*}}$ do not factorize, and the states $|\psi_{\boldsymbol{\sigma},\sigma_{i^*}}\rangle$ depend also on σ_{i^*}. Acting with the projector we obtain

$$\frac{\hat{\mathbb{1}} + s\prod_{i\in\mathcal{S}}\hat{Z}_i}{2}|\Psi_1\rangle = \sum_{\boldsymbol{\sigma}}A_{\boldsymbol{\sigma},s\bar{\sigma}}|\boldsymbol{\sigma}\rangle|s\bar{\sigma}\rangle|\psi_{\boldsymbol{\sigma},s\bar{\sigma}}\rangle\,. \tag{F.6}$$

Proceeding as in the previous case, we achieve the final form of Eq. (8.14), but the state $|\Psi'\rangle$ takes the non-trivial form

$$|\Psi'\rangle = \mathcal{N}\sum_{\boldsymbol{\sigma}}A_{\boldsymbol{\sigma},s\bar{\sigma}}(i^{-q^*})^{\frac{1-s\bar{\sigma}}{2}}|\boldsymbol{\sigma}\rangle|+\rangle|\psi_{\boldsymbol{\sigma},s\bar{\sigma}}\rangle\,, \tag{F.7}$$

where $\mathcal{N}$ is a normalization prefactor (not necessarily equal to $\sqrt{2}$ as in the previous case). We see explicitly that the stabilizer dimension increases by one, as the initially non-stabilizer target qubit i^* is brought to $|+\rangle$. Instead, the state of the other qubits increases in complexity, because in general it develops entanglement even when starting from a product state configuration.

Appendix G

Optimal way to treat T gates in the ICCR algorithm

The ICCR algorithm can be applied to circuits doped with T gates using the T gadgets introduced in Sec. 8.2. The straightforward implementation of this method requires the introduction of n_T ancilla qubits, where n_T is the number of T gates in the circuit, which increases the computational cost of the simulation. We now show a better strategy to proceed that requires only a single ancilla qubit that can be reused for all T gates.

Consider an initial state $|\Psi_S\rangle$ evolved with a Clifford circuit and then with a single T gate. Using the T gadget replacement, we can reformulate the evolution as in Fig. 8.3a, where now the initial state $|\Psi\rangle = |\Psi_S\rangle\,|T_A\rangle$ is the product of the N-physical-qubit state $|\Psi_S\rangle$ and the ancilla-qubit state $|T_A\rangle$, and the projector acts on the ancilla. We implement the ICCR algorithm, which approximates the end-circuit state as

$$|\Psi_f\rangle = \hat{U}'\,|\Psi'\rangle\,. \tag{G.1}$$

We can make some exact statements on both $|\Psi'\rangle$ and $|\Psi_f\rangle$. The renormalized initial state $|\Psi'\rangle$ contains at least one stabilizer qubit (i.e., the target qubit i^*) in the factorized state $|+\rangle$ as in Fig. 8.3d, and can thus be written as $|\Psi'\rangle = |\Phi\rangle\,|+_{i^*}\rangle$. Then, the final state can always be written as $|\Psi_f\rangle = |\Psi_{f,S}\rangle\,|+_A\rangle$ because the projector disentangles the ancilla from the physical qubits. If we swap the ancilla with the qubit i^* by defining $|\Psi'_S\rangle\,|+_A\rangle = \mathrm{S\hat{W}AP}_{i^*\leftrightarrow A}\,|\Psi'\rangle$, where $\mathrm{S\hat{W}AP}$ is the (Clifford) SWAP gate, we have

$$|\Psi_{f,S}\rangle\,|+\rangle_A = \hat{U}'\,\mathrm{S\hat{W}AP}_{i^*\leftrightarrow A}(|\Psi'_S\rangle\,|+_A\rangle) = \hat{U}''(|\Psi'_S\rangle\,|+_A\rangle). \tag{G.2}$$

We see that the Clifford unitary $\hat{U}''$ leaves the ancilla in the state $|+\rangle$. This means that there must exist a Clifford operator $\hat{W}_S$ acting only on S such that $\hat{U}''(|\Psi'_S\rangle\,|+_A\rangle) = (\hat{W}_S\,|\Psi'_S\rangle)\,|+_A\rangle$. Notice however that in general $\hat{U}'' \neq \hat{W}_S\hat{\mathbb{1}}_A$. We now show how to determine $\hat{W}_S$.

Our goal is to find a new Clifford unitary $\hat{\tilde{U}}$ such that it acts in the same way as $\hat{U}''$ and at the same time has both $\hat{Z}_A$ and $\hat{X}_A$ in its stabilizer set. Hence, we require

$$\hat{\tilde{U}}(|\Psi'_S\rangle\,|+_A\rangle) = \hat{U}''(|\Psi'_S\rangle\,|+_A\rangle), \tag{G.3}$$

$$\hat{\tilde{U}}^\dagger \hat{Z}_A \hat{\tilde{U}} = \pm\hat{Z}_A, \tag{G.4}$$

and

$$\hat{\tilde{U}}^\dagger \hat{X}_A \hat{\tilde{U}} = \pm\hat{X}_A. \tag{G.5}$$

Notice that the sign $\pm$ of Eq. (G.5) does not necessarily need to be the same as that of Eq. (G.4). Since $\hat{U}''$ does not change the state $|+\rangle$ of the ancilla, one may think that $\hat{Z}_A$ already belongs to its stabilizer set. However, this is not necessarily the case, as the unitary gate $\hat{U}''$ may also generate Pauli operators that act trivially on the initial state. In general, we have

$$(\hat{U}'')^\dagger \hat{Z}_A \hat{U}'' = \pm \left(\prod_{i=1}^{r} \hat{P}_i \right) \hat{Z}_A, \tag{G.6}$$

where the string of $\hat{P}_i \in \{\hat{\mathbb{1}}_i, \hat{X}_i, \hat{Y}_i, \hat{Z}_i\}$ acts only on the stabilizer qubits and must satisfy $\left(\prod_{i=1}^{r} \hat{P}_i\right) |\Psi_S\rangle = \pm |\Psi_S\rangle$. For each i, we define

$$\hat{C}[\hat{P}_i] = \begin{cases} \hat{\mathbb{1}} & \text{if } \hat{P}_i = \hat{\mathbb{1}}_i, \\ \hat{CX}_{A\to i} & \text{if } \hat{P}_i = \hat{X}_i, \\ \hat{CY}_{A\to i} & \text{if } \hat{P}_i = \hat{Y}_i, \\ \hat{CZ}_{A\to i} & \text{if } \hat{P}_i = \hat{Z}_i, \end{cases} \tag{G.7}$$

where $\hat{CY}_{A\to i}$ and $\hat{CZ}_{A\to i}$ are respectively the controlled Y and Z gates that use the ancilla as reference and i as target. We introduce

$$\hat{U}''' = \hat{U}'' \prod_{i=1}^{r} \hat{C}[\hat{P}_i], \tag{G.8}$$

which acts on the state in the same way as $\hat{U}''$ due to the definition of $\hat{C}[\hat{P}_i]$. Moreover, it easily checked that $\hat{Z}_A$ is in the stabilizer set of $\hat{U}'''$.

Regarding $\hat{X}_A$, in general the unitary gate will map it to a complicated string

$$(\hat{U}''')^\dagger \hat{X}_A \hat{U}''' = \pm \left(\prod_{i=1}^{N} \hat{P}'_i \right) \hat{P}'_A, \tag{G.9}$$

where $\hat{P}'_i \in \{\hat{\mathbb{1}}_i, \hat{X}_i, \hat{Y}_i, \hat{Z}_i\}$ and $\hat{P}'_A \in \{\hat{X}_A, \hat{Y}_A\}$. Notice that $\hat{P}'_A$ cannot be neither $\hat{\mathbb{1}}_A$ nor $\hat{Z}_A$ because $\left[(\hat{U}''')^\dagger \hat{Z}_A \hat{U}''', (\hat{U}''')^\dagger \hat{X}_A \hat{U}'''\right] = (\hat{U}''')^\dagger \left[\hat{Z}_A, \hat{X}_A\right] \hat{U}''' \neq 0$. Similarly to how we proceeded before, we introduce

$$\hat{\tilde{U}} = \hat{U}''' \left(\prod_{i=1}^{N} \hat{C}[\hat{P}'_i] \right) \hat{u}_A, \tag{G.10}$$

where $\hat{u}_A = \hat{S}_A$ if $\hat{P}'_A = \hat{Y}_A$ and $\hat{u}_A = \hat{\mathbb{1}}_A$ otherwise. It is easily checked that Eqs. (G.3), (G.4), and (G.5) are satisfied. In particular, the last two imply that the gate $\hat{\tilde{U}}$ is unable to entangle the system with the ancilla for all initial states. We thus conclude that $\hat{\tilde{U}} = \hat{W}_S \hat{Q}_A$, where $\hat{Q}_A$ is a single-qubit gate that acts as a phase on $|+_A\rangle$. Finally, the stabilizer tableau of $\hat{W}_S$ is obtained by dropping the rows and columns of the tableau of $\hat{\tilde{U}}$ corresponding to the ancilla qubit, yielding the final identity

$$|\Psi_{f,S}\rangle = \hat{W}_S |\Psi'_S\rangle \tag{G.11}$$

for the physical qubits alone.

Appendix H

Clifford-Gaussian Page curve

Here we derive an explicit formula for the bipartite entanglement entropy $\overline{S_i}$, averaged over the set of Gaussian stabilizer states. Thanks to the mapping to the arc model, sampling a random Gaussian stabilizer state is equivalent to selecting a random configuration of the N arcs. As a straightforward combinatorial exercise, one finds that the total number of such arc configurations is given by $a_N = \frac{(2N)!}{N!\,2^N}$. The problem now reduces to counting how many of these configurations contain a given number of arcs crossing between the region $A = \{1, 2, \ldots, 2i\}$ and its complement $\overline{A} = \{2i+1, 2i+2, \ldots, 2N\}$. This number must be even, so we denote it by $2j$ (if the number was odd, it would be impossible to pair all the sites in A that are not connected to $\overline{A}$ among themselves). There are respectively $\binom{2i}{2j}$ and $\binom{2N-2i}{2j}$ ways of selecting the points to connect in A and in $\overline{A}$ respectively, and $(2j)!$ different ways of connecting them once selected. The unpaired sites in A, $\overline{A}$ can be arranged in a_{i-j} and a_{N-i-j} different configurations, respectively. Overall, this yields: $[\#\text{ configurations with } 2j \text{ arcs connecting } A \text{ and } \overline{A}] = \binom{2i}{2j}\binom{2N-2i}{2j}(2j)!\,a_{i-j}\,a_{N-i-j}$. The average entanglement is therefore obtained by summing over all possible values of $2j$ in the range $[0, \min(2N, 2N-2i)]$, which gives

$$\overline{S_i} = \frac{1}{2\,a_N} \sum_{j=0}^{\min(i,N-i)} \left[2j \binom{2i}{2j} \binom{2N-2i}{2j} (2j)! a_{i-j} a_{N-i-j} \right]. \tag{H.1}$$

With simple manipulations this expression can be simplified, and the sum performed analitically. This yields

$$\overline{S_i} = \frac{2i(N-i)}{2N-1}\,. \tag{H.2}$$

Finally, fixing $i = N/2$, we obtain the half-chain entanglement $\overline{S_{N/2}} = \frac{N^2}{2(2N-1)} = \frac{N}{4} + \frac{1}{8} + O(N^{-1})$.